Theses and Dissertations   Graduate School

2018

Advances in dual-energy computed tomography imaging of radiological properties

Dong Han

Advances in dual-energy computed tomography imaging of radiological properties

A dissertation submitted in partial fulfillment of the requirements for the degree of Doctor of Philosophy at Virginia Commonwealth University.

by

Dong Han

Director: Joshua D. Evans, Ph.D.

Assistant Professor, Medical Physics Division

Department of Radiation Oncology

Virginia Commonwealth University

Richmond, Virginia

May 2018

Acknowledgement

My deepest appreciations go to my advisor, Dr. Jeffrey Williamson for his supervision in the past six and half years. His commitment to excellence and high expectation has driven me to the fullest potential. "Being skeptical and curious", "question authority", "thinking from first principles" are the best lessons I have ever learnt in my life.

I would also like to thank my committee members: Dr. Joshua Evans, Dr. Bruce Whiting and Dr. John Chetley Ford for their guidance and support. I am also grateful to my collaborators at Washington University: Shuangyue Zhang, Dr. David Politte and Dr. Joseph O'Sullivan

Last but not the least, I am grateful for support, patience and love from my family members: Shirong Chen (mother-in-law), Le Han (sister) and Xudong Wang (brother-in-law).

Dedication

献给我的妻子：姜晓丽

To my wife - Xiaoli Jiang

献给我的妈妈和爸爸：李玉珍和韩树新

To my parents - Yuzhen Li and Shuxin Han

Table of Contents

Preface

This dissertation is based on the following peer-reviewed papers referred to in the text by the roman numerals

I. Dong Han, Jeffrey V. Siebers and Jeffrey. F. Williamson, "A linear, separable two-parameter model for dual energy CT imaging of proton stopping power computation", **Med. Phys. 43(1), , 2016, 600-612**

II. Dong Han, Mariela Porra-Chaverri, Joseph O'Sullivan, David Politte and Jeffrey Williamson, "Technical Note: On the accuracy of parametric two-parameter photon cross-section models in dual-energy CT applications", **Med. Phys. 44(6), 2017, 2438-2446**

Abstract

ADVANCES IN DUAL-ENERGY COMPUTED TOMOGRAPHY IMAGING OF RADIOLOGICAL PROPERTIES

By Dong Han, M.S.

A dissertation submitted in partial fulfillment of the requirements for the degree of Doctor of Philosophy at Virginia Commonwealth University.

Virginia Commonwealth University, 2018

Major Director: Joshua. D. Evans, Ph.D.
Assistant Professor, Medical Physics
Department of Radiation Oncology

Dual-energy computed tomography (DECT) has shown great potential in the reduction of uncertainties of proton ranges and low energy photon cross section estimation used in radiation therapy planning. The work presented herein investigated three contributions for advancing DECT applications. 1) A linear and separable two-parameter DECT, the basis vector model (BVM) was used to estimate proton stopping power. Compared to other nonlinear two-parameter models in the literature, the BVM model shows a comparable accuracy achieved for typical human tissues. This model outperforms other nonlinear models in estimations of linear attenuation coefficients. This is the first study to clearly illustrate the advantages of linear model not only in accurately mapping radiological quantities for radiation therapy, but also in providing a unique model for accurate linear forward projection modelling, which is needed by the statistical iterative reconstruction (SIR) and other advanced DECT reconstruction algorithms. 2)

Accurate DECT requires knowledge of x-ray beam properties. Using the Birch-Marshall[1] model and beam hardening correction coefficients encoded in a CT scanner's sinogram header files, an efficient and accurate way to estimate the x-ray spectrum is proposed. The merits of the proposed technique lie in requiring no physical transmission measurement after a one-time calibration against an independently measured spectrum. This technique can also be used in monitoring the aging of x-ray CT tubes. 3) An iterative filtered back projection with anatomical constraint (iFBP-AC) algorithm was also implemented on a digital phantom to evaluate its ability in mitigating beam hardening effects and supporting accurate material decomposition for in vivo imaging of photon cross section and proton stopping power. Compared to iFBP without constraints, both algorithms demonstrate high efficiency of convergence. For an idealized digital phantom, similar accuracy was observed under a noiseless situation. With clinically achievable noise level added to the sinograms, iFBP-AC greatly outperforms iFBP in prediction of photon linear attenuation at low energy, i.e., 28 keV. The estimated mean errors of iFBP and iFBP-AC for cortical bone are 1% and 0.7%, respectively; the standard deviations are 0.6% and 5%, respectively. The achieved accuracy of iFBP-AC shows robustness versus contrast level. Similar mean errors are maintained for muscle tissue. The standard deviation achieved by iFBP-AC is 1.2%. In contrast, the standard deviation yielded by iFBP is about 20.2%. The algorithm of iFBP-AC shows potential application of quantitative measurement of DECT. The contributions in this thesis aim to improve the clinical performance of DECT.

1 Introduction

1.1 Introduction to computer tomography and research background

The term tomography comes from Greek words tomos (a cut, or a slice) and graphein (to write, express). X-ray computed tomography (CT) refers to a procedure of imaging that utilizes the x-ray to view the organs, bones or other tissues inside of the body in thin "slices". It provides a noninvasive technique for mapping the 2D distribution of attenuation coefficients of anatomic organs within a transverse section of the body from a series of 1D projection made over a wide range of angular positions.

Since the introduction of first clinical scanners, due to the advances in hardware and developments in reconstruction algorithms, the acquisition time for a single slice has dramatically decreased and spatial, temporal and low-contrast resolutions have been greatly improved. Images acquired on modern CT scanners not only show an accurate representation of patient's anatomical information, but also characterize the physiological functions of tissues in the case of CT perfusion.[2] CT scanners are used to acquire volumetric scans of patients for radiation therapy planning. Thanks to the development of flat panel detector system, it now has been integrated into the radiation delivery system, i.e., using cone-beam CT (CBCT) to minimize the inter-fractional targeting error or for daily dose recalculation. [3] Recently, CT has been combined with positron emission tomography (PET),[4] so that functional images can be fused or co-registered with anatomical images to help physicians stage cancer patients.

The most important output information from a CT image is its intensity. Although the reconstructed images represent the linear attenuation distribution of scanned objects, the actual intensity used in CT is the Hounsfield Unit (HU) and defined as

$$CT \ number = \frac{\langle \mu \rangle - \langle \mu_{water} \rangle}{\langle \mu_{water} \rangle} \times 1000 \quad (1)$$

$\langle \mu \rangle$ and $\langle \mu_{water} \rangle$ refer to the averaged linear attenuation of scanned object and water over the acquisition spectrum. Specifically, quantitative measurement of CT number has

become an effective and accurate method for non-invasive quantitative determination of bone mineral content. For example, quantitative CT (QCT) images can help establish the one-to-one correspondence of attenuation coefficients with bone mineral density. [5–7] Nowadays, QCT has also been widely applied in a broader sense to dose calculation in radiation therapy.

       o   Clinical Rationale

Since its launch more than two decades ago, the American Association of Physicists in Medicine Task Group 43 (AAPM-TG43) [8, 9] dose calculation formalism has become a standard of brachytherapy dosimetry clinical practice. The TG43 dose calculation method is based on the parameterization and superposition of a single source symmetrically positioned in a pure liquid water phantom. Recent studies [10, 11] have pointed out the limitations of TG43 due to inherent physical simplifications: 1) difference between absorbed dose in water and tissues; 2) difference between radiation attenuation in water and tissues, etc. The extent to which such limitations influence the dose accuracy depends on the treatment site and source energy. For example, the assumption that human tissues are considered water-equivalent for dosimetric purposes is valid only for MV photons and high energy brachytherapy sources, e.g. ^{192}Ir and ^{137}Cs, but not so for low energy seeds ^{125}I and ^{103}Pd, where photoelectric effect dominates the energy deposition. As the photoelectric effect is approximately proportional to the cube of effective atomic number and inversely proportional to the cube of photon energy, the differences in mass-energy absorption coefficients between tissues (e.g. cortical bone) and water can result in significant dosimetric difference. [12, 13] Some recent studies found that for ^{103}Pd permanent seed implant dose calculations based on TG43 formalism overestimate the dose to the target (D_{90} by 10-40%).[14] In contrast, the recently release Task Group 186 [15]report delivered a guidance on model-based dose calculation algorithms (MBDCA) for brachytherapy dose calculations. MBDCAs offer the possibility of modeling radiation transport in non-water media, leading to more physically accurate reconstruction of dose distribution. One of key steps of MBDCAs is the assignment of interaction cross sections on a voxel-by-voxel basis for computing the dose. For low energy brachytherapy, particularly, it is crucial to have the

knowledge of tissue mass density and atomic number distributions on voxel-wise. This is achieved by single energy CT (SECT) imaging and patient modeling.[15] Through the QCT images, segmentation, i.e., the spatial delineation of different regions and bulk assignment of known elemental composition, can be realized. However, the difficulties associated with SECT and bulk assignment approaches are: first, it is difficult to know the achieved accuracy due to missing in vivo gold standard; second, patient specific composition may deviate from the recommended composition significantly, e.g., calcification in breast or prostate. [13]

In proton radiation therapy, the QCT technique has been used clinically in estimation of proton stopping power ratio (SPR),[16] which is a crucial parameters for proton treatment planning. The stoichiometric calibration technique based on SECT is the most widely implemented method for determining proton stopping power ratios for human tissues. This technique assumes the existence of a one-to-one correspondence between HU and proton stopping power, then creates a look-up-table to derive stopping power based on calculated HU of ICRU tissues with known elemental composition at a single tube potential. However, the stoichiometric technique based on SECT in proton therapy still cannot provide sufficiently accurate guidance for the task of mapping the stopping power on a voxel-by-voxel basis [17] due to the fact that there is no one-to-one correspondence between HU and SPR.

A promising family methods for non-invasively but more quantitatively characterizing the tissue heterogeneities quantitatively based on DECT, has been investigated.[18–20] The exuberance of early work in DECT is reflected in the adoption of term "tomochemistry"[21]following DECT success in quantifying the bone mineral content[22], measuring the composition of dense tumor,[23] and determining red marrow distribution.[24] The idea of DECT imaging is to scan patients at two different spectra, commonly low- and high-energies, sequentially or simultaneously. Based on the measurements of two values of each voxel, DECT technique, is able to distinguish the variations in the radiological quantity of interest due to changes in morphology (electron density) and chemical composition (effective atomic number), or due to changes of basis material weight. This

technique involves two basic steps: two-parameter modeling and decomposition process.

- Two parameter modeling is a mathematical approximation process, which is able to reproduce the radiological quantity of interest for naturally occurring biological tissues in terms of two parameters, which represent computable (given density and atomic composition, there exists an algorithm for computing the associated parameter values) pseudo-properties of the underlying tissue. More discussions of two-parameter models can be found in Chapter 2.

- Decomposition process is a process of estimating the parameter values given the signal intensities from low and energy images.

  o Engineering Rationale

The CT image reconstruction algorithm also contributes to uncertainties of estimating radiological quantities. The most commonly used algorithm is filtered backprojection (FBP), [25] which is a closed-form and highly efficient reconstruction solution. In the derivation of FBP algorithm, it is assumed that an infinitely small x-ray source is able to emit monoenergetic photons through scanned objects. There is no statistical noise associated with acquisition process. The shape and size of detectors and pixels are disregarded. Each line integral from source to detector represents an accurate measurement and not influenced by statistical fluctuations. However, those assumptions may not be valid in reality. In practice, the size of the x-ray focal spot is not negligible, and the emitted spectrum is broad and polyenergetic, which is the main cause of beam hardening artifacts (see Ch.5 for more discussions). The reconstructed image voxel size is dependent on the choice of field of view (FOV) and slice thickness. The measured response of CT detectors is affected by photon counting statistics and absorption of scattered photons. Thus, images reconstructed by FBP suffer from data non-ideality on real CT scanners. One way of incorporating acquisition data statistically is to implement a new algorithm called statistically iterative reconstruction (SIR). [26] In general, the measured noise signal can be modelled as a simple Poisson distribution or

a compound Poisson [27, 28]. The data formation process can be more accurately approximated by models including the characterization of x-ray tube, the presence of bow-tie filter, beam hardening effects, scatters and so on. With accurate modelling, the advantages of SIR over the FBP algorithm include improvements in spatial resolution, noise, low-contrast visibility and artifacts.[29, 30] The cost of SIR is that the computation complexity is significantly higher than that of the analytical reconstruction algorithm FBP.[25]

In the stage of decomposition, the uncertainties may arise from the inherent instability of decomposition process, i.e. its ill-conditionedness.[31] For an ill-conditioned decomposition process, minor uncertainties in the input data may cause the errors in the final radiological quantity value to be amplified in the decomposition result. Besides reducing random and systematic uncertainties of the input data, earlier in reconstructed images or projection measurement, one can improve the conditioning of decomposition process by increasing the separation or minimizing the overlap of two x-ray spectra,[21] Recent studies have confirmed its efficacy in increasing numerical stability of decomposition process.[32]

The goal of this research presented here is to showcase the progress we have made in related aspects of DECT for mapping radiological quantities for both proton and photon radiotherapy. Three aspects are covered. First, a simple linear two-parameter model, which is compatible with the polyenergetic SIR algorithm, is investigated for estimation of proton stopping powers and photon cross sections. Second, a practical method for deriving DECT x-ray spectra, a crucial step in modeling the formation of signal of acquired signal by CT scanner, is outlined. Third, as an alternative to computationally intensive SIR reconstruction algorithms, an iterative FBP algorithm is adapted using a priori information on tissue composition uniformity to improve the conditioning of the decomposition process.

The following sections spell out the rationale and background of this research. First, the most commonly used x-ray CT image reconstruction algorithm filtered backprojection is reviewed along with its inherent uncertainties is reviewed. The premise of quantitative CT application is also presented. The specific issues of applying quantitative SECT to

proton therapy and low energy brachytherapy are also outlined. Second, techniques of x-ray spectrum determination are reviewed. Third, the rationale of development of a mode-based polyenergetic iterative FBP algorithm is presented. Last, the research organization is outlined.

1.1.1 Filtered back-projection (FBP) x-ray CT image reconstruction

In order to elucidate the uncertainties associated with images reconstructed by FBP, an introduction of FBP is presented below.

Suppose we take a series of projection measurements, also called line integrals, each of which represents the summation of attenuation coefficients of the object along a particular ray path under spectrum $S(E)$, i.e., forward projection (FP) (shown in Fig.1.1)

$$FP\big(\mu(x,E)\big) = -\log \int S(E) \exp\Big(-\int \mu(x,E)\,dx\Big)\,dE \quad (2)$$

$\mu(x,E)$ denotes the linear attenuation coefficient of the scanned subject at location x and energy of E. In this study, photon cross-section collectively refers to the attenuation coefficients, including linear attenuation, photoelectric, Compton scattering, and energy absorption coefficients, etc.
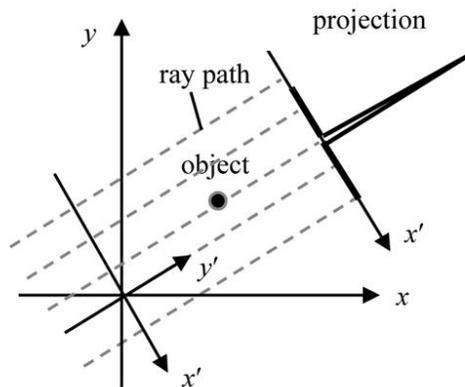

Fig.1.1. Illustration of FP of unknown object to produce projection measurement.

Figure Credit: Jiang Hsieh[25]

These measurements are collected along different angles and distances from the isocenter. For CT image reconstruction, the problem is how to recover the distribution of attenuation coefficients of a scanned object based on these measurements. The Back-projection process simply treats this problem as "painting" or "superimposing" the measurements uniformly along the ray path that produces a sample of projection. A filter function in spatial domain $1/r$ is applied to remove the blurring caused by back-projection process.[33] A further modification of filter function can be multiplied with the window function to shape the filter's frequency response. Filtered backprojection (FBP) was introduced to incorporate the step of backprojection in the 1970s. Although the advancement of hardware of CT scanner has taken place in the past decades, FBP is still well recognized and remains the dominant and most popular image reconstruction algorithm due to its low computation cost and acceptable image quality.

1.1.2 Uncertainties of CT images

As indicated in previous section, the uncertainties in FBP reconstructed images are due to mismatch between assumption and reality on CT scanners. There are two types of errors occurring in CT images if those assumptions are violated.

- **Random errors**

Measured projections exhibit statistical fluctuations or noise due to the random processes of photon generation, photons exiting from the patient, and photons absorbed in the detectors. Photon counting noise in the projections will propagate into image and introduce uncertainties in image interpretation, specifically in resolving low contrast objects. Noise levels in the CT projection acquisition stage can be affected by factors including slice thickness, tube voltage, tube current, reconstruction algorithms and size of scanned objects. This source of noise is dominated by number of photons that are collected by detectors. For example, this type of noise can be reduced by increasing the tube current, tube voltage or slice thickness. The tradeoff of these techniques emerges between noise level or 3D image quality and partial-volume effect. Noise levels in a CT image reconstruction stage can be attributed to the choice of reconstruction kernels, reconstruction algorithm, and image matrix size. For example,

the noise can be reduced by using a kernel function that only preserves low-frequency contents of projections. The tradeoff of this technique is to compromise the resolution of reconstructed image, i.e. the edges of high frequency structures will be smeared.

- **Systematic errors**

The FBP algorithm also assumes that the logarithm of transmission sinogram is linearly proportional to the attenuation line integral, a condition that is satisfied only if the photons emitted from x-ray source are approximately monoenergetic. This assumption implies a linear relationship between measured projections and scanned object thickness. In reality, the photon energy spectrum of clinical scanners beam contains a wide range of energies up to the tube potential. The linear attenuation coefficients of scanned objects vary rapidly with the x-ray energy; thus the nature of poly-chromaticity leads to a non-linear effect, called the beam hardening (BH) effect, which can cause average energy of the x-ray beam to increase as the beam transverses the scanned materials since lower energy x-ray photons are preferentially attenuated, yielding artifacts in the FBP reconstructed images, i.e., cupping, streaking and non-uniformities. In order to linearize the data, one of the most commonly used correction methods is water-based BH correction proposed by Brooks et al. [34] and McDavid et al.[35] This method uses a look-up-table or polynomial correction, so that the corrected projection represents monoenergetic attenuation based on the assumption that the scanned subject is water equivalent. As pointed out by Joseph and Spital,[36] in the real clinical world, residual artifacts may persist if patients contain tissue that significantly deviate from water.

Another important effect that FBP fails to incorporate is photon scattering due to coherent and incoherent scattering of primary photons by the scan subjects, and causing lower attenuation estimation on the reconstructed images.[37–41] A consequence of ignoring scatter effect in the image reconstruction is a reduction of contrast and signal-to-noise ratio. For example, a cupping effect can be easily visible similar to BH artifact. To characterize the scatter contribution, a quantity, called scatter-to-primary ratio (S/P), is used but rather difficult to determine. And with exact knowledge of S/P, scatter signal can be subtracted from transmission raw data.

There are other sources of measurement inaccuracies that can contribute to systematic errors in FBP reconstructed images. For example, patient motion during the data acquisition, off-focal radiation of x-ray source, the photon starvation caused by presence of metal objects, etc. Those uncertainties will undermine the accuracy of quantitative CT images applications, which will be described later in this chapter.

1.2 Quantitative Applications of CT

Historically, quantitative CT referred to using absolute HU numbers to evaluate bone mineral density at lumber spine and hip, this technique was invented in the 1970s. [5, 22, 42, 43] Nowadays quantitative CT implies any utilization of CT image intensities, including spatial measurements, radiological attenuation, etc., to make numerical estimates of a well-defined attribute of the underlying tissue.[7, 24] For example, in the diagnostic imaging field, the volume measurements of lung nodules in CT images can be used in lung cancer screening.[44] For treatment planning of light ion charged particles, CT images of the patients are used to map stopping power to estimate the range of ions. Regardless of applications of QCT, one of the requirements for CT images is consistency, which indicates that the reconstructed CT values need to be a true representation of the material and not influenced by the presence of other objects[25], i.e., no severe deviations from ambient uniformity occur. The challenges of achieving high consistency lie in the fundamental physics of CT signal formation, e.g., beam hardening effect. The CT values of the material are therefore subject to the presence of other objects in the FOV. For example, in low energy brachytherapy, in order to achieve a 3%-4% linear attenuation estimation error at 30 keV, an error propagation analysis suggests that uncertainties in reconstructed image intensities must be less than 0.5%.[20, 45] To achieve the 0.5% bias of accuracy, it demands that the CT image reconstruction algorithms should be able to incorporate all physical processes of signal formation to suppress uncertainties, such as beam hardening, since CT number of the scanned object may be influenced by the surrounding materials inside of FOV. For example, the presence of metal objects can cause streaking artifacts to the near objects.

With consistent CT images, the technique of QCT has shown great promise in applications of radiation therapy, i.e., heavy charged particle therapy [46]and

brachytherapy with low energy seeds. [15]The following subsections will review the specific issues that have arisen in the above fields, which in turn inspire us to develop a task-driven framework, i.e., quantitative imaging for radiation therapy, including physics modeling, derivation of spectrum and an accurate and robust CT image reconstruction algorithm to suppress the uncertainties of QCT problem.

1.2.1 Range uncertainties due to tissue heterogeneity in proton therapy

Currently, proton beam therapy has gained popularity due to its ability to deposit highest dose to target while sparing the normal tissues distal to the Bragg peak.[47] The position of the Bragg Peak, where the maximum dose is deposited just before the proton stops, is determined by the proton stopping power ratios (SPR) relative to water along the proton beam path.

Therefore, in order to accurately predict the proton range, one requires the knowledge of the SPR along the proton path, or alternatively, the atomic composition and density of all tissues along the path so that SP can be computed via the Bethe equation.[48] In the current state-of-the-art clinical practice, the SPR distribution is derived from single-energy CT (SECT) images for treatment planning, via a process called stoichiometric calibration,[16] which can be found with more detailed discussions in Chapter 2.

Stoichiometric calibration introduces two sources of SPR estimation errors: first, the random and systematic image-intensity uncertainties embedded in CT images can propagate uncertainties into the SPR predictions.[49] The second is associated with the uncertainties inherent to the stoichiometric calibration process itself.

The second uncertainty in the SECT based stoichiometric calibration is that the one-to-one correspondence between CT number and SPR of human tissues is compromised by the "degeneracy issue" suggested by Yang et al.[50] Human tissues with different CT numbers may have similar SPRs, while those with different SPRs may have similar CT numbers. Because of this issue, the conversion curve of CT values to SPR has uncertainties that can't be ignored. Moreover, elemental compositions of tissues in the patients may deviate from standard tissue composition data provided by values recommended by ICRU or ICRP reports.[51, 52] Thus, the degeneracy issue and

dependence on calibration training samples makes the stoichiometric calibration method more susceptible to variations in tissue compositions from expected configurations. These uncertainties associated with stoichiometric calibration method introduce errors into patient SPRs maps. For example, Schneider et al [53] found that the measured Bragg peak depth in dogs treated for nasal tumors deviated from the peak depth estimated by a state-of-the-art quantitative single energy CT (QSECT) stoichiometric calibration method by 3.6 mm on average. To overcome the above shortcomings of SECT, DECT methods were introduced to characterize tissue heterogeneities for mitigation of range uncertainties associated with CT images. For example, Yang et al. [54] first presented a framework using DECT to estimate electron density and effective atomic number of tissues for determining their proton SPRs. Bourque et al. [55] and Hünemohr et al [56] introduced extensions the SECT based stoichiometric calibration to a DECT based calibration to improve the estimation accuracy of SPR. Reported theoretical errors for typical tissues could be below 0.3%, [55] while the achieved experimental accuracy for phantom materials could be up to 1%.[56]

1.2.2 Low energy brachytherapy dosimetry

Brachytherapy refers to placing sealed radioactive source within or close to the target tissues. Due to rapidly falling-off dose with increasing the distance, high dose may be delivered safely to a localized region compared to conventional external beam therapy. Permanent seed brachytherapy (PSB) with low energy (<50 keV) photon emitters plays an important role in the treatment of prostate cancer and breast cancer.

Since the 1980s, the emergence of ultrasound-guided transperineal techniques and computer-optimized preplanning has improved prostate and breast cancer treatment, as it allows more accurate placement of seeds to deliver the prescribed dose to the prostate reliably. Zelefsky et al. [57] claimed that suboptimal D_{90} dose levels in PSB conferred an approximate 2.5-fold increase for biochemical relapse to the patient. However, Chen et al.[58] reported that morbidity after prostate brachytherapy was common due to escalated doses. In their series, 54.5% of men were given a complication-related diagnosis within 2 years, with 14.1% undergoing an invasive procedure to manage complications. Morbidity rates for urinary, bowel and erectile

function were 33.8%, 21.0% and 16.7%, respectively. [58] Thus, the goal of improving the outcome of PSB, while reducing the morbidity of escalated dose to patients, is highly desirable.

It was reported that among the newly diagnosed breast cancers, 20-30% of them are ductal carcinoma in situ (DCIS) cancers. [59]To treat the DCIS, a breast-conserving surgical excision followed by adjuvant radiotherapy, e.g., accelerated partial breast irradiation (APBI) is usually implemented. One type of APBI implementations is called permanent breast seed implant (PBSI), which uses ultrasound guidance to permanently implant ^{103}Pd brachytherapy seeds.[60] Among the possible systematic and random uncertainties of adversely affecting PBSI clinical outcomes, it is estimated that systematic dose errors in ^{103}Pd dosimetry due to ignoring the non-water equivalence of tissue could be as high as 10%-40% for breast tumors. [59] More specifically, the results based on calculations using the TG43 formalism overestimate dose to target (D_{90}) by 10-40%,[14, 61, 62] and underestimate the dose to the skin (D_{10}) up to 30%.[14] compared to Monte Carlo dose calculations. Such dose discrepancy is mainly due to the fact that the standard TG43 dose computation algorithm disregards complexity and variation of patient tissue composition inhomogeneities by assuming that patients consist of uniform liquid water. Another example of APBI implementations is using a miniature x-ray electronic brachytherapy source called the Xoft Axxent Source.[63, 64] The Source has the capabilities of operating voltages covering from 20 to 50 kV, providing the photons with energies less than 50 keV. It is reported that dosimetric uncertainties associated with tissue heterogeneities, e.g. skin does, could be up to 24%.[65]

To reduce dose computation errors due to tissue heterogeneities, one possible strategy is to integrate the knowledge of patient tissue composition into the dose computation algorithm. Hence, in the past decades, in response to heterogeneities and other shortcomings, brachytherapy dose calculation algorithms have evolved to 3D images-based model-based dosimetry algorithms (MBDCA), which collectively refer to deterministic and Monte Carlo solvers of the linear Boltzmann transport.[66]

One of the challenges in deploying MBDCA is the assignment of interaction photon cross section on a voxel-by-voxel basis. For low energy brachytherapy dosimetry, the

knowledge of tissue composition distribution, i.e., electron density and atomic number distribution is required. There are several schemes proposed: the first is tissue assignment scheme through segmentation as tissue with known composition. The caveat of this scheme is that although the average composition of human tissues and organs are reported by ICRU,[51, 67] the prostate, breast, and other surrounding tissues may have highly variable patient and position-dependent compositions, in other words, actual tissue compositions may deviate from the recommended values. Recent studies suggest that using dual-energy CT (DECT) technique can achieve more accurate tissue segmentation[18, 19, 59, 68, 69], with assigned recommended tissue composition than SECT implementations. For example, dose comparison studied on phantom material showed that D_{90} could be underestimated by up to 2.3% using SECT, compared to 0.75% for DECT.[70] Bazalova et al.,[18] Landry et al.,[19] and Remy et al.[69] proposed a DECT-based segmentation schemes to assign tissue composition for dose calculation. With the known composition for the assignment, the dosimetry errors are reported below 5%.[69]

The second scheme is through DECT voxel-wise estimation. As the time of writing, very few studies of DECT techniques have been reported to address the challenge in the 20-50 keV energy range. For example, Evans et al.[20] first experimentally implemented image-domain decompositions of DECT images on a Philips Brilliance scanner. They demonstrated that the linear attenuation coefficients at 28 keV could be measured with an accuracy of 1% or better provided that the phantom geometries of the unknown substances and basis substance calibrations were identical. They also systematically evaluated the sensitivity of reconstructed images uncertainties and identified that maximum image intensity uncertainties threshold for acceptable (3%) linear attenuation coefficient uncertainty in low energy range (20-30 keV). Goodsitt et al.[71] recently reported the estimated accuracy of effective atomic number from synthesized monochromatic CT image using GE fast-switching DE scanner is on the order of 1% to 20% in the range of 40-120 keV. Although no attenuation coefficients estimated in lower energy range, the sensitivity analysis were also implemented.

1.3 X-ray spectrum determination

As indicated above, the knowledge of the x-ray spectrum is required to implement polychromatic SIR algorithms that remove the beam-hardening and scatter effects in a principled way. Accurate knowledge of dual-energy spectra is also required to implement a sinogram-based DECT decomposition technique. In addition, x-ray CT spectra are also needed in dose computation for CT scan, Monte Carlo simulation for energy deposition in a human body and quantitative DECT material characterization. [72]

Fukuda et al found that the x-ray spectra on CT scanners can drift over time, by as much as 11.4% [73] This drift may be due to tube aging, replacement or high voltage power supply. For quantitative CT application, the spectrum needs not only to be measured accurately, but also evaluated on a regular basis, which would otherwise cause inaccurate estimation of effective atomic number. [74]

Thus far, there are roughly three categories of methods to determine the x-ray spectra: direct measurement via spectroscopy using pulse-height detectors, [75] indirect measurement-based [72, 76–80] and Monte Carlo simulation. [81,82] Direct measurement involves usage of energy-resolving detectors, i.e., cadmium telluride (CdTe), [75] cadmium zinc telluride (CdZnTe) [83] or high purity germanium. [84] However, pulse-height counting detectors produce accurate results only for relatively low photon flux rates, much smaller than high flux rates employed by CT scanners. Thus direct measurement of CT spectra is not trivial. In addition, such instrumentation requires a very strict measurement procedure: low measurement temperature, calibration with radioactive material (^{241}Am and ^{133}Ba), [72] and pulse height spectra processing, i.e. "stripping", to extract the primary spectra from the raw measurement s which are degraded by escape of characteristic x-rays and Compton photons form the detector, which most radiation oncology or radiology departments do not have access to. Other direct measurement techniques may include Compton scattering based method. Yaffe et al. [38] and Matscheko et al. [85] used the spectrometer to record scattered photon energy flux at a particular angle, and reconstructed the incident primary spectrum.

Indirect measurement refers to techniques that estimate spectra from narrow-beam transmission or attenuation measurements of mental attenuators of known thicknesses and compositions. Reconstructing spectra directly from transmission data is to solve a set of linear equations for weights of each energy bin in spectrum. Although it is straightforward, this empirical method is highly ill-conditioned and sensitive to uncertainties of transmission measurement. [76] To avoid such issues, semi-empirical models, e.g. the Birch-Marshall thick target Bremsstrahlung model[1] that are based on physical parameters, including target angle, kinetic energy of incident electrons, target materials and inherent infiltration, are used to estimate spectra.[1, 86] The characteristic radiation can also be included to the continuum radiation according to an empirical power law relationship.[1] Another example of semi-empirical model is called TASMIP by Boone et al. [87] TASMIP is a code that takes the published spectra data by Fewell et al. [88]and tries to interpolate them with constant potentials. One of the drawbacks of semi-empirical models is that they still require narrow-beam transmission measurements. In addition, these measurements have to be acquired using a special service mode, which is not always available to physicists. A comparison was implemented by Ay et al. [89]to show that the Birch-Marshall model predictions and direct measurements within 1.1% for 140 kVp spectrum for tungsten target.

Monte Carlo (MC)[81, 82, 90,89,91, 92] simulation provides another alternative to estimate x-ray spectrum, given that the x-ray tube, beam filters, accelerating potential, phantom (patient) geometry and detector components are accurately modeled. It simulates the direct transport of electrons and produced photons in the target and filter to estimate X-ray spectra. This method is potentially superior to any other.[81] However, it is unable to fully account for the details of scanner-specific hardware parameters, i.e. the used condition of individual tube and bowtie filter at the time of simulation.[78] Also, it would be difficult to acquire the knowledge of electron energy spectrum incident on the target required by MC simulations. Other factors, including knowledge of kVp, ripple and any impedances in series with target and cathode, limit the routine use of MC method.

1.4 Model-based iterative x-ray CT image reconstruction

Evans et al. [20] experimentally found that an advanced polyenergetic statistical reconstruction could support cross-section estimation at low energy range (20 -30 keV) to a target accuracy of 3% or less, with less imaging dose and significantly better spatial resolution than estimates derived from FBP images. By using identical calibration and experimental geometries, they managed to control the systematic errors and found that for a given dose, SIR propagates much random errors than FBP, necessitating less voxel averaging.

In order to mitigate the systematic errors that are failed to be considered by FBP algorithm, a variety of techniques have been developed.[93–98] One of the most sophisticated techniques is model-based iterative reconstruction (MBIR). MBIR allows incorporation of accurate and realistic modelling of the signal formation process to match its counterpart on the CT scanners. For example, such modelling includes the characterization of the x-ray spectrum, the filtration including bowtie, detector's response, beam hardening effect, scatter and other non-linear effects.[25] The x-ray spectrum exiting the tube is modulated by the bowtie filter, of which its path-length is function of fan-beam angle. The detector response as function of energy and each projection angle is also modelled. Theoretically, a forward projection model that better mirrors the actual signal formation will better match measured raw CT scanner projections, thereby mitigating artifacts; consequently, reconstructed images will show an improved image quality, including HU improved accuracy and consistency.

Due to the statistical nature of measurements, the measured projections will randomly deviate from their expected mean values, in other words, the above modelled forward projections can be fully accurate only for noiseless measured projections. Thus, statistical modelling is incorporated into the model and leading to the name "statistical iterative reconstruction (SIR)". [30, 95, 99]

In general, MBIR and SIR algorithms have shown improvement in image quality in noise, spatial resolution and low-contrast visibility.[25] With reduction of systematic errors in

reconstructed images, SIR has demonstrated promise in application of quantitative DECT for more consistent and accurate estimation of photon cross section.[20]

Another advantage of the SIR algorithm is its potential of reducing radiation dose to patients, especially for pediatric patients, where dose reduction is of great concern. It is has been shown by Evans et al. that alternating minimization (AM), one type of the SIR algorithms, has the potential to reconstruct images with comparable noise and spatial resolution using only 10%-70% of the FBP dose.[100]

However, the main disadvantage of a model-based iterative algorithm lies in their high computational cost and not ideal for clinical applications. Unlike FBP reconstruction with its single iteration, SIR requires many hundreds of iterations, each involving multiple forward and backprojections. Moreover, forward projecting the patient linear attenuation map for each spectral energy bin is also time-consuming. Although computer hardware has advanced and SIR has been implemented on modern GPUs, clusters and workstations, the needed time for convergence is still high compared to analytical method; therefore it is not ready for clinical applications. Another hurdle is that SIR images may exhibit noise and streaking artifacts quite different than those of the conventional analytical method. It may result in image misinterpreted by radiologist and require a relatively long time for them to become experts in interpreting images reconstructed by iterative algorithm. [101] Combining the fast convergence of FBP, and maintaining the consistent and accurate estimation of photon cross section of SIR motivates us to develop a model-based iterative FBP reconstruction algorithm.

1.5 Research Organization

The purpose of this dissertation is to summarize my studies that advance the capability of DECT to accurately map radiological quantities. To date, there are several two-parameter cross-section models useful for DECT,[102, 103] which have been adapted to proton stopping power estimation.[54] Simulations [54, 55, 104] and some clinical experiments [56] demonstrate improved accuracy relative to the SECT stoichiometric technique.[54] However, most of these two-parameter models are non-linear and lack closed form solutions. Moreover, almost all of the above models have been used for image domain

analysis, i.e., post-processing analysis, which is vulnerable to various image uncertainties, especially CT image intensity nonuniformity artifacts. A major goal of this dissertation is to assess performance of a linear model-based dual-energy x-ray CT reconstruction algorithm, especially how it is compared with conventional methods that have been extensively used image-domain analysis. Chapter 2 explores the possibility of using a linear and separable two-parameter model for mapping of proton stopping powers. A systematic comparison between two distinct models has also been implemented, including achieved stopping power prediction accuracy for recorded tissues, and robustness to composition and CT imaging uncertainties.

Chapter 3 proposes a modified parametric fit model (mPFM), designed to improve two-parameter modeling of linear attenuation coefficients for mixtures and compounds, and evaluated its performance relative to competing models. The linear basis vector model with single and double basis pairs, as well as the widely used Torikoshi PFM (tPFM) [102]model were implemented and compared to our proposed mFPM model. By evaluating the achieved accuracy of monoenergetic photon cross sections estimated by above models, this chapter will provide theoretical foundation for building a model-based reconstruction algorithm. In this thesis, photon cross-section refers to a collective set of definitions of attenuation coefficients, including total, photoelectric, scattering and energy absorption.

Chapter 4 outlines a new method of deriving x-ray CT spectra from the vendor's beam hardening correction, the parameters of which are embedded in the header of every acquired CT sinogram. It aims to provide a simple and accurate x-ray spectrum estimation technique, which can also be applied in quality assurance of an x-ray source, which may drift from expected values due to tube aging.

Chapter 5 describes development of a model-based iterative polychromatic filtered back projection x-ray CT image reconstruction algorithm. The motivation of this algorithm is to seek an iterative algorithm for quantitative DECT application that is able to account for non-linear artifacts but with much lower computational cost than SIR. We propose to anatomically constrain a BVM surrogate for atomic composition to better condition the decomposition of DECT. Effectively, our method assumes that atomic composition is

uniform in each a priori segmented tissue type, but allows voxel-to-voxel variations in density. Initial simulation results of photon cross-section estimation and comparison with similar algorithm are also reported.

Finally, Chapter 6 concludes with remarks on current research on quantitative dual-energy CT imaging research.

2 A linear, separable two-parameter model for dual energy CT imaging of proton stopping power

2.1 Background

Treating deep-seated tumors with protons was first proposed by Wilson[47] in 1946. In that paper, the biophysical rationale and engineering delivery issues were outlined. The main advantages of proton therapy are the decreased total energy deposited inside patient and finite range of the proton beam.[105] Before protons stop, monoenergetic protons can present a low entrance dose, deposit the maximum dose close to the end of range, where sharp dose fall-off region is termed as Bragg-Peak. The unique high dose gradient area, around Bragg-Peak, can possibly better conform dose to the target while sparing the surrounding normal tissues. Thus, it is desired to have exact knowledge of how much energy is lost due to interactions between protons and human tissues for proton therapy treatment planning.

However, one of major limitations in proton therapy is range uncertainties,[105] i.e., uncertainty in our knowledge of Bragg-peak depth. Due to range uncertainties, the advantages of proton therapy may be compromised. [105] In the current proton therapy practice, a margin with (2.5% - 3.5%) of proton range plus additional 1 mm is often used.[105] For example, a typical proton range with energy 200 MeV in muscle tissue is about 27 cm,[106] the uncertainties of range can be translated into 6.8 mm – 9.5 mm. There are many sources contributing to the range uncertainty e.g. beam energy uniformity, patient setup, motion, tissue inhomogeneity and relative biological effectiveness [105]One of the major contributions is due to the limited accuracy of single-energy CT calibration of proton stopping power relative to water, [54]called stopping power ratio (SPR), which is used to describe the energy loss of protons in the tissue relative to water. There are mainly four types of interactions between protons and matter in proton therapy: elastic Coulomb interactions between protons and target atomic electrons, target atomic nucleus, inelastic nuclear reactions and proton Bremsstrahlung. Energy loss of protons is mainly due to the frequent inelastic interactions with atomic electrons. [107] Bethe [48] first formulated a physical theory of energy loss or stopping power as summarized below

$$S\left(E_{proton}\right) = -\frac{dE_{proton}}{dx} = \frac{k_1\rho_e}{\beta^2}\left[\frac{1}{2}\ln\frac{k_2\beta^2 T_{max}}{I^2\left(1-\beta^2\right)} - \beta^2 - \frac{\delta(\beta)}{2} - \frac{C(\beta)}{2}\right] \qquad (3)$$

where k_1 and k_2 are products of physical constants; $\beta = v/c$; v is the proton velocity, c is the speed of light; T_{max} is the maximum energy transferred to a single electron; and ρ_e and I are the electron density and mean excitation energy (I-value), respectively. The I-value depends on the composition and the density of the medium. The density correction, $\delta(\beta)$ is significant only at proton energies above several hundred MeV. The shell correction $C(\beta)$ is significant only when proton velocity is comparable to that of atomic electrons. These two corrections are usually ignored since they are negligible for the proton energies considered in this study.

2.1.1 SECT techniques

Conventionally, the proton stopping power distributions inside patients are determined based on stoichiometric calibration curve, which converts CT number to SPR values. The calibration procedure consists of four main steps:

1. Scan the calibration phantoms incorporating phantom substitute inserts whose elemental composition and density are available, and acquire the Hounsfield Units (HU)
2. Determine the best fit parameters K^{ph}, K^{coh} and K^{KN} by fitting Eqn.(4) to the measured HUs and Z* defined as effective atomic number

$$HU = \frac{1000\mu}{\mu_w}$$
$$\mu = \rho_e\left(K^{ph}\left(Z^*\right)^{3.62} + K^{coh}\left(Z^*\right)^{1.86} + K^{KN}\right) \qquad (4)$$

3. Estimate the HUs of standard ICRU tissues with provided elemental composition by using the constants from step 2.
4. Generate the calibration curve by plotting stopping power and HU for standard human tissues (Fig. 2.1).
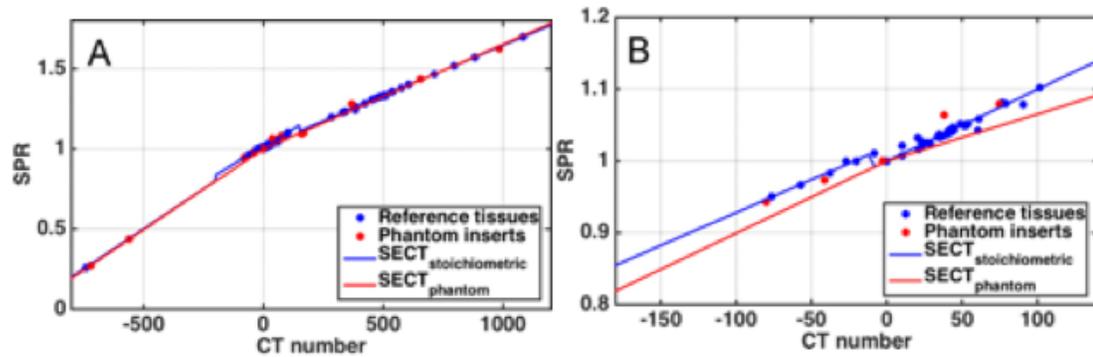
Fig.2.1 (A) Example of SECT stoichiometric calibration at 150 kVp using two linear segments implemented by Hudobivnik et al.[108]. Blue dots denote the tissues from ICRU reports, while red dots are for tissue phantom materials. (B) Enlargement of the soft tissue region. The stoichiometric calibration curves are obtained by plotting the HU and stopping power of phantom materials and tissues based on the procedure outlined in 2.1.1

The stoichiometric calibration technique has several limitations. First, it assumes that there is a one-to-one correspondence between HU and SPR. It cannot accommodate variation in electron density for a fixed tissue composition or type. In reality, the same HU may have different SPR, or tissues with different HU can also have similar SPR. Second, the stoichiometric calibration curve is built on the tissue compositions and densities recommended by ICRU tissues, which may deviate from patient-specific tissues of the same type. This causes the estimation of SPR from calibration method susceptible to variations of tissue composition. Third, commercially reconstructed SECT images often carry random and systematic errors contributing to calibration errors.[109]

2.1.2 DECT and other techniques

In the past decades, numerous methods have been proposed to determine the SPR by using proton CT or dual-energy CT (DECT) techniques theoretically and experimentally.[55, 56, 104, 108–116]

Proton radiograph (pCR) or computed tomography (pCT) use proton beams to generate 2D or 3D images, whose pixel value represents the direct measurement of SPR. It has been theoretically shown that achieved accuracy of SPR by pCT is comparable to DECT. [112] One of the issues for pCT is that the spatial resolution is limited due to the small-angle scattering of Coulomb interactions.[117]   Another limitation of pCT is that

exiting fluence of proton beam from patient is not high enough to have statistically significant output data.[118]

The principle of applying DECT techniques on proton stopping power estimation is that the two parameters used by models of photon interactions depending upon in CT measurement can be related to meaningful quantities used in Eq (3), i.e., ρ_e and *I*-value. To implement DECT techniques, there existing three different approaches and several DECT models.

DECT decomposition approaches

i. An image-domain decomposition approach is derived from two reconstructed images using x-ray projections from different energy spectra. The approximate extraction of two parameters, e.g. ρ_e and Z^*, for photon cross section model is carried out as a subsequent step. A recent typical ensemble work of using DECT on proton SPR determination based on image-domain can be found. [54–56]. Image domain decomposition can also be used in conjunction with the BVM model. [20]

ii. A sinogram-domain decomposition approach decomposes the two different energy raw sinograms into two separate two component projections, each corresponding to one of the BVM basis components before the image reconstruction process. Then the images of two components are reconstructed via FBP. The mapping process from two-component images (i.e., ρ_e and Z^*) to stopping power can be accomplished.[110]

iii. Joint decomposition approaches solve the reconstruction and material decomposition problem jointly, and their typical output consists of a basis pair images. This image pair may be used for mapping stopping power in pixel wise.[119, 120]

DECT two-parameter models and material characterization

1. Yang et al. [54] first reported that the use of DECT to extract ρ_e and Z^* can substantially reduce SPR estimation errors compared to conventional

stoichiometric calibration, potentially reducing range uncertainty. by a factor of two. The two most important parameters, ρ_e and Z* are derived from a non-linear relationship (i.e. Torikoshi parametric fit model (tPFM), discussed more details in Chapter 3) of HUs at low and high energy spectra.[18, 102]

$$\mu(x,E) = \rho_e(x)\left(Z^{*4}(x)F(E,Z^*) + G(E,Z^*)\right) \qquad (5)$$

The terms $\rho_e(x)Z^{*4}(x)F(E,Z^*(x))$ and $\rho_e(x)G(E,Z^*(x))$ represent photoelectric absorption and scattering, respectively. The pre-tabulated correction functions $F(E,Z^*)$ and $G(E,Z^*)$ were determined by forcing Eqn. (5) to reproduce exactly the linear attenuation coefficients for the elements ($Z = 2$ to 20), as tabulated by the National Institute of Standards and Technology (NIST) XCOM database. [121] To relate the Z* to *I*-values of human tissues, the empirical relationship is used

$$\ln(I) = aZ_{eff} + b \qquad (6)$$

where a and b are predetermined for soft and bony tissues separately using the theoretical I-values for ICRU standard tissues. The estimates of parameter Z* can either be spectrally averaged or treated as independent variable of monoenergetic $\mu(E,Z^*)$. Thus, this model can be applied to any one of decomposition approaches in theory.

Hünemohr et al.[56] developed an image-domain based method to estimate ρ_e and Z*. From two CT measurements, a framework based on Alvarez and Macovski [31] method was proposed to solve for ρ_e and Z*.

$$\frac{\rho_e}{\rho_{e,water}} = c_e HU_L + (1 - c_e) HU_H \qquad (7)$$

$$Z^* = \left(\left(\frac{\rho_e}{\rho_{e,water}} \right)^{-1} \left(d_e HU_L + \left(Z^* - d_e \right) HU_H \right) \right)^{1/n} \qquad (8)$$

where HU_L and HU_H represent the CT number of low-and high- energy. Two coefficients c_e and d_e spectra-specific, and a calibration protocol thus is needed to determine them.

A similar relationship between *I*-values and Z* in Eq. (6) was also used. Although this model was originally implemented on image-domain decomposition, it can easily be adapted to sinogram-domain or jointly decomposition approach. [120]

2. Bourque et al. [55] proposed a dual-energy stoichiometric calibration procedure to convert HU_L and HU_H into ρ_e and Z* with a set of polynomial functions.

$$Z^* = \sum_{k'=1}^{K'} c_k \left(\frac{HU_L - HU_H}{HU_L + HU_H} \right)^{(k'-1)} \qquad (9)$$

$$\frac{\rho_e}{\rho_{e,water}} = \frac{HU_{L/H}}{\sum_{m'=1}^{M} b_{m',L/H} Z^{*(m'-1)}} \qquad (10)$$

$b_{m'}$ and c_k are also spectra-specific parameters determined from a calibration scan. The relationship between I-value and Z* is approximated by a five-order polynomial function. With the estimation of ρ_e and I-value, they claimed less than 0.21% RMSE can be achieved experimentally for proton stopping powers estimation. This model can be implemented on image-domain decomposition.

3. Other DECT models include the ρ_e parameterized by Saito[122] and effective atomic number model proposed by Landry et al.[123] For example, a weighted subtraction of ΔHU, or ratio of image intensities, from two different energy spectra are parameterized into models of Z* and ρ_e, respectively. Hudobivinik [124]et al. studied the performance of SPR prediction by using above methods of

Saito and Landry on CIRS phantom. It was shown that SPR root mean square errors (RMSE) for SECT stoichiometric and DECT could achieve 1.8% and 1.2% respectively. These two models can only be implemented on image-domain decomposition since the quantities of Z^* and ρ_e are spectral averaged.

4. Han et al.[113] extended a linear basis vector model (BVM) from estimation of photon cross section to proton stopping power. It is postulated that a linear relationship of the ρ_e and I-value of an arbitrary biological material can be accurately predicted by the following linear combinations where c_1 and c_2 were derived from a basis vector model (BVM) DECT analysis.

$$\rho_e = c_1 \rho_{e,1} + c_2 \rho_{e,2} \qquad (11)$$

$$I = f\left(c_1, c_2\right) \cdot \exp\left(\frac{c_1 \rho_{e,1} \ln I_1 + c_2 \rho_{e,2} \ln I_2}{c_1 \rho_{e,1} + c_2 \rho_{e,2}}\right) \qquad (12)$$

$$f\left(c_1, c_2\right) = a' \frac{c_1}{c_1 + c_2} + b' \qquad (13)$$

where $\rho_{e,i}$ and I_i are the electron densities and mean excitation densities of the two basis materials, respectively. An empirical correction function in (12) is used to correct the residual errors of I-values estimation.

Thus far, in the application of estimating SPR, ρ_e and Z^* are obtained either by a two-parameter model, which is representation of linear attenuation coefficients as function of energy Z^* and ρ_e, or by a linear or polynomial function of ratio of dual-energy scans.

Along with decomposition approaches, a series of common two-parameter models that have been implemented in the literature at the time of this thesis writing are listed in the table 2.1 below

Table 2.1 Published work on implementations of DECT technique on proton stopping power estimation

Models Decomposition	Parametric fit model for (Z^* and ρ_e)	Polynomial fit model for (Z^* and ρ_e)	BVM
Image	Yang et al.;[54] Hünemohr et al.;[56, 125] Bazalova et al.[18] Abbema et al.[115]	Bourque et al.;[55] Taasti et al.;[126] Lalonde et al.[127] Landry et al.[108, 128, 129] Saito[122]	Han et al.[113]
Sinogram	Tremblay et al.[110] Zhang et al.[120]		Zhang et al.[120]
Joint			Zhang et al.[120]

In this chapter, a slightly different BVM model from Appendix I in determining the I-values was implemented. The determination of I-value in Appendix I was based on Bragg additivity rule with linear correction function (Eqn. (12) and Eqn. (13)). A simpler with similar accuracy method of I-values computation is discussed in the following sections.

2.2 Methods and Results

In this section, two different types of DECT models were implemented and compared; one is a linear model of photon cross section model [45, 113, 130] that approximates the tissue cross sections as a linear combination of two dissimilar basis substances, and the other is a non-linear model of photon cross section as explicit function of ρ_e and Z^*, including Torikoshi Parametric Fit Model (tPFM) [18, 102] as implemented by Yang et al.[54]. As mentioned above, the Yang tPFM model can be implemented either in image- or sinogram- decomposition, while other two-parameter models, i.e. models of Bourque et al[55] and Hünemohr et al, [56] can only be performed in image-domain since Z^* out of these models are spectra-specific quantity.

2.2.1 Basis Vector Model (BVM)

$$\rho_{ex} = c_1\rho_{e1} + c_2\rho_{e2}$$

$$I_{x,\text{BVM}} = a \cdot \frac{c_1}{c_1 + c_2} + b \quad (14)$$

where ρ_{e1} and ρ_{e2} are the ρ_e of basis materials: water and polystyrene or $CaCl_2$ solution. The double basis pairs are chosen according to tissue types and based upon the ratio of image intensity of high and low energies. For example, soft tissues are assigned with basis pair of water and polystyrene, while for bone tissues, the basis can be water and $CaCl_2$ solution. For some tissues near the boundary between soft and bone tissues, either basis pair provides reasonable accuracy, provided negative weighting coefficients are allowed. In this study, a double basis is chosen instead of single basis pair due to more accurate estimation of photon cross-section for energy less than 1000 keV, reported by Williamson et al. [45] for more details. The electron densities of basis mixtures can be determined by

$$\rho_{e\_basis} = \rho_m N_A \sum_i \omega_i \frac{Z_i}{A_i} \quad (15)$$

where ρ_m is the mass density of the mixture and ω_i is the mass fraction of the i-th element. It was assumed that the I-values and $c_1/(c_1 + c_2)$ can be linearly fit as in Eqn. (14). To determine the parameters a and b in Eqn. (14), the pre-computed I-values and $\frac{c_1}{c_1 + c_2}$ for soft and bony tissues from ICRU reports are used to derive. (Fig.2.2)
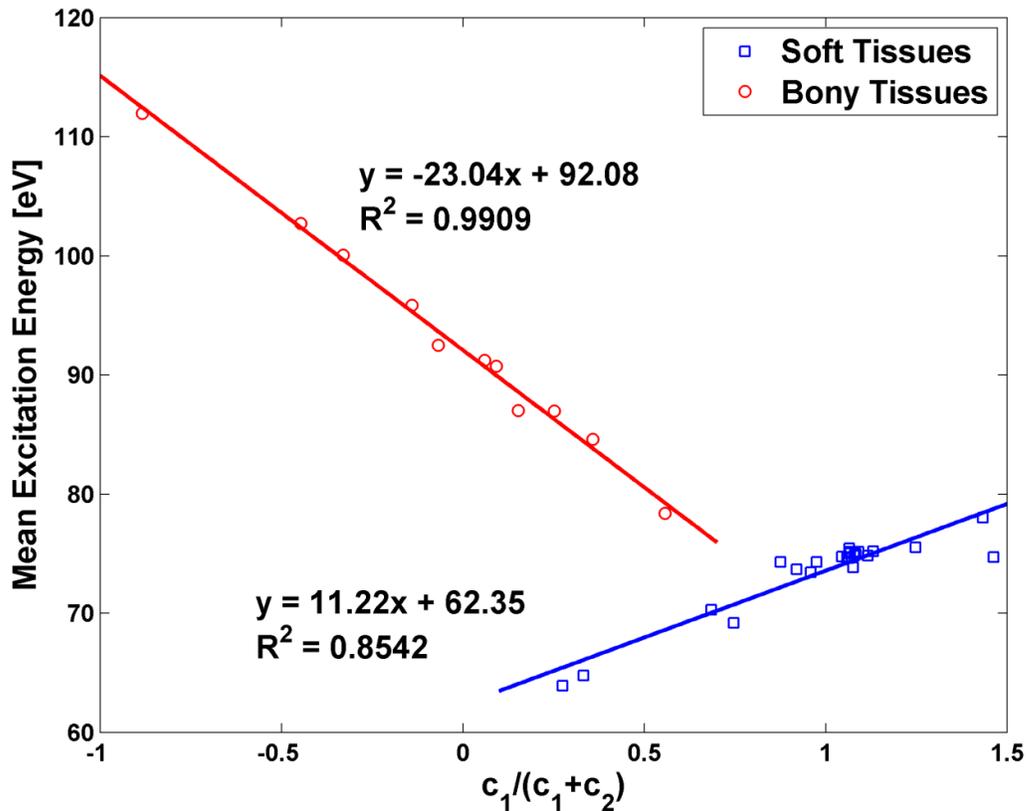
Fig. 2.2. The relationship between $c_1/(c_1+c_2)$ and the I-values of 34 standard human tissues is shown. There are two separate linear fits, one for soft tissues and one for bony tissues. This relationship provides an alternative method to estimate I-value without knowing the Z^* of the substances. It was found the goodness of fit (R^2) had minor impact on the achieved accuracy of proton stopping power estimation.

2.2.2 Torikoshi parametric fit models

The non-linear, non-separable two-parameter model described by Eqn. (5) was also implemented in this study (hereafter designated as the VCU tPFM) and by Yang et al (hereafter termed the Yang tPFM).[54] ρ_e and Z^* can be explicitly iteratively solved from Eqn.(5). To estimate I-values for VCU tPFM, an empirical relationship between *I*-value and Z^* was fit in a polynomial function shown in Fig.2.3, where the composition of each data point was from ICRU reports.[51] The parameter of Z^* was also defined below in Eqn.(16).
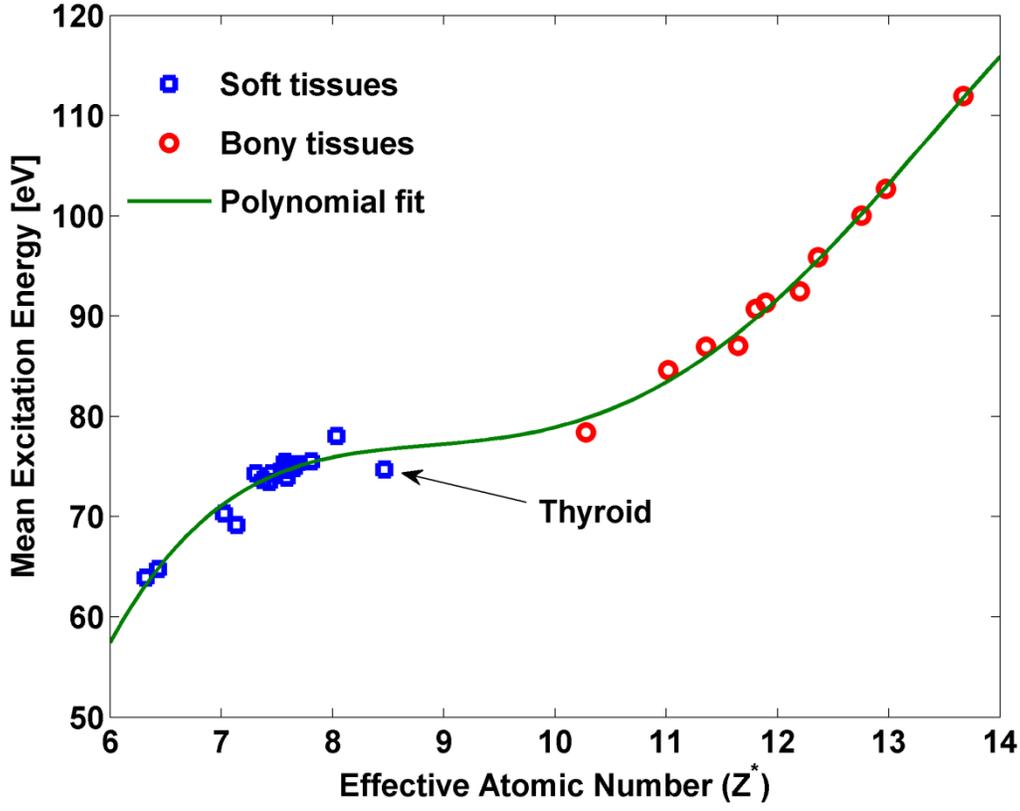
Fig.2.3 The polynomial relationship [55] between Z* and mean excitation energy was implemented in the VCU tPFM. The fit of R^2 is 0.9603. Data for 34 soft tissues and bony tissues are shown.

$$Z_{std}^{m} = \frac{\left(\sum \frac{\omega_i Z_i}{A_i} Z_i^{m} \right)}{\sum \frac{\omega_i Z_i}{A_i}} \quad (16)$$

where A_i and Z_i are atomic weight and atomic number for i-th element, respectively. m was determined to be 3.4 by minimizing the sum of the squared difference between Z_{std} and Z*, which was calculated using Eqn. (5).

In Yang's simulation study, the linear attenuation coefficients were approximated by:

$$\langle \mu \rangle_j = \int S(E)\mu(E)dE \approx \rho_e \sum_{j=1}^{2} \phi_{l,j} \left[Z^{*4}(x) F\left(E_{l,j}, Z^* \right) + G\left(E_{l,j}, Z^* \right) \right] \quad (17)$$

where $\phi_{l,j}$ is the weighting function of the *l*-th energy bin of the *j*-th spectrum (*j*=1,2 denoting 100 kVp and 140 kVp spectra, respectively). The beam spectra $\phi_{l,j}$ of the CT scanner at two energies were calculated by the SpekCalc x-ray spectrum generator in the implementation of Yang et al.[54] The estimated radiological quantities of standard ICRU tissues from study of Yang et al. were used in comparison.
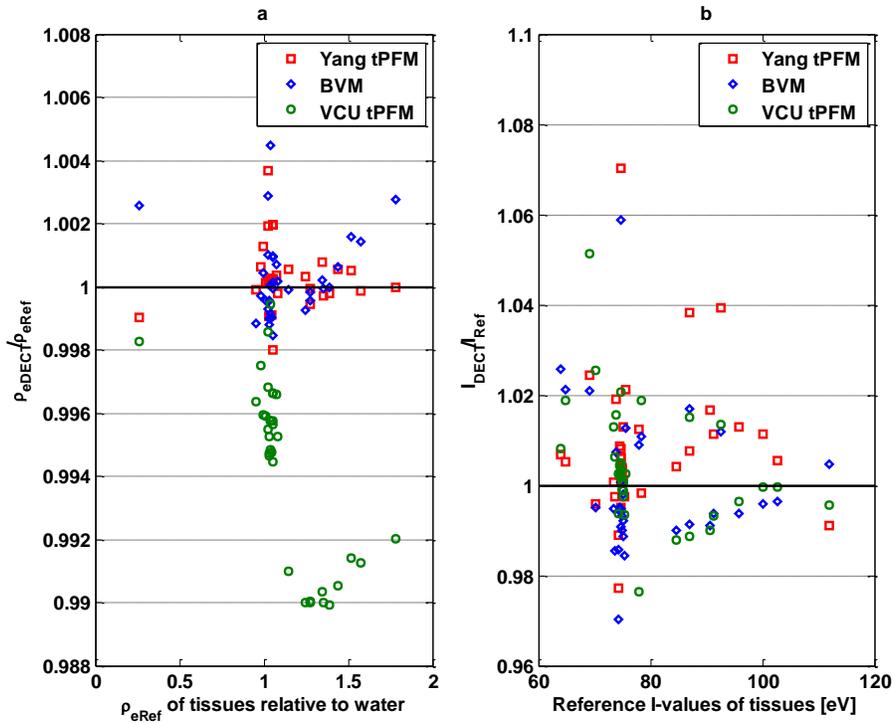

Fig. 2.4. The ratio of electron density and I-values estimation by three different models: the Yang tPFM, BVM, and VCU tPFM, respectively, to the reference value of stopping power. (a) Electron density and (b) I-values. The reference electron density of tissues is shown in the form of electron density relative to water. The reference I-values were computed based on the Bragg additivity rule.

Fig.2.4 (a) shows that the Yang tPFM and BVM both predict the electron density within 0.5% for most tissues, while the VCU tPFM has a slightly larger prediction error of nearly 1%. The mean relative errors in estimated electron density averaged over 34 standard tissues, were 0.09% ± 0.10% for the BVM, 0.07% ± 0.08% for the Yang tPFM, and 0.57% ± 0.29% for the VCU tPFM. Within the different DECT models, the BVM showed comparable accuracy to the Yang tPFM, while the VCU tPFM was slightly less accurate. Fig. (b) shows that the BVM, Yang tPFM, and VCU tPFM models predict the I-

values with comparable accuracy with mean errors of 1.14% ± 1.15%, 1.16% ± 1.06%, and 0.94% ± 1.03%, respectively. The BVM had slightly reduced I-values prediction errors compared to the Yang tPFM. The RMSE(%) defined in Appendix I for electron density and I-values are summarized in Table 2.2.

Table 2.2. RMSE(%) of electron density, I-values and SPR for standard tissues, including the thyroid tissue by different models.

DECT Models	ρ_e (%)	I-value (%)	SPR (%)
BVM	0.13	1.48	0.20
Yang tPFM	0.11	1.84	0.23
VCU tPFM	0.63	1.38	0.68
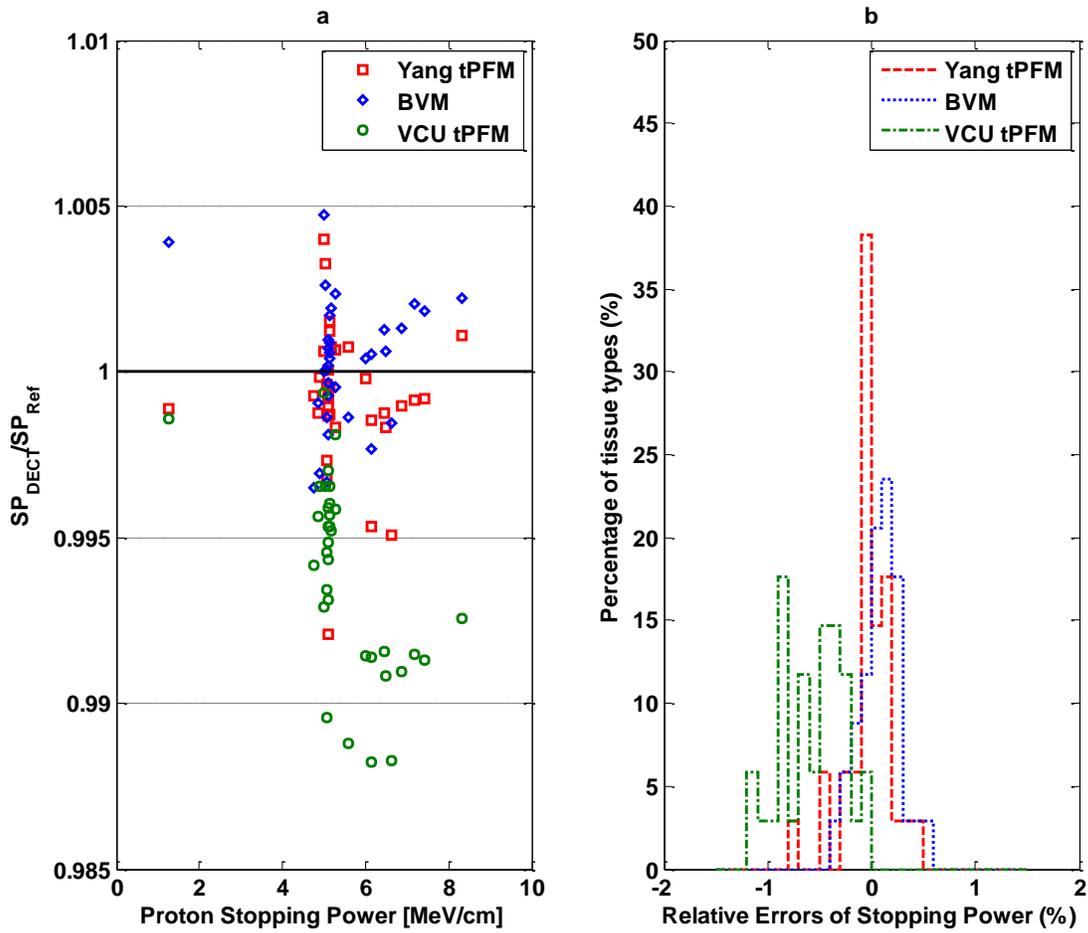
Fig. 2.5 (a) A comparison of errors in the stopping power predictions from different DECT models with reference values. The maximum relative error of prediction using the BVM was well below 0.5%. (b) The distribution of relative errors of the stopping power of 34 standard human tissues estimated by the BVM, Yang tPFM and VCU tPFM is shown.

Proton stopping powers estimated by the three DECT models were comparable to reference values computed by the Bethe formula, Eqn. (3) at a proton kinetic energy of 175 MeV. The RMSEs of the stopping power are also included in table 2.2. Fig.2.5 (b) shows the error distribution of the predicted stopping power using three different models for 34 human tissues. These data indicate that BVM had similar prediction accuracy to the Yang tPFM model but better accuracy than the VCU tPFM.

2.2.3 Robustness to variations of elemental composition

Our study also investigated robustness to variations in elemental composition of various tissues. To make conservative estimates of the impact of poorly characterized tissue composition variability on QDECT estimates, we varied the mass fraction of major components: water, lipid, protein, carbohydrate, and mineral ash (Table 2.3) rather than varying the elemental composition itself. Three typical tissues adipose, muscle and trabecular bone were selected to evaluate the robustness. The estimation accuracy of SPR was reported.

For soft tissues, using adipose tissue as an example, assuming that the main component is lipid with a range of mass fraction of 30% to 80%, [131, 67] protein mass fraction range of 1% to 7.5%, and constant mineral mass fraction, the water content can be computed based on the normalization of all components to 100%. Note that since the range of each component was chosen in a way that can accommodate large variability reported by ICRU report 44, [132] the values of mass fraction reported here may not be realistic.

For trabecular bone tissues, the fractions of bone mineral matrix (approximated by cortical bone composition) and bone marrow (red marrow and yellow marrow) were varied. The mass densities of tissues were estimated from the mass fractions and mass densities of the components.

Table 2.3. Variations in mass or volume fractions of component mixtures comprising soft tissues and trabecular bone considered in this study.

Body tissues (mass fraction)	Water	Lipid	Protein	Carbohydrate	Ash (mineral)
Adipose	62.2-4.7	30-88	1.0-7.5	-	0.3
Muscle-like tissue	83-73	1-5	10-20	1	0.9
	Cortical Bone (volume fraction)	Red marrow (mass fraction)			

Trabecular bone (Spongiosa)	5-70	30-100
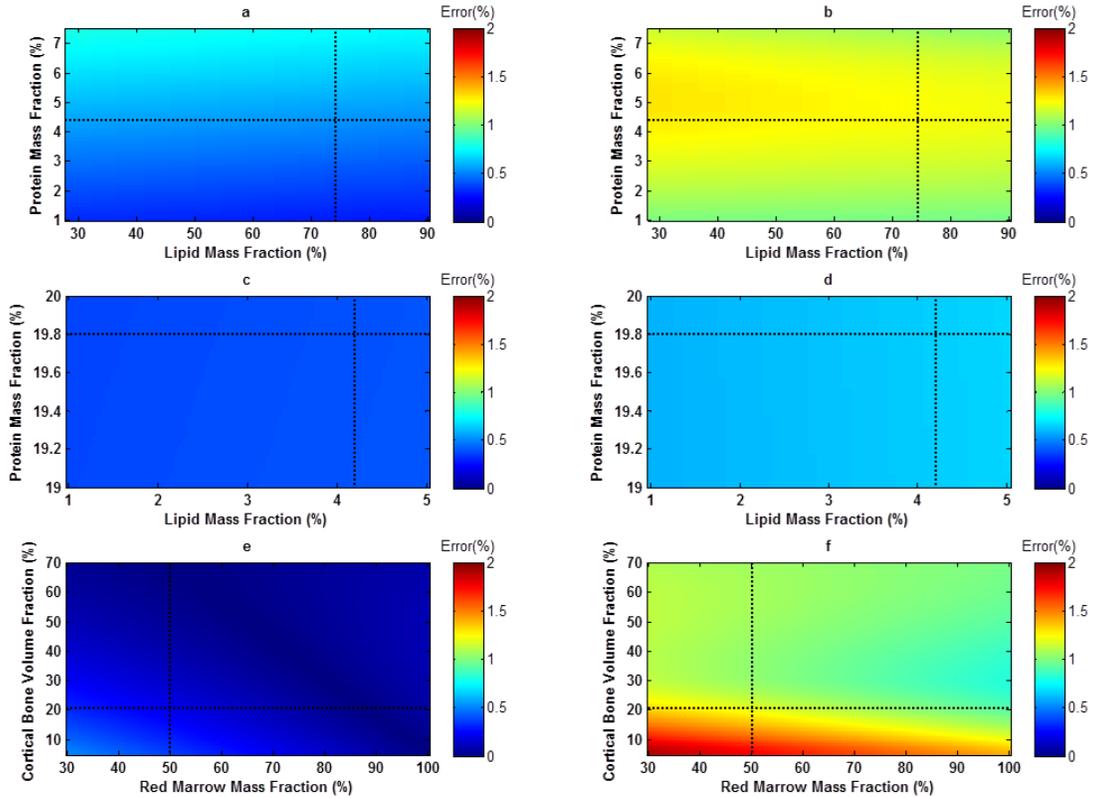
Fig. 2.6 The relative errors distribution of adipose-like (a, b) and muscle-like (c, d) stopping power at 175 MeV as a function of lipid and water mass fractions for constant mass fractions of 0.3% ash was predicted by BVM (a, c) and the VCU tPFM (b, d), respectively. The relative errors distribution of trabecular bone (e, f) stopping power are predicted by BVM (e) and VCU tPFM (f) by varying cortical volume (5%-70%), and red marrow mass fraction over the range of 30%-100%. Note the difference in the color bar scale in (e) and (f). The black crosses correspond to ICRU-44 published values of adipose, muscle, and spongiosa composition.

Fig. 2.6(c) and (d) show that the BVM and tPFM models' prediction errors for muscle-like tissues are insensitive to variations in lipid and water mass fractions for constant protein and mineral ash mass fractions, with a maximum error of 0.8%. The BVM performs better than the tPFM model. Fig. 2.6(e) and (f) show that estimation errors by BVM are not sensitive to the variation in composition for tissues of trabecular bones.

The errors are all well below 0.8%, which is better than the performance of the tPFM model. The results of this study demonstrate that both the BVM and non-separable parametric models maintain good accuracy over a wide range of assumed bony and soft tissue compositions that are not included in the original ICRU training dataset from ICRU reports.

2.2.4 Sensitivity to CT image uncertainty

Due to the image noise, beam-hardening, nonuniformity and other systematic image-intensity artifacts, the one-to-one correspondence between underlying tissue characteristics and CT image intensity may be compromised. In this study, the impact of these uncertainties in CT image intensities on proton stopping power estimation was evaluated for each of the three investigated two-parameter models used the uncertainty propagation model described by NIST.[133]

Image density is defined as $D_{j,k} = \left(\mu_k \middle/ \mu_{wat} \right)_{E_j}$, where j=1,2 denote E_1 and E_2 and k=1,2,3 denote basis material 1, basis material 2, and unknown material, respectively. c_1 and c_2 are functions of these six independent image intensities, which are assumed to have uncertainties of $\sigma_{j,k}$. Assuming these six quantities are independent, uncorrelated random variables, the resultant uncertainties in predicted electron density prediction by the law of error propagation for a coverage factor of 1.0 can be written as:

$$
\begin{aligned}
u_{unknown,\rho_e}(E) &= \left[\sum_{j=1}^{2} \sum_{k=1}^{3} \left(\frac{\partial \rho_e}{\partial D_{jk}} \sigma_{jk} \right)^2 \right]^{1/2} = \left[\sum_{j=1}^{2} \sum_{k=1}^{3} \left(\frac{\partial \rho_e}{\partial c_{1,jk}} \frac{\partial c_{1,jk}}{\partial D_{jk}} \sigma_{jk} + \frac{\partial \rho_e}{\partial c_{2,jk}} \frac{\partial c_{2,jk}}{\partial D_{jk}} \sigma_{jk} \right)^2 \right]^{1/2} \\
&= \left[\left(\frac{\partial \rho_e}{\partial c_{1,jk}} \right)^2 \sum_{j=1}^{2} \sum_{k=1}^{3} \left(\frac{\partial c_{1,jk}}{\partial D_{jk}} \sigma_{jk} \right)^2 + \left(\frac{\partial \rho_e}{\partial c_{2,jk}} \right)^2 \sum_{j=1}^{2} \sum_{k=1}^{3} \left(\frac{\partial c_{2,jk}}{\partial D_{jk}} \sigma_{jk} \right)^2 \right. \\
&\quad \left. + 2 \left(\frac{\partial \rho_e}{\partial c_{1,jk}} \right) \left(\frac{\partial \rho_e}{\partial c_{2,jk}} \right) \sum_{j=1}^{2} \sum_{k=1}^{3} \left(\frac{\partial c_{1,jk}}{\partial D_{jk}} \frac{\partial c_{2,jk}}{\partial D_{jk}} \sigma_{jk}^2 \right) \right]^{1/2}
\end{aligned}
$$

$$(18)$$

The uncertainty of the product of electron density and the logarithm of I-value can be obtained in a similar fashion.

Thus, the uncertainty of the stopping power estimation via the BVM was given by:

$$u_S^2\left(E_{proton}\right) = S^2\left(K^2\left(\frac{u_{\rho_e}}{\rho_e}\right)^2 + \left(\frac{k_1}{\beta^2}\right)^2\left(\frac{u_{\rho_e \ln I}}{\rho_e \ln I}\right)^2 + 2K\left(\frac{k_1}{\beta^2}\right)\text{cov}\left(\rho_e, \rho_e \ln I\right)\right) \quad (19)$$

where the constants K and k_1 were defined by Eq. (1), and Cov(ρ_e, $\rho_e$ln$I$) was the co-variance of ρ_e, and $\rho_e$ln$I$. For the parameterized QDECT models, the uncertainty of the stopping power can be obtained similarly. All uncertainties described above were evaluated numerically (ratio of change in numerator to 1% change in denominator), at three different image uncertainty levels for standard human tissues.

Three different levels of CT image intensity uncertainty were investigated. [45] Following the NIST guidance [133] on uncertainty analysis, the image intensity uncertainties were the quadrature sum of random (Type A) and systematic errors (Type B), e.g. streak, cupping, etc., in terms of coefficients of variation (COV). The lowest uncertainty levels, with COV of 0.2% and 0.1% for low- and high-energy scans, respectively, supported recovery for a low-energy photon cross-section with 3% accuracy and acceptable spatial resolution,[45] but are not achievable on current commercial scanners with clinically acceptable patient doses. The intermediate levels (0.6%, 0.3%) are minimum uncertainties achievable by fourth-generation CT scanners, while the highest uncertainties (1.5%, 1.0%) are characteristic of clinical pelvic CT imaging.
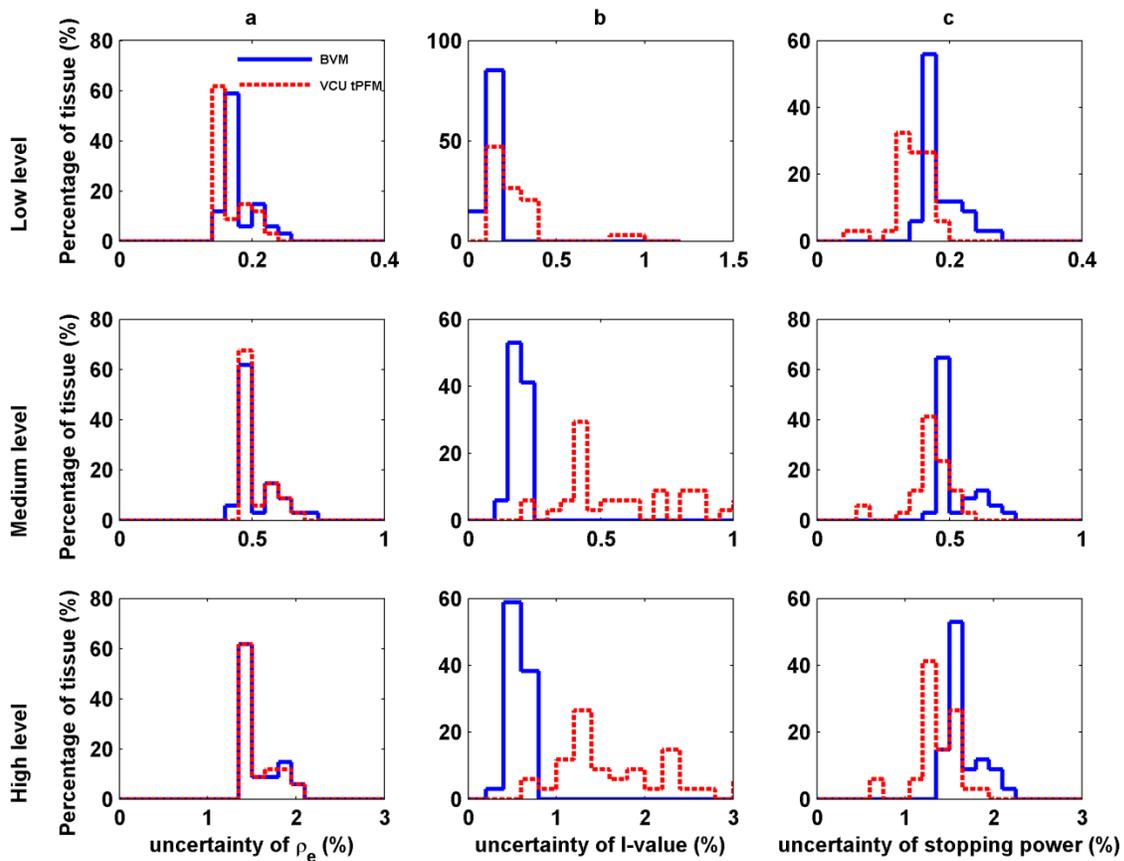
Fig. 2.7 The distribution of the uncertainties of 34 standard human tissues in electron density (a), I-values (b), and stopping power (c) from three different CT image uncertainty levels (low- and medium-, high-energy): top row: low 0.2% and 0.1%; middle row: medium 0.6% and 0.3%; and bottom row: high 1.5% and 1.0%.

Fig. 2.7 shows the impact of image intensity uncertainties on electron densities, I-values, and stopping power estimated by the BVM and VCU tPFM. Since the BVM and VCU tPFM models use the same monoenergetic approximation of CT spectra, the Yang tPFM is excluded from the sensitivity study. The BVM model outperforms the I-value estimation compared to VCU tPFM, however, similar performance of estimation of electron density leads to a consistent estimation accuracy for stopping power. For example, due to roughly 1% uncertainties from images, the added uncertainties to SPR could be around 0.8%.

2.3 Discussion

In this study, our results indicated a theoretical estimation stopping power estimation accuracy, with RMS error 0.2% has been achieved by using BVM. Our study also showed that the BVM estimation accuracy is relatively insensitive to uncertainties of elemental composition of test tissues. Error propagation analysis also suggested that the one-to-one correspondence between the linear attenuation and proton stopping power may be affected by the uncertainties of CT measurements, including scattering and beam hardening, which may add another 1-2% to the measurement of uncertainties.

To our knowledge, this is the first study to extend a linear, separable two-parameter from modeling only photon linear attenuation coefficients to modelling stopping powers in the context of idealized DECT. The mean absolute error of electron density 0.08% (excluding the thyroid tissue) was obtained by using the BVM model. This accuracy is also comparable to the DECT stoichiometric algorithm proposed by Bourque *et al.*,[55] which showed that the mean absolute error of electron density is 0.08% for standard human tissues excluding the thyroid tissue. The estimation of ρ_e can also be used in treatment planning of photon beam. Our assumption that $c_1/(c_1 + c_2)$ can be treated as a surrogate of Z^* is applied to predict the I-values of standard tissues, which yields the RMS error of 1.48%. Since the impacts of I-value to estimation of stopping power are seconddary compared to electron dentsity, this could translate to range uncertainties improvement about 0.2%. More discussions about relationship between electron density accuracy versus range uncertainties can be found in Appendix I.

There are uncertainties associated with this work.

- o The mean excitation energy, I-value, is a quantity independent of properties of the projectile, independent of DECT parameters, and depends only on the properties of the tissues. It was suggested by Bloch [134] for Thomas-Fermi model of atom, the I-values are proportional to the atomic number,

$$I = I_0 Z^* \qquad (20)$$

with I_0 approximately equal to 10 eV. Similar to this method, the relationship in Eq. (13) is also defined with $c_1/(c_1 + c_2)$. An alternative to the current method that is correction based can be found in Appendix I.

- o I-values are logarithmically related to stopping power equation, e.g.,relative I-value 10% uncertianties could result in relative uncertianties of stopping power with 1.5%. Although stopping powers are less sensitive to I-values uncertianties than ρ_e as pointed out by Andreo [135], uncertainties introduced by I-values can cause noticeable range uncertanties. For different I-values of water 67 eV, 75 eV and 80 eV, the range of Bragg peak may vary up to 6 mm for 183 MeV proton beam. [135]

- o Our study did not optimize either the choice of basis materials or DECT energy pair on mapping accuracy of stopping power. Evans et al.[20] demonstrated that by adding additional tin filtration for more separation between low and high effective energy, the prediction accuracy of photon cross sections can be improved. It is hypothesized that similar improvements of estimation accuracy of SPR can also be found.

In this work, the BVM model not only provides a conceptually and numerically simpler method for accurately mapping proton stopping power, but serves a useful parameterization of the linear attenuation coefficient appropriate for polyenergetic iterative DECT reconstruction algorithms, in which a forward polyenergetic projection is required (see Eqn. (2) in Ch.1), allowing $\mu(x,E)$ to be accurately estimated for any specified energy E in the scanning spectrum. Most of the competing current two-parameter models for proton stopping power estimation are calibration-based image-domain approaches, in other words, ρ_e and Z* are used to model only spectrally averaged linear attenuation coefficients, while the more versatile linear BVM model can accurately model either $<\mu>$ or $\mu(E)$. More details will be covered in Chapter 3.

3 On the accuracy of parametric two-parameter cross-section models in dual-energy CT applications

3.1 Background

For the low energy brachytherapy, a two-parameter model with DECT implementations is a promising approach to noninvasively and quantitatively characterize the patient-specific heterogeneities to be used in model-based dose calculation algorithms (MBDCAs) suggested by TG186.[15] For MBIR or SIR algorithms, accurate modeling of linear attenuation is also desirable for forward projection operators.[96, 136]

The photon interactions of low energy (< 1 MeV) include three distinct effects: photoelectric, coherent scattering, and incoherent scattering (Compton scattering). [137] Each of the above effects can be approximately modeled by power functions of atomic number and energy. For example, the cross-section of photoelectric effect per electron is roughly given by

$$\sigma_{ph} \propto \frac{Z^q}{E^3} \qquad (21)$$

where Z represents atomic number of elements, E is photon energy, q is a number which varies between 3 and 4 depending on Z and energy range. Similarly, incoherent scattering can be approximated by

$$\sigma_{in} \propto \sigma^{KN}(E)Z \qquad (22)$$

The cross-section for scattering from a single free electron is given by Klein-Nishina formula[45] $\sigma^{KN}(E)$. The total linear attenuation coefficient can be treated as the sum of the partial cross section for each mechanism, times the electron or atomic density.[130] Williamson et al. [45] reported that prediction errors of cross-section in Eqn. (23) based on power functions can be up to 40% for pure elements substance. For mixture and compound substances, whose atomic number is not well defined, the errors could be more than 10%, especially at when energy lower than 30 keV, these errors could be up to 15%.

$$\mu(E, Z^*, \rho_e)_{PFM} = \rho_e \cdot \left[a \cdot \frac{Z^{*b}}{E^c} + \sigma^e_{KN}(E) + d \cdot \frac{Z^{*e}}{E^f} \right] \quad (23)$$

where the unknown parameters a-f are determined by minimizing the difference of estimated photon cross sections and ground truth of elements in the energy range 20 keV to 1 MeV.

The basis vector function (BVM) is another way of representing total cross-section $\sigma(E)$ in which $\sigma(E)$ is expressed as a linear combination of basis functions that depend only on energy [31]

$$\sigma(E) = \sum_{i=1}^{n} a_i f_i(E) \quad (24)$$

The fundamental difference between Eqn. (24) and Eqn. (23) is that BVM model is a more generalized representation of Eqn. (23) if $f_1 = \frac{1}{E^c} \left(or \ \frac{1}{E^f} \right)$ and $f_2 = \sigma_{KN}$.

In this chapter, a family of mPFM models was developed to estimate photon cross sections for arbitrary monoenergetic energies as the standard PFM mode fails to support accurate estimation of photon cross sections.[45]

One of the motivations for this study is to identify an accurate two-parameter model for estimating photon cross-section of compound and mixtures as functions of energy in the range of interest to community of low-energy brachytherapy.

In contrast, Most of the competing candidates of two-parameter models are based upon PFM, e.g., Spiers [138] model, which is only able to predict spectrally averaged linear attenuation coefficients in a relative narrow energy range and widely used by most image-domain decomposition methods. In recent literature, mPFM emerged as the only model to approximate $\mu(E)$.as function of energy with reasonable accuracy, given that Williamson et al. discredited the Spiers [138] model for this purpose.

Thus, it is imperative to assess the performance of mPFM in mapping the photon cross sections using the family of mPFM models at monoenergetic energies. The estimated accuracy of non-linear mPFM models were also compared to the performance of the linear BVM, especially at low energy for compound and mixtures. The other motivation is to search an accurate and computationally cheap two-parameter model for polyenergetic SIR algorithms in estimating forward projections over a wide energy range of a spectrum. The study presented in this chapter facilitates to choose accurate model for forward projections utilized in model-based reconstruction algorithms. Besides the reported accuracy, the propagated uncertainties analysis due to DECT images can be found in Appendix II.

3.2 Methods and Results

We evaluated photon cross-section prediction accuracy of BVM and tPFM in the energy range from 20 keV to 1000 keV, along with a more complex modified PFM that we call the "VCU modified parametric fit model" (vPFM). The photon cross sections in this study included the total linear attenuation, photoelectric effect, scattering, and energy-absorption coefficients, all as functions of energy E. The model accuracy was evaluated for 43 tissues and tissue substitutes with elemental compositions recommended by ICRU,[51] or other references,[139, 140] in terms of mean percent relative error in the lower energy range (20 keV to 50 keV), and higher (50 keV to 1000 keV) energy ranges.

The BVM model assumes that the photon cross sections of both mixtures and elemental substances can be approximated by a linear combination of two dissimilar basis materials. [31] For example, the total linear attenuation of an unknown tissue at energy E (20 keV ≤ E ≤ 1000 keV), position $\mathbf{x}$ can be written in the following form

$$\mu(\mathbf{x}, E) = c_1(\mathbf{x})\mu_1(E) + c_2(\mathbf{x})\mu_2(E) \qquad (25)$$

where $\mathbf{x}$ refers to the image voxel location and $\mu_i(E)$ (i=1,2) denotes the linear attenuation coefficient of the i-th basis material in the pure form. In this work, a water-polystyrene pair was chosen for soft tissues, while a water-$CaCl_2$ solution (23% concentration) pair was used for bony tissues. $c_i(\mathbf{x})$ images from DECT imaging were computed from low (90 kVp) and high (140 kVp + tin filter) energy scanning spectra

approximated by effective energies 45 keV and 90 keV.[113] The photoelectric and scattering cross sections were also computed by using the $c_i(\mathbf{x})$ images.

Two modified parametric fit models (PFM) based on Z* and ρ_e were also developed and compared. One of the non-separable and non-linear parametric fit models, proposed by Torikoshi et al (tPFM) by assuming that the total linear attenuation coefficient can be parameterized in a closed form for elements

$$\mu\left(\mathbf{x}, E, \rho_e, Z^*\right)_{tPFM} = \rho_e(\mathbf{x})\left(Z^{*4}(\mathbf{x})F\left(E, Z^*\right) + G\left(E, Z^*\right)\right) \quad (26)$$

The pre-tabulated correction functions $F\left(E, Z^*\right)$ and $G\left(E, Z^*\right)$ were determined by forcing Eqn.(26) to reproduce exact linear attenuation coefficients for the elements (Z = 2 to 20) based on the NIST XCOM database.[121] For mixtures of elemental materials, Z^* may assume non-integer values (Z*). The non-linear Eq. (14) can be solved iteratively for the idealized DECT scenario where there is exact knowledge of total linear attenuation coefficient at two discrete effective energies (45 keV and 90 keV) for each voxel.

Our vPFM approach combines the more detailed Spiers[138] PFM (Eqn (23) above) with the elemental correction tables introduced by Torikoshi et al.[102] We hypothesized that the more complete parametric model would support more accurate interpolation for intermediate E and Z^* values, thereby improving the prediction accuracy for mixtures and compounds.

$$\mu(E, Z^*, \rho_e)_{vPFM} = \rho_e \cdot \left[a \cdot \frac{Z^{*b}}{E^c} \cdot F'(E, Z^*) + \left(\sigma_{KN}^e(E) + d \cdot \frac{Z^{*e}}{E^f}\right) \cdot G'(E, Z^*)\right] \quad (27)$$

where we have dropped the spatial coordinate, $\mathbf{x}$, for simplicity. The energy- and position independent *a-f* are the best fit parameters which maximize the accuracy with which the PFM (Eqn. (23)) predicts the elemental photoelectric effect and total scattering cross sections (NIST XCOM) for $2 \le Z \le 20$ and $20 \le E \le 1000$ keV without the empirical correction factors. $F'(E, Z^*)$ and $G'(E, Z^*)$ were also derived by comparing

best-fit PFM predictions to the known XCOM elemental cross sections. Since the prediction accuracy of tPFM and vPFM turned out to be nearly identical, contrary to our hypothesis, detailed results only for the former are presented. More discussions can be found in Appendix II.

Monte Carlo simulations often require the linear energy-absorption coefficient, $\mu_{en}(\mathbf{x}, E)$. This quantity also serves as a useful surrogate for absorbed dose[45] in the approximation where energy impartation is dominated by first-order photon collisions. For relatively light (Z<= 20) elements, $\mu_{en}(E, Z)$ is given by

$$\mu_{en}(E, Z) = \rho_e \left[\sigma_{KN} \left(1 - \frac{\overline{E_{sca,KN}}}{E} \right) + \sigma_{PE} \left(1 - \frac{E - P_K \cdot E_K \cdot \omega_K}{E} \right) \right] \cdot (1 - g_K) \qquad (28)$$

where σ_{KN} and σ_{PE} denote the electronic Klein-Nishina and photoelectric cross sections, respectively, per electrons; $\overline{E_{sca,KN}}$ is the average energy scattered per collision; and P_K, E_K and ω_K denote the K-shell vacancy probability, binding energy and fluorescent yield, respectively. The quantities of P_K and E_K are functions of effective atomic numbers; linear interpolation between their elemental values is used to evaluate $\mu_{en}(E, Z^*)$ at non-integer Z^* values. The average fraction of the secondary charged-particle energy that is subsequently lost in radiative process is denoted by g_k. Photon energy of interest in this chapter is assumed greater than the shell binding energy.

Once $\left(c_1(\mathbf{x}), c_2(\mathbf{x}) \right)$ and $\left(Z^*(\mathbf{x}), \rho_e(\mathbf{x}) \right)$ pairs have been determined, the mean relative error of photon cross sections prediction error for the *j*-th tissue can be written as

$$\text{Root-mean-sqaure Error(\%)} = 100\% \times \left[\sum_{i=1}^{N} \left(1 - \frac{\mu_{i,\Delta,DECT}(E)}{\mu_{i,\Delta,ref}(E)} \right)^2 \bigg/ N \right]^{1/2}_{\Delta = Tot, PE, EN} \qquad (29)$$

Δ = *Tot, PE*, and *EN* represent total linear, photoelectric absorption, and energy-absorption coefficients, respectively. The subscript "ref" refers to the ground truth values derived from the XCOM library. [121]

The comparison results for total linear attenuation, photoelectric effect, scattering and energy absorption are shown in the Figs (3.1) to (3.3). In this study, the energy of 50 keV was considered as the up limit for dominance of photoelectric, and down limit for scattering effect.

Fig. 3.1 shows the BVM and tPFM root-mean-square (RMS) prediction errors of total cross-section estimation as functions of effective atomic number derived from tPFM model for the low $20 \leq E \leq 50$ keV and high $50 \leq E \leq 1000$ keV energy ranges. The BVM model outperforms the tPFM, achieving RMS errors of less than about 0.5% and 0.1% for the low and high energy ranges, respectively, except for Teflon and inflated lung tissues. At low energies, tPFM predictions exhibit RMS errors over 1% for most tissues and up to 2% for tissue substitutes (phantom materials) with RMS errors that are less than 0.6% at higher energies. The tPFM prediction errors are generally larger for bony tissues. Due to its high iodine content (0.1% by weight with Z = 53), both BVM and tPFM fail to accurately model the thyroid tissue cross sections, with errors as large as 7.9% and 7.7%, respectively.
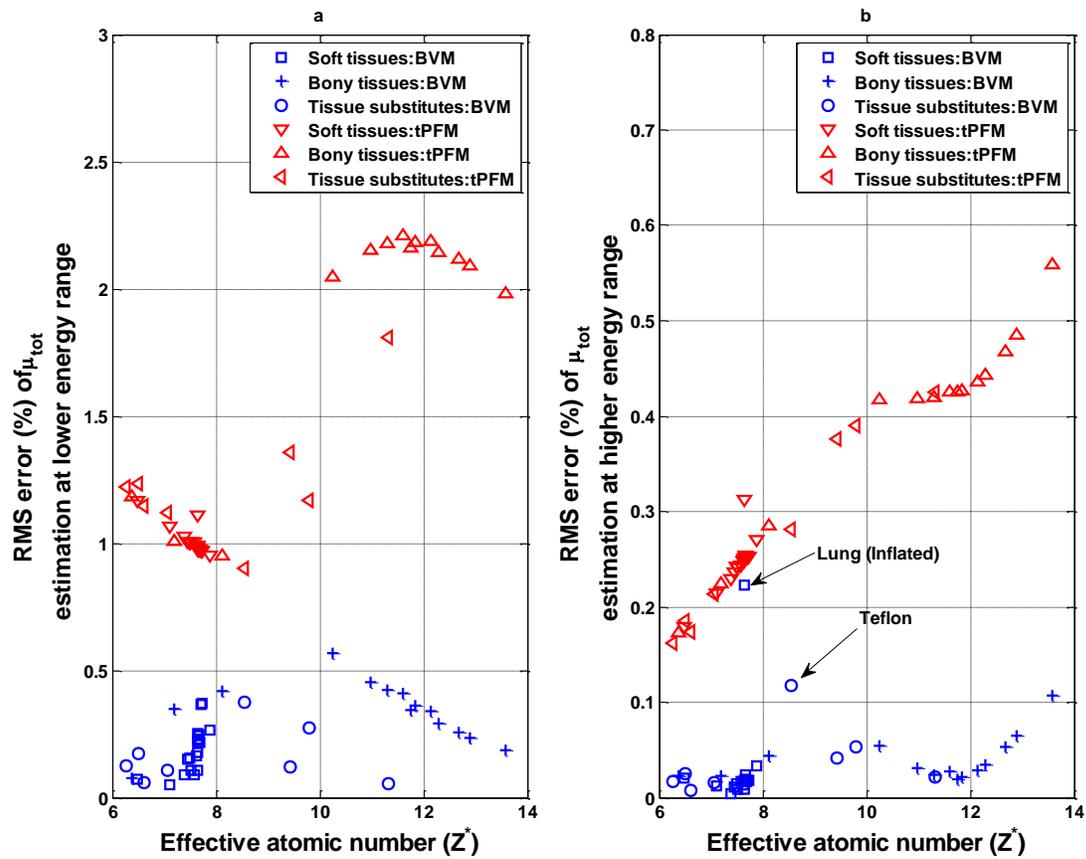
Fig. 3.1. Percent RMS error of the total linear attenuation coefficient predicted by BVM or tPFM for 43 tissues and phantom substitutes as functions of tPFM effective atomic number for the (a) $20 \leq E \leq 50$ keV and (b) $50 \leq E \leq 1000$ keV energy ranges. The thyroid tissue prediction error is outside the plotting range of the low energy plot.
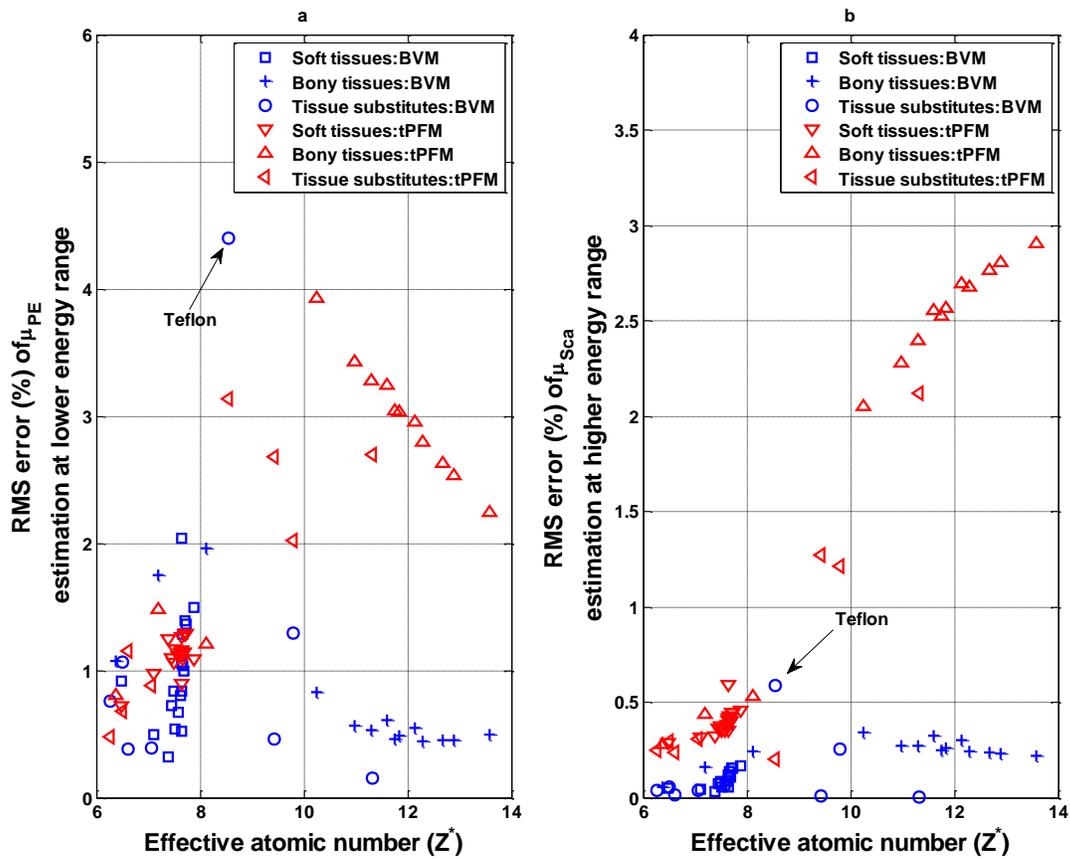
Fig 3.2 tPFM and BVM percent RMS predictions for 43 tissues and phantom substitutes as functions of tPFM effective atomic number for (a) photoelectric effect cross sections in the $20 \le E \le 50$ keV range and (b) photon scattering cross sections in the $50 \le E \le 1000$ keV range. The thyroid tissue prediction error is outside the plotting range of the low energy plot.

Fig 3.2 demonstrates the estimation errors of photoelectric effect for energy less than 50 keV, and for photon scattering for energies greater than 50 keV. The BVM predicts soft and bony tissues' low-energy photoionization cross sections with accuracies 0.5% to 2% except for a 4.5% error for Teflon. In contrast, tPFM models the soft tissue photoionization cross section with comparable accuracy but exhibits much larger errors (2%-4%) for bony tissues. A similar pattern obtains for higher-energy scattering cross sections: BVM prediction accuracy is generally better than 0.25%, while tPFM exhibits errors in excess of 2% for bony tissues.
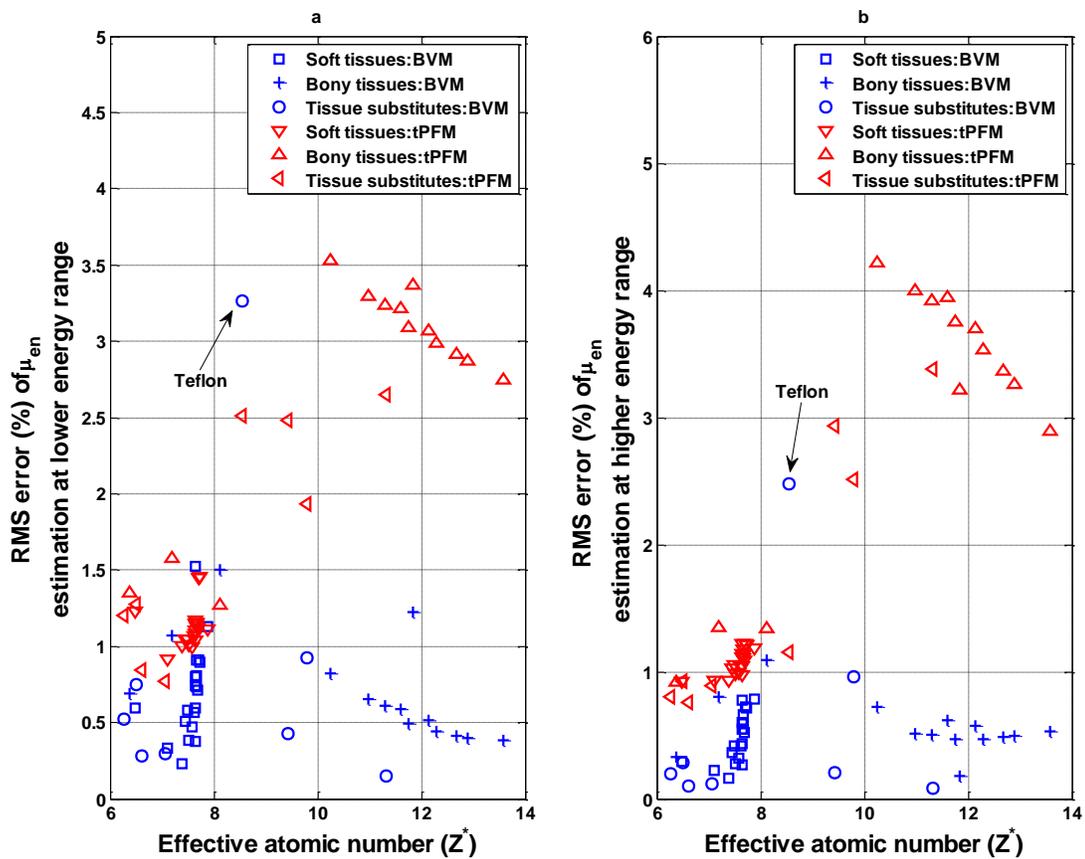

Fig 3.3. Percent RMS error of energy-absorption coefficients estimate for 43 tissues and phantom materials as functions of tPFM effective atomic number for the (a) $20 \leq E \leq 50$ keV and (b) $50 \leq E \leq 1000$ keV energy ranges. The thyroid tissue prediction error is outside the plotting range of the low energy plot

For tPFM, in Fig.3.3, soft tissue estimation errors of energy-absorption coefficients are mostly larger than 1% and, 2% to 3.5% for bony tissues, while BVM exhibits error less than 1% (except for Teflon and thyroid). Iodine based tissues have $\mu_{en}(E)$ estimation errors of 14.7% and 16.2% for BVM and tPFM across the two energy ranges, respectively.

Despite the fact that the Spiers formula yields a much better fit to the elemental total cross section data than the uncorrected Torikoshi formula, tPFM and vPFM modelled total, photoelectric, scattering and energy absorption coefficient data with equivalent accuracies. In general, prediction errors rarely deviated by more than 0.5% to 1.0% between the two models. As an example, Fig. 3.4 (b) shows that in the range of 20-1000 keV, RMS errors for prediction $\mu_{en}(E)$ are virtually identical for the vPFM and tPFM models.
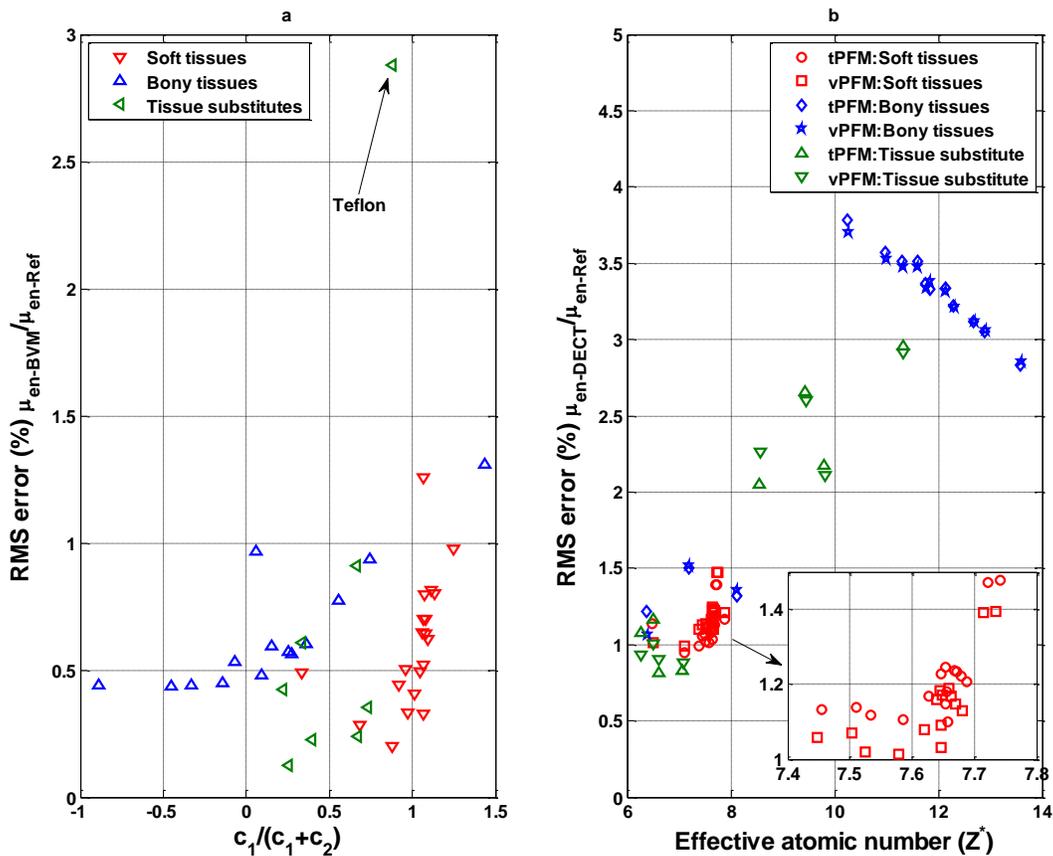
Fig 3.4. $\mu_{en}(E)$ of RMS estimation errors as functions of (a) $c_1/(c_1+c_2)$ for BVM and (b) effective atomic number for tPFM and vPFM in the energy range of 20 keV to 1000 keV. Thyroid tissue is excluded.

3.3 Discussion

For a wide range of tissues and tissue substitutes, our study demonstrates that BVM models linear attenuation, photoelectric effect and energy-absorption coefficients with significantly better accuracy than tPFM. This confirms our earlier work,[45] which showed that the simple, linear two-parameter BVM implementation can accurately represent (within 2%) photoelectric cross sections and other radiological quantities needed to implement model-based brachytherapy dose-calculations for energies as low as 20 keV, just below the mean energy of photons emitted during [103]Pd decay.

Our study also confirms that tPFM models can significantly reduce prediction error by PFM model, i.e. estimation maximum error of photoelectric cross section decreased from 22.4% to 4.5%. However, tPFM models are still not suitable for mapping low energy brachytherapy dose calculation since they introduce RMSE errors exceeding 3% in the low energy (20-40 keV) energy range.

A systematic uncertainties analysis for different models can be found in Appendix II.

It is still arguable whether Z* is a meaningful quantity that is independent of photon energy, an issue also investigated by Jackson et al. [137] Our study also computed the Z* of typical tissues based on Eqn.(30) using single energy linear attenuation and known ρ_e from ICRU reports [51](shown in Fig.3.5). Three representative tissues: adipose, muscle and bone tissues are investigated.

$$\frac{\mu\left(\mathbf{x},E,\rho_e,Z^*\right)_{tPFM}}{\rho_e}=\left(Z^{*4}\left(\mathbf{x}\right)F\left(E,Z^*\right)+G\left(E,Z^*\right)\right) \qquad (30)$$

The elemental compositions of three tissues are abstracted from ICRU report. The linear attenuation coefficients of tissues were computed from their elemental cross sections via the mixture rules. The electron densities on LHS of Eqn. (30) are also provided by ICRU report. By solving the non-linear Eqn. (30) iteratively, the Z* can be

obtained as a function of energy. It is noted that for each type of tissue, Z* is no longer a constant and shows variation as a function of low photon energy, where the photoelectric effect is more prominent than Compton scattering. For example, for cortical bone and muscle tissues, the maximum difference of Z* at 200 keV at 50 keV are up to 3%, while for adipose, this error could be up to 5%. Fig 3.5 clearly demonstrates that Z* is not a representative constant for compounds and mixtures.

A classical definition of Z* was first proposed by Mayneord,[141] $Z^* = \sqrt[m']{\sum_i w_i Z_i^m}$ ($m' = 2.94$). Although it is overly simplistic and was derived from a particular spectrum, it is well accepted in radiation therapy. For comparison, the Z* of adipose, muscle and bone were also computed based Mayneord formula shown in table 3.1

Table 3.1. Z* of three typical tissues computed from Mayneord formula

Tissues	Z*
Adipose	6.56
Muscle	7.71
Bone	11.19

For muscle tissue, the maximum errors between Mayneord formula and Z^* derived from Eqn. (30) could be as large as 4.6%. Such difference may not be significant for MV beam of radiation therapy, but may become an important factor when photon energy is less than 50 keV. We may also conclude that Z^* based estimates of linear attenuation are not accurate enough for forward projection modeling. It is worth pointing out that although Z* may not have physical meaning in photon cross section modeling, it can be used for tissue type indexing, which will be covered in Ch.5.
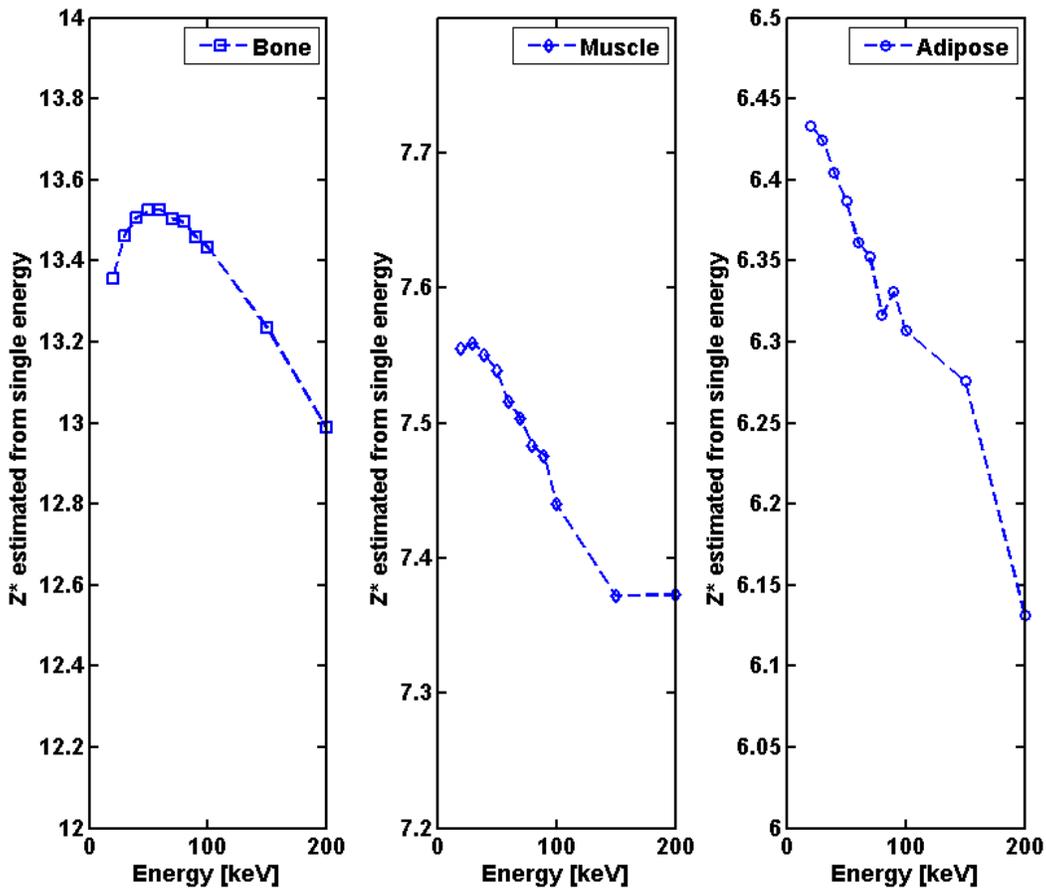
Fig 3.5. Z* of three typical tissues; cortical bone, muscle and adipose computed from Eqn.(30)

Finally, we would like to emphasize that tPFM and related PFM-based DECT [54–56, 123] stoichiometric methods have been shown to support reasonably accurate proton stopping power and higher energy (> 100 keV) photon cross-section mapping. However, all of these studies have been limited to the post-image reconstruction scenario where only spectrally-averaged linear attenuation coefficients needed to be accurately estimated.

Our prior [136] and current work [98] demonstrate the potential of iterative statistical image reconstruction (SIR) algorithms, based on physically accurate spectral and scatter distribution measurements, to limit input errors to the < 0.5% level required to address the poorly conditioned problem of DECT low energy photon cross-section mapping. For

instance, by using the polyenergetic alternating minimization (AM) method, [96, 98, 142] Evans et al. [20] were able to limit experimentally measured image-nonuniformity errors to 0.3%, independently of phantom size and location therein using raw sinograms (not subjected to preprocessing corrections for beam hardening) exported from a commercial 16-row CT scanner. Our subsequent SIR extensions reconstruct the $\left(c_1(\mathbf{x}), c_2(\mathbf{x})\right)$ images directly by operating jointly on unprocessed low- and high-energy experimentally-acquired sinograms.[136] Such innovations would not be possible without the BVM model, which accurately and efficiently (due to its linearity and separability [113]), supports estimation of monoenergetic linear attenuation coefficients.

4   On deriving x-ray CT spectra from the vendor's beam hardening correction polynomials

4.1 Background

Beam hardening (BH) is produced due to polychormaticity of the x-ray CT spectrum and energy dependence of attenuation coefficients.[25] Thus, the low energy photons are more likely to be attenuated than the photons with higher energy, such that the x-ray beam gradually becomes harder or more penetrating, i.e. mean energy increases with increasing thickness of absorbing materials. Fig. 4.1 shows the original 140 kVp x-ray spectrum before and after passing through a 15 mm thick aluminum absorber. It is noted that the spectra were normalized to unit area. As the low energy is preferentially absorbed, the mean energy of the x-ray beam (15 mm Al) is 86.1 keV, compared to its original mean energy (0 mm Al) in 79.5 keV. This figure clearly shows a spectral shift to the higher energy x-rays.

The fraction of photons attenuated by an object follows an exponential function of the attenuation coefficient, which is a function of energy. The transmitted intensity is the summation of exponential transmission of each energy in the spectrum, each of which undergoes a different attenuation due to the energy dependence of the attenuation coefficients along the photon path. The transmitted intensity can be written mathematically[143]

$$I = I_0 \int_E S(E) \exp\left(-\int \mu(x,E)\,dx\right) dE \qquad (31)$$

where S(E) is the normalized x-ray spectrum, I_0 and I represent the total number of incident and transmitted photons, respectively. The integral in the Eqn. (31) includes the energy range of the spectrum.

As described in Ch.1, the acquired forward projection is obtained by taking the logarithm of the ratio of transmitted to incident intensity photons.

$$FP(\mu(x,E)) = p = -\log \int S(E) \exp\left(-\int \mu(x,E)\,dx\right) dE \qquad (32)$$

Eqn. (32) indicates that the acquired projections follow the non-linear function of photon path length. If such non-linearity is not accounted by the reconstruction algorithm, beam-hardening effect may yield artifacts in images. [34, 144, 145]
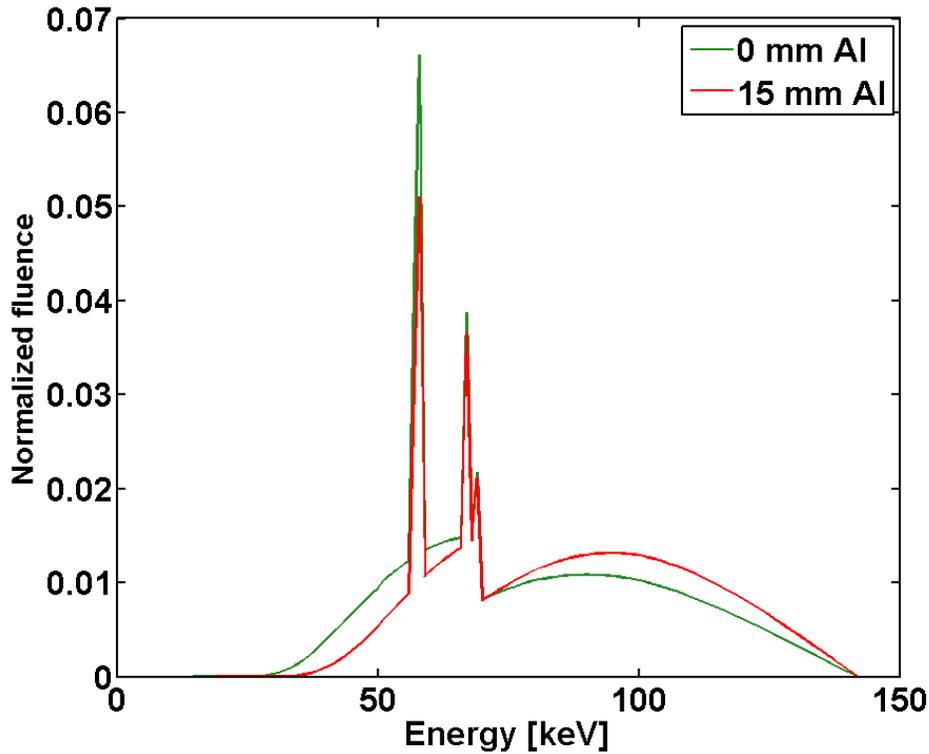
Fig. 4.1 Two normalized 140 kVp spectra penetrated aluminum plates with thickness of 0 mm and 15 mm, respectively

Such artifacts are illustrated by Fig.4.2, where the path length is the longest through the center of the image and approaches to zero close to the boundaries. Thus, the profile shown in Fig.4.2 (a) exhibits smaller spectrally-average linear attenuation coefficients in the center (where mean energy is high) than near the edges (where mean energy is lower), giving a characteristic "cup-like" appearance. However, with first order water-based linearization, the cupping nearly disappears (Fig. 4.2 (b)).

| (a) Without Correction | (b) With Correction |
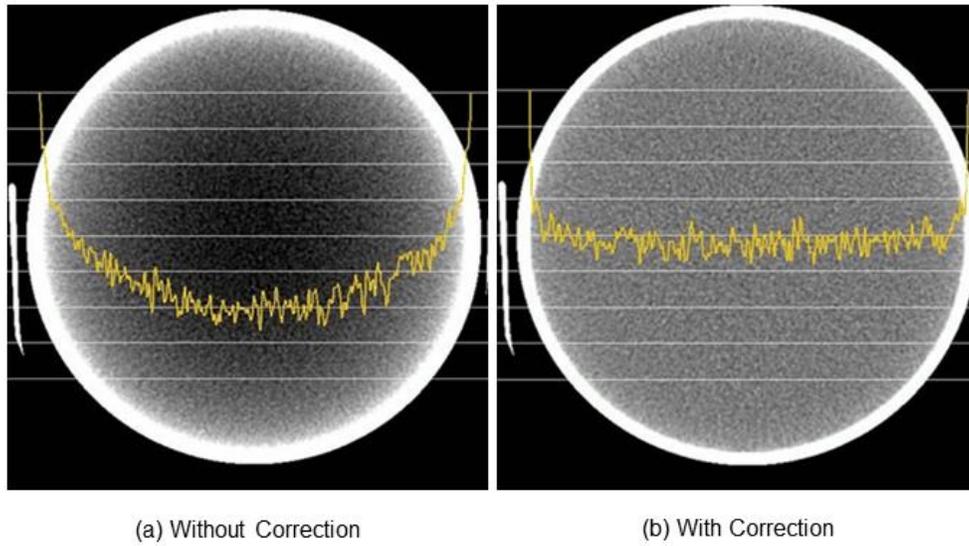
Fig. 4.2 (a) Cupping effects shown in the center region of 35-cm water phantom without correction applied (b) with BH correction scheme implemented, the BH artifacts nearly disappear.[25]

BH artifacts can be reduced by different approaches.[31, 34, 35, 99, 146–150] One approach is putting additional beam filters between patients and x-ray source to pre-harden the spectrum. [25, 34] The filter is designed to remove the low energy photons before they reach patients.

Another approach that has been extensively implemented on the third and fourth generation of CT scanners is the water-based BH correction proposed by McDavid et al. [35].

The assumption is that BH errors can be compensated by remapping the measured polyenergetic projections to precomputed monoenergetic projections based on water attenuation coefficient.[35, 147] Given the non-linear measured projections p from Eqn. (32), it can be mapped to a straight line by an n-th order polynomial function. The f(p) refers to projections of $f(p) = \int \mu_w(E^*, x)dx$, where μ_w and E^* are linear attenuation of water and target effective energy.

$$f(p) = A_n p^n + A_{n-1} p^{n-1} + \cdots A_1 p + a_0 \qquad (33)$$

A_i is the coefficient for i-th polynomial term, which can be determined by a minimum difference using non-linear curve as the independent variable and ideal straight line as the dependent variable.[25] A similar principle can be applied to correction towards other calibration materials.

To demonstrate this process, two spectra in Fig.4.1 are used to simulate the projections with beam hardening effects when they pass through polyoxymethylene (POM) layers of varying thickness from 0 cm to 50 cm. A straight line corresponding to corrected target of monoenergetic (60 keV) projection of POM is shown in Fig.4.3 (a) along with two uncorrected projections. To show the BH artifacts, the attenuation per unit thickness is demonstrated in Fig.4.3 (b). In order to correct the two hardened projections, two 4-th order polynomial functions are shown in Eqn. (34).
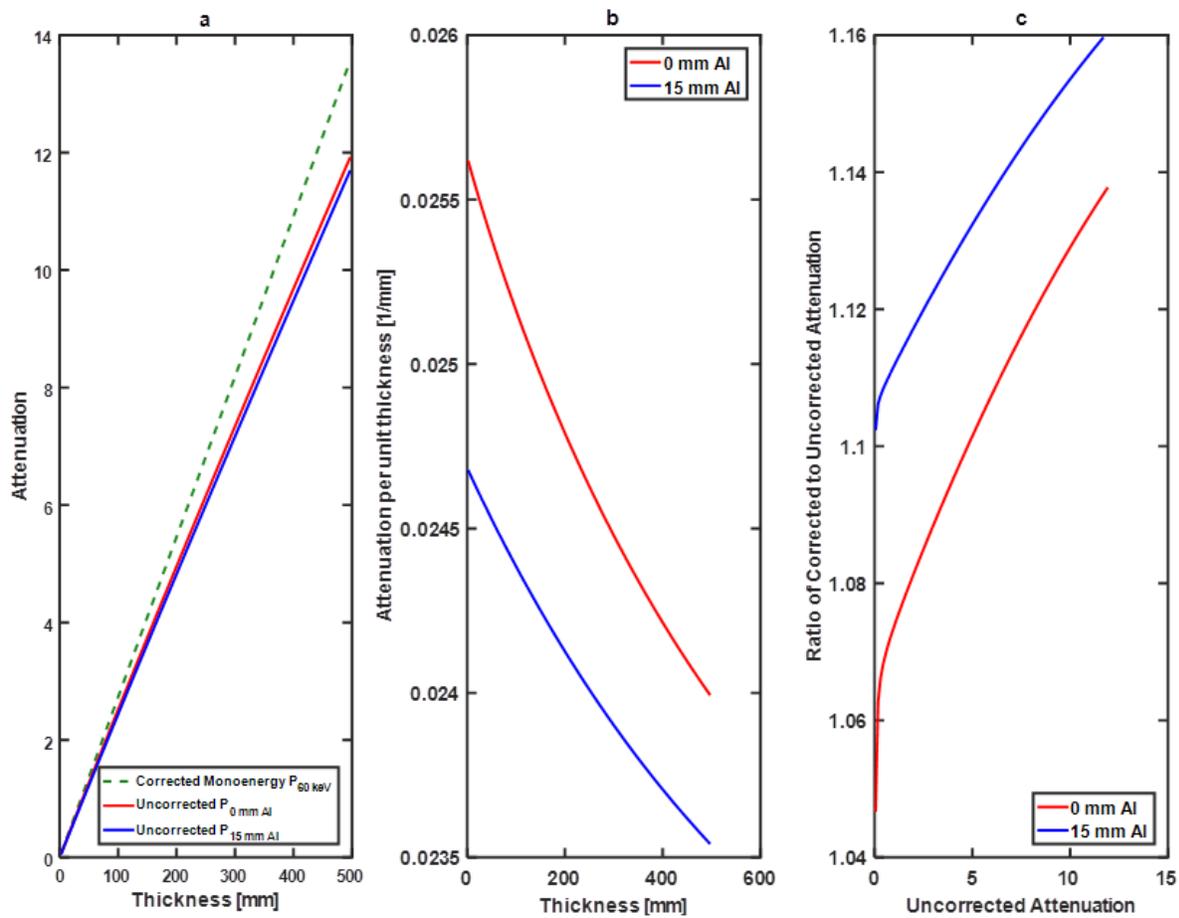
Fig. 4.3 illustration of BH water-based attenuation corrections for two different spectra passing through POM with varying thickness from 0 cm to 50 cm. (a) Uncorrected projections from spectra 0 mm Al and 15 mm Al and target monoenergetic (60 keV) projections; (b) Attenuation per thickness of two spectra, showing non-constant attenuation coefficient, i.e., beam-hardening effect; (c) ratios of corrected to uncorrected projections, showing the spectra dependent polynomial correction

$$f(p_0) = -1.3675 \times 10^{-4} p_0^3 + 0.075 p_0^2 + 1.0675 p_0^1 - 0.0012$$
$$f(p_{15}) = -9.7047 \times 10^{-5} p_{15}^3 + 0.0057 p_{15}^2 + 1.1064 p_{15}^1 - 2.3983 \times 10^{-4}$$

(34)

where p_0 and p_{15} represent the projections from spectra of 0 mm Al and 15 mm Al, respectively. After applying the correction of Eqn. (34), a nice match between the remapped projections and ideal linear function is shown in Fig.4.3 (a). One can notice that the polynomial coefficients are highly dependent on x-ray spectra. The two different spectra corresponding to different sets of coefficients are shown in Eqn. (34). The ratios of corrected to uncorrected projections are also illustrated for two spectra in Fig.4.3. (c). This suggests that CT x-ray spectra are encoded in the water-based beam-hardening correction.

When the scanned objects contain materials whose attenuation coefficients deviate from water significantly, i.e., bone, a water-based BH correction is not adequate. A second-order approach addressing BH induced by bone was suggested by Joseph and Spital. [36] It starts with an initial reconstruction depicting the approximate distribution of bone, and with the residual amount of projections produced by bone, the original projections can be possibly compensated. Alvarez and Macovski [31] proposed a more general approach based on DECT to correct the projections.

More advanced BH correction algorithms often require the knowledge of x-ray spectrum to accurately model the forward projection of Eqn. (31). Yan et al.[149] applied the method of Alvarez and Macovski to iteratively mitigate BH effect. Fessler et al [151]and O'Sullivan et al [142] implemented statistical model-based reconstruction algorithms that can remove BH artifacts effectively. These algorithms are implemented with a priori knowledge of the x-ray spectrum.

In order to obtain the x-ray CT spectrum, different indirect models are proposed. [1, 81, 90, 152] For example, Bazalova et al. [81] evaluated a Monte Carlo (EGSnrc) based method to simulate an x-ray tube, and found that differences between modeled spectra and directly measured spectrum using CdTe detectors were within 1.8%. Birch and Marshall (BM) implemented a semi-empirical, transmission-based, tungsten-target x-ray model to theoretically compute the spectra. [1] The thick-target BM model was derived from the simple Kramer [153] thin-target bremsstrahlung spectrum, with corrections for target self-attenuation and characteristic x-ray production, and requires specifications of the anode angle, kVp, and equivalent aluminum filter thickness spectrum. These three parameters can be obtained by fitting the spectrum to from narrow-beam transmission measurements, as originally proposed by Boone. [154] A non-linear optimization process is implemented to find the two parameter values (anode angle is known a priori) that minimize the relative fractional differences between measured transmission and modeled transmission values derived from the best-fit BM model. [98, 154] This three-parameter model has been evaluated and compared with directly measured spectra by many groups. [81, 89, 154] For example, Ay et al. [89] identified that discrepancies between the BM model and directly measured spectra within 1.1% for 140 kVp spectrum for tungsten target.

There are also limitations associated with above indirect methods. For example, Monte Carlo based methods are unable to account for the individual tube hardware variations and require exact knowledge of accelerating potential and ripple. [78] While conceptually straightforward, the estimation of spectrum using BM model and the processes of acquiring the transmission data can be tedious for clinical practice. Also, the access to raw, energy uncompensated proprietary data from the scanner detector array is required. Otherwise an independent detector with a known energy response model is needed.

The purpose of this chapter is to present an efficient method to derive a CT x-ray spectrum from the vendor's BH proprietary correction process accounted for spectral hardening. The process operator is denoted as $\mathcal{B}$ and its associated parameters can be extracted from the sinogram header.

This technique can be used to facilitate model-based x-ray CT reconstruction algorithms and sinogram-based material decomposition. It can also be used to routinely monitor changes in the spectrum as the scanner tube ages.[73, 155]

This technique demands the access to x-ray CT raw data and hardware design, including scanner geometrical dimensions and the knowledge of bowtie filter geometry and composition. The associated BH corrections, usually embedded in header of the raw data files, must be accessible. The calibration phantom information, including composition, density and dimensions is also needed along with the capacity to duplicate the vendor's beam-hardening correction in an independent computer code.

The proposed technique in this study focuses on the reconstruction of spectra of 90 kVp and 140 kVp, which are widely used in quantitative DECT studies. It is anticipated that this technique can also be applied to derivation of spectrum 120 kVp, which is more widely used for clinical imaging.

4.2 Methods and Materials

This section starts with the procedure of phantom-based calibration process implemented by Philips, and our best understanding as to how BH coefficients (also called "BH parameters") are determined is also presented. Our method of derivation of spectrum is followed by a narrow beam transmission measurement for BM model spectrum determination.

4.2.1 Implementation of beam-hardening correction by Philips

An eye-shaped calibration phantom, made of POM, is used for the calibration procedure. The dimensions of calibration phantom are shown in Fig.4.4
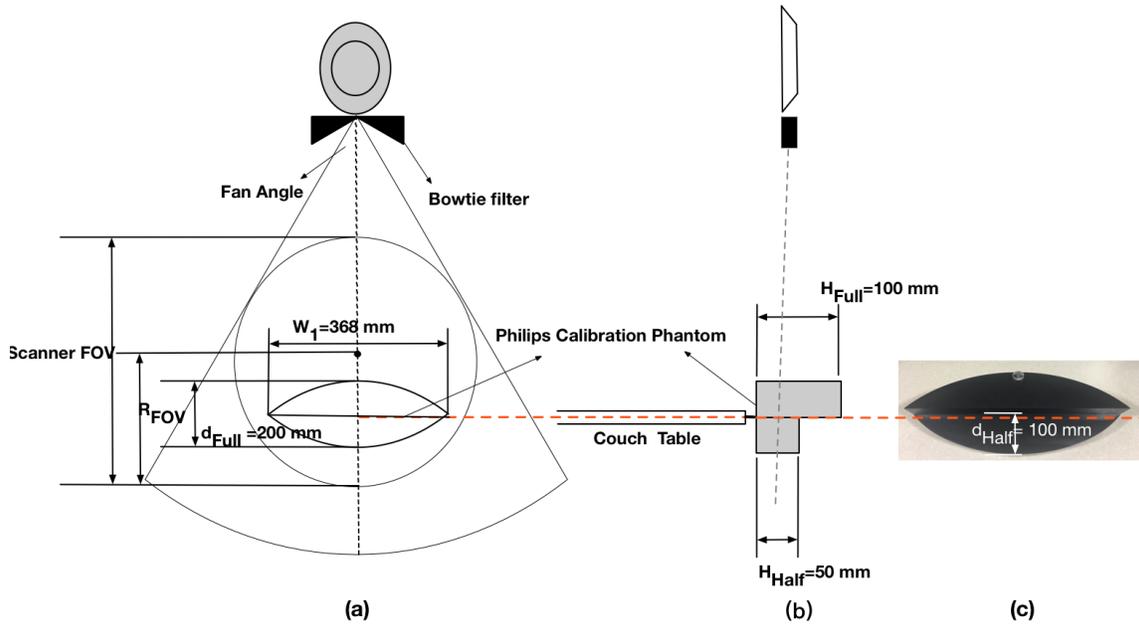
Fig 4.4. The calibration phantom utilized by Philips for determination of BH hardening correction coefficients

The phantom has two components, each of which has the vertical central thicknesses 100 mm and 200 mm, respectively. The first component is called "half phantom", and the second one is called "full phantom". When the calibration procedure is performed, the whole phantom is hung off the end of the couch as shown in Fig.4.4 (b). Three spectra 90 kVp, 120 kVp and 140 kVp with the collimator settings of 12 mm and 24 mm are used to scan the phantom. During the calibration scan, the scanner is operated in a scout view mode with the gantry parked at the 6 o'clock position while the table is translated to acquire multiple readings for both full and half components. The BH correction function is a fourth-order polynomial function, specified by $\mathcal{B}$, that maps the polyenergetic projection data to monoenergetic data in the attenuation domain.

The primary transmission signal through inherent filtration of tube d_{Al}, bowtie filter, and calibration phantom is given by

$$\Pr\left(\gamma|kvp,d_{Al}\right)=\int_{E}\Phi_{BM}\left(E|kvp,d_{Al}\right)Q(E)e^{-\mu_{BT}(E)d_{BT}(\gamma)-\mu_{P}(E)d_{P}(\gamma)}dE \qquad (35)$$

where $\mu_{BT}(E)$ and $\mu_P(E)$ are the attenuation coefficient of the bowtie (BT) filter and calibration phantom at photon energy E, respectively; $d_{BT}(\gamma)$ and $d_P(\gamma)$ are the thickness of bowtie filter and calibration phantom material traversed by primary photons with fan beam angles γ, respectively. $\Phi_{BM}(E|kVp, d_{Al})$ specifies an equivalent spectrum (intensity) determined by the BM model using free parameters: kVp, inherent filtration of tube d_{Al}, and anode angle, which was provided by the vendor.

The detector response function $Q(E)$ was defined as product of photon energy and quantum detection efficiency (QDE) as CT detectors are energy integrators

$$Q(E) = E \cdot \left(1 - e^{-\mu_{\det}(E)d_{\det}}\right) \qquad (36)$$

where $\mu_{\det}(E)$ and $d_{\det}$ are attenuation coefficients of the scintillator medium at energy E, and its thickness, respectively.

It is assumed that the coefficients of $\mathcal{B}$ are determined by minimizing the deviation from unity of the following quality function (or QF for short) of the calibration phantom. Ideally, $QF_{P,\text{model}}(\gamma|kVp, d_{Al}, B)$ will be unity across all subtended fan beam angles

$$QF_{P,\text{model}}(\gamma|kVp, d_{Al}, \mathcal{B}) = \frac{\mathcal{B}\left(-\log\left(\Pr_F(\gamma) + (S/P)_F \Pr_F(0)\right)\right) \Big/ \mathcal{B}\left(-\log\left(\Pr_H(\gamma) + (S/P)_H \Pr_H(0)\right)\right)}{d_{P,F}(\gamma) \Big/ d_{P,H}(\gamma)}$$

$$(37)$$

S/P refers to the scatter-to-primary ratio through the calibration phantom at beam angle 0 during the procedure of calibration, when the x-ray tube is parked at 12 o'clock. Subscripts of F and H represent full and half phantom, respectively.

With the measured signal $M(\gamma)$ including primary transmission and scatter, Eqn. (37) can be rewritten as

$$QF_{P,meas}\left(\gamma\middle|kVp,d_{Al},\mathscr{B}\right)=\frac{\mathscr{B}\left(-\log\left(M_{F}\left(\gamma\right)\right)\right)\Big/\mathscr{B}\left(-\log\left(M_{H}\left(\gamma\right)\right)\right)}{d_{P,F}\left(\gamma\right)\Big/d_{P,H}\left(\gamma\right)} \quad (38)$$

4.2.2 Derivation of a spectrum based upon beam hardening correction

The quality function $QF_{P,meas}$ is assumed to be unchanged with respect to time of raw data acquisition. The drift of spectrum is correlated with the variation of coefficients of BH operator $\mathscr{B}$.

The x-ray spectra from were independently measured (γ =0) at two different years (Y1 = 2010, Y2 = 2017) for the tube potentials of 90 kVp and 140 kVp based on the narrow-beam transmission measurement discussed in 4.2.3. The BH correction parameters are computed by the vendor's dedicated software, based on the linearizing projections from the Philips calibration phantom. The BH parameters for Y1 and Y2 were extracted from the raw sinogram file header. The measured spectrum of time point Y1 $\Phi_{Y1}\left(E\middle|kVp,d_{Al}\right)$ was treated as a reference spectrum to produce a quality function (which is close to, but not exactly unity) of the calibration phantom using the associated vendor's BH correction coefficients. $\mathscr{B}_{Y_1}$ and Eqn. (37). The measured spectrum at Y2 was used to validate the spectrum derived from the BH correction of Y2. The distance of calibration phantom to iso-center of the field-of-view (FOV) was set according to the manual provided by vendor for calibration purpose. For each fan beam angle γ, the path length through half and full phantom were computed, and $QF_{P,model}\left(\gamma\middle|kVp_1,d_{Al,1},\mathscr{B}_1\right)$ can be simulated based on the Eqn. (37) using measured spectrum of Y1.

Since we have only two independent spectrum measurements on single scanner, a simulation study (see section 4.2.3) was performed to assess the robustness and uncertainty of the method.

For each fan beam angle γ, the path length through half and full phantom were computed, and $QF_{P,\text{model}}\left(\gamma|kVp_1, d_{Al,1}, \mathcal{B}_1\right)$ can be simulated based on the Eqn. (37) using measured spectrum of Y1.

In order to derive the spectrum from updated coefficients $\mathcal{B}_{Y_2}$ at Y$_2$, the optimization problem is formulated as follows

$$\left(kVp_{Y_2}, d_{Al,Y_2}\right) = \underset{kVp, d_{Al}}{\textbf{argmin}} \sum_{\gamma} \left(\frac{QF_{P,\text{model}}\left(\gamma|kVp, d_{Al}, \mathcal{B}_{Y_2}\right) - QF_{P,\text{model}}\left(\gamma|kVp_{Y_1}, d_{Al,Y_1}, \mathcal{B}_{Y_1}\right)}{QF_{P,\text{model}}\left(\gamma|kVp_{Y_1}, d_{Al,Y_1}, \mathcal{B}_{Y_1}\right)}\right)^2$$

(39)

Our spectrum derivation for free parameters kVp_{Y_2}, d_{Al,Y_2} of Y$_2$ was carried out with exhaustive search for all candidate pairs of $\left(kVp, d_{Al}\right)$.

The values of $\left(S/P\right)$ can also be incorporated in the computation of $QF_{P,\text{model}}\left(\gamma|kVp_1, d_{Al,1}, \mathcal{B}_1\right)$. A heuristic measurement of scatter using high attenuating tungsten rod with diameter of 6.35 mm was performed.[156] The calibration protocol of Philips was followed to setup the eye phantom with the rod placed on the top. The setup of the measurement is shown in Fig. 4.6 below. The assumption is that the signal from the detectors blocked by tungsten rod can be attributed from scatter.

Fig. 4.6 An experimental setup for scatter signal measured is shown. A tungsten rod was placed on top of calibration phantom

A combination of 12 mm and 3 mm collimation size were used with two energetic spectra, including 90 kVp and 140 kVp.

The assumed S/P values for both accelerating potentials, full and half phantom are shown in table 4.1. A consistent pair of S/P values for full and half phantom should be maintained in Eqn. (37) and Eqn. (39) for each energy spectrum.

Table 4.1. S/P values for the 12 mm collimation used in the simulation of $QF_{P,\text{mod}el}\left(\gamma|kVp,d_{Al},\mathscr{B}\right)$ for 90 kVp and 140 kVp

	Half Phantom	Full Phantom
90 kVp	0.0146	0.0348
140 kVp	0.0163	0.0302

The flow chart in Fig. 4.7 below demonstrates the proposed procedure to reconstruct the spectrum of Y2 based on the simulated objective function of BH correction from Y1 and Y1 spectrum.

In order to evaluate the accuracy of derived spectrum Y2, the differences of mean energy, kVp, d_{Al}, A root-mean-square-error was used to evaluate the difference of two spectra. $RMSE = \sqrt{\dfrac{\sum\limits_{i=1}^{N_E}\left(S_{i,meas} - S_{i,ref}\right)^2}{N_E}}$ where N_E is the total number of energy bins of spectra S_{meas} and S_{ref}, respectively.
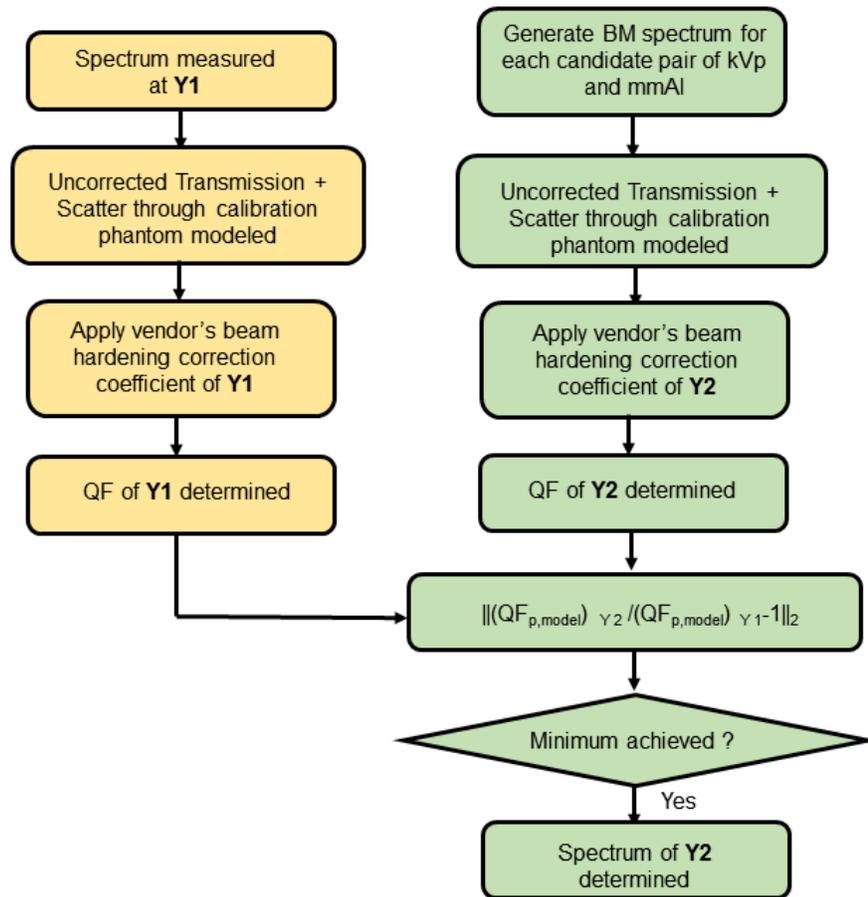

Fig.4.7. Flowchart of the proposed method of spectrum derivation based on BH polynomials correction

4.2.3 Robustness and uncertainty analysis

In order to evaluate the robustness of proposed method to large variations of BH correction polynomial coefficients, a simulation experiment was performed. A family of

perturbed BM spectra were created by varying the parameters of kVp, d_{Al}. The raw calibration phantom was measured $QF_{P,meas}$ through the calibration procedure. Based on our understanding of the goals of Philips' BH correction, an objective function was formulated and BH correction polynomial coefficients determined by minimizing the calibration objective function, i.e., linearized the half- and full-attenuation profiles, for each perturbed spectrum $\Phi'_{BM}\left(E\middle|kVp, d_{Al}\right)$.

The robustness analysis consists of searching for the BH correction coefficients to correct the simulated noiseless data of $QF_{P,\mathrm{mod}el}$ that match the $QF_{P,meas}$. Relative to the nominal spectra of 90 kVp and 140 kVp, the perturbed spectral kVp's ranged from 85 kVp to 93 kVp and 135 kVp to 143 kVp, respectively. The inherent aluminum filtration ranged from 10 mm to 18 mm. The step sizes of searching were set as 0.5 mm and 1 keV, respectively. The contributions of scatter were ignored in the analysis. For each perturbed spectrum, $\Phi'_{BM}\left(E\middle|kVp, d_{Al}\right)$ and associated BH correction, $\mathcal{B}\left(\left(P_{noiseless}(\gamma)\middle|\Phi'_{BM}\left(E\middle|kVp, d_{Al}\right)\right)\right)$ the spectrum was derived from our method in Fig. 4.7, compared against the synthetic ground truth spectrum $\Phi'_{BM}\left(E|kVp, d_{Al}\right)$.

The uncertainty analysis was also performed by adding Poisson noise to the expected transmission in the $QF_{P,\mathrm{mod}el}$ simulated by perturbed spectrum, $\Phi'_{BM}\left(E\middle|kVp, d_{Al}\right)$. The Poisson noise level was chosen to mimic the sinogram noise of BH calibration scans by adjusting absolute source intensities. The noisy $QF_{P,\mathrm{mod}el}$ was used to determine the updated BH polynomial correction $\mathcal{B}\left(\left(P_{noisy}(\gamma)\middle|\Phi'_{BM}\left(E\middle|kVp, d_{Al}\right)\right)\right)$, and spectrum was then derived from the our proposed method and compared with true perturbed spectrum. The procedure of the robust analysis is shown in the flowchart of Fig.4.8. And the flowchart of uncertainty analysis is also shown in Fig.4.9.
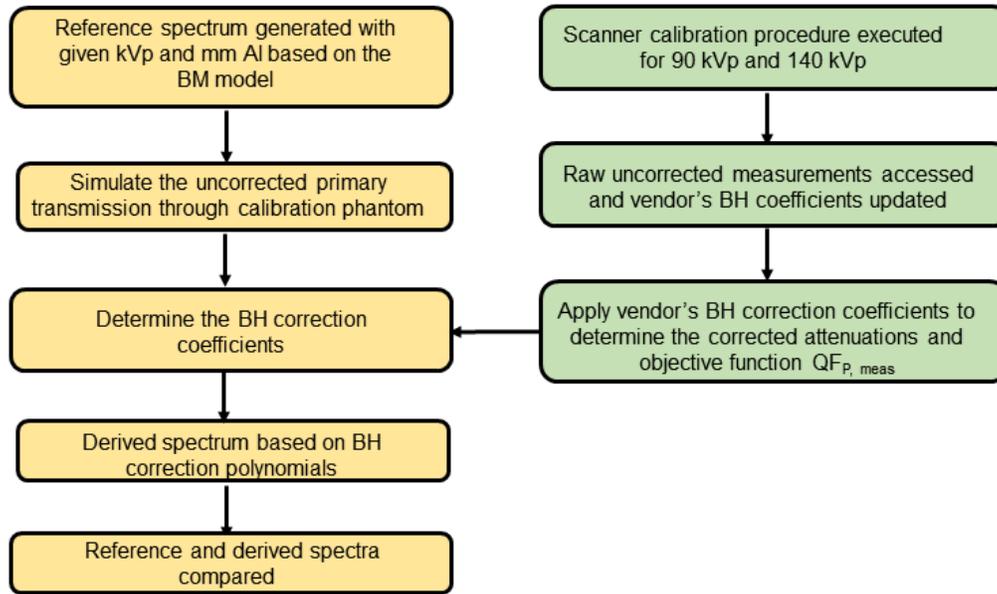
Fig.4.8. Flowchart of the procedure of robustness analysis of spectrum. Given a wide range of variations of spectral parameters, the robustness analysis compares the reference and derived spectra for each pair of parameters
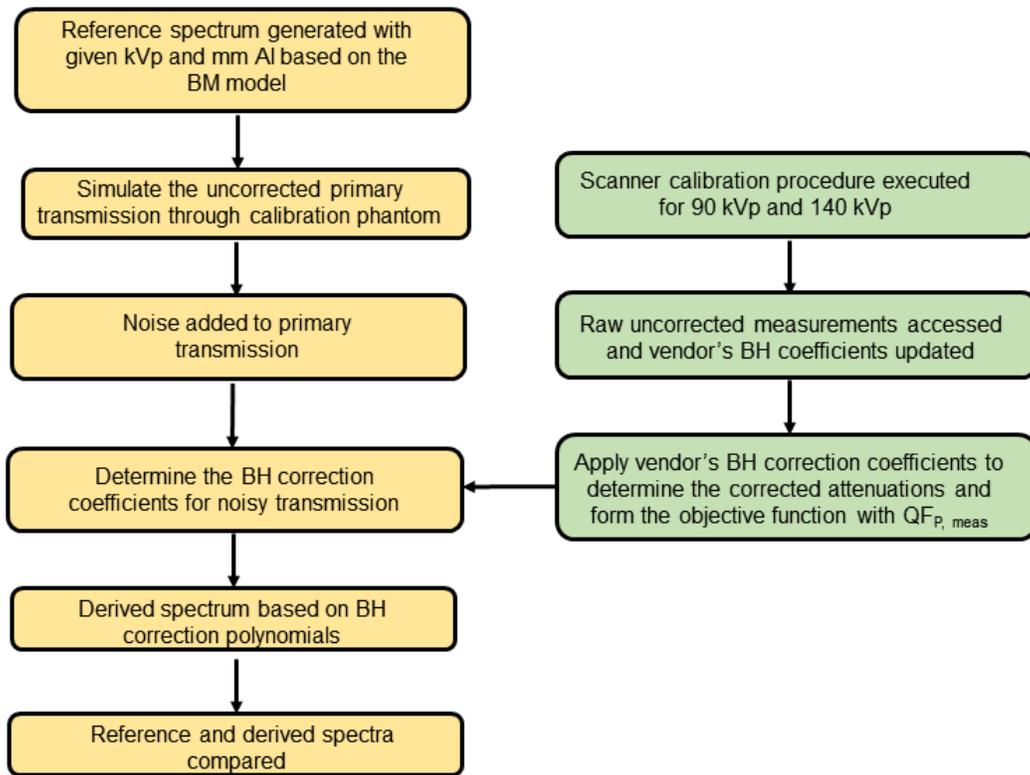
Fig.4.9. Flowchart of the procedure of uncertainty analysis of spectrum. A Poisson noise was added to primary transmission from reference spectrum, which yielded an updated set of BH polynomial correction coefficients. The derived spectrum was also compared against reference spectrum.

Similarly, the differences between estimated and ground truth mean energy, kVp, d_{Al} and root-mean-squared-errors of the derived and simulated spectra were reported. For uncertainty analysis, the spectral parameters between reference and derived were reported.

4.2.4 Birch-Marshall spectrum model and experimental setup

The Birch-Marshall spectrum model [1] is an empirical model that predicts bremsstrahlung spectrum produced in a thick target with given anode angle, including target self-absorption and characteristic radiation. With free parameters kVp, anode angle and equivalent inherent filtration d_{Al} determined, a spectrum $\Phi_{BM}\left(E|kVp, d_{Al}\right)$ can be specified.

In this study, a BM spectrum method,[1, 154] in which parameters kVp, d_{Al} are determined by narrow-beam transmission measurement, was adopted to determine the spectrum for our Philips Brilliance Big Bore scanner.

For each tube potential investigated in this study (90 kVp and 140 kVp), narrow beam transmission measurements through stacks of aluminum (Al) and copper (Cu) plates with varying thickness were carried out on the central axis (CAX) of the scanner. Narrow beam geometry was achieved by using a small collimator assembly, [98] which ensured that the transmission measurements were free from scatter contamination. The apparatus of collimator assembly, including Al and Cu filters, was shown in Fig.4.10. A total of 21 foils were used, including 15 Al foils and 6 Cu filters.

Fig.4.10. A collimator assembly [98] and stacks of Al and Cu are shown

The 3 mm beam collimation was used. Three parameters of a BM model: anode tube angle, inherent aluminum infiltration, and tube potential were utilized to specify the equivalent spectrum. To determine the equivalent spectrum, a simplified BM model , which includes detector efficiency, is shown below

$$\Phi^{eq}(E) = \Phi_{BM}\left(E \middle| \arg\min_{\left(kVp_{eq},d_{Al,eq}\right)} \left[\sum_d \left(\frac{T_{model}\left(d\middle|kVp,d_{Al}\right) - T_{meas}(d)}{T_{meas}(d)} \right)^2 \right] \right) \qquad (40)$$

where $T_{model}(d)$ and $T_{meas}(d)$ represent the modeled and measured transmission through stacks of aluminum or copper filters of thickness d, respectively.

$$T_{model}\left(d|kVp,d_{Al}\right) = \Phi_{BM}\left(E|kvp,d_{Al}\right)e^{-\mu_{Al}d} \quad (41)$$

The pre-filtered source spectrum can be written as

$$\Phi_{BM}\left(E|kVp,d_{Al}\right) = \Phi_{BM}\left(E|kVp,0\right)e^{-\mu_{Al}d_{Al}} \quad (42)$$

The equivalent BM spectrum Φ_{BM} at CAX with equivalent kVp_{eq} and inherent filtration ($d_{Al,eq}$) can be found by minimizing the relative fractional difference between measured and modeled transmission by Eqn. (40). An exhaustive search was also implemented to find the kVp_{eq} and inherent filtration $d_{Al,eq}$. The detector efficiency $Q(E)$ was also included.

4.3 Results

4.3.1 Independent spectrum measurement at two different years

At Y1 (2010) and Y2 (2017), the procedures outlined in 4.2.4 were implemented to measure the narrow-beam transmission through Al and Cu filters, from which the equivalent spectra based on BM model were estimated for 90 kVp and 140 kVp, respectively. For example, for 140 kVp, the comparisons of transmission through Al and Cu filters between year 1 and year 2 are shown in Fig. 4.11. (for 90 kVp) and Fig. 4.12 (for 140 kVp), respectively. The comparison of spectra measured at Y1 and Y2 is also shown for 90 kVp and 140 kVp in table 4.2 and table 4.3, respectively.

Table 4.2. Comparisons of 90 kVp measured at Y1 and Y2

	kVp	d_{Al} [mm]	mean energy (keV)
Y2	90	12.7	57.3868
Y1	90	11.9	56.9835

Table 4.3. Comparisons of 140 kVp measured at Y1 and Y2

	kVp	d_{Al} [mm]	mean energy (keV)
Y2	141	12.8	72.697
Y1	141	12.6	72.565
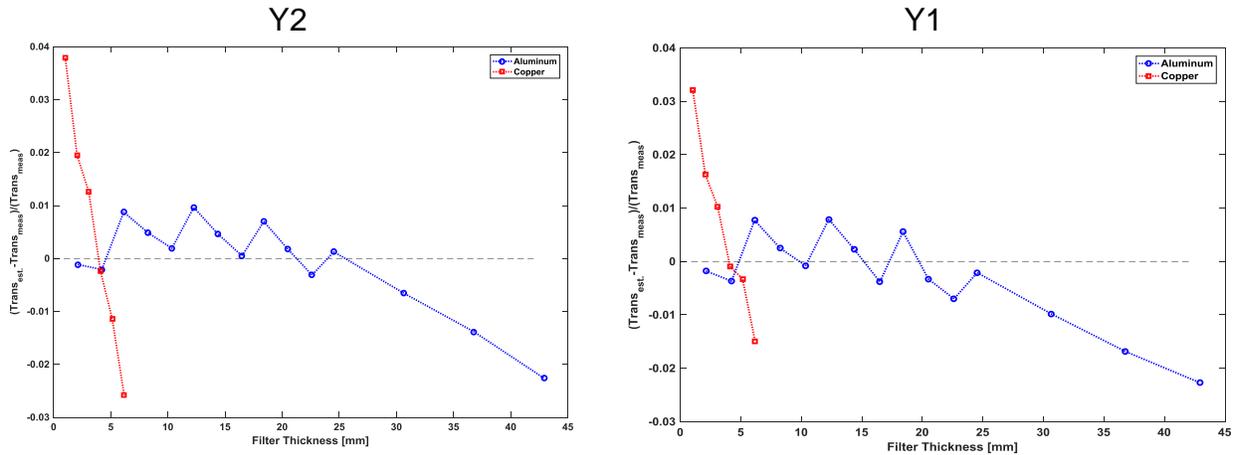
Fig. 4.11. The transmission comparisons for spectra of 90 kVp at Y1 and Y2 through Al and Cu filters
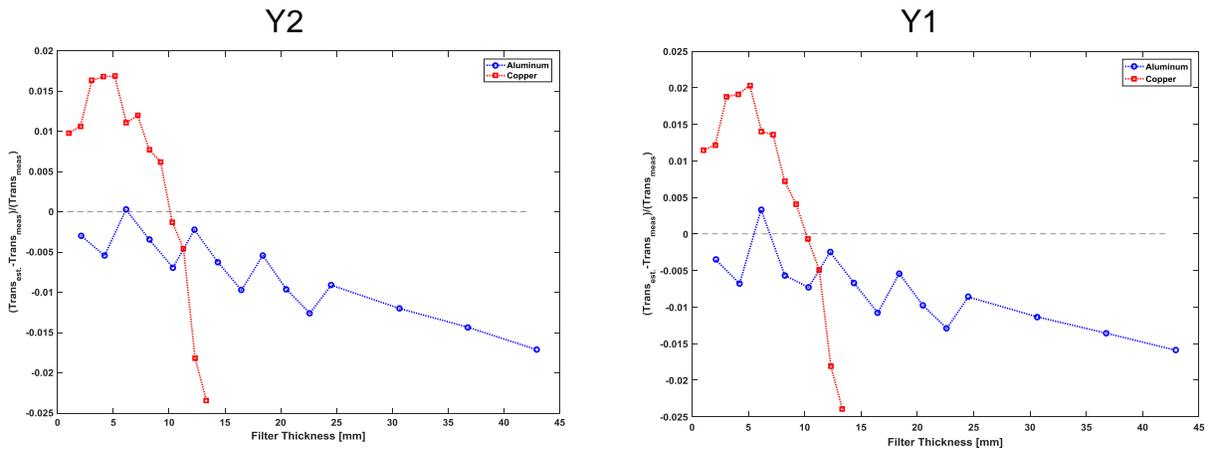
Fig. 4.12. The transmission comparisons for spectra of 140 kVp at Y1 and Y2 through filters

The mean differences of Al transmission between measured and estimated spectra are 0.2 % for 140 kVp at two different years, while for Cu transmission differences are 0.5%.

Thus, there is no substantial spectrum quality drift between two years for 140 kVp. Similar accuracy was achieved for 90 kVp for Al and Cu transmission measurement. These results were also corroborated by the fact that the BH correction polynomial

coefficients of these two years were similar and not identical, which indicates the deviation of the spectra of two years was not notable.

4.3.2 Spectrum derivation from BH correction

The results of spectrum derivation are shown in Fig. 4.13 and Fig. 4.14. No significant difference was found between reference spectra and derived spectra for 90 and 140 kVp at Y2, respectively.
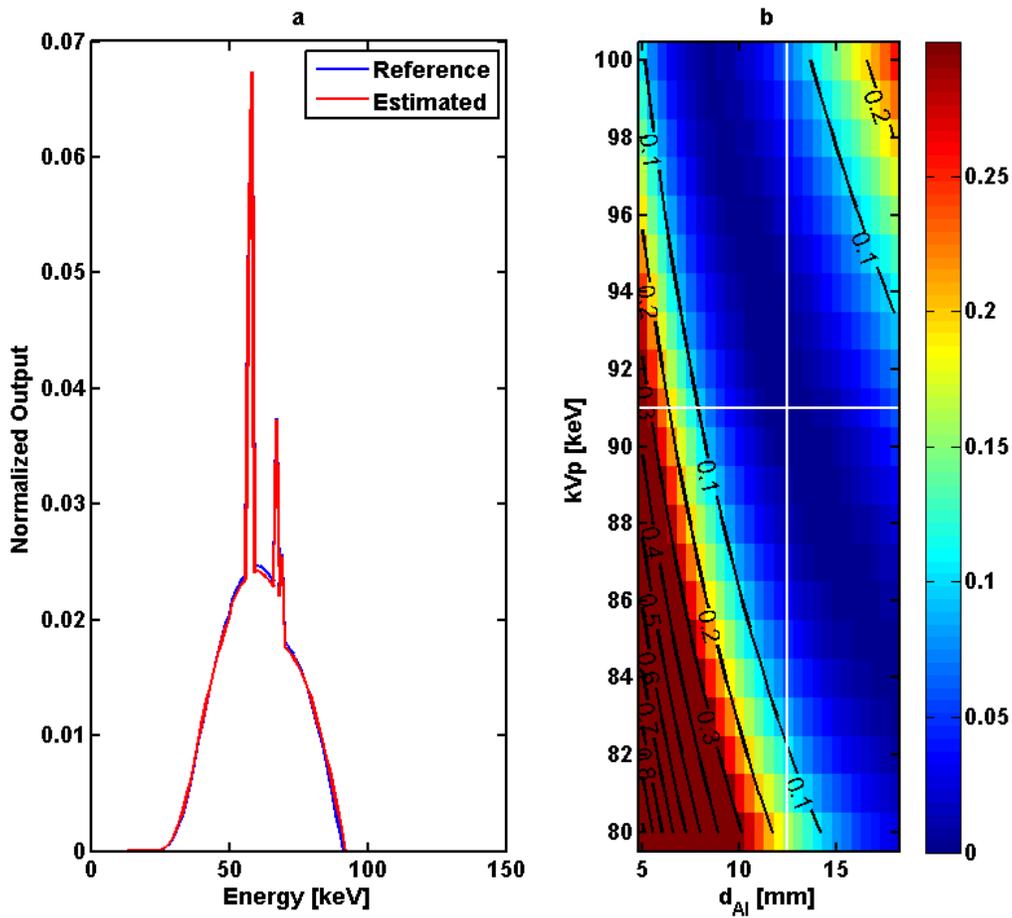
Fig.4.13 Comparison of derived spectrum and independent measured spectrum for 90 kVp of Y2 shown in (a), and the white cross in (b) correspoding to parameters for specifying a spectrum base on BM model.

Table 4.3. Quantitative comparison results of Fig. 4.13

|	kVp	d_{Al} [mm]	mean energy (keV)	RMSE
Meas.	90	12.8	57.40	
Estimated	91	12.5	57.63	0.03
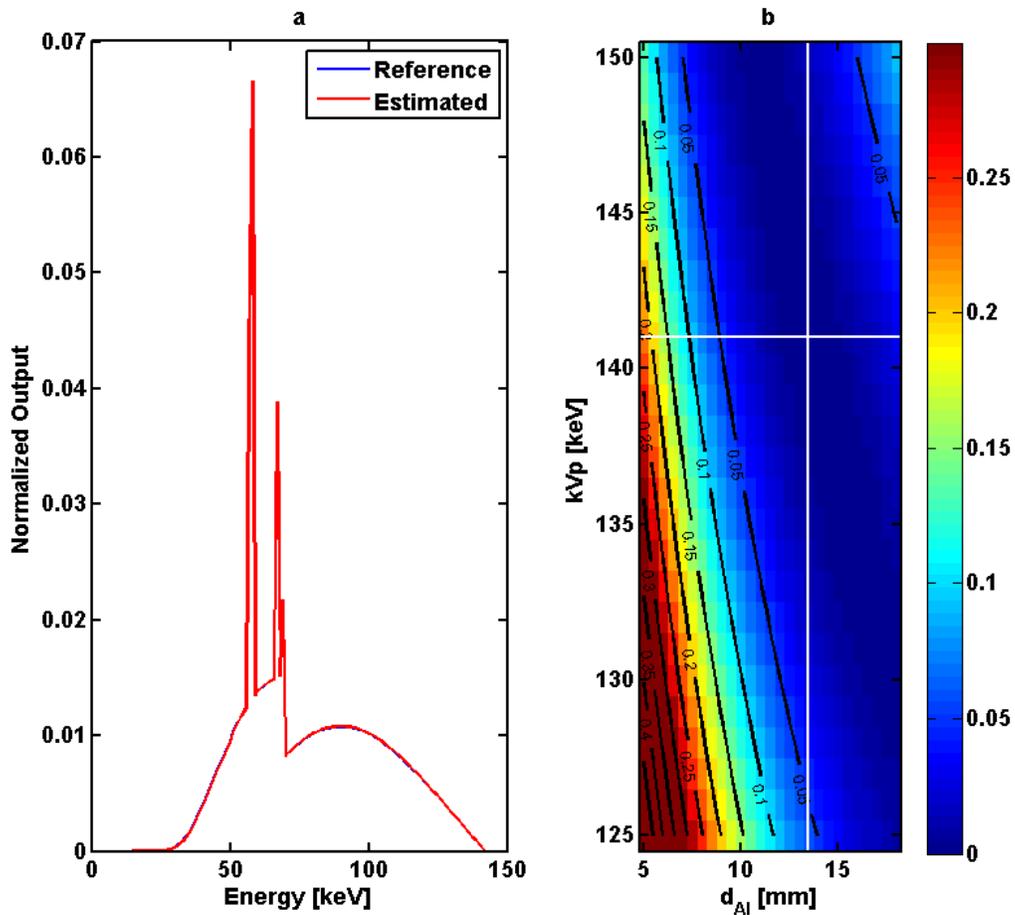
Fig.4.14 Comparison of derived spectrum and independent measured spectrum for 140 kVp of Y2 shown in (a), and the white cross in (b) correspoding to parameters for specifying a spectrum based on BM model.

Table 4.4 Quantitative comparison results of Fig. 4.14

	kVp	d_{Al} [mm]	mean energy (keV)	RMSE
Meas.	141	12.8	72.70	

| Estimated | 141 | 13.5 | 72.14 | 0.004 |

The mean energy difference for 90 kVp and 140 kVp between reference and derived spectra are 0.23 keV and 0.56 keV, respectively.

4.3.3 Robustness and uncertainty analysis of spectrum derivation

The high fidelity between the synthetic ground truth spectra and derived from the corresponding vendor beam-hardening corrections for the case of noiseless $QF_{P,\text{model}}$ is demonstrated in Fig. 4.15 and Fig. 4.16 for 90 kVp and 140 kVp, respectively. For example, each pixel in 4.15 (a) shows the discrepancy of mean energy for reference and derived spectra. The differences are well within 0.5 keV. Most of the pixels in (c) and (d) show the difference of kVp and $d_{Al,eq}$ are either 0 keV or -1 keV, and 0 mm for inherent aluminum thickness, respectively.
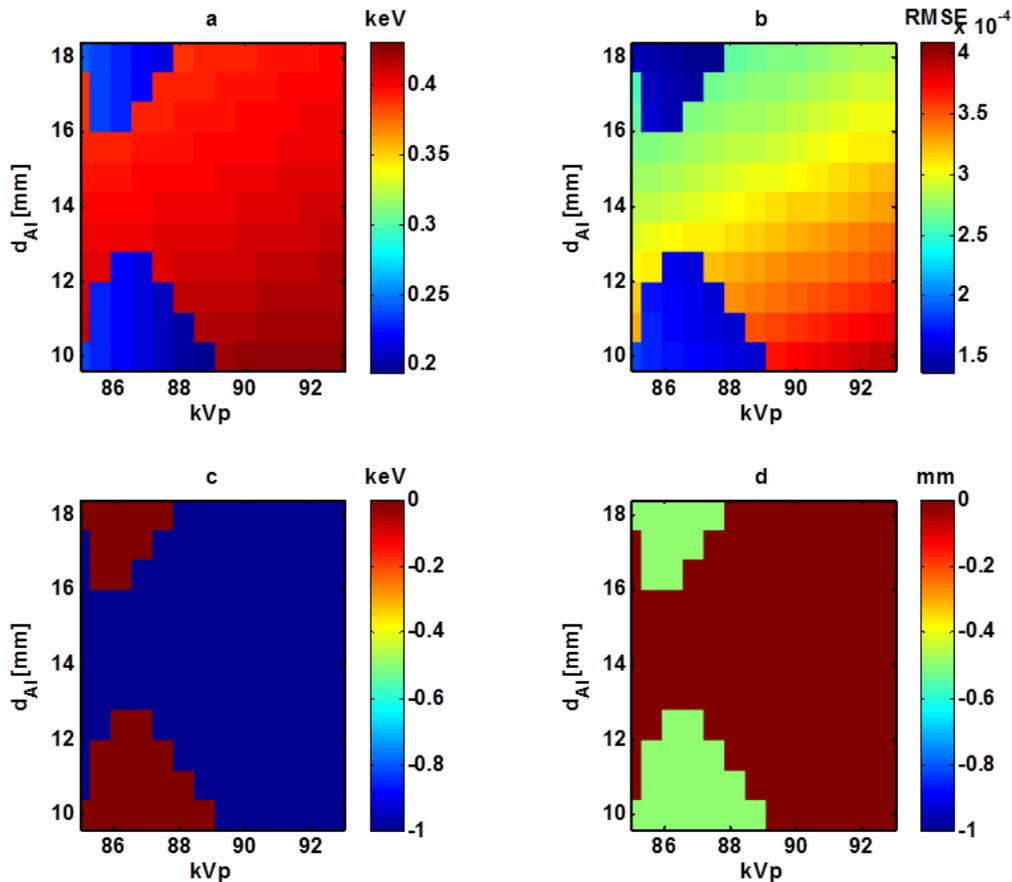
Fig.4.15 Comparisons of derived spectrum and independently simulated reference spectra for nomial 90 kVp with inherent filtration of aluminum ranging from 10 mm to 18 mm for the noiseless $QF_{P,\mathrm{model}}$ The differences of mean energy (a), RMSE (b), kVp(c), and d_{Al} (d) are shown, respectively. Each pixel on the figures corresponded to the discrenpance for each candidate of reference spectrum.

A similar distribution of accuracy results for the 140 kVp nominal family of perturbed ground truth spectra. The RMSEs are well within 0.0002 for all possible pairs of spectra. The results of robustness analysis here show the indistinguishable difference of two spectra, in other words, with provided wide range of BH correction polynomial correction coefficients, our proposed method is able to reproduce the spectrum with high accuracy.
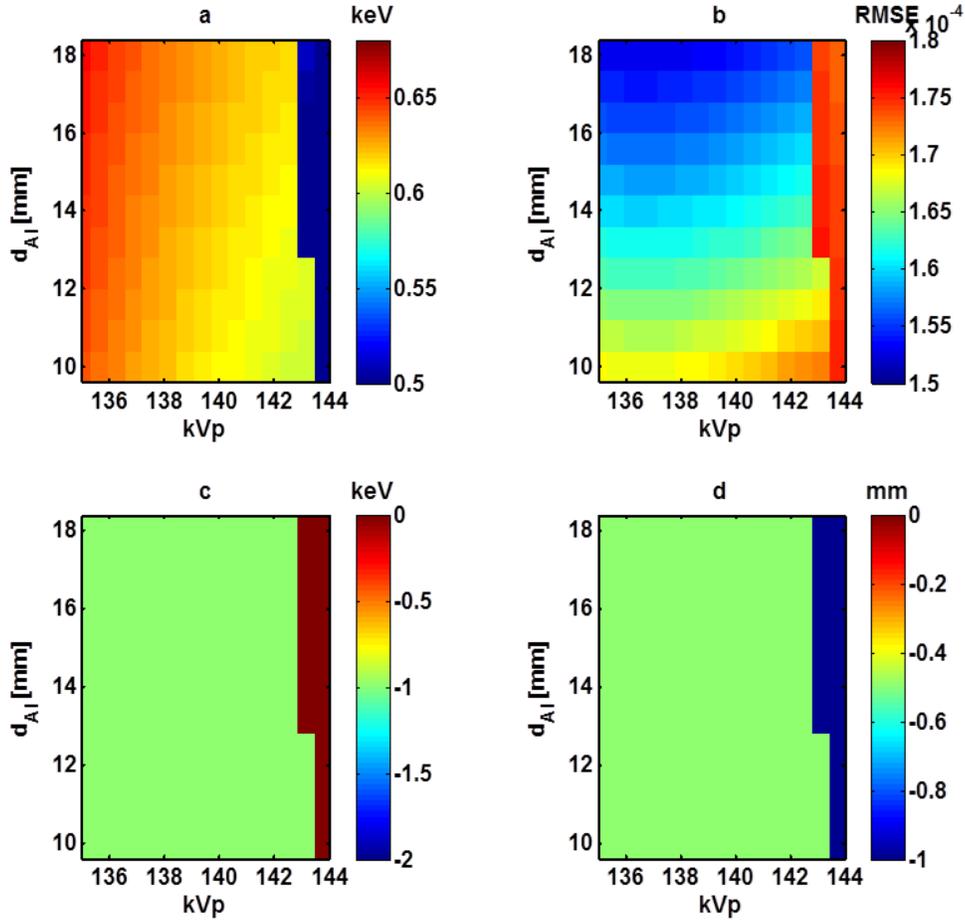
Fig.4.16 Comparisons of derived spectrum and independently simulated reference spectra for nomial 140 kVp with inherent filtration of aluminum ranging from 10 mm to 18 mm for the noiseless $QF_{P,\mathrm{mod}el}$. The differences of mean energy (a), RMSE (b), kVp(c), and d_{Al} (d) are shown, respectively. Each pixel on the figures corresponded to the discrenpance for each candidate of spectrum.

Fig 4.17 shows the comparisons of forward projections for full calibration phantom with and without Poisson noise produced by typical spectra of 90 kVp and 140 kVp. The added noise levels, e.g. standard deviation, are shown in table 4.5. Even with noisy $QF_{P,\mathrm{mod}el}$, the derived spectra for 90 kVp (Fig. 4.18) and 140 kVp (Fig. 4.19) could reproduce the reference spectra accurately. For example, the differences of mean energy for 90 kVp and 140 kVp are within 0.4 keV and 0.8 keV, respectively, while for aluminum filtration, the differences are within 0.5 mm and 1 mm, respectively. By comparing the two reconstructed families of spectra for cases of noiseless and noisy projections, our proposed method shows its insensitivity to noise.
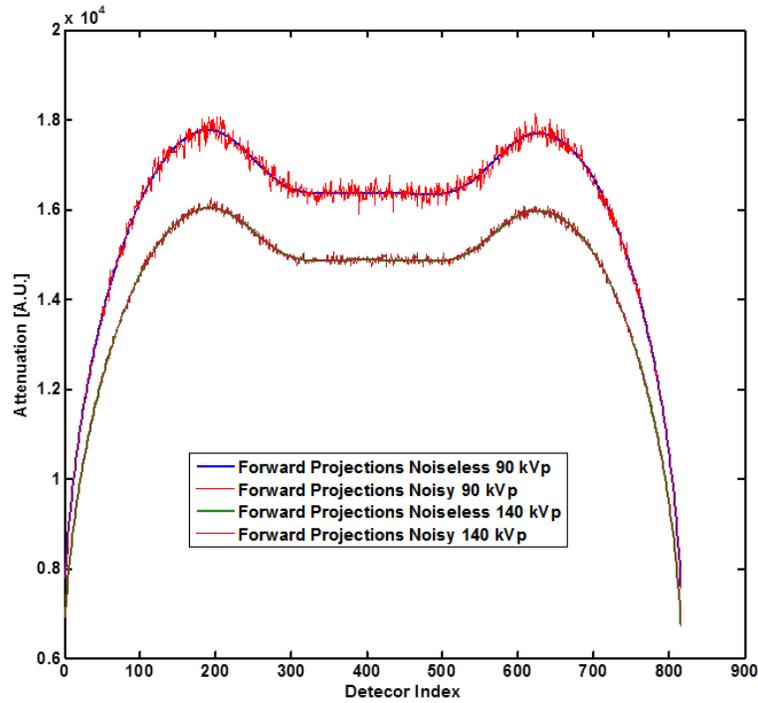
Fig.4.17 Comparisons of forward projections with and without noise for full calibration phantom at spectra of 90 kVp and 140 kVp.

Table 4.5 Standard deviation of noisy forward projections of full and half phantoms

|	Full Phantom	Half Phantom
90 kVp	0.24	0.12
140 kVp	0.12	0.08
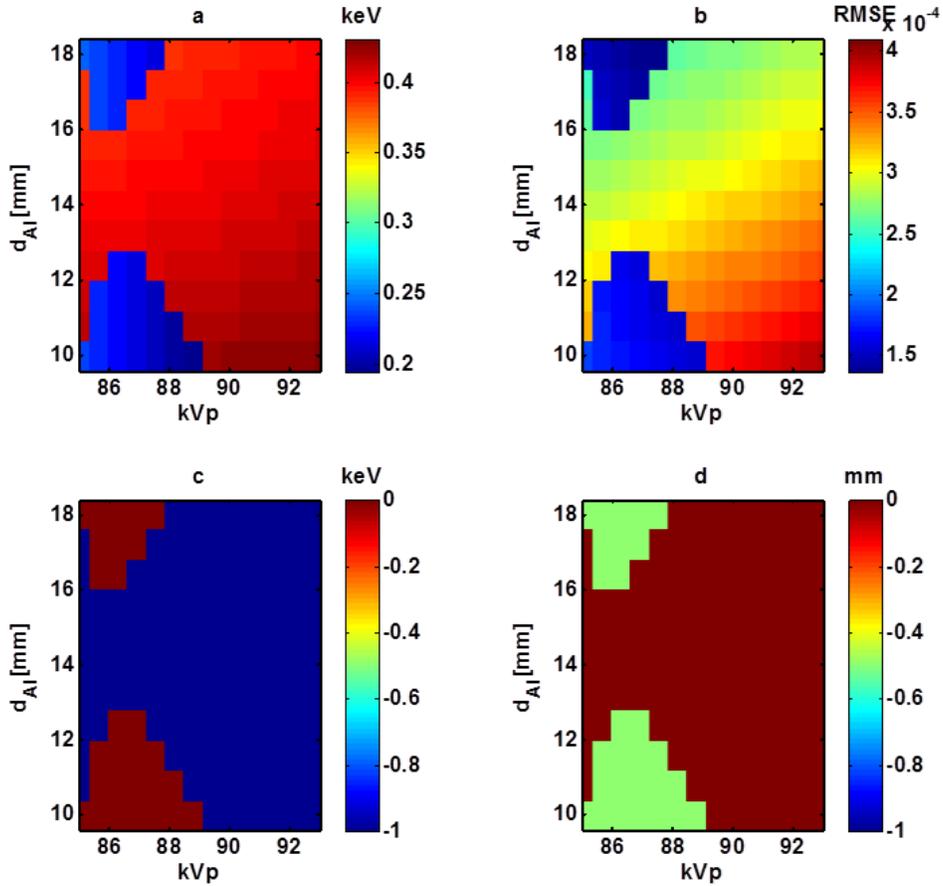
Fig.4.18 Comparisons of derived spectrum and independently simulated reference spectra for nomial 90 kVp with inherent filtration of aluminum ranging from 10 mm to 18 mm for the noisy $QF_{P,\mathrm{model}}$ The differences of mean energy (a), RMSE (b), kVp(c), and d_{Al} (d) are shown, respectively. Each pixel on the figures corresponded to the discrenpance for each candidate of reference spectrum
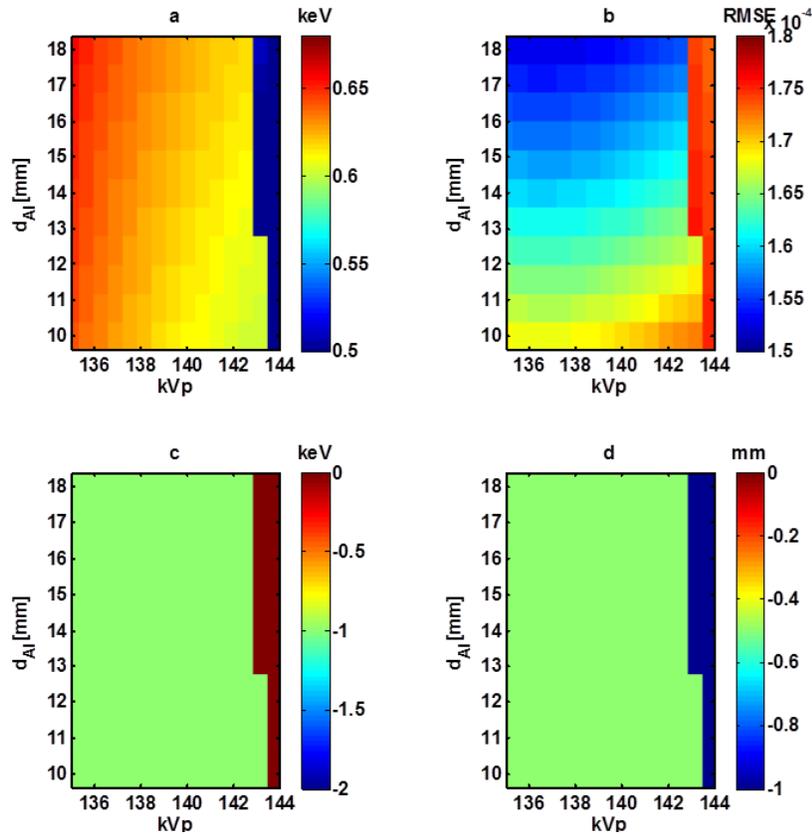
Fig.4.19 Comparisons of derived spectrum and independently simulated reference spectra for nomial 140 kVp with inherent filtration of aluminum ranging from 10 mm to 18 mm for the noisy $QF_{P,\mathrm{model}}$ The differences of mean energy (a), RMSE (b), kVp(c), and d_{Al} (d) are shown, respectively. Each pixel on the figures corresponded to the discrenpance for each candidate of reference spectrum

4.4 Discussion

This study investigates a technique to derive a BM-equivalent spectrum from the beam-hardening corrections encoded in the header of all sinogram files. This technique provides an efficient and accurate way to estimate the spectrum. Based on a one-time calibration against an independently measured spectrum for each beam quality, our proposed technique requires no additional physical transmission measurements to estimate photon spectra at other time points, during which tube replacement or x-ray system aging may have changed the x-ray spectrum and prompted the operators to recalibrate the system using the vendor's procedure. With the assumption that the BH

compensation is effectively updated at different times and the BH objective function and calibration phantom S/P values remain approximately the same for the same collimator setting, the spectrum can be estimated accurately. The differences of mean energy for 90 kVp and 140 kVp are less than 1 keV. Our robustness analysis also demonstrates that based on the quality functions produced by reference spectra with large variations of free parameters kVp, d_{Al} , our proposed method could yield sufficiently accurate estimation of reference spectra. The uncertainty analysis shows that with added noise to the objective function, this technique is immune to the small variations. For example, the RMSE of reference and derived spectra for noisy objective function are 0.0004, and 0.0002 for 90 kVp and 140 kVp, respectively. This technique can be used for spectrum monitoring for routine quality assurance of CT x-ray scanner or to reconstruct spectra corresponding to archived raw datasets.

This method requires the access to proprietary information, including

- Export of raw data with vendor-supplied beam hardening corrections
- Sufficient knowledge of beam transport geometry, including dimensions, compositions, and density of all structures traversed by the beam, that raw uncorrected sinograms can be accurately computed and meaningfully compared to their measured counterparts. This includes bowtie filter geometry and material.
- Ability to access beam hardening coefficients in sinogram headers and to utilize these coefficients to duplicate the vendor's correction for both central and off-axis ray fan locations.

In this study, an experimentally measured spectrum was used to simulate a quality function, which may not include scatter contribution. Otherwise if the modelling of $QF_{P.\mathrm{model}}$ takes into account the scatter contribution, as long as values of S/P are consistent in the stage of derivation. Our proposed method is insensitive to the accuracy of the scatter estimation. In the scenario where a measured spectrum not available to create a reference $QF_{P.\mathrm{model}}$, spectra can still be extracted from the vendor BH correction provided that a reasonably accurate pair of S/P for full- and half- thickness phantoms.

Although an accurate estimation of scatter for fan-beam CT is beyond the scope of this thesis, it is suggested that methods used to estimate scatter in cone-beam CT can be adapted [3, 38, 156, 157] Monte Carlo simulation for estimating S/P is also an alternative.[158, 159] The modified objective function is given by Eqn. (43). Flowchart in Fig.4.20 illustrates the steps of deriving the spectrum with the knowledge of scatter

$$\left(kVp_{Y_1},d_{Al,Y_1}\right)=\underset{kVp,d_{Al}}{\textbf{argmin}}\sum_{\gamma}\left(\frac{QF_{P,model}\left(\gamma|kVp,d_{Al},\mathscr{B}_{Y_1}\right)-QF_{P,meas}\left(\gamma|\mathscr{B}_{Y_2}\right)}{QF_{P,meas}\left(\gamma|\mathscr{B}_{Y_2}\right)}\right)^2 \quad (43)$$

It is noted that the difference between Eqn. (39) and Eqn. (43). Although Eqn. (43) relies on the BH correction coefficients of Y2, it doesn't require the knowledge of spectrum at Y2, while in order to model the $QF_{P.model}$ in Eqn. (39), the measured spectrum at Y1 is demanded.
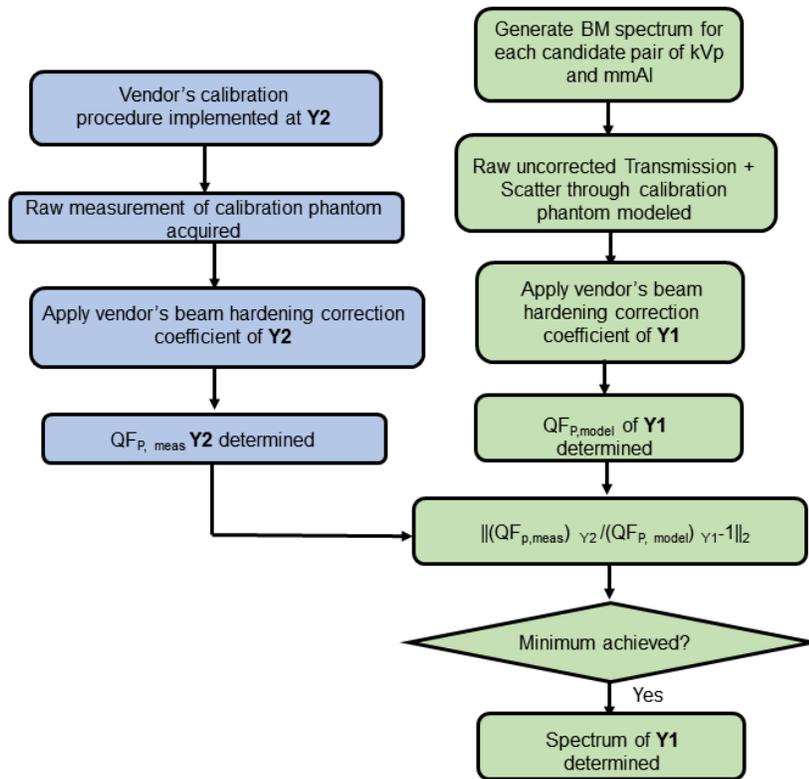
Fig.4.20. Flowchart of the method of spectrum derivation when a reference spectrum is not available

Fig. 4.21 illustrates the distributions of measured forward projections for full- and half-phantoms, respectively. The projections were used to determine the spectrum according to Eqn. (43), given updated $\mathscr{B}_Y$ and knowledge of scatter at the time point of Y.
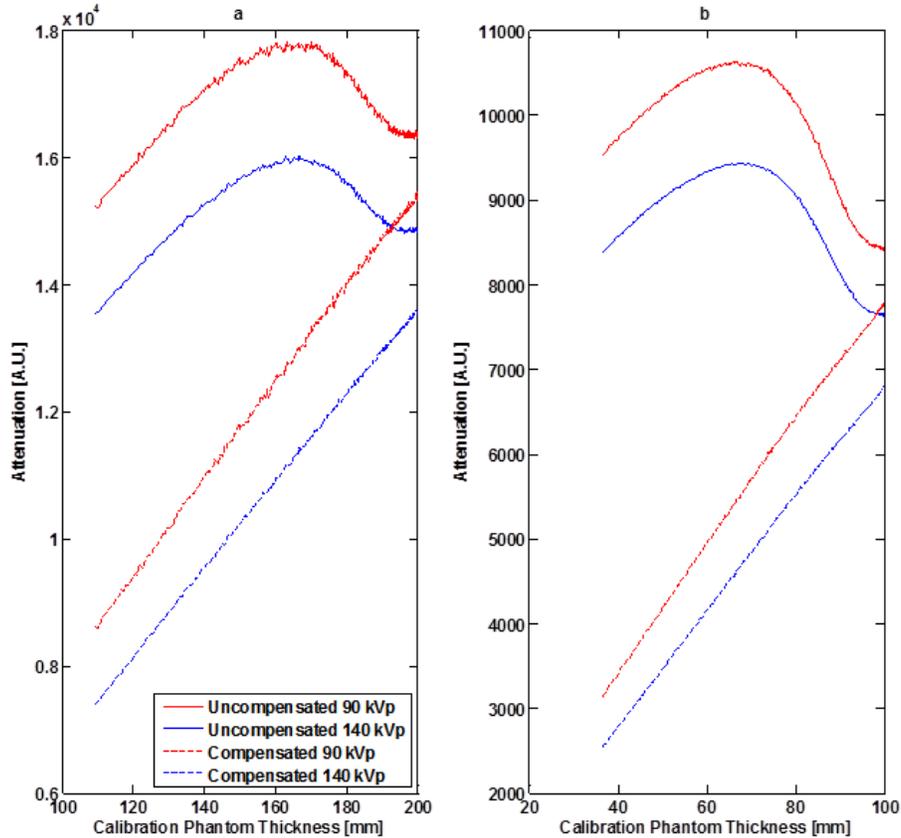
Fig.4.21 The measured forward projections through (a) full and (b) half phantom for the spectra of 90 kVp and 140 kVp, respectively

For example, using the central axis S/P ratios of 0.065 and 0.025 for full and half phantom at time of Y1 in a uniformed scatter profile model for 90 kVp spectrum, Eqn. (43) results in BM parameters of 89 kVp and 12.5 mm, which are close to the Y1 parameters derived from narrow beam measurements (90 kVp, 12.8 mm). The

measured forward projections are illustrtaed in Fig. 4.21. The simulated $QF_{P,\text{model}}\left(\gamma\,\middle|\,\mathcal{B}_{Y_2}\right)$ was generated using measured spectrum of Y1 and above referenced S/P values.
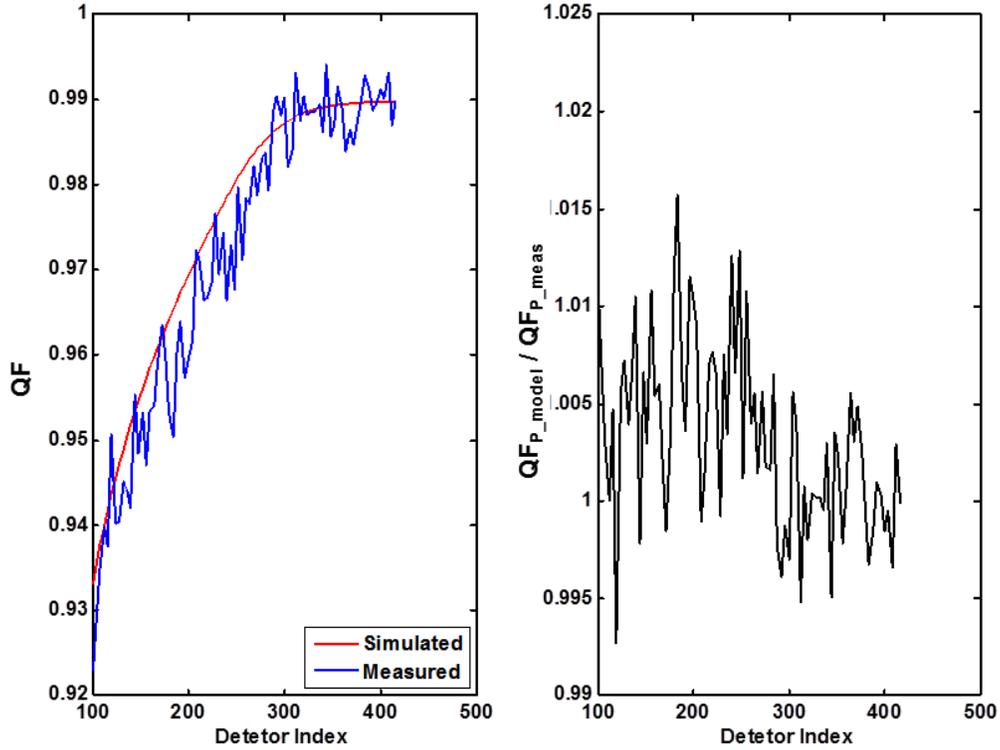
Fig.4.22. Comparison between $QF_{P,\text{model}}\left(\gamma\,\middle|\,\mathcal{B}_{Y_2}\right)$ and $QF_{P,\text{meas}}\left(\gamma\,\middle|\,\mathcal{B}_{Y_2}\right)$ for detector range [100,418] in (a), the $QF_{P,\text{model}}\left(\gamma\,\middle|\,\mathcal{B}_{Y_2}\right)\middle/ QF_{P,\text{meas}}\left(\gamma\,\middle|\,\mathcal{B}_{Y_2}\right)$ is also illustrated in (b)

The comparisons between $QF_{P,\text{model}}\left(\gamma\,\middle|\,\mathcal{B}_{Y_2}\right)$ and in $QF_{P,\text{meas}}\left(\gamma\,\middle|\,\mathcal{B}_{Y_2}\right)$ Fig. 4.22 also demonstrate the level of accuracy of S/P needs to be in order to derive the spectrum accurately.

This framework in the study can be extended to commonly used beam qualities without too much effort, e.g., 120 kVp, which are more widely used scanning technique for CT simulations or diagnostic CT imaging.

Our study also has limitations. One of major limitations is that the only slight deviations of BH polynomials were observed between Y1 and Y2, only one of the BH coefficients

only changes 10%, which does not give rise to a noticeable change in the spectrum. Hence our experiment validation based only a single data point is not very strong. We performed an extensive simulation-based robustness analysis, since we do not have the ability to experimentally perturb the beam quality on our clinical Big Bore scanner. It would be highly desirable to have access to broader base of experimentally realized spectra and associated BH corrections on clinical scanner to further corroborate our techniques.

For each pair of source-detector, the path lengths inside the bowtie filter and calibration phantom are modeled and required for simulation of transmission. However, the accumulation of the modeling errors of dimensions can contribute the deviations of derived spectra. Since such errors were not investigated quantitatively in this study, it warrants future study how much differences of estimated spectra can be attributed to geometrical errors.

5 An iterative model-based polyenergetic filtered backprojection x-ray DECT reconstruction algorithm

5.1 Background

One of the non-linear artifacts arising during the CT acquisition is beam hardening (BH) effect. It is produced due to an oversimplified assumption that the x-ray beam is monoenergetic. If this assumption is true, each detector measurement corresponds to the survival probability along the beam path at the energy of incident photons. Thus, a CT image reconstructed from monoenergetic projections provides attenuation coefficient images of all materials at the same photon energy. However, in reality, the Bremsstrahlung spectra from x-ray tubes exhibit a very broad distribution of photon energies, therefore, the monoenergetic assumption is undermined. A frequently visualized artifact is streaking due to bone or mental-related BH. [101] BH correction schemes are not only important for image reconstructions, but also crucial for quantitative CT applications. Inability to account for the BH artifacts in the CT images makes the quantitative DECT applications extremely challenging.[149] Ideally, BH correction attempts to linearize the polychromatic projections to monoenergetic ones, which would eliminate BH artifacts completely.

There are a variety of schemes proposed in the literature for implementing the linearization process. These methods can be roughly divided into three categories. The first category is pre-processing correction in which polyenergetic projection values are mapped into monoenergetic ones through a predetermined look-up-table for water.[34, 35, 146] Then an image with reduced BH artifacts can be reconstructed from the corrected sinogram. While this method works well for soft tissue, it becomes quite inaccurate when Z^* deviates significantly from water.

The second category is post-processing BH correction, which has been intensively investigated in the past decades.[36, 99, 148] One way to implement the post-processing BH correction is to assume the scanned object consists of bony and soft tissues. An initial reconstructed and segmented image is used to identify the regions of soft tissue and bony tissues. Then the image is forward projected for estimation of the amount of

nonlinear effect generated by soft tissues and bony tissues. Assuming prior knowledge of the x-ray spectrum is available, the projections can be corrected. Applying the FBP on corrected projections, the updated image may show reduction of artifacts.

The third category is dual-energy CT-based approaches, which represent the energy-dependent attenuation coefficients using two-parameter models, either ρ_e and Z* [31]or weights of two dissimilar basis materials. [45, 103] The advantage of this method is its ability to transform the polychromatic measurements into two energy independent projections, and thereby supporting reconstruction of artifact-free attenuation coefficient images at any desired energy.[160] Yan et al. [149] developed a non-statistical FBP-based iterative BH correction algorithm, assuming each voxel in the scan field can be expressed as a mixture of two known substances, for example, a mixture of trabecular bone and marrow, or mixture of fat and flesh. It showed greatly improved capabilities in reduction of BH effects compared to pre- and post-approaches. Our group at Washington University [120, 136, 150] recently developed a joint SIR algorithm, dual-energy alternating minimization (DEAM) based on BVM model, to simultaneously reconstruct basis weight images with free artifacts and high accuracy for proton stopping power applications. Evans et al[20] experimentally implemented single-energy AM of single energy version on a commercial CT scanner and compared with FBP reconstructed images on estimation of photon cross-section of phantom materials.

Each approach has its advantages and drawbacks. Pre-processing correction is fast and widely used on modern CT scanners, however, the nonvisible residual uncorrected BH effects may still persist in the reconstructed images, which may limit the quantitative accuracy of the images. The post-processing approach requires accurate segmentation, and a priori knowledge of the spectrum as well as composition and density on inhomogeneities in the images, the results of which are not accurate and robust as SIR. [95, 99, 161, 162]Although SIR algorithms evidently are more accurate and robust in reconstruction, but the computation cost is relatively high.[162]

As mentioned in chapter 1, one of the decomposition approaches is based on image-domain. The accuracy of the image-domain approach can achieve in quantitative DECT (QDECT) measurement suffers not only from uncertainties in reconstructed images, but

also from the decomposition process, which is a highly ill-conditioned problem. The residual errors from images can lead the amplification of small errors in the stage of decomposition for image-domain DECT methods.[109]

Another non-linear artifact is from scatter radiation. The presence of scatter can induce significant image quality degradation, i.e., the cupping, streaks and intensity non-uniformity on reconstructed CT images.[37, 39, 145, 163] For SIR algorithms, scatter contribution is often included in the measurement model as an additive term, i.e. a priori knowledge of mean amount of scatter as a pre-processing step. [99, 136, 142] On a third generation fan beam commercialized CT scanners, vendors utilize a 1-D anti-scatter grid (ASG) for physical scatter signal rejection and do not apply any additional scatter correction to the raw data before reconstruction. Even with the aid of ASG, a scatter correction is needed to reconstruct mean image intensities with an accuracy of 0.5% or better. [98] The impact of scatter radiation on quantitative CT has been demonstrated by a few studies.[98, 99]

Thus, a scheme of alleviating non-linear effects of BH and scatter is desired for CT image reconstruction. Only a few reconstruction algorithms, including SIR, which explicitly model the non-linear effects, have been proposed to support application of QDECT. Among the algorithms, the most straightforward one is taking the advantage of simplicity of FBP. Yan's [149] iterative FBP algorithm is designed for QCT measurement, which is usually performed on a single-energy protocol. The full capabilities of Yan's algorithm on DECT were not investigated so far. In their experimental implementations, the uncertainties, including the residual BH errors and random noise, were still present on the resulted images. The estimation error of linear attenuation was on the order of 5%. However, the advantage of this algorithm lies in its fast convergence. It was reported that only 3-4 iterations are needed to significantly remove the BH artifacts.[149]

A statistically motivated joint SIR (JSIR) algorithm based on BVM was proposed by O'Sullivan et al. [120, 150] and Williamson et al. [96]This algorithm showed a robust response to the inherent uncertainties of the acquired sinogram data including systematic bias and random fluctuations. Unlike sinogram and image domain decomposition methods, which separate stages of image reconstruction and material decomposition as

independent processes, JSIR unifies the stages and greatly reduce the uncertainties based on the linear and separable accurate BVM model. However, SIR algorithms often are very slow to converge and each iteration is too computationally expensive to be adopted in clinical settings. For example, unlike Yan's algorithm, it often takes JSIR hundreds of iterations to converge.[120, 136]

In this chapter, a model-based iterative FBP DECT algorithm based on a linear BVM model is proposed with two focused goals: a) mitigating the BH and scatter artifacts in a principled but efficient fashion, b) supporting accurate material decomposition for in vivo imaging of stopping powers and photon cross sections, and c) applying anatomical constraints to better condition the problem of DECT material decomposition, which is not included in the algorithm developed by Yan et al. (Yan's algorithm). [149] To these ends, we have implemented our joint model-based iterative FBP with anatomical constraints (iFBP-AC). In this work, Yan's work is termed as iFBP for short. A series of comparisons on noiseless and noisy simulated sinograms were performed for iFBP-AC and iFBP.

5.2 Materials and Method

5.2.1 Symbols and definitions

The symbol and their definitions used throughout the chapter are summarized in table I.

Symbols	Definitions
$S_m(y, E)$	Normalized energy-integrated spectra for each energy bin E and source-detector pair y with weight of S_m (= s_1, s_2)
$\mathbf{x}$	Index of Image pixel
$c_i(\mathbf{x})$	Image weight of i-th basis material at image pixel x (i =1, 2)

(k)	Iteration index
$\bar{\mu}_{S_m}(\mathbf{x})$	Spectrally averaged attenuation coefficients of unknown materials in the unit of mm^{-1}
$\bar{\mu}_{i,S_m}(\mathbf{x})$	Spectrally averaged attenuation coefficients of basis material (i =1, 2) in the unit of mm^{-1}
FBP	Filtered backprojection operator
FP	Forward projection operator
I_{0,S_m}	Unattenuated photon flux for spectrum S_m
l	Index of segmented regions
j	Index of pixel within segmented regions
γ	fan beam angle, corresponding to detector index
β	Source angle, corresponding source sampling index
f_{Ny}	Nyquist frequency
$W(f)$	Window function
$G(f)$	Fourier transform of Gaussian smoothing kernel
y	Detector-source pair
$P_{meas,S_m}(y)$	Measured raw energy uncompensated projection with spectrum S_m for each source-detector pair y
$h(y|x)$	Point spread function of a scanner, corresponding to the effective length of the intersection between the beam path y and image pixel x . $h(y|x)$ is

	precalculated for the geometry of Philips Brilliance CT scanner.

5.2.2 Description of the Algorithms

Our proposed algorithm iFBP-AC is based on a weighted filtered backprojection as described in Kak and Slaney [33] to backproject the sinogram data. A modified ramp filter is used in FBP throughout this study.

$$H(f) = |f| \cdot W(f) \cdot G(f) \quad (44)$$

The cut-off frequency is chosen at Nyquist frequency, and the window function $W(f)$ is rolled off at $f \geq 0.9 f_{Ny}$. The details of window function can be found in the Ref. 97. An additional Gaussian kernel $G(f)$ is used to suppress the high-frequency image noise. In our implementation, $G(f)$ is chosen to approximate the image resolution achieved by the Philips Brilliance Big Bore CT scanner. The details of implementation are outlined in the subsequent sections.

For demonstration of proof-of-concept, a single-basis pair version of BVM based iFBP-AC is implemented. The pair of single basis is selected as polystyrene and aqueous $CaCl_2$ solution (23% concentration by mass).[120, 136]

Given spectrum $S_m(E, y)$,

$$S_m(E, y) = \frac{E \cdot s_m(E, y)}{\int E \cdot s_m(E, y) dE} \quad (45)$$

The spectral-averaged attenuation coefficients of basis materials over the spectrum can be defined

$$\bar{\mu}_{i,s_m} = \int S_m(E, y) \mu_i(E) dE \quad (46)$$

The problem of reconstruction can be rephrased as, given the spectrum $S_m(E, y)$, and measured sinogram $P_{meas,S_m}(y)$, find the distribution of linear attenuation.

Pseudocode of iFBP

A. Set $k = 0$, Initialize $\mathbf{c}_i^{(k)}(\mathbf{x})$

B. Update $FP_{mono}\left(\mathbf{y} \mid \mathbf{c}_i^{(k)}(\mathbf{x}), \boldsymbol{\mu}_{S_m}\right)$ and $FP_{Poly}\left(\mathbf{y} \mid \mathbf{c}_i^{(k)}(\mathbf{x}), S_m(E)\right)$

$$FP_{mono}\left(\mathbf{y} \mid \mathbf{c}_i^{(k)}(\mathbf{x}), \boldsymbol{\mu}_{S_m}\right) \equiv \int \left(c_1(\mathbf{x})\bar{\mu}_{1,s_m} + c_2(\mathbf{x})\bar{\mu}_{2,s_m}\right)h(y|x)\,dx$$

$$FP_{Poly}\left(\mathbf{y} \mid \mathbf{c}_i^{(k)}(\mathbf{x}), S_m(E)\right) \equiv -\log\left(\int_0^{E_{max}} S_m(E, y)\cdot\exp\left(-\sum_{i=1}^2 \int \mu_i(E)c_i(\mathbf{x})h(y|x)\,dx\right)dE\right)$$

C. Update $\bar{\mu}_{S_m}^{(k+1)}(\mathbf{x})$

$$\bar{\mu}_{S_m}^{(k+1)}(\mathbf{x}) = \mathbf{FBP}\left\{FP_{mono}\left(\mathbf{y} \mid \mathbf{c}_i^{(k)}(\mathbf{x}), \boldsymbol{\mu}_{S_m}\right) - \mathbf{FP}_{poly}\left(\mathbf{y} \mid \mathbf{c}_i^{(k)}(\mathbf{x}), S_m(E)\right) + P_{meas,S_m}(y)\right\}$$

D. Update $c_i^{(k+1)}(\mathbf{x})$ through $\bar{\mu}_{S_m}^{(k+1)}(\mathbf{x})$

$$\begin{bmatrix} c_1^{(k+1)}(\mathbf{x}) \\ c_2^{(k+1)}(\mathbf{x}) \end{bmatrix} = \begin{bmatrix} \bar{\mu}_{1,s_1} & \bar{\mu}_{2,s_1} \\ \bar{\mu}_{1,s_2} & \bar{\mu}_{2,s_2} \end{bmatrix}^{-1} \cdot \begin{bmatrix} \bar{\mu}_{S_1}^{(k+1)}(\mathbf{x}) \\ \bar{\mu}_{S_2}^{(k+1)}(\mathbf{x}) \end{bmatrix}$$

E. Iterate B to D until convergence

$$\frac{\left\| \mathbf{FP}_{poly}\left(\mathbf{y} \mid \mathbf{c}_i^{(k+1)}(\mathbf{x}), S_m(E)\right) - P_{meas,S_m}(y) \right\|}{\left\| \mathbf{FP}_{poly}\left(\mathbf{y} \mid \mathbf{c}_i^{(k)}(\mathbf{x}), S_m(E)\right) - P_{meas,S_m}(y) \right\|} \geq 0.98$$

Through step C adopted from work of Yan et al,[149] the $\mu_{S_m}^{(k)}(x)$ is linearized, and beam hardening effect is completely removed until

$$\mathbf{FP}_{poly}\left(\mathbf{y} \mid \mathbf{c}_i^{(k)}(\mathbf{x}), S_m(E)\right) = P_{meas,S_m}(y) \qquad (47)$$

Although iFBP method can efficiently remove the BH effect, the accumulated random noise caused by multiple iterations of FBP can result unfavorable image quality, i.e. there is a tradeoff of noise and resolution.

In order to find the stable solutions with less impact from noise, an anatomical constraint is proposed to regularize the problem. We introduce fractional contribution of the first basis material $\alpha(\mathbf{x})$ to voxel $\mathbf{x}$

$$\alpha(\mathbf{x}) = \frac{c_1(\mathbf{x})}{c_1(\mathbf{x}) + c_2(\mathbf{x})} \quad (48)$$

The BVM can be rewritten as

$$\mu(\mathbf{x}, E) = \left(c_1(\mathbf{x}) + c_2(\mathbf{x})\right)\left(\alpha(\mathbf{x})\mu_1(E) + \left(1 - \alpha(\mathbf{x})\right)\mu_2(E)\right) \quad (49)$$

$$\left(c_1(\mathbf{x}) + c_2(\mathbf{x})\right) = \frac{\mu(\mathbf{x}, E)}{\left(\alpha(\mathbf{x})\mu_1(E) + \left(1 - \alpha(\mathbf{x})\right)\mu_2(E)\right)} \quad (50)$$

Heismann et al. [164] identified that density reflects the morphology of the objects, whereas the atomic number describes the material distribution. In our study,[113] it was found that $\alpha(\mathbf{x})$ is linearly correlated with Z^*, and thus can be treated as surrogate for atomic composition of tissue.[130, 164]
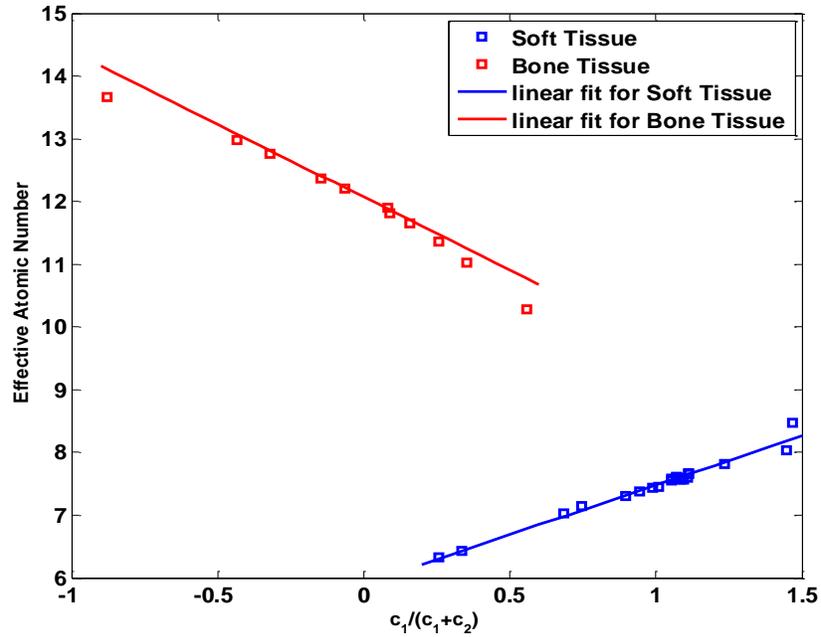
Fig.5.1 Linear correlation exists for Z* and $\alpha(\mathbf{x})$ of ICRU tissues. The effective atomic number Z * is computed from tPFM model, described in Ch.2.

For each well-defined, and well-segmented tissue type, a constant value of $\alpha(\mathbf{x})$, representing a surrogate of Z*,[113] is assigned to the all pixels inside each segmented tissue region (Fig.5.2).
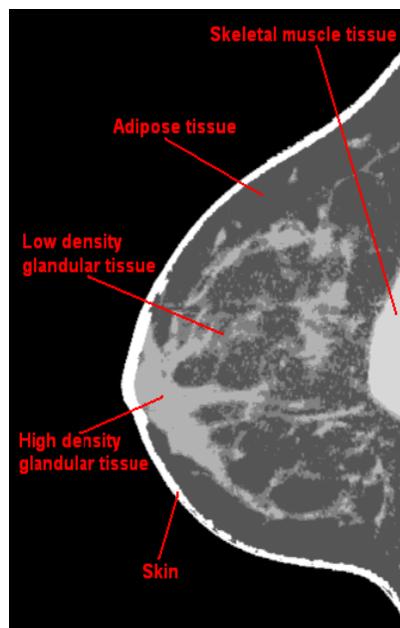
For example, in a typical breast tissue, each pixel of breast tissue is classified as being one of four types of glandular tissue, adipose, skin or skeleton-muscle. Each tissue type corresponds to a constant value of $\alpha(x)$, which was updated iteratively.

The segmentation result was used as a priori knowledge in each iteration. In this study, the boundary of each phantom insert is perfectly defined. Thus, there are no errors associated with segmentation added to reconstruction process.

Pseudocode of iFBP-AC

A'. Initial reconstruction $\mathbf{c}_i^{(k)}(\mathbf{x})$ and segmentation of L tissue types

B'. Update $FP_{mono}\left(\mathbf{y}\,|\,\mathbf{c}_i^{(k)}(\mathbf{x}),\boldsymbol{\mu}_{S_m}\right)$ and $FP_{Poly}\left(\mathbf{y}\,|\,\mathbf{c}_i^{(k)}(\mathbf{x}),S_m(E)\right)$

$$FP_{mono}\left(\mathbf{y}\,|\,\mathbf{c}_i^{(k)}(\mathbf{x}),\boldsymbol{\mu}_{S_m}\right) \equiv \int \left(c_1(\mathbf{x})\bar{\mu}_{1,s_m}+c_2(\mathbf{x})\bar{\mu}_{2,s_m}\right)h\left(y|x\right)dx$$

$$FP_{Poly}\left(\mathbf{y}\,|\,\mathbf{c}_i^{(k)}(\mathbf{x}),S_m(E)\right) \equiv -\log\left(\int_0^{E_{\max}} S_m(E,y)\cdot\exp\left(-\sum_{i=1}^2 \int \mu_i(E)c_i(\mathbf{x})h\left(y|x\right)dx\right)dE\right)$$

C'. Update $\bar{\mu}_{S_m}^{(k+1)}(\mathbf{x})$

$$\bar{\mu}_{S_m}^{(k+1)}(\mathbf{x}) = \mathbf{FBP}\left\{\mathbf{FP}_{mono}\left(\mathbf{y}\,|\,\mathbf{c}_i^{(k)}(\mathbf{x}),\boldsymbol{\mu}_{S_m}\right)-\mathbf{FP}_{poly}\left(\mathbf{y}\,|\,\mathbf{c}_i^{(k)}(\mathbf{x}),S_m(E)\right)+P_{meas,S_m}(y)\right\}$$

D'. Update $\mathbf{c}_i^{(k+1)}(\mathbf{x})$ through $\bar{\mu}_{S_1}^{(k+1)}(\mathbf{x})$ and $\bar{\mu}_{S_2}^{(k+1)}(\mathbf{x})$

$$\begin{bmatrix} c_1^{(k+1)}(\mathbf{x}) \\ c_2^{(k+1)}(\mathbf{x}) \end{bmatrix} = \begin{bmatrix} \bar{\mu}_{1,s_1} & \bar{\mu}_{2,s_1} \\ \bar{\mu}_{1,s_2} & \bar{\mu}_{2,s_2} \end{bmatrix}^{-1}\cdot\begin{bmatrix} \bar{\mu}_{S_1}^{(k+1)}(\mathbf{x}) \\ \bar{\mu}_{S_2}^{(k+1)}(\mathbf{x}) \end{bmatrix}$$

E'. For each pixel in the l-th tissue type region R_l

$$\alpha^{(k+1)}(x) = \frac{\sum_{x' \in R_l} \dfrac{\tilde{c}_1^{(k+1)}(x')}{\tilde{c}_1^{(k+1)}(x') + \tilde{c}_2^{(k+1)}(x')}}{\sum_{x' \in R_l} 1}$$

F'. Update $\left(\tilde{c}_1(x) + \tilde{c}_2(x)\right)_{S_m}^{(k+1)}$

$$\left(\tilde{c}_1(x) + \tilde{c}_2(x)\right)^{(k+1)} = \frac{1}{2} \sum_{S_m=1}^{2} \left[\frac{\bar{\mu}_{S_m}^{(k+1)}(x)}{\left(\alpha^{(k+1)}(x)^{(k+1)} \bar{\mu}_{1,S_m} + \left(1 - \alpha^{(k+1)}(x)^{(k+1)}\right) \bar{\mu}_{2,S_m} \right)} \right]$$

G'. Update $c_i^{(k+1)}(\mathbf{x})$ through

$$c_1^{(k+1)}(\mathbf{x}) = \left(\tilde{c}_1(x) + \tilde{c}_2(x)\right)^{(k+1)} \left(\alpha^{(k+1)}\right)$$

$$c_2^{(k+1)}(\mathbf{x}) = \left(\tilde{c}_1(x) + \tilde{c}_2(x)\right)^{(k+1)} \left(1 - \alpha^{(k+1)}\right)$$

H'. Iterate D to I until convergence

$$\frac{\left\| \mathbf{FP}_{poly}\left(\mathbf{y} \mid c_i^{(k+1)}(\mathbf{x}), S_m(E)\right) - P_{meas,S_m}(y) \right\|}{\left\| \mathbf{FP}_{poly}\left(\mathbf{y} \mid c_i^{(k)}(\mathbf{x}), S_m(E)\right) - P_{meas,S_m}(y) \right\|} \geq 0.98$$

The iterative process of iFBP-AC is also illustrated in Fig.5.3
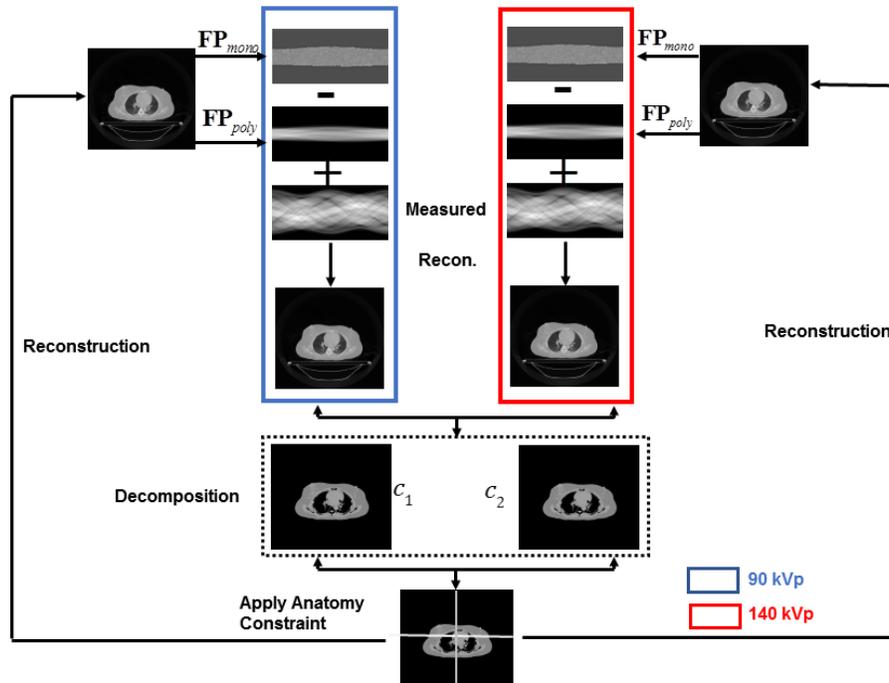
Fig. 5.3 illustration of iterative process of pseudocode of iFBP-AC

In this study, the step E' uses the pixels that are one-pixel away from tissue type boundary to compute the $\alpha(\mathbf{x})$ (shown in Fig.5.4). For example, the $\alpha(\mathbf{x})$ of tissue type I and II computed from pixel A and D would be assigned to transition regions of B and C, repectively.
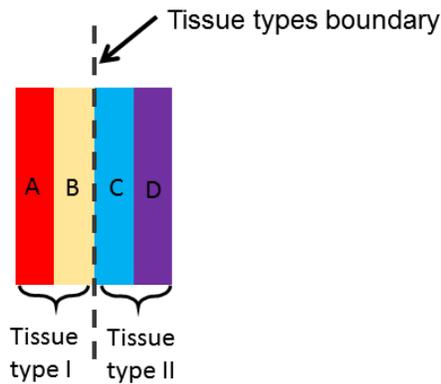
Fig. 5.4 Scheme of avoiding the pixels of B and C to compute $\alpha(\mathbf{x})$ for tissue type I and II

5.2.3 Simulation and evaluation environment

A series of simulations are designed to evaluate the baseline performance of proposed algorithm, iFBP-AC, in reconstructing cases of noiseless and noisy sinograms in a well-controlled environment. Each case of sinogram is produced from two types of phantom materials: the first type of fabricated synthetic phantoms is made from the ICRU recommended elemental composition, while the other type of synthetic phantoms' attenuation coefficients is faked by the BVM model. The latter type of phantom materials is designed to exclude the two-parameter modelling error The reconstruction accuracy is assessed by comparing the c-values and photon cross sections against the corresponding ground truth values.

The simulations are carried out on a digital phantom shown in Fig 5.5. Experimentally measured spectra of 90 kVp and 140 kVp from Ch. 4 are used. In the simulation experiments, number of detectors and gantry positions are 284 and 660, respectively. Two different sets of inserts were included in the water phantom with diameter of 220 mm. The first set (ICRU tissues) includes inserts 1 and 3 of muscle and bony tissues, whose elemental composition data are provided by ICRU report. [51] The attenuation coefficients of the first set are computed based on NIST XCOM table.[121]

The second set (BVM tissues) includes insert 2 (muscle) and 4 (cortical bone), whose attenuation coefficients are calculated from Eqn. (25) using the single-basis pair of (c_1, c_2). The linear attenuation coefficients of basis pair are similarly determined as ICRU tissues. The pair of (c_1, c_2) was computed based on a least square fitting between BVM model and true attenuation coefficients.

Both cases of noiseless and noisy sinogram were investigated in this study.

To evaluate the performance of iFBP-AC, the accuracy of reconstructed c-values was compared against the corresponding true values of BVM tissues (inserts 2 and 4), while the estimation accuracy of photon cross section was validated with true values of ICRU tissues (inserts 1 and 3). A quantified metric of interest quantities Q of ROI with total pixels N , is listed below for evaluation of performance of iFBP and iFBP-AC.

$$\text{mean errors: } \bar{e}_Q = \frac{1}{N} \sum_{\mathbf{x} \in ROI} \frac{Q_{estimated}(\mathbf{x}) - Q_{true}(\mathbf{x})}{Q_{true}(\mathbf{x})} \quad (51)$$

$$\text{RMS errors: } e_{Q_{RMS}} = \sqrt{\frac{\sum\limits_{\mathbf{x} \in ROI} \left(\frac{Q_{estimated}(\mathbf{x}) - Q_{true}(\mathbf{x})}{Q_{true}(\mathbf{x})} \right)^2}{N}} \quad (52)$$

$$\text{SNR: } \frac{\bar{Q}}{\sigma(Q)} \quad (53)$$

where σ is standard deviation
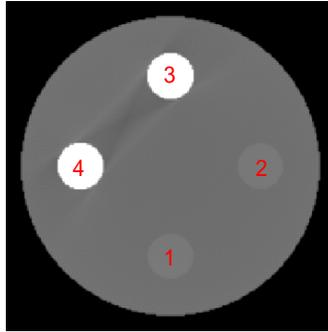
Fig. 5.5 Digital phantom of four inserts reconstructed with conventional FBP of OCCT software. The streaks are visible between two high density bones. The window is set [0.01, 0.03]

5.2.4 Noise and resolution matching

5.2.4.1 Noise level matching

The two noisy energy projections were simulated with typical total dose for a pelvis scanning, whose recommended value is 50-60 mGy. In other words, the dose for 90 kVp scan is 30 mGy, for 140 kVp the simulated dose is approximately 30 mGy. With the dose assignment for two scan, the mAs used for simulation and associated with 30 mGy can be determined through the correlation between mAs and CTDI on our Philips Brilliance scanner. In our noise matching analysis, the values of mAs for 90 kVp and 140 kVp were 600 mAs and 200 mAs, respectively were used.

5.2.4.2   Resolution matching

To assess the resolution of the reconstructed images, a metric based on modulation transfer function (MTF) developed previously by our group was used.[165] MTF is considered to be an effective measure of local impulse response and level of edge blurring. The MTF was computed from a model fit to the edge-spread function (ESF) arising from the highest contrast insert (Cortical Bone of Gammex phantom).[100] The sampled ESF was constructed by plotting each pixel's intensity as a function of distance to the insert edge. To accommodate the image noise, the ESF was modeled by an error function, which is slightly different from implementation of Ref. 100.

$$ESF(r) = a_1 \cdot \left[erf\left(a_2^{1/2} \cdot |r - a_3|\right)\right] + a_4$$

$$LSF(r) = \frac{d}{dr}\left(ESF(r)\right) \qquad\qquad (54)$$

$$MTF(r) = \left| FT\left(LSF(r)\right)\right|$$

The edge-spread function ESF was differentiated to obtain the line-spread function LSF and the Fourier transform of the LSF was calculated to obtain the MTF. Here r is the distance between the pixel center and known edge position. The parameters of a_1 to a_4 were determined by minimizing the relative least-squares difference between ESF modeling and actual ESF of images.

Images were reconstructed from the experimentally acquired Gammex phantom sinogram by both the scanner's reconstruction algorithm and our in-house FBP algorithm using OCCT software to assess the tradeoff of noise and resolution.[100] A series of Gaussian smoothing kernels with strength of 0 mm to 1.5 mm were used to determine the strength value that utilized in CT scanner.

5.3 Results

5.3.1 Noiseless sinogram

The reconstructed of c_1 images by iFBP-AC and iFBP are shown in Fig. 5.6, and c_2 images are shown in Fig. 5.7.
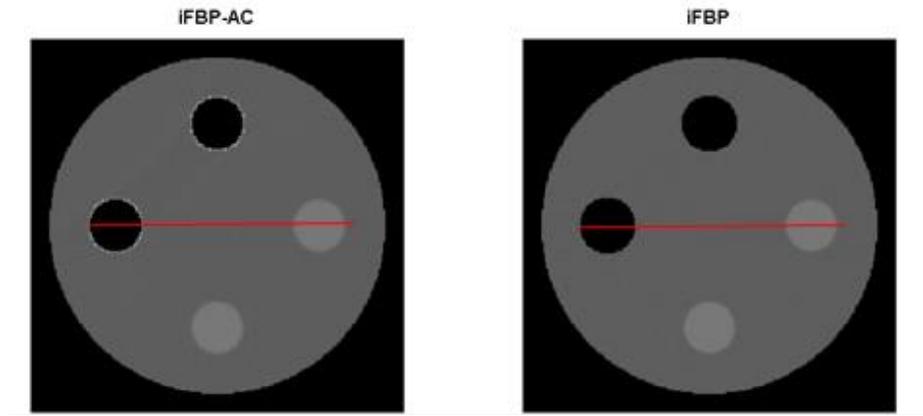
Fig. 5.6 Reconstructed c_1 images. The view window is set [0.75 1].
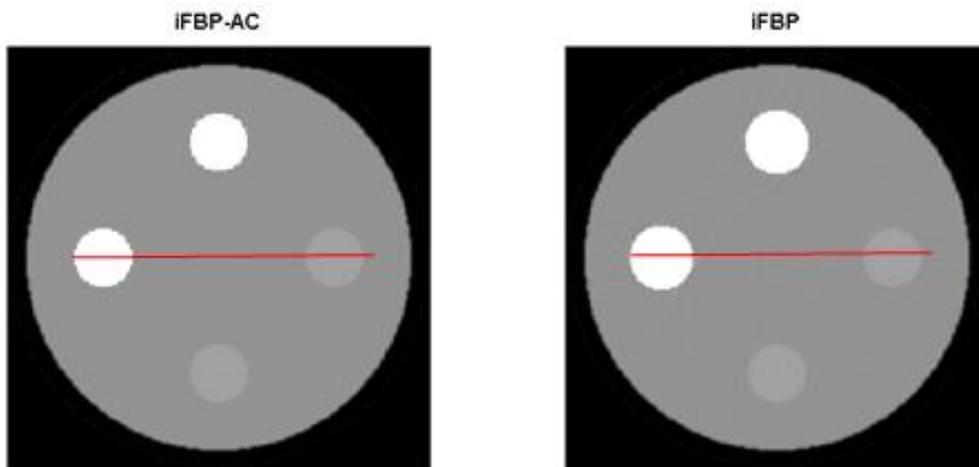
Fig. 5.7 Reconstructed c_2 images. The view window is set [0 0.2].

The profiles of c_1 and c_2 images along red straight lines from both algorithms are shown in Fig. 5.8
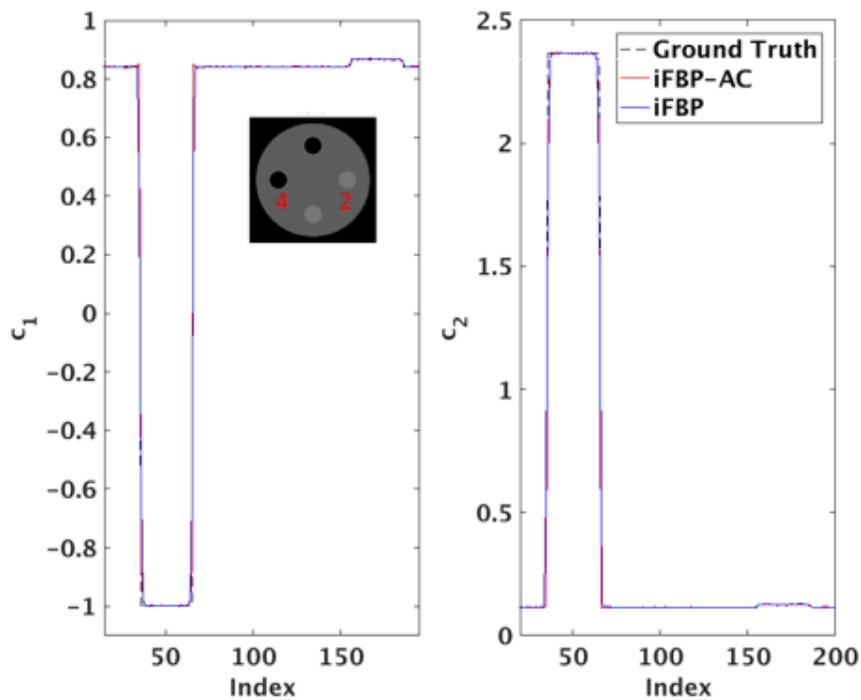
Fig 5.8 Profiles of component images along the red lines through inserts 2 and 4 from above images are shown. The ground truth c-values of components from BVM tissues are also shown.

Ruling out the modeling error of BVM, the two results of iFBP and iFBP-AC demonstrate similar reconstruction accuracy for the components images (for BVM tissues of inserts 2 and 4). No significant systematic bias was observed for either model. A zoomed view of profile for inserts 2 and 4 are shown on Fig. 5.9 to examine the level of random fluctuations in the images. For example, both of the reconstructed c_1 images inside of insert 4 have less than 0.1% random noise. A detailed performance of reconstructed c images is reported in table 5.1. The achieved accuracy of iFBP-AC and iFBP is quite close , i.e., the mean errors of c-values are within 0.1% for both algorithms.
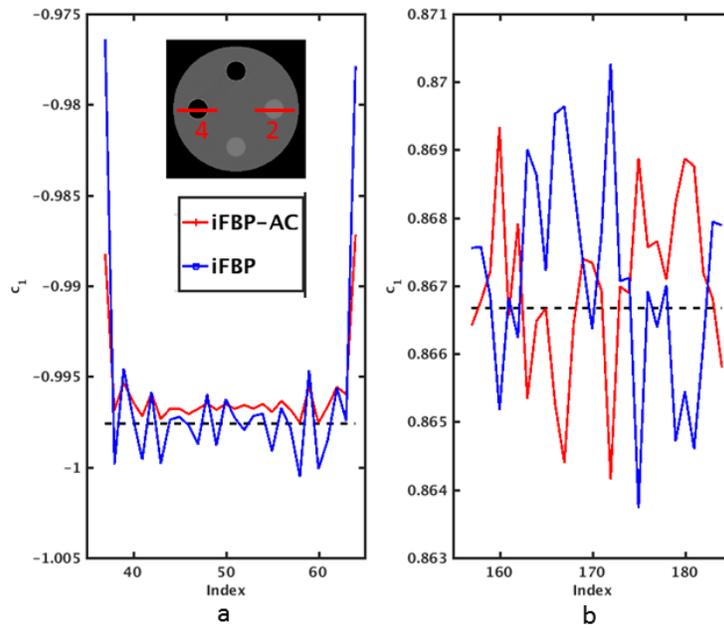
Fig. 5.9 Profiles of c_1 images along the red lines through inserts 2 (b) and 4 (a) from above images are shown.

Table 5.1. Evaluation performance of reconstruction accuracy of inserts 2 and 4 in noiseless sinogram

	True c-values		Mean errors	RMS errors	SNR
BVM Muscle (c_1, c_2)	(0.87,0.13)	iFBP-AC	(-0.0007,-0.003)	(0.0037,0.0047)	(277.3, 277.3)
		iFBP	(-0.0007,-0.0028)	(0.0027,0.0127)	(382.1,80.4)
BVM Bone (c_1, c_2)	(-1.00, 2.37)	iFBP-AC	(-0.02,-0.02)	(0.06,0.06)	(16.76,16.76)
		iFBP	(-0.06,-0.03)	(0.16,0.09)	(6.17,6.17)

It is expected that without sinogram noise, the estimation error of the total linear attenuation by using reconstructed c_1 and c_2 images should coincide with the errors from the BVM modeling. The estimation errors for ICRU muscle tissues (insert 1) as the function of photon energy are shown in Fig.5.10. Both of the algorithms have the largest estimation errors at 25 keV around 1.1 %. This is close to our theoretical prediction errors (1%) in Ch. 3.
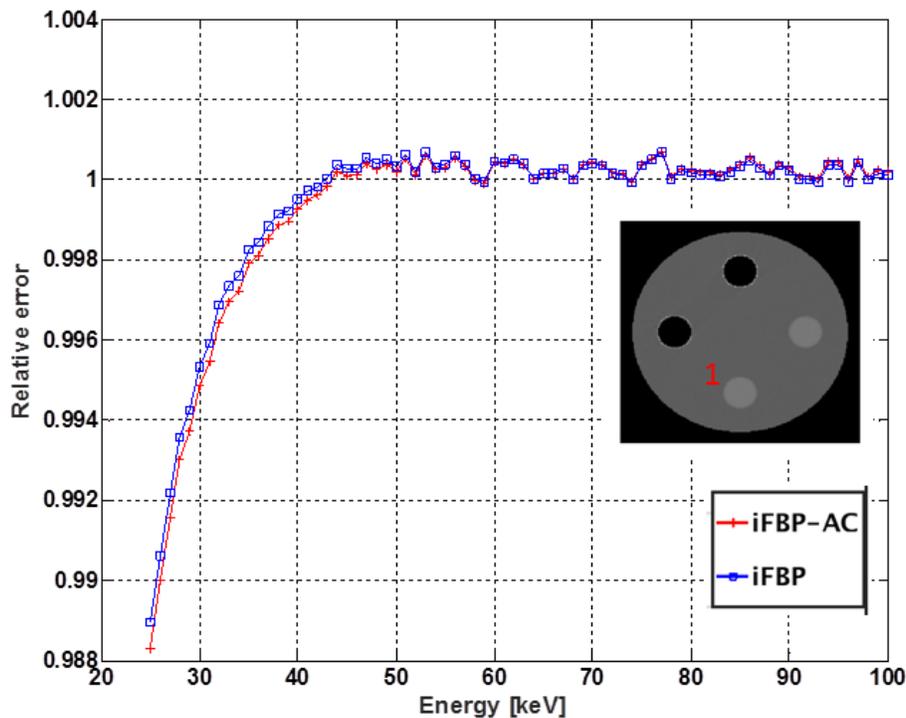
Fig 5.10 Relative estimation linear attenuation estimation errors of ICRU tissues insert 1, of which linear attenuation coefficients are determined based on ICRU composition data of muscle.

5.3.2 Noisy sinogram reconstruction

5.3.2.1 Noise and resolution matching

The image noise levels reconstructed by scanner from experimental Gammex sinogram are 1.7% and 0.7% for 90 kVp and 140 kVp, respectively.

The ESF curves are shown in Fig.5.11. The noise-resolution tradeoff curves corresponding to varied smoothing kernel strengths are also demonstrated in the Fig.5.11 (b). The two crosses on Fig. 5.11(b) represent the resolution and noise levels on scanner reconstructed images of two spectra. Every dot on the two curves refers to pair of noise-resolution reconstructed with FBP algorithm but different Gaussian smoothing strength. It can be found the fourth point in red and blue, corresponding to 1.1 mm smoothing kernel, can yield approximately the same performance of resolution from scanner images. Thus, the smoothing kernel was determined as 1.1 mm for 90 kVp and 140 kVp sinogram reconstruction throughout this study.
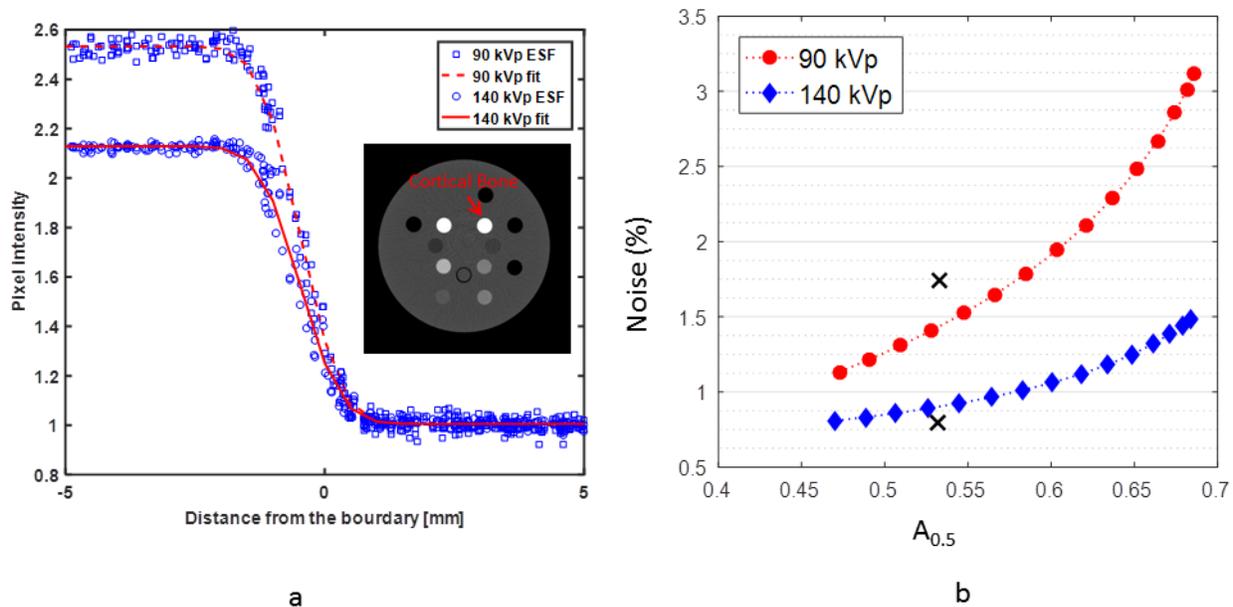
Fig 5.11 The ESFs from 90 kVp and 140 kVp of cortical bone is shown on (a). The two crosses in (b) correspond to MTF derived from ESF curves in (a). Each point on the tradeoff curves corresponds to Gaussian smoothing kernel in a range of 0 mm to 1.5 mm.

5.3.2.2 *Noisy sinogram Reconstruction*

The reconstructed c_1 images by iFBP-AC and iFBP are shown in Fig. 5.12, and c_2 images are shown in Fig. 5.13. It is obvious that the algorithm of iFBP yielded extremely noisy and unacceptable image. For instance, the regions of two soft tissue inserts on the component images are highly indiscernible. A systematic report can be found in Table 5.2. Compared to the table 5.1, the degradation in component image quality of iFBP-AC is far less than that of iFBP. For example, for BVM tissue, RMS errors of component images of iFBP-AC remain close to the counterpart in the case noise-free case, while for iFBP reconstructed images, the RMS errors are almost doubled compared to noiseless case.

Table 5.2. Evaluation performance of reconstruction accuracy of inserts 2 and 4 in noisy sinogram

	True c-values		Mean errors	RMS errors	SNR
BVM Muscle		iFBP-AC	(0.0098, -0.0488)	(0.02, 0.05)	(88.12, 88.12)
(c_1, c_2)	(0.87, 0.13)	iFBP	(0.0042, -0.023)	(0.17, 0.75)	(5.74, 1.30)
BVM Bone		iFBP-AC	(-0.0063, -0.02)	(0.06, 0.06)	(16.64, 19.64)
(c_1, c_2)	(-1.00, 2.37)	iFBP	(-0.05, -0.03)	(0.28, 0.11)	(3.41, 3.41)

A profile (Fig.5.14) through the inserts 4 and 2 reveals that both algorithms are able to produce unbiased images, however, the images reconstructed by iFBP suffers from up to 50% noise off to true values. In contrast, iFBP-AC algorithm successfully suppresses the random fluctuations in the component images. For a low contrast region (insert 2), the zoomed details of profile are shown in Fig. 5.15.
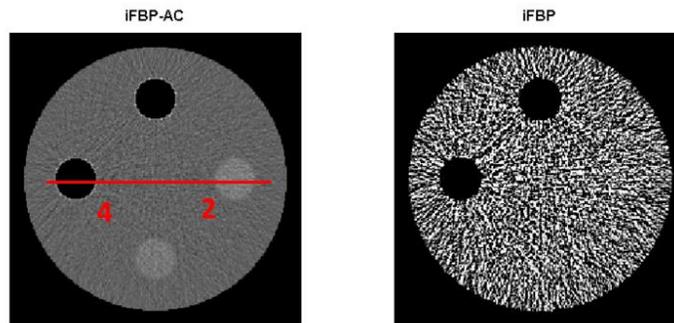
Fig. 5.12 Reconstructed c_1 images from noisy sinogram. A profile line across inserts 2 and 4 is shown. The noise levels in BVM muscle insert 2 for iFBP-AC and iFBP are 0.009 and 0.125, respectively. The true c_1 value of insert is 0.87. The view window is set [0.75 1]
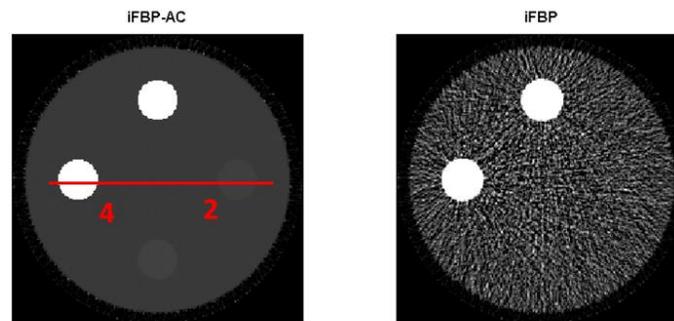
Fig. 5.13 Reconstructed c_2 images from noisy sinogram. A profile line across inserts 2 and 4 is shown. The noise levels in BVM muscle insert 2 for iFBP-AC and iFBP are 0.0012 and 0.077, respectively. The true c_2 value of insert is 0.13. The view window is set [0 0.2]
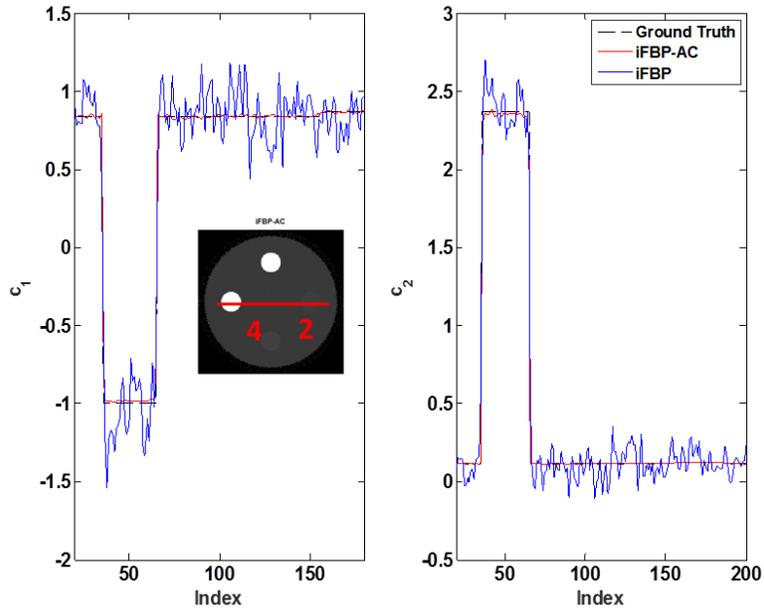
Fig. 5.14 Profiles of component images along the red lines through inserts 2 and 4 from above images are shown. The truth values of components are also shown.

The total linear attenuation coefficient in each pixel can be estimated at any energy using basis components images and Eqn. (49). The estimation errors of linear attenuation coefficients at 28 keV were also analyzed for inserts 1 and 3, corresponding ICRU muscle and cortical bone tissues. Component images reconstructed from iFBP-AC and iFBP are used. Circular ROIs with 10 mm diameter to sample 176 pixels are used. The errors relative to NIST of each pixel are computed based on BVM models. The distributions of errors relative to NIST for all pixels within the ROIs are shown in Fig.5.16.
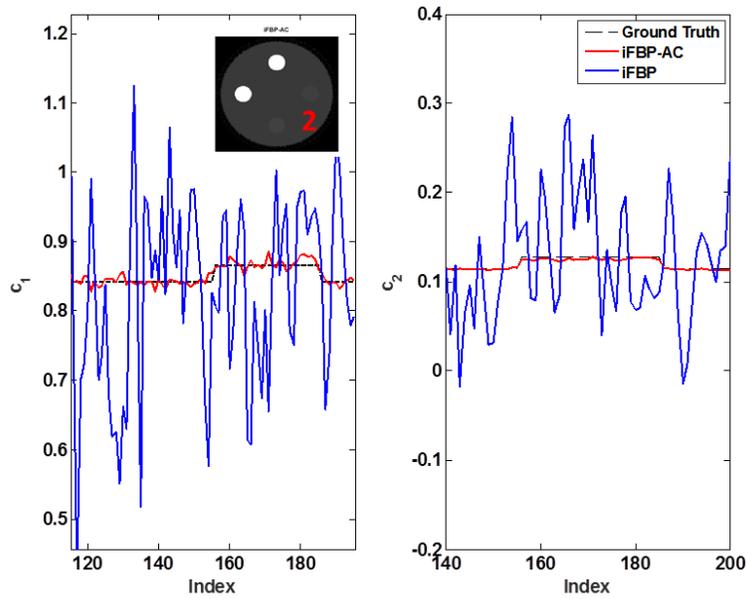
Fig. 5.15 A zoomed view of profile of muscle region (insert 2) of c_1 and c_2 images is shown

Although iFBP images are highly noisy, the mean attenuation values are centered on true values. For instance, the fitting Gaussian curves to the histogram of estimation errors for muscle and bone of 0.25% and 1.0%, with standard deviations 20.2% and 5%, respectively. In contrast, for images reconstructed by iFBP-AC, the mean errors for muscle and bone are 0.5% and 0.7%, respectively, with standard deviations of distribution are 1.2% and 0.6%, respectively.

5.3.3 Uncertainty Analysis

With added Poisson noise, the mean c-value intensities are used to investigate the response of two algorithms to errors in the reconstructed images. Noise levels of 1.7% and 0.7% for 90 kVp and 140 kVp are chosen to mimic that of clinical head scans.

The mean errors in estimated linear attenuation coefficients as a function of energy are shown in Fig.5.17 for cortical bone and muscle tissues, respectively. For high contrast insert bony tissue, it can be seen that the maximum errors could be up to 10%. For example, at energy of 25 keV, it is found that the uncertainties within the range of 11% for iFBP, while for iFBP-AC, the range is within 1.0%. For low contrast region (muscle tissue), the iFBP-AC significantly outperforms iFBP. At low energy of 25 keV, the

prediction uncertainties range could be up to 50%, while for iFBP-AC, the range of errors is within 2%. These results clearly demonstrate that the noise mitigation capabilities of iFBP-AC algorithm regardless image contrast.
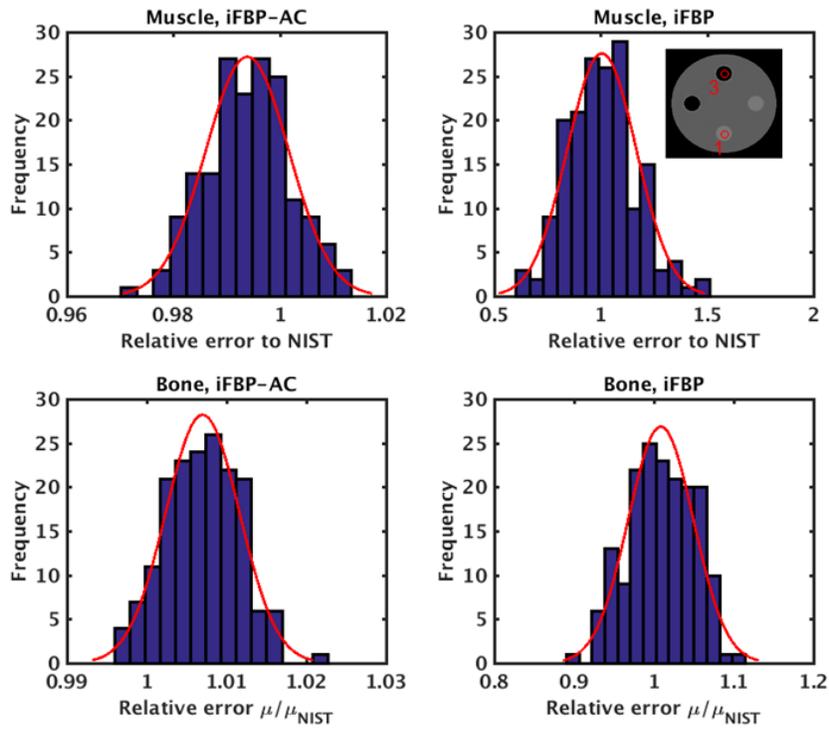
Fig. 5.16 Distribution of total linear attenuation bias at 28 keV for pixels within the muscle and cortical bone ROIs. The component images of iFBP-AC and iFBP are used. For a better visualization purpose, x-axis of each subplot uses different scales. The red circles represent the ROIs in each insert.
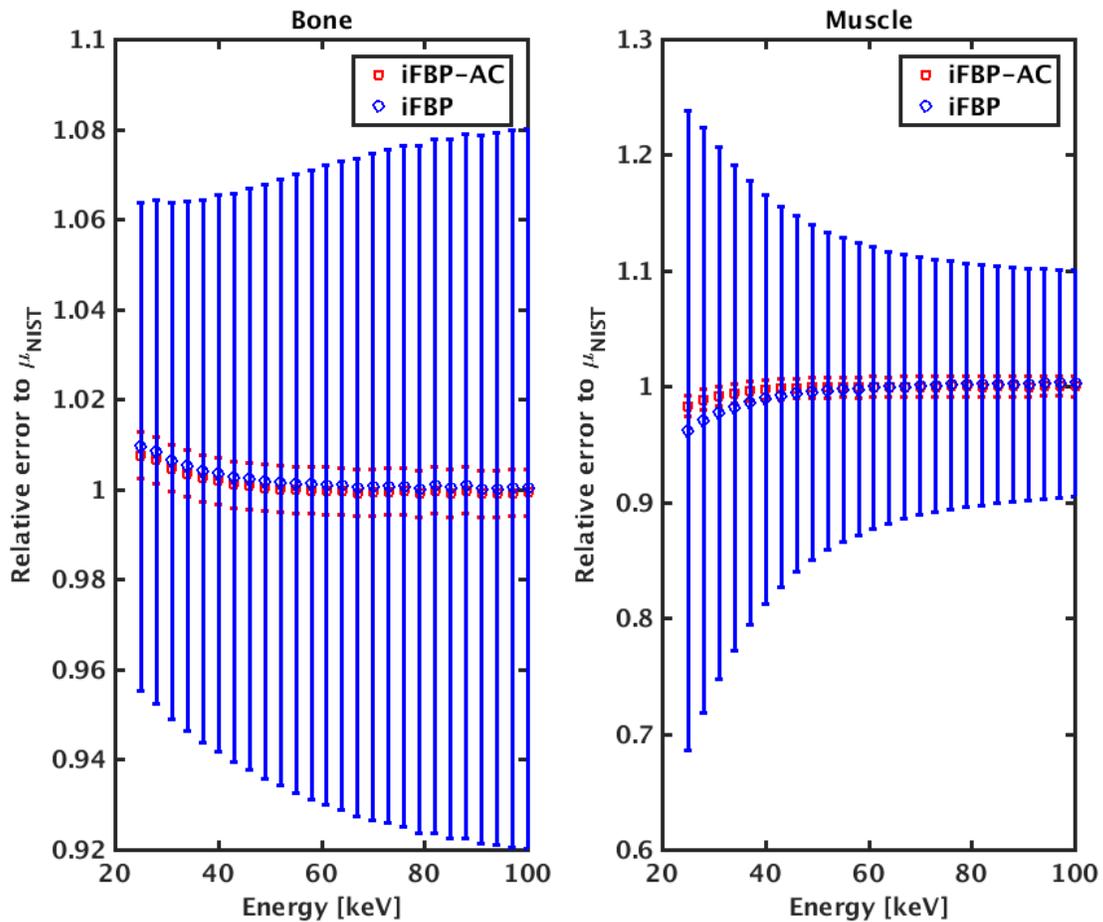
Fig. 5.17 Mean errors with 95% uncertainties error bars in estimated linear attenuation coefficient of ICRU bone and muscle tissue are shown for both iFBP and iFBP-AC algorithms, respectively.

The relative estimation error for iFBP-AC is less 1% for photon energy between 28 keV to 100 keV.

5.4 Discussions

A joint model-based algorithm has been adapted from the work of Yan et al. By requiring tissue composition to assume a fixed, uniform value for voxels of the same tissue type, we have shown that achieved mean errors could be less than 1% for both ICRU muscle and bone tissues at low photon energy under a reasonable noise level.

The performance of predicting the total linear attenuation coefficients was evaluated and compared with results from iFBP algorithms of Yan's work in the simulation framework. In the case of noiseless sinogram, both algorithms show similar accuracy in reconstructed component images and attenuation estimates. Given the reasonable noise and Gaussian smoothing kernel added, iFBP-AC outperforms iFBP in image quality. The uncertainties of estimated accuracy are significantly lower than the results from iFBP. Such high accuracy of iFBP-AC shows insensitivity to contrast level, for example, at photon energy of 28 keV, the uncertainties of iFBP-AC estimation errors remain similar for both bone and muscle tissues, while the maximum errors reconstructed from iFBP for muscle could up to 20%. This implies that iFBP-AC can support QDECT photon cross-section estimation to a desired target uncertainty with less pixel averaging.

The success of iFBP-AC in this study is mainly due to the fractional of the first component weight was treated as surrogate of tissue characterization, which effectively suppress ill-conditioning of DECT decomposition. For each iteration, the constant value of ratio assigned to homogeneous tissue voxels can substantially mitigate the small errors produced from multiple FBP reconstructions, making it robust to random noise. It was shown that iFBP can alleviate non-linear BH artifact effectively,[149] however, this algorithm may suffer from its inability to suppress the random noise demonstrated in this study.

Both of the investigated algorithms show fast convergence speed. For example, it only requires several iterations for them to converge to optimal and stable solutions. For example, the relative difference of estimated projections and measured projection of two algorithms as a function of iterations is shown in Fig. 5.18. Within 4 iterations, the difference is able to converge to a stabilized solution. Compared to SIR algorithms, which often require hundreds of iterations, both iFBP algorithms demonstrate a fast and efficient way to remove systematic uncertainties.
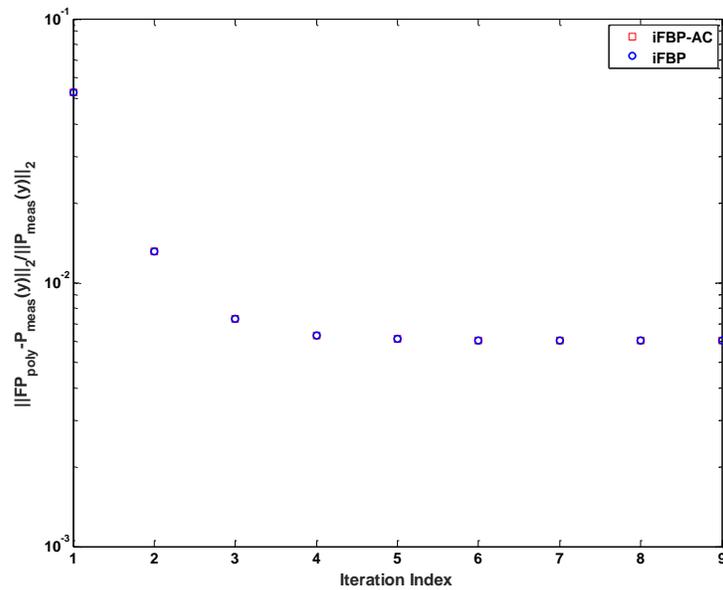
Fig.5.18 Relative difference between estimated and measured projections as a function of iteration

In this study, for a proof of concept purpose, a single basis pair (polystyrene and $CaCl_2$ solution (23%)) is implemented. It is reported in Chapter 4 that a double basis version of BVM theoretically outperforms the single-basis version in estimating attenuation coefficients, i.e. an estimated RMS error of 0.25% with double basis BVM compared to 0.6% of single basis BVM. Thus, for a noiseless sinogram, it is anticipated that iFBP-AC algorithm implemented with double basis may have better prediction accuracy than iFBP-AC with single basis. However, such improvements could be marginal and compromised in estimation accuracy with added noise or other uncertainties in the sinogram in reality. It is expected that there is no significant accuracy difference between iFBP-AC single basis and double basis implementations based on the investigations in Ch.3.

Segmentation on CT images, especially on whole CT, is crucial to the successful implementations of iFBP-AC algorithm. According to different tissue types, there are a variety of techniques proposed for future work.

Breast tissues

Breast tissue classification can provide quantitative measurement regarding breast composition, density and tissue distribution changing with age. Most of the investigated techniques focus on separating the tissues into three types of tissues, i.e., skin, fat and glandular tissue.

- Histogram based method

Nelson et al. [166] used a two-compartment Gaussian fitting of the histogram followed by a region-growing algorithm for the breast tissues. The group led by Boone described a histogram based two-means clustering algorithm along with a seven-point median filter to reduce quantum noise.[167] It is also feasible to classify the breast tissues with thresholding feature available on commercial software.

- Fuzz C-mean (FCM) based method

The FCM clustering algorithm is an automated and unsupervised technique that has been widely used in medical image segmentation.[168, 169] Briefly, FCM technique clusters the image based on its features, e.g. intensity, into known number of classifications through iteratively minimizing an objective function. A commonly used objective function is the least square error that uses Euclidean norm as the metric.[168] It was reported that FCM using Euclidean norm for an objective function can be affected by noise.[170] Recently, a new FCM technique incorporating spatial constraint (sFCM) was proposed. [171] The idea is that pixels on an image are highly correlated so that spatial relationship of neighboring pixels is used to aid segmentation.

A preliminary study of sFCM was performed by our group on cartoon and breast tissue images. Prior to applying sFCM, a non-linear filter, called bilateral filter (BF),[172] was also implemented to denoise the image while preserving the strong edges in the images. We hypothesized that sFCM in conjunction with BF can reduce the impact from image noise to the segmentation result. For example, a synthetic image with (10% noise) contrast ratio 5:4 is shown in Fig. 5.19. The results showing segmentation with sFCM and FCM are compared in Fig. 5.20.

1000   800
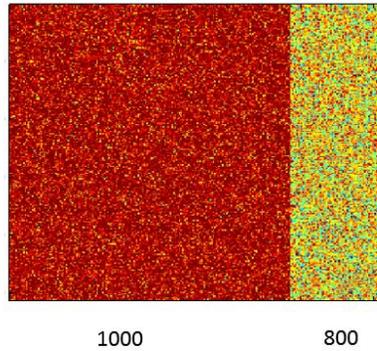
Fig.5.19. A synthetic image with 10% noise is shown. The contrast of two compartments is set 5:4

a   b
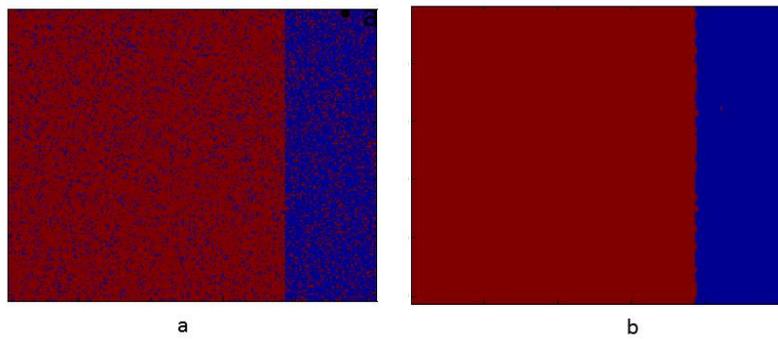
Fig.5.20. Segmentation with a) conventional FCM and b) sFCM and BF technique

The results in Fig.5.20 show that vulnerability of FCM to image noise, while with the aid of BF and spatial constraint, a greatly improved segmentation is realized. An initial test of sFCM on a breast patient image has also implemented. The results are shown in Fig.5.21. The feasibility of segmentation on breast tissues are also demonstrated by other technique KFCM (kernel FCM) [170]and multiscale bilateral FCM[173] on breast CT images.
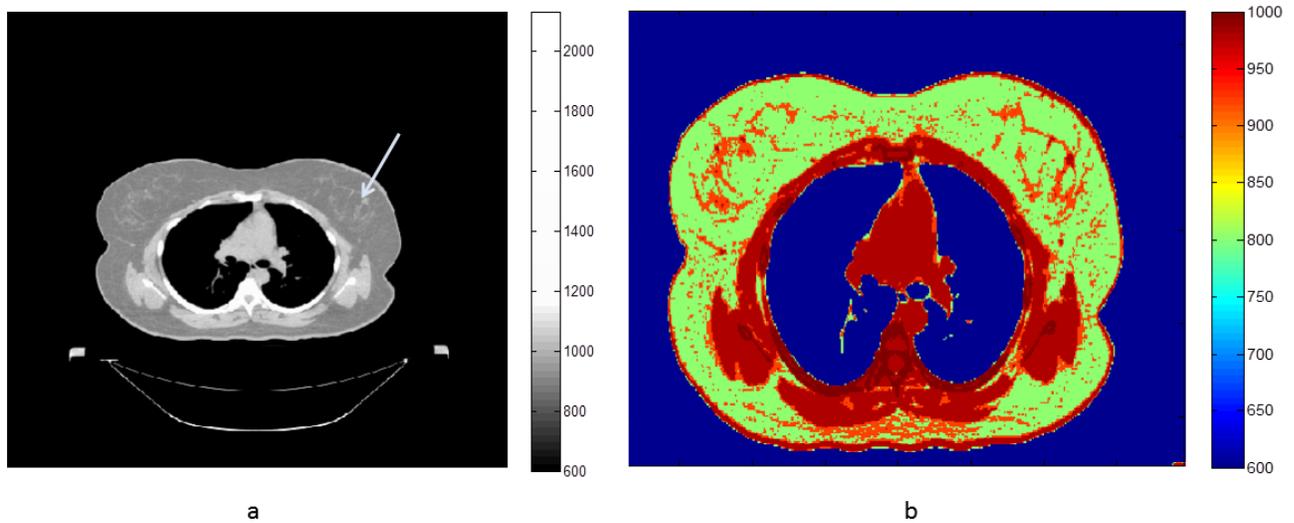
Fig.5.21. a) A breast patient image was acquired with 140 kVp, 150 mAs, b) sFCM applied to cluster the left breast (white arrow) into three groups: fat, skin, and glandular tissue

Non-breast tissues

- Bony tissue. Bony tissues models often consider that each voxel as linear combination of cortical bone and mixture of marrow tissues, including yellow and red marrow. A function of cellularity[174], defined as volume ratio of hematopoiesis and adipose tissues, is known to be correlated with patient age. It is hypothesized that with age information provided, iFBP-AC is able to model the voxel inside bony tissue as combination of age dependent cellularity and fraction of cortical bone.

- Lung tissues. Since lung tissue has large volume of air, it is assumed each voxel inside lung is composed as combination of muscle and air.

The promise of iFBP-AC algorithm demonstrated in this study warrants more studies in the future work. For example, a full and systematic uncertainties analysis, including, spectrum mismatch, is needed before applying this algorithm to real experimental data. The tradeoff of noise and resolution of iFBP-AC, especially compared with statistically-motivated algorithms, remains to be investigated.

The research presented here highlights the potential of a non-statistical model-based algorithm to improve the DECT reconstruction accuracy in support of quantitative CT applications. The results demonstrated in this study are encouraging and warrant studies including aspects as below before being applied to clinical DECT reconstruction:

- The reconstruction errors introduced by improper segmentation. The analysis of error propagation due to mis-segmentation of tissue type on reconstruction error, especially, photon cross section prediction error is needed.

- To develop a metrics system that is sinogram based for estimating the accuracy of photon cross sections when ground truth of elemental compositions are not available

One of the challenges of DECT imaging is lack of a gold standard for validating patient specific DECT reconstruction, since by definition we lack prior knowledge of atomic composition of patient tissues. To address this challenge, we propose to use physical phantoms with exact known elemental composition to correlate their sinogram prediction errors and DECT photon cross-section imaging accuracy. The hypothesis is that prediction accuracy of DECT imaging on photon cross-section can be estimated by backprojecting the sinogram prediction errors. This method is outlined as follows

a. With the precise knowledge of atomic composition, spectra, off-focal radiation, scatter profile and beam hardening effect, a minimal discrepancy can be achieved between $\mathbf{FP}_{poly}\left(\mathbf{y} \mid \mathbf{c}_i^{(k)}(\mathbf{x}), S_m(E)\right)$ and measured sinograms $P_{meas,S_m}(y)$

b. Estimate the sinogram prediction errors

$$\varphi_{S_m}(\mathbf{y}) = \left\| \frac{\left[\mathbf{FP}_{poly}\left(\mathbf{y} \mid \mathbf{c}_i^{(k)}(\mathbf{x}), S_m(E)\right) - P_{meas,S_m}(y) \right]}{P_{meas,S_m}(y)} \right\|_2 \qquad (55)$$

c. Bakproject the Eqn. (55) into spatial domain to acquire the error distribution in space $\Lambda_{S_m}(\mathbf{x})$

d. Correlate the metrics of photon cross-section estimation error

$$\Lambda_{S_m}\left(\mathbf{x}\right) \rightarrow \left|\frac{\mu_{est}\left(\mathbf{x}, E\right)}{\mu_{true}\left(\mathbf{x}, E\right)} - 1\right| \qquad (56)$$

6   Conclusions

The dissertation research presented herein has focused on the key stages of applying DECT techniques to mapping of proton stopping powers and photon cross-section.

Chapter 2 outlined a linear and separable model, BVM, which can be used in accurate estimation of electron density and mean excitation energy (I-values), two parameters needed for the computation of proton stopping power. Our simulation results indicated a theoretical estimation stopping power estimation accuracy, with root-mean-square (RMS) error 0.2% of standard tissues can be achieved by using BVM. This error is comparable to the reported results estimated by other non-linear two-parameter models that are based on Z* and ρ_e. Error propagation analysis suggested that the one-to-one correspondence between the photon cross section and proton stopping power may be undermined by the uncertainties of CT measurements. The robustness of BVM model on estimation of proton stopping power to elemental composition is also reported. To our knowledge, our paper[113] was the first study to extend a linear two-parameter from modeling only photon linear attenuation coefficients to modelling stopping powers in the context of idealized DECT. The merits of BVM model not only lie in providing the accurate prediction of proton stopping power, but also in supporting an accurate modeling for polyenergetic iterative DECT reconstruction algorithms.

Chapter 3 develops a family of modified PFM model, which was too inaccurate for modeling low energetic photon cross sections.[45] Our study confirms our earlier studies[45] that the BVM model is much more accurate in prediction of photon cross sections for compound and mixtures than using mPFM models. The RMS errors of less than about 0.5% and 0.1% for the low ($20 \leq E \leq 50$ keV) and high energy ($50 \leq E \leq 1000$ keV) ranges, were achieved by the BVM model for typical tissues with Z* equal to 7.8, respectively, while the counterpart errors achieved by tPFM models are 0.6% and 2%, respectively. This shows that tPFM models based on spectrally-averaged quantity Z* may not yield sufficiently accurate linear attenuation estimations for use in implementing model-based brachytherapy dose-calculations for energies as low as 20 keV.

In Chapter 4, an efficient and accurate method of deriving x-ray CT spectrum was investigated. Our method seeks to drive a Birch-Marshall equivalent spectrum from the beam hardening correction coefficients embedded in header of vendor's sinogram files. Instead of measuring the transmission experimentally each time for BM model, this technique requires only one-time calibration against an independently measured spectrum to derive the spectrum at other time points by simulation. The technique can be used for spectrum monitoring for routine quality assurance of CT x-ray scanner or to reconstruct spectra corresponding to archived raw datasets. The accurate derivation of spectrum lays the foundation for the development of an advanced iterative filter backprojection reconstruction algorithms.

Chapter 5 showcases a model-based iterative FBP DECT algorithm based on a linear BVM model with anatomical constraints, called iFBP-AC. It was adapted from Yan's iFBP algorithm [149] with similar ability to mitigate the BH effect in an efficient fashion. In order to suppress the uncertainties due to ill-conditioned DECT problem and multiple iterations of FBP, an anatomical constraint, fractional contribution of the first basis material $\alpha(\mathbf{x})$ to voxel, is also suggested to regularize the problem. For each well-defined, and well-segmented tissue type, a constant value of $\alpha(\mathbf{x})$, representing a surrogate of Z* is assigned to all pixels inside each segmented tissue region.

A series of comparisons were implemented for algorithms of iFBP and iFBP-AC. In the case of a noiseless sinogram, no significant difference in reconstructed component images and attenuation estimates was found for both algorithms. The mean errors of c-values are within 0.1% for both algorithms and attenuation errors of muscle at 25 keV are about 1.1% for both algorithms. When representative noise with a Gaussian smoothing kernel added, iFBP-AC outperforms iFBP significantly in image quality. For example, at low energy of 28 keV, the mean estimated uncertainties for bone are 5% and 0.6% by iFBP and iFBP-AC, respectively. In principle, the iFBP-AC shows the potential of reducing the mapping errors of photon cross sections and proton stopping power.

The research, demonstrated here as a whole, supports the potential of the linear BVM model in mapping radiological quantities and confirms its ability to be used as an accurate forward projection modeling. The efficient and accurate method of x-ray spectrum derivation provides a convenient pathway for accessing a priori knowledge needed to implement SIR and other iterative x-ray CT reconstruction algorithms which demand high accuracy of forward projection. The demonstrated noise reduction advantages of iFBP-AC algorithm have the potential to benefit a wide range of quantitative DECT applications. While future work remains to be implemented to exploit this potential, this thesis advances the capabilities of quantitative DECT.

7 References

1   R. Birch and M. Marshall, "Computation of bremsstrahlung X-ray spectra and comparison with spectra measured with a Ge(Li) detector.," Phys. Med. Biol. **24**(3), 505–517 (1979).

2   M. Koenig, E. Klotz, B. Luka, D.J. Venderink, J.F. Spittler, and L. Heuser, "Perfusion CT of the brain: diagnostic approach for early detection of ischemic stroke," Radiology **209**(1), 85–93 (1998).

3   J.H. Siewerdsen and D.A. Jaffray, "Cone-beam computed tomography with a flat-panel imager: Magnitude and effects of x-ray scatter," Med. Phys. **28**(2), 220–231 (2001).

4   T. Beyer, D.W. Townsend, T. Brun, P.E. Kinahan, M. Charron, R. Roddy, J. Jerin, J. Young, L. Byars, and R. Nutt, "A Combined PET / CT Scanner for Clinical Oncology," J. Nucl. Med. **41**(8), 1369–1380 (1999).

5   C.E. Cann, "Quantitative CT for determination of bone mineral density: A review.," Radiology **166**(2), 509–522 (1988).

6   C.H. Yan, R.T. Whalen, G.S. Beaupré, S.Y. Yen, and S. Napel, "Modeling of polychromatic attenuation using computed tomography reconstructed images.," Med. Phys. **26**, 631–642 (1999).

7   M.M. Goodsitt, P. Hoover, M.S. Veldee, and S.L. Hsueh, *The Composition of Bone Marrow for a Dual-Energy Quantitative Computed Tomography Technique*, Invest. Radiol. **29**, 695–704 (1994).

8   R. Nath, L.L. Anderson, G. Luxton, K.A. Weaver, J.F. Williamson, and A.S. Meigooni, "Dosimetry of interstitial brachytherapy sources: Recommendations of the AAPM Radiation Therapy Committee Task Group No. 43," Med. Phys. **22**(2), 209–234 (1995).

9   M.J Rivard, B.M. Coursey, L.A. DeWerd, W.F. Hanson, M.S Huq, G.S. Ibbott, M.G. Mitch, R. Nath, and J.F. Williamson "Update of AAPM Task Group No. 43 Report: A revised AAPM protocol for brachytherapy dose calculations," Med. Phys. **31**(3), 633–674 (2004).

10   Y. Yang and M.J. Rivard, "Evaluation of brachytherapy lung implant dose distributions from photon-emitting sources due to tissue heterogeneities," Med. Phys. **38**(11), 5857–5862 (2011).

11   M.J. Rivard, J.L.M. Venselaar, and L. Beaulieu, "The evolution of brachytherapy treatment planning," Med. Phys. **36**(6Part1), 2136–2153 (2009).

12   J.-F. Carrier, L. Beaulieu, F. Therriault-Proulx, and R. Roy, "Impact of interseed attenuation and tissue composition for permanent prostate implants.," Med. Phys. **33**(3), 595–604 (2006).

13   J.F. Williamson and D.J. Brenner, "Chapter 19 Physics and Biology of Brachytherapy," in *Perez Brady's Princ. Pract. Radiat. Oncol.*(2008), pp. 422–467.

14   H. Afsharpour, J.-P. Pignol, B. Keller, J.-F. Carrier, B Reniers, F. Verhaegen, and L. Beaulieu, "Influence of breast composition and interseed attenuation in dose calculations for post-implant assessment of permanent breast [103]Pd seed implant," Phys. Med. Biol. **55**(16), 4547–4561 (2010).

15   L. Beaulieu, Å.C. Tedgren, J.-F. Carrier, S.D. Davis, M.J. Rivard, R.M. Thomson, F. Verhaegen, T.A. Wareing, and J.F. Williamson "Report of the Task Group 186 on model-based dose calculation methods in brachytherapy beyond the TG-43 formalism: Current status and recommendations for clinical implementation," Med. Phys. **39**(10), 6208–6236 (2012).

16   U. Schneider, E. Pedroni, and A. Lomax, "The calibration of CT Hounsfield units for radiotherapy treatment planning," Phys. Med. Biol. **41**(1), 111–124 (1996).

17   M. Yang, X.R. Zhu, P.C. Park, U. Titt, R. Mohan, G. Virshup, J.E Clayton, and L. Dong "Comprehensive analysis of proton range uncertainties related to patient stopping-power-ratio estimation using the stoichiometric calibration," Phys. Med. Biol. **57**(13), 4095–4115 (2012).

18   M. Bazalova, J.-F. Carrier, L. Beaulieu, and F. Verhaegen, "Dual-energy CT-based material extraction for tissue segmentation in Monte Carlo dose calculations.," Phys. Med. Biol. **53**, 2439–2456 (2008).

19   G. Landry, P. V. Granton, B. Reniers, M.C. Öllers, L. Beaulieu, J.E. Wildberger, and F. Verhaegen, "Simulation study on potential accuracy gains from dual energy CT tissue segmentation for low-energy brachytherapy Monte Carlo dose calculations," Phys. Med. Biol. **56**(19), 6257–6278 (2011).

20   J.D. Evans, B.R. Whiting, J.A. O'Sullivan, D.G. Politte, P.H. Klahr, Y. Yu, and J.F. Williamson "Prospects for in vivo estimation of photon linear attenuation coefficients using postprocessing dual-energy CT imaging on a commercial scanner: Comparison of analytic and polyenergetic statistical reconstruction algorithms," Med. Phys. **40**(12), 121914 (2013).

21   F. Kelcz, P. Joseph, and H. Sadek, "Noise considerations in dual energy CT scanning," Med. Phys. **6**(5), 418–425 (1979).

22   M. Weissberger, R. Zamenhof, R. Saul, and R. Neer, "Computed Tomography Scanning for the Measurement of bone mineral in the human spine," J. Comput. Assist. Tomogr. **2**, 253–262 (1978).

23   W.H. Marshall, W. Easter, and L.M. Zatz, "Analysis of the Dense Lesion at Computed Tomography with Dual kVp Scans," Radiology **124**(1), 87–89 (1977).

24   M.M. Goodsitt, A. Shenoy, J. Shen, D. Howard, M.J. Schipper, S. Wilderman, E. Christodoulou, S.Y. Chun, and Y.K. Dewaraja, "Evaluation of dual energy

quantitative CT for determining the spatial distributions of red marrow and bone for dosimetry in internal emitter radiation therapy.," Med. Phys. **41**(5), 051901 (2014).

25   Jiang Hsieh, *Computed tomography : principles, design, artifacts, and recent advances*, 2nd ed. (SPIE, John Wiley & Sons, Inc, 2009).

26   K. Lange and R. Carson, "EM Reconstruction Algorithms for Emission and Transmission Tomography," J. Comput. Assist. Tomogr. **8**(2), 306–316 (1984).

27   B.R. Whiting, P. Massoumzadeh, O.A. Earl, J.A. O'Sullivan, D.L. Snyder, and J.F. Williamson, "Properties of preprocessed sinogram data in x-ray computed tomography," Med. Phys. **33**(9), 3290–3303 (2006).

28   G.M. Lasio, B.R. Whiting, and J.F. Williamson, "Statistical reconstruction for x-ray computed tomography using energy-integrating detectors," Phys. Med. Biol. **52**(8), 2247–2266 (2007).

29   M. Beister, D. Kolditz, and W.A. Kalender, "Iterative reconstruction methods in X-ray CT," Phys. Medica **28**(2), 94–108 (2012).

30   J. Nuyts, B. De Man, J.A. Fessler, W. Zbijewski, and F.J. Beekman, "Modelling the physics in the iterative reconstruction for transmission computed tomography," Phys. Med. Biol. **58**(12), R63-96 (2013).

31   R.E. Alvarez and A. Macovski, "Energy-selective reconstructions in X-ray computerized tomography.," Phys. Med. Biol. **21**(5), 733–744 (1976).

32   A.N. Primak, J.C. Ramirez Giraldo, X. Liu, L. Yu, and C.H. McCollough, "Improved dual-energy material discrimination for dual-source CT by means of additional spectral filtration," Med. Phys. **36**(4), 1359–1369 (2009).

33   A.C. Kak and M. Slaney, *Principles of Tombgraphic Imaging* (1987).

34   R.A. Brooks and G. Di Chiro, "Beam Hardening in X-ray Reconstructive Tomography," Phys. Med. Biol. **21**(3), 390–398 (1976).

35   W.D. Mcdavid, R.G. Waggener, W.H. Payne, and M.J. Dennis, "Correction for spectral artifacts in the cross-sectional reconstruction from x rays," Med. Phys. **4**(1), 54–57 (1977).

36   P.M. Joseph and R.D. Spital, *A method for correcting bone induced artifacts in computed tomography scanners*, J. Comput. Assist. Tomogr. **2**(1), 100–108 (1978).

37   P.C Johns and M Yaffe, "Scattered radiation in fan beam imaging sytems," Med. Phys. **9**(2), 231–239 (1981).

38   M. Yaffe, K.W. Taylor, and H.E. Johns, "Spectroscopy of diagnostic x rays by a Compton-scatter method," Med. Phys. **3**(5), 328–334 (1976).

[39]   G.H. Glover, "Compton scatter effects in CT reconstructions," Med. Phys. **9**(6), 860–867 (1982).

[40]   H. Kanamori, N. Nakamori, K. Inoue, and E. Takenaka, "Effects of scattered X-rays on CT images.," Phys. Med. Biol. **30**(3), 239–49 (1985).

[41]   B. Ohnesorge, T. Flohr, and K. Klingenbeck-Regn, "Efficient object scatter correction algorithm for third and fourth generation CT scanners," Eur. Radiol. **9**(3), 563–569 (1999).

[42]   G. Di Chiro, R.A. Brooks, R.M. Kessler, G.S Johnston, A.E. Jones, J.R. Herdt, and W.T. Sheridan, "Tissue signatures with dual-energy computed tomography," 68–70 (1979).

[43]   C.E. Cann and G. Harry, "Precise measurement of vertebral mineral content using computed tomography," J. Comput. Assist. Tomogr. **4**(4), 493–500 (1980).

[44]   C.I. Henschke., D. I. McCauley, D.F. Yankelevitz, D.P. Naiditch, G. McGuinness, O.S. Miettinen, D.M. Libby, M.W. Pasmantier, J. Koizumi, N.K. Altorki, and J.P. Smith, "Early Lung Cancer Action Project: Overall design and findings from baseline screening," Lancet **354**(9173), 99–105 (1999).

[45]   J.F. Williamson, S. Li, S. Devic, B.R. Whiting, and F.A Lerma, "On two-parameter models of photon cross sections: application to dual-energy CT imaging.," Med. Phys. **33**, 4115–4129 (2006).

[46]   H. Paganetti, "Range uncertainties in proton therapy and the role of Monte Carlo simulations," Phys. Med. Biol. **57**(11), R99–R117 (2012).

[47]   R.R. Wilson, "Radiological use of fast protons.," Radiology **47**(July), 487–491 (1946).

[48]   H. Bethe, "Zur Theorie des Durchgangs schneller Korpuskularstrahlen durch Materie," Ann. Phys. **397**, 325–400 (1930).

[49]   H. Paganetti, "Range Uncertainties in Proton Therapy Proton Beam Range Medulloblastoma Protons," (n.d.).

[50]   M. Yang, Dual Energy Computed Tomography for Proton Therapy (2011).

[51]   International Commission on Radiation Units and Measurement, *ICRU Report 46: Photon, electron, proton and neutron interaction data for body tissues* (1992).

[52]   J. Valentin, "Basic Anatomical and Physiological Data for use in radiological protection references values: ICRP publication 89," Ann.ICRP **32**, 1–277 (2002).

[53]   U. Schneider, P. Pemler, J. Besserer, E. Pedroni, A. Lomax, and B. Kaser-Hotz, "Patient specific optimization of the relation between CT-hounsfield units and proton stopping power with proton radiography.," Med. Phys. **32**(2005), 195–199 (2005).

54   M. Yang, G. Virshup, J. Clayton, X.R. Zhu, R. Mohan, and L. Dong, "Theoretical variance analysis of single- and dual-energy computed tomography methods for calculating proton stopping power ratios of biological tissues.," Phys. Med. Biol. **55**, 1343–1362 (2010).

55   A.E. Bourque, J.F. Carrier, and H. Bouchard, "A stoichiometric calibration method for dual energy computed tomography," Phys. Med. Biol. **59**(8), 2059–2088 (2014).

56   N. Hünemohr, B. Krauss, C. Tremmel, B. Ackermann, O. Jäkel, and S. Greilich, "Experimental verification of ion stopping power prediction from dual energy CT data in tissue surrogates," Phys. Med. Biol. **59**(1), 83–96 (2014).

57   M.J. Zelefsky, Y. Yamada, G.N. Cohen, A. Shippy, H. Chan, D. Fridman, and M. Zaider "Five-year outcome of intraoperative conformal permanent I-125 interstitial implantation for patients with clinically localized prostate cancer," Int. J. Radiat. Oncol. Biol. Phys. **67**(1), 65–70 (2007).

58   A.B. Chen, A. V. D'Amico, B.A. Neville, and C.C. Earle, "Patient and treatment factors associated with complications after prostate brachytherapy," J. Clin. Oncol. **24**(33), 5298–5304 (2006).

59   N. Miksys, J.E. Cygler, J.M. Caudrelier, and R.M. Thomson, "Patient-specific Monte Carlo dose calculations for (103)Pd breast brachytherapy.," Phys. Med. Biol. **61**(7), 2705–2729 (2016).

60   J.P. Pignol, B. Keller, E. Rakovitch, R. Sankreacha, H. Easton, and W. Que, "First report of a permanent breast 103Pd seed implant as adjuvant radiation treatment for early-stage breast cancer," Int. J. Radiat. Oncol. Biol. Phys. **64**(1), 176–181 (2006).

61   H. Afsharpour, G. Landry, B. Reniers, J.P. Pignol, L. Beaulieu, and F. Verhaegen, "Tissue modeling schemes in low energy breast brachytherapy," Phys. Med. Biol. **56**(22), 7045–7060 (2011).

62   A. Sampson, Y. Le, and J.F. Williamson, "Fast patient-specific Monte Carlo brachytherapy dose calculations via the correlated sampling variance reduction technique," Med. Phys. **39**(2), 1058–1068 (2012).

63   M. Dinsmore, K.J. Harte, A.P. Sliski, D.O. Smith, P.M. Nomikos, M.J. Dalterio, A.J. Boom, W.F. Leonard, P.E. Oettinger, and J.C. Yanch, "A new miniature x-ray source for interstitial radiosurgery: Device description," Med. Phys. **23**(1), 45–52 (1996).

64   M.J. Rivard, S.D. Davis, L.A. DeWerd, T.W. Rusch, and S. Axelrod, "Calculated and measured brachytherapy dosimetry parameters in water for the Xoft Axxent X-Ray Source: An electronic brachytherapy source," Med. Phys. **33**(11), 4020–4032 (2006).

65   S.A. White, G. Landry, G.P. Fonseca, R. Holt, T. Rusch, L. Beaulieu, F. Verhaegen, and B. Reniers, "Comparison of TG-43 and TG-186 in breast irradiation using a low energy electronic brachytherapy source," Med. Phys. **41**(6), 1–12 (2014).

66   O.N. Vassiliev, T.A. Wareing, J. McGhee, G. Failla, M.R. Salehpour, and F. Mourtada, "Validation of a new grid-based Boltzmann equation solver for dose calculation in radiotherapy with photon beams," Phys. Med. Biol. **55**(3), 581–598 (2010).

67   ICRU, *Photon, Electron, Proton and Neutron Interaction Data for Body Tissues* (1992).

68   A. Vaniqui, L.E.J.R. Schyns, I.P. Almeida, B. van der Heyden, S.J. van Hoof, and F. Verhaegen, "The impact of dual energy CT imaging on dose calculations for pre-clinical studies," Radiat. Oncol. **12**(1), 181 (2017).

69   C. Remy, A. Lalonde, D. Béliveau-Nadeau, J.F. Carrier, and H. Bouchard, "Dosimetric impact of dual-energy CT tissue segmentation for low-energy prostate brachytherapy: A Monte Carlo study," Phys. Med. Biol. **63**(2), (2018).

70   N. Côté, S. Bedwani, and J.-F. Carrier, "Improved tissue assignment using dual-energy computed tomography in low-dose rate prostate brachytherapy for Monte Carlo dose calculation," Med. Phys. **43**(5), 2611–2618 (2016).

71   M.M. Goodsitt, E.G. Christodoulou, and S.C. Larson, "Accuracies of the synthesized monochromatic CT numbers and effective atomic numbers obtained with a rapid kVp switching dual energy CT scanner," Med. Phys. **38**(4), 2222–2232 (2011).

72   W. Zhao, K. Niu, S. Schafer, and K. Royalty, "An indirect transmission measurement-based spectrum estimation method for computed tomography," Phys. Med. Biol. **60**(1), 339–357 (2015).

73   A. Fukuda, K. Matsubara, and T. Miyati, "Long-term stability of beam quality and output of conventional X-ray units," Radiol. Phys. Technol. **8**(1), 26–29 (2015).

74   Z. Ying, R. Naidu, and C.R. Crawford, "Dual energy computed tomography for explosive detection," J. Xray. Sci. Technol. **14**, 235–256 (2006).

75   S. Miyajima, "Thin CdTe detector in diagnostic x-ray spectroscopy," Med. Phys. **30**(5), 771–777 (2003).

76   E.Y. Sidky, L. Yu, X. Pan, Y. Zou, and M. Vannier, "A robust method of x-ray source spectrum estimation from transmission measurements: Demonstrated on computer simulated, scatter-free transmission data," J. Appl. Phys. **97**(12), 1–11 (2005).

77   X. Duan, J. Wang, L. Yu, S. Leng, and C.H. McCollough, "CT scanner x-ray spectrum estimation from transmission measurements," Med. Phys. **38**(2), 993–

997 (2011).

78   Y. Lin, J.C. Ramirez-Giraldo, D.J. Gauthier, K. Stierstorfer, and E. Samei, "An angle-dependent estimation of CT x-ray spectrum from rotational transmission measurements," Med. Phys. **41**(6Part1), 062104 (2014).

79   R. Zhang, J.-B. Thibault, C. Bouman, K. Sauer, and J. Hsieh, "Model-Based Iterative Reconstruction for Dual-Energy X-Ray CT Using a Joint Quadratic Likelihood Model.," IEEE Trans. Med. Imaging **33**(1), 117–134 (2013).

80   R.G. Waggener, M.M. Blough, J.A. Terry, D. Chen, N. E. Lee, S. Zhang, and W.D. McDavid, "X-ray spectra estimation using attenuation measurements from 25 kVp to 18 MV," Med. Phys. **26**(7), 1269 (1999).

81   M. Bazalova and F. Verhaegen, "Monte Carlo simulation of a computed tomography x-ray tube," Phys. Med. Biol. **52**(19), 5945–5955 (2007).

82   K.P. Ng, C.S. Kwok, and F.H. Tang, "Monte Carlo simulation of x-ray spectra in mammography," Phys. Med. Biol. **45**, 1309–1318 (2000).

83   S. Miyajima, K. Imagawa, and M. Matsumoto, "CdZnTe detector in diagnostic x-ray spectroscopy," Med. Phys. **29**(7), 1421–1429 (2002).

84   M. Bhat, J. Pattison, G. Bibbo, M. Caon, and G. Bibbo, "Diagnostic x-ray spectra : A comparison of spectra generated by different computational methods with a measured spectrum Diagnostic x-ray spectra : A comparison of spectra generated by different computational methods with a measured spectrum," Med. Phys. **114**(1998), 114–120 (2014).

85   G. Matschekot and R. Ribberforss, "A compton scattering spectrometer for determining x-ray photon energy spectra," Phys. Med. Biol **32**(5), 577–594 (1987).

86   J.M. Boone and J.A. Seibert, "An accurate method for computer-generating tungsten anode x-ray spectra from 30 to 140 kV," Med. Phys. **24**(11), 1661–1670 (1997).

87   J.M. Boone, T.R. Fewell, and R.J. Jennings, "Molybdenum, rhodium, and tungsten anode spectral models using interpolating polynomials with application to mammography," Med. Phys. **24**(12), 1863–1874 (1997).

88   T.R. Fewell, S.R. E., and H. Kermit, *Handbook of computed tomography x-ray spectra* (1981).

89   M.R. Ay, S. Sarkar, M. Shahriari, D. Sardari, and H. Zaidi, "Assessment of different computational models for generation of x-ray spectra in diagnostic radiology and mammography," Med. Phys. **32**(6Part1), 1660–1675 (2005).

90   M.R. Ay and H. Zaidi, "Development and validation of MCNP4C-based Monte Carlo simulator for fan- and cone-beam x-ray CT," Phys. Med. Biol. **50**(20), 4863–4885 (2005).

91   G.G. Poludniowski and P.M. Evans, "Calculation of x-ray spectra emerging from an x-ray tube. Part I. Electron penetration characteristics in x-ray targets," Med. Phys. **34**(6), 2164–2174 (2007).

92   G.G. Poludniowski, "Calculation of x-ray spectra emerging from an x-ray tube. Part II. X-ray production and filtration in x-ray targets," Med. Phys. **34**(6), 2175–2186 (2007).

93   W.A. Kalender, R. Hebel, and E. Johannes, "Reduction of CT artifacts caused by metal implant," Radiology (August), 576–577 (1987).

94   J. Hsieh, "Adaptive streak artifact reduction in computed tomography resulting from excessive x-ray photon noise," Med. Phys. **25**(11), 2139–2147 (1998).

95   B. De Man, J. Nuyts, P. Dupont, G. Marchal, and P. Suetens, "An iterative maximum-likelihood polychromatic algorithm for CT.," IEEE Trans. Med. Imaging **20**(10), 999–1008 (2001).

96   J.F. Williamson, B.R. Whiting, J. Benac, R.J. Murphy, G.J. Blaine, J.A. O'Sullivan, D.G. Politte, and D.L. Snyder, "Prospects for quantitative computed tomography imaging in the presence of foreign metal bodies using statistical image reconstruction.," Med. Phys. **29**, 2404–2418 (2002).

97   R.J. Murphy, J. A. O'Sullivan, J. Benac, D. L. Snyder, B.R. Whiting, D. G. Politte, and J. F Williamson, "Incorporating known information into image reconstruction algorithms for transmission tomography," Proc. SPIE **4684**(314), 29–37 (2002).

98   J.D. Evans, B.R. Whiting, D.G. Politte, J. A. O'Sullivan, P.F. Klahr, and J.F. Williamson, "Experimental implementation of a polyenergetic statistical reconstruction algorithm for a commercial fan-beam CT scanner," Phys. Medica **29**, 500–512 (2013).

99   I.A. Elbakri and J.A. Fessler, "Segmentation-free statistical image reconstruction for polyenergetic x-ray computed tomography with experimental validation," Phys. Med. Biol **48**, 2453–2477 (2003).

100   J.D. Evans, D.G. Politte, B.R. Whiting, J.A.O'Sullivan, and J.F.Williamson, "Noise-resolution tradeoffs in x-ray CT imaging: A comparison of penalized alternating minimization and filtered backprojection algorithms," Med. Phys. **38**(3), 1444–1458 (2011).

101   Y. Lin and E. Samei, "A fast poly-energetic iterative FBP algorithm.," Phys. Med. Biol. **59**, 1655–78 (2014).

102   M. Torikoshi, T. Tsunoo, M. Sasaki, M. Endo, Y. Noda, Y. Ohno, T. Kohno, K. Hyodo, K. Uesugi, and N. Yagi, "Electron density measurement with dual-energy x-ray CT using synchrotron radiation.," Phys. Med. Biol. **48**, 673–685 (2003).

103   W.A. Kalender, W.H. Perman, J.R. Vetter, and E. Klotz, "Evaluation of a prototype dual-energy computed tomographic apparatus. I. Phantom studies,"

Med. Phys. **13**(3), 334–339 (1986).

104   E. Bär, A. Lalonde, G. Royle, H.M. Lu, and H. Bouchard, "The potential of dual-energy CT to reduce proton beam range uncertainties," Med. Phys. **44**(6), 2332–2344 (2017).

105   H. Paganetti, "Range uncertainties in proton therapy and the role of Monte Carlo simulations.," Phys. Med. Biol. **57**, R99–R117 (2012).

106   Joseph F Janni, "Calculations of energy loss, range, pathlength, straggling, multiple scattering, and the probability inelastic nuclear collisions for 0.1-to 1000-MeV protons," (1966)

107   M. Durante and H. Paganetti, "Nuclear physics in particle therapy: a review," Reports Prog. Phys. **79**(9), 096702 (2016).

108   G. Landry, N. Hudobivnik, B. Berndt, F. Schwarz, G. Dedes, and T. Tessonnier, *Dual energy CT for proton therapy*, (2016).

109   B. Li, H.C. Lee, X. Duan, C. Shen, L. Zhou, X Jia, and M. Yang, "Comprehensive analysis of proton range uncertainties related to stopping-power-ratio estimation using dual-energy CT imaging," Phys. Med. Biol. **62**, 7056–7074 (2017).

110   J.-É. Tremblay, S. Bedwani, and H. Bouchard, "A theoretical comparison of tissue parameter extraction methods for dual energy computed tomography," Med. Phys. **41**(8Part1), 081905 (2014).

111   L.I.R. Garcia, J.F.P. Azorin, and J.F. Almansa, "A new method to measure electron density and effective atomic number using dual-energy CT images," Phys. Med. Biol. **61**(1), 265–279 (2016).

112   D.C. Hansen, J. Seco, T. Sørensen, J. Peterson, J. Wildberger, F. Vahaegen, and G. Landry "A simulation study on proton computed tomography (CT) stopping power accuracy using dual energy CT scans as benchmark," Acta Oncol. **54**(9), 1638–1642 (2015).

113   D. Han, J.V. Siebers, and J.F. Williamson, "A linear, separable two-parameter model for dual energy CT imaging of proton stopping power computation," Med. Phys. **43**(1), 600–612 (2016).

114   M. Saito, "Technical Note: Relation between dual-energy subtraction of CT images for electron density calibration and virtual monochromatic imaging," Med. Phys. **42**(7), 4088–4093 (2015).

115   J.K. Van Abbema, M.J. Van Goethem, M.J.W. Greuter, A. Van Der Schaaf, S. Brandenburg, and E.R. Van Der Graaf, "Relative electron density determination using a physics based parameterization of photon interactions in medical DECT," Phys. Med. Biol. **60**(9), 3825–3846 (2015).

116   A. Lalonde, E. Bär, and H. Bouchard, "A Bayesian approach to solve proton

stopping powers from noisy multi-energy CT data," Med. Phys. **44**(10), 5293-5302 (2017).

117   T. Li, Z. Liang, J. V. Singanallur, T.J. Satogata, D.C. Williams, and R.W. Schulte, "Reconstruction for proton computed tomography by tracing proton trajectories: A Monte Carlo study," Med. Phys. **33**(3), 699–706 (2006).

118   C. Talamonti, V. Reggioli, M. Bruzzi, M. Bucciolini, C. Civinini, L. Marrazzo, D. Menichelli, S. Pallotta, N. Randazzo, V. Sipala, G. Cirrone, M. Petterson, N. Blumenkrantz, J. Feldt, J. Heimann, D. Lucia, A. Seiden, D. Williams, H. Saddrozinski, V. Nashkirov, and R. Schulte, "Proton radiography for clinical applications," Nucl. Instruments Methods Phys. Res. Sect. A Accel. Spectrometers, Detect. Assoc. Equip. **612**(3), 571–575 (2010).

119   X. Wu, D. A. Langan, D. Xu, T. M. Bensen, J. D. Pack, A. M. Schmitz, and J . E. Tkaczyk, "Monochromatic CT image representation via fast switching dual kVp," **7258**, 725845 (2009).

120   S. Zhang, D. Han, D.G. Politte, J.F. Williamson, and J.A. O'Sullivan, Impact of joint statistical dual-energy CT reconstruction of proton stopping power images: Comparison to image- and sinogram-domain material decomposition approaches, Med. Phys. Accepted (2018).

121   K. Berger, M.J., Hubbell, J.H., Seltzer, S.M., Chang, J., Coursey, J.S., Sukumar, R., Zucker, D.S., and Olsen, "XCOM: Photon Cross Section Database" (2010).

122   M. Saito, "Potential of dual-energy subtraction for converting CT numbers to electron density based on a single linear relationship," Med. Phys. **39**(4), 2021–2030 (2012).

123   G. Landry, K. Parodi, J.E. Wildberger, and F. Verhaegen, "Deriving concentrations of oxygen and carbon in human tissues using single- and dual-energy CT for ion therapy applications," Phys. Med. Biol. **58**(15), 5029–5048 (2013).

124   N. Hudobivnik, F. Schwarz, T. Johnson, L. Agolli, G. Dedes, T. Tessonnier, F. Verhaegen, C. Thieke, C. Belka, W. Sommer, K. Parodi and G. Landry., "Comparison of proton therapy treatment planning for head tumors with a pencil beam algorithm on dual and single energy CT images," Med. Phys. **43**(1), 495–504 (2016).

125   N. Hünemohr, H. Paganetti, S. Greilich, O. Jäkel, and J. Seco, "Tissue decomposition from dual energy CT data for MC based dose calculation in particle therapy," Med. Phys. **41**(6), 061714 (2014).

126   V.T. Taasti, J.B.B. Petersen, L.P. Muren, J. Thygesen, and D.C. Hansen, "A robust empirical parametrization of proton stopping power using dual energy CT," in *4th Int. Conf. Image Form. X-Ray Comput. Tomogr.*(2016), pp. 5547–5560.

127   A. Lalonde and H. Bouchard, "A general method to derive tissue parameters for Monte Carlo dose calculation with multi-energy CT," Phys. Med. Biol. **61**(22), 8044–69 (2016).

128   G. Landry, B. Reniers, P. Granton, B. Rooijen, L. Beauliu, J. Wildberger and F. Verhaegen, "Extracting atomic numbers and electron densities from a dual source dual energy CT scanner: Experiments and a simulation model," Radiother. Oncol. **100**(3), 375–379 (2011).

129   G. Landry, J. Seco, M. Gaudreault, and F. Verhaegen, "Deriving effective atomic numbers from DECT based on a parameterization of the ratio of high and low linear attenuation coefficients," Phys. Med. Biol. **58**(19), 6851–6866 (2013).

130   D. Han, M.A. Porras-Chaverri, J.A. O'Sullivan, D.G. Politte, and J.F. Williamson, "Technical note: On the accuracy of parametric two-parameter photon cross-section models in dual-energy CT applications," Med. Phys. **44**(6), 2438–2446 (2017).

131   D.R. White, E.M. Widdowson, H.Q. Woodard, and J.W.T. Dickerson, "The composition of body tissues. (II) Fetus to young adult," Br. J. Radiol. **64**, 149–159 (1991).

132   ICRU, *Tissue Substitutes in Radiation Dosimetry and Measurement* (1989).

133   B.N. Taylor and C.E. Kuyatt, *Guidelines for Evaluating and Expressing the Uncertainty of NIST Measurement Results* (1994).

134   F. Bloch, "Zur Bremsung rasch bewegter Teilchen beeim Durchgang durch Materie," Ann. Phys. **16**, 285–320 (1933).

135   P. Andreo, "On the clinical spatial resolution achievable with protons and heavier charged particle radiotherapy beams," Phys. Med. Biol. **54**(11), N205–N215 (2009).

136   Y. Chen, J. A. O'Sullivan, D. Politte, J. Evans, D. Han, R. Whiting, and J. F. Williamson., "Line integral alternating minimization algorithm for dual-energy X-ray CT image reconstruction," IEEE Trans. Med. Imaging **35**(2), 685–698 (2016).

137   D.F. Jackson and D.J. Hawkes, "X-ray attenuation coefficients of elements and mixtures," Phys. Rep. **70**(3), 169–233 (1981).

138   Spiers, "Effective atomic number and energy absorption in tissues," Br.J.Radiol. **19**(218), 52–63 (1946).

139   H.Q. Woodard and D.R. White, "The composition of body tissues," Br. J. Radiol. **59**(12), 1209–1219 (1986).

140   D.R. White, H.Q. Woodard, and Hammond B.A, "Average soft-tissue and bone models for use in radiation dosimetry," Br. J. Radiol. **60**, 907–913 (1987).

141   W.V. Mayneord, "The significance of the Rontgen," Acta Int. Union against Cancer **2**, 271–282 (1937).

142   J.A. O'Sullivan and J. Benac, "Alternating minimization algorithms for transmission tomography," IEEE Trans. Med. Imaging **26**(3), 283–297 (2007).

143   J. Hsieh, R.C. Molthen, C.A. Dawson, and R.H. Johnson, "An iterative approach to the beam hardening correction in cone beam CT," Med. Phys. **27**(1), 23–29 (2000).

144   E.C. McCullough, H.L. Baker, O.W. Houser, and D.F. Reese, "An evaluation of the quantitative and radiation features of a scanning x-ray transverse axial tomograph: the EMI scanner.," Radiology **111**(3), 709–715 (1974).

145   M.J. Peter and D.S. Robin, "The effects of scatter in x- ray computed tomography," Med. Phys. **9**(5), 464 (1982).

146   G.T. Herman, "Correction for beam hardening in computed tomography.," Phys. Med. Biol. **24**(1), 81–106 (1979).

147   K. Peter and B. Bengt, "Correction for beam hardening in computed tomography," Med. Phys. **5**(3), 209–214 (1978).

148   O. Nalcioglu and R.Y. Lou, "Post-reconstruction method for beam hardening in computerised tomography," Phys. Med. Biol. **24**(2), 330–340 (1979).

149   C.H. Yan, R.T. Whalen, G.S. Beaupré, S.Y. Yen, and S. Napel, "Reconstruction algorithm for polychromatic CT imaging: application to beam hardening correction," IEEE Trans. Med. Imaging **19**(1), 1–11 (2000).

150   J. A. O'Sullivan, J. Benac, and J.F. Williamson, "Alternating minimization algorithm for dual energy X-ray CT," 2004 2nd IEEE Int. Symp. Biomed. Imaging Nano to Macro (IEEE Cat No. 04EX821) 579–582 (2004).

151   J. Fessler, "Statistical Image Reconstruction Methods for Transmission Tomography," in *Handb. Med. Imaging, Vol. 2. Med. Image Process. Anal.*(n.d.), pp. 1–70.

152   J.M. Boone, "Equivalent spectra as a measure of beam quality," Med. Phys. **13**(6), 861–868 (1986).

153   H.A. Kramers, "XCIII . On the theory of X- ray absorption and of the continuous X-ray spectrum," Philos. Mag. Ser. 6 **46**(275), 836–871 (1923).

154   J.M. Boone, *The three parameter equivalent spectra as an index of beam quality.*, Med. Phys. **15**(3), 304–310 (1988).

155   R.S. Bradley, "Estimation of bias and variance of measurements made from tomography scans," Meas. Sci. Technol. **27**(9), 95402 (2016).

156   J.H. Siewerdsen, M. Daly, B. Bakhtiar, D. Moseley, S. Richard, H. Keller, and D.

A. Jaffray "A simple, direct method for x-ray scatter estimation and correction in digital radiography and cone-beam CT.," Med. Phys. **33**(1), 187–197 (2006).

157   M. Endo, T. Tsunoo, N. Nakamori, and K. Yoshida, "Effect of scattered radiation on image noise in cone beam CT," Med. Phys. **28**(4), 469–474 (2001).

158   M. Baer and M. Kachelrieß, "Hybrid scatter correction for CT imaging," Phys. Med. Biol. **57**(21), 6849–6867 (2012).

159   S. Kim, H. Song, B. Movsas, and I.J. Chetty, "Characteristics of x-ray beams in two commercial multidetector computed tomography simulators: Monte Carlo simulations," Med. Phys. **39**(1), 320–329 (2011).

160   L. Yu, J.A. Christner, S. Leng, J. Wang, J.G. Fletcher, and C.H. McCollough, "Virtual monochromatic imaging in dual-source dual-energy CT: Radiation dose and image quality," Med. Phys. **38**(12), 6371–6379 (2011).

161   I. a. Elbakri and J. A. Fessler, "Statistical image reconstruction for polyenergetic X-ray computed tomography," IEEE Trans. Med. Imaging **21**(2), 89–99 (2002).

162   J. Nuyts, B. De Man, J.A. Fessler, W. Zbijewski, and F.J. Beekman, "Modelling the physics in the iterative reconstruction for transmission computed tomography," Phys. Med. Biol. **58**(12), 63–96 (2013).

163   M. Endo, S. Mori, T. Tsunoo, and H. Miyazaki, "Magnitude and effects of x-ray scatter in a 256-slice CT scanner," Med. Phys. **33**(9), 3359–3368 (2006).

164   B.J. Heismann, J. Leppert, and K. Stierstorfer, "Density and atomic number measurements with spectral x-ray attenuation method," J. Appl. Phys. **94**(3), 2073–2079 (2003).

165   J.D. Evans, Statistical image reconstruction for quantitative computed tomography (2011).

166   T.R. Nelson, L.I. Cerviño, J.M. Boone, and K.K. Lindfors, "Classification of breast computed tomography data," Med. Phys. **35**(3), 1078–1086 (2008).

167   N. Packard and J.M. Boone, "Glandular segmentation of cone beam breast CT volume images," **6510**, 651038 (2007).

168   J.C. Dunn, "A Fuzzy Relative of the ISODATA Process and Its Use in Detecting Compact Well-Separated Clusters A Fuzzy Relative of the ISODATA Process and Its Use in Detecting Compact Well-Separated Clusters," J. Cybern. **3**(3), 32–57 (1974).

169   S. Egmentation, D.L. Pham, C. Xu, and J.L. Prince, "Currentmethods Inmedical Image Segmentation," Annu. Rev. Biomed. Eng. 2000. 02315–37 **2**, 315–337 (2000).

170   S. Vedantham, L. Shi, A. Karellas, and A. O'connell, "Dedicated Breast CT: Skin

Thickness Measurements in a Diagnostic Population," Med. Phys. **39**(6), 3914–3915 (2012).

171   K.-S. Chuang, H.-L. Tzeng, S. Chen, J. Wu, and T.-J. Chen, "Fuzzy c-means clustering with spatial information for image segmentation," Comput. Med. Imaging Graph. **30**(1), 9–15 (2006).

172   C. Tomasi and R. Manduchi, "Bilateral filtering for gray and color images," Sixth Int. Conf. Comput. Vis. (IEEE Cat. No.98CH36271) 839–846 (1998).

173   X. Yang, S. Wu, I. Sechopoulos, and B. Fei, "Cupping artifact correction and automated classification for high-resolution dedicated breast CT images," Med. Phys. **39**(10), 6397-6406 (2012).

174   M. Cristy, "Active bone marrow distribution as a function of age in humans.," Phys. Med. Biol. **26**, 389–400 (1981).

Appendix I

A linear, separable two-parameter model for dual energy imaging of proton stopping power computation

A linear, separable two-parameter model for dual energy CT imaging of proton stopping power computation

Dong Han[a]
Medical Physics Graduate Program, Department of Radiation Oncology, Virginia Commonwealth University, Richmond, Virginia 23298

Jeffrey V. Siebers
Department of Radiation Oncology, University of Virginia, Charlottesville, Virginia 22908

Jeffrey F. Williamson
Medical Physics Graduate Program, Department of Radiation Oncology, Virginia Commonwealth University, Richmond, Virginia 23298

Purpose: To evaluate the accuracy and robustness of a simple, linear, separable, two-parameter model (basis vector model, BVM) in mapping proton stopping powers *via* dual energy computed tomography (DECT) imaging.

Methods: The BVM assumes that photon cross sections (attenuation coefficients) of unknown materials are linear combinations of the corresponding radiological quantities of dissimilar basis substances (i.e., polystyrene, $CaCl_2$ aqueous solution, and water). The authors have extended this approach to the estimation of electron density and mean excitation energy, which are required parameters for computing proton stopping powers via the Bethe–Bloch equation. The authors compared the stopping power estimation accuracy of the BVM with that of a nonlinear, nonseparable photon cross section Torikoshi parametric fit model (VCU tPFM) as implemented by the authors and by Yang *et al.* ["Theoretical variance analysis of single- and dual-energy computed tomography methods for calculating proton stopping power ratios of biological tissues," Phys. Med. Biol. **55**, 1343–1362 (2010)]. Using an idealized monoenergetic DECT imaging model, proton ranges estimated by the BVM, VCU tPFM, and Yang tPFM were compared to International Commission on Radiation Units and Measurements (ICRU) published reference values. The robustness of the stopping power prediction accuracy of tissue composition variations was assessed for both of the BVM and VCU tPFM. The sensitivity of accuracy to CT image uncertainty was also evaluated.

Results: Based on the authors' idealized, error-free DECT imaging model, the root-mean-square error of BVM proton stopping power estimation for 175 MeV protons relative to ICRU reference values for 34 ICRU standard tissues is 0.20%, compared to 0.23% and 0.68% for the Yang and VCU tPFM models, respectively. The range estimation errors were less than 1 mm for the BVM and Yang tPFM models, respectively. The BVM estimation accuracy is not dependent on tissue type and proton energy range. The BVM is slightly more vulnerable to CT image intensity uncertainties than the tPFM models. Both the BVM and tPFM prediction accuracies were robust to uncertainties of tissue composition and independent of the choice of reference values. This reported accuracy does not include the impacts of *I*-value uncertainties and imaging artifacts and may not be achievable on current clinical CT scanners.

Conclusions: The proton stopping power estimation accuracy of the proposed linear, separable BVM model is comparable to or better than that of the nonseparable tPFM models proposed by other groups. In contrast to the tPFM, the BVM does not require an iterative solving for effective atomic number and electron density at every voxel; this improves the computational efficiency of DECT imaging when iterative, model-based image reconstruction algorithms are used to minimize noise and systematic imaging artifacts of CT images. © *2016 American Association of Physicists in Medicine.* [http://dx.doi.org/10.1118/1.4939082]

1. INTRODUCTION

Dual energy computed tomography (DECT) imaging consists of scanning an object (patient) at two distinct energies, usually at low- and high-energy photon spectra. The underlying problem of establishing one-to-one correspondence between CT image intensity [i.e., Hounsfield Units (HUs)] and material composition is addressed by quantitative dual energy CT (QDECT). QDECT measures two properties of each voxel, thereby disambiguating the dependence of HU on material

composition and density. For example, the earliest QDECT applications characterized tissues in terms of the effective atomic number Z^* and electron density ρ_e.[1] Numerous QDECT applications have been developed, including bone mineral density estimation[2,3] and production of iodine-free images from contrast images.[4] Recently, it has been proposed that QDECT be applied to estimate radiological quantities[5] in support of radiation therapy treatment planning both for charged particle therapy[6] and low-energy brachytherapy.[7] In proton-beam therapy, the goal is to more accurately estimate the depth of the Bragg peak in patients. For example, Schneider et al.[8] found that the measured Bragg peak depth in dogs treated for nasal tumor deviated from the estimated peak depth by 3.6 mm on average when a state-of-the-art quantitative single energy CT (QSECT) stoichiometric calibration method[9] was used to determine the proton stopping power. Yang et al.[6] first proposed a QDECT process for imaging stopping power ratios (SPRs) based upon a simplified parametric fit model of linear attenuation coefficients first introduced by Torikoshi.[10] Using idealized simulated QDECT, Yang et al.[6] showed that DECT can outperform single energy CT (SECT) in prediction accuracy and robustness. A root-mean-square error (RMSE) of 0.26% with maximum relative errors of about 1% was reported for standard human tissues. Bourque et al.[11] extended SECT stoichiometric calibration to DECT and found that the mean absolute error of proton stopping power is about 0.08% for 34 standard human tissues, excluding the thyroid tissue. Hünemohr et al.[12] first experimentally implemented post processing DECT SPR mapping and validated it for different materials. By taking into account both the effective atomic number Z^* and electron density ρ_e, indicating that a mean accuracy of 0.6% could be achieved from the measured 80/140Sn kVp DECT images. Hünemohr et al.[13] also estimated SPR by correlating electron density ρ_e calculated from acquired DECT images. In the application of tissue characterization, Landry et al.[14] first proposed that DECT outperforms the assignments of % wt. of oxygen and carbon than SECT in the absence of image noise. Hünemohr et al.[15] suggested that QDECT can improve the accuracy of tissue characterization in predicting mass density and elemental compositions of representative tissues.

A possible problem of current proton QDECT is that most models are based on nonlinear, nonseparable parametric models that are computationally complex. Obtaining estimates of $(\rho_{e,x}, Z_x^*)$ requires solving nonlinear equations iteratively using Newton–Raphson or similar techniques, at each voxel x. While this is not a problem for the postprocessing (image domain) QDECT techniques investigated to date, it could significantly add to the computational burden of iterative model-based QDECT reconstruction algorithms. Since QDECT solutions are sensitive to noise and image artifacts,[11,12] there is growing interest in iterative techniques, e.g., maximum likelihood techniques or compressed sensing,[17] to implement principled beam hardening and scatter corrections to improve the image uniformity and dose efficiency beyond the level achieved by sinogram preprocessing corrections.[5] Such techniques use physically realistic signal formation models, i.e., polyenergetic forward projectors, based upon the previously characterized scanning beam spectra, with judiciously chosen regularization penalties, to produce smoother, more uniform, and less artifactual images with a lower patient dose than conventional filtered backprojection techniques.[5,18] Forward projections require an accurate estimation of linear attenuation coefficients, $\mu(x,E)$ at any energy E in the scanning spectrum and voxel x in the scan subject. The polyenergetic forward projectors used by the iterative QDECT techniques reported to date[5,18,19] have been based upon the linear, separable, closed basis vector model (BVM),[16] which was first introduced into the CT image reconstruction field by Alvarez and Macovski.[20]

In this study, we propose an adaptation of the linear separable two-parameter DECT BVM model for estimating proton stopping powers. Previously, our group demonstrated the accuracy of the two-parameter model in parameterizing linear attenuation coefficients in the photon energy range of 20 keV to 1 MeV for elemental and composite biological media.[21] In this work, we show that our simple BVM extension accurately estimates proton stopping powers for 175 MeV protons with an accuracy equivalent to that of the more computationally intensive Torikoshi parametric fit models (tPFMs).[10] In addition, we assess the sensitivity of QDECT performance to both image uncertainties and tissue composition variations lying outside the International Commission on Radiation Units and Measurements (ICRU) published values.

2. METHODS AND MATERIALS

In this study, we evaluated two-parameter models for mapping the proton stopping power by means of an idealized QDECT process. Using this highly idealized model, we were able to isolate radiological quantity modeling errors from image intensity uncertainties and artifacts. Hence the errors identified in this study represent the lower bound of clinically achievable performance. The images intensity HU_{S_k} of each pixel in CT images for unknown tissue were termed

$$\left\langle \frac{\mu}{\mu_{\text{wat}}} \right\rangle_{S_k} = \frac{HU_{S_k}}{A_{S_k}} + B_{S_k}, \tag{1}$$

where μ_{wat}, μ are the linear attenuation coefficients of water and unknown tissue. The subscripts $S_k = 1, 2$ represent the low- and high-energy CT spectra, respectively. By convention, A_{S_k} and B_{S_k} take values near 1000 and 1, in quantitative CT, these parameters are determined by maximizing the fit between experimentally measured HU_{S_k} values and spectrally averaged $\langle \mu_x/\mu_{\text{wat}} \rangle_{S_k}$ values calculated values for scanned samples of known composition and density.

Protons lose energies primarily by means of Coulombic interactions with electrons when passing through tissues. The Bethe–Bloch equation[22] approximates the rate of energy loss and stopping power of tissues at a given proton energy (E_{proton}) as follows:

$$
\begin{aligned}
S(E_{\text{proton}}) &= -\frac{dE_{\text{proton}}}{dx} \\
&= \frac{k_1 \rho_e}{\beta^2} \left[\frac{1}{2} \ln \frac{k_2 \beta^2 T_{\max}}{I^2(1-\beta^2)} - \beta^2 - \frac{\delta(\beta)}{2} - \frac{C(\beta)}{2} \right] \\
&\approx \rho_e \underbrace{\left[\frac{k_1}{\beta^2} \ln(2m_e c^2 \beta^2) - \frac{k_1}{\beta^2} \ln(1-\beta^2) - k_0 \right]}_{K} \\
&\quad - \frac{k_1}{\beta^2} \rho_e \ln I = K \rho_e - \frac{k_1}{\beta^2} \rho_e \ln I,
\end{aligned} \tag{2}
$$

where k_1 and k_2 are products of physical constants; $\beta = v/c$; c is the speed of light; $T_{\max}$ is the maximum energy transferred to a single electron; and ρ_e and I are the electron density and mean excitation energy (I-value), respectively. The I-value depends on the composition and the density of the medium. The density correction, $\delta(\beta)$ is significant only at proton energies above several hundred MeV. The shell correction, $C(\beta)$ is significant only when proton velocity is comparable to that of atomic electrons. These two corrections were ignored since they are negligible for the energies considered in this study.

In this work, reference stopping power values were computed by Eq. (2) for 34 standard tissues[6] using the elemental compositions, electron density and mass density data, along with I-value for each constituent element from ICRU reports.[23,24] The mean excitation energy for each tissue was computed from elemental I-values (including ICRU recommended solid/liquid phase to gaseous phase corrections)[35] using the Bragg additivity rule:

$$
\ln(I) = \frac{\sum_i \omega_i \left(\frac{Z}{A}\right)_i \ln(I_i)}{\sum_i \omega_i \left(\frac{Z}{A}\right)_i} \tag{3}
$$

where ω_i, Z_i, A_i and I_i are the mass fraction, atomic number, atomic mass and mean excitation energy of the i-th element in the tissue, respectively. For water and polystyrene, the experimentally measured I-values recommended by ICRU were used,[25] while for $CaCl_2$ solution, the I-value was estimated by applying the Bragg additivity rule to the recommended water I-value of water and the I-value of $CaCl_2$, which is estimated by the Bragg additivity rule from elemental values.

In this study, we evaluated the accuracy of stopping power predicted by competing DECT models at proton energy of 175 MeV for 34 standard tissues. To assess the relationship between accuracy and proton energy, prediction errors were evaluated for three typical tissues (adipose, muscle, and cortical bone) for energies ranging from 5 to 300 MeV.[26] We also computed proton range for each of 34 tissues starting from 175 MeV by utilizing the continuous slowing down approximation (CSDA),

$$
R(E_0) = -\int_{E_0}^{E_{\min}} \frac{dE_{\text{proton}}}{S(E_{\text{proton}})}. \tag{4}
$$

$S(E_{\text{proton}})$ is the stopping power of protons at energy E. E_0 is the initial energy at the tissue-phantom surfaces. $E_{\min}$ is the energy where integration of the model is terminated, which was set to 1 MeV.

2.A. Basis vector model

The BVM (Ref. 16) assumes that the linear attenuation coefficient of an unknown material at location x can be represented as a linear combination of the linear attenuation coefficients of two dissimilar basis materials, e.g., polystyrene and aluminum,

$$
\mu(x,E) = c_1(x)\mu_1(E) + c_2(x)\mu_2(E), \tag{5}
$$

where $\mu_k(E)$ represents the linear attenuation coefficient of pure samples of the basis materials, $k = 1,2$. Once the voxel dependent, but energy independent and possibly negative $c_1(x)$ and $c_2(x)$ images from DECT images are derived, the linear attenuation coefficient for any energy within the range that the BVM has been validated can be obtained. Let us assume that a phantom consisting of unknown compounds and/or mixtures is scanned with a commercial CT scanner at low- ($S_k = 1$) and high-energy ($S_k = 2$) spectra, characterized by normalized photon fluence spectra $\varphi_{S_k}(E)$, where $\int_0^\infty \varphi_{S_k}(E)dE = 1$. Because the BVM is separable and expressed as the sum of the products of energy- and position-dependent terms, Eq. (5) becomes

$$
\begin{aligned}
\left\langle \frac{\mu(x,E)}{\mu_{\text{wat}}(E)} \right\rangle_{S_k} &\equiv \frac{\int E \cdot \varphi_{S_k}(E)\mu(x,E)dE}{\int E \cdot \varphi_{S_k}(E)\mu_{\text{wat}}(E)dE} \\
&= c_1(x)\left\langle \frac{\mu_1(E)}{\mu_{\text{wat}}(E)} \right\rangle_{S_k} + c_2(x)\left\langle \frac{\mu_2(E)}{\mu_{\text{wat}}(E)} \right\rangle_{S_k}.
\end{aligned} \tag{6}
$$

Since spectra of commercial CT scanner are generally unknown, and HU measurements may be affected by beam hardening, scattering, noise and preprocessing corrections, $S_k(E)$ is often approximated by a single effective energy, E_{S_k}, such that $\mu_k(E_{S_k})/\mu_{\text{wat}}(E_{S_k}) \approx \langle \mu_k(E)/\mu_{\text{wat}}(E) \rangle_{S_k}$ for the two basis materials. Experimentally, this is commonly achieved[27] by scanning a series of samples, x, of known composition, including pure basis materials, and then finding the effective energy for each spectrum that maximizes the accuracy of Eq. (1). With this calibration in hand, Eq. (6) becomes

$$
\frac{\mu(x,E_{S_k})}{\mu_{\text{wat}}(E_{S_k})} = c_1(x)\frac{\mu_1(E_{S_k})}{\mu_{\text{wat}}(E_{S_k})} + c_2(x)\frac{\mu_2(E_{S_k})}{\mu_{\text{wat}}(E_{S_k})}. \tag{7}
$$

For low- and high-energy scans, Eq. (7) describes a system of two linear equations with two unknowns which can be solved for $c_1(x)$ and $c_2(x)$ at each voxel. If the scanning beam spectra are known, then the need for effective mean energies can be avoided since $\langle \mu_x(E)/\mu_{\text{wat}}(E) \rangle_{S_k}$ can be calculated directly, simplifying the identification of optimal parameters A_{S_k} and B_{S_k}. In iterative statistical image reconstruction, the need for this calibration procedure is completely avoided. Given estimates of the spectra and detector scatter profiles, optimal $c_1(x)$ and $c_2(x)$ images can be iteratively estimated by minimizing the discrepancy between the predicted polyenergetic forward projections and measured transmission sinograms. Since this investigation focuses only on the accuracy of the BVM model itself, in isolation from any additional uncertainties with the image acquisition process, the idealized monoenergetic DECT scanning process described by Eq. (7) is assumed. In this study, DECT with 90 and 140 kVp beams was

approximated[5,16] using effective energies of 45 (E_1) and 80 (E_2) keV. Thus, the linear attenuation coefficients of the basis materials and 34 ICRU standard human tissues were evaluated at these two effective energies based on the knowledge of the elemental composition.

The choice of basis material has been discussed previously by Weaver and Huddleston,[28] who used principal components analysis. However, the choice of water as the boundary material between low-Z and high-Z mixtures was suggested by Williamson et al.[16] For our study, a water and polystyrene pair was selected for soft tissues (low-Z materials), while a water and aqueous $CaCl_2$ solution (23% concentration) pair was chosen for bony tissues (high-Z materials).[16] The ratio of coefficients $c_1/(c_1+c_2)$ for each material is closely correlated with its effective atomic number, Z^* (Fig. 1). The details of the Z^* calculation are described in Sec. 2.B. As suggested by Williamson et al.,[16] the basis pair for a given voxel x can be selected by evaluating the ratio $\xi(x)$ $= (\mu(x,E_2)/\mu_{wat}(x,E_2))/(\mu(x,E_1)/\mu_{wat}(x,E_1))$: x is assigned to the polystyrene–water pair if $\xi(x) \geq 1$ and water–$CaCl_2$ solution otherwise. Figure 1 shows that the boundary between low-Z and high-Z tissues falls near the thyroid tissue data point, which has about 8.4. Figure 1 also shows that $c_1/(c_1+c_2)$ can be used as an alternative to Z^* for characterizing material composition.

To apply the BVM to the estimation of proton stopping power, we hypothesized that the electron density and mean excitation energy of an arbitrary biological material can be accurately predicted by the following linear combinations where c_1 and c_2 were derived from DECT analysis Eq. (7):

$$\rho_{ex} = c_1\rho_{e1} + c_2\rho_{e2},$$
$$\rho_{ex}\ln I_{x,BVM} = c_1\rho_{e1}\ln I_1 + c_2\rho_{e2}\ln I_2, \quad (8)$$

where ρ_{e1} and ρ_{e2} are the electron density of water and polystyrene or $CaCl_2$ solution. The electron densities of basis

mixtures was estimated by

$$\rho_{e\_mixture} = \rho_m N_A \sum_i \omega_i \frac{Z_i}{A_i}, \quad (9)$$

where ρ_m is the mass density of the mixture and ω_i is the mass fraction of the ith element. The mean excitation energy of an arbitrary tissue is given by

$$I_{x,DECT} = f_I\left(\frac{c_1}{c_1+c_2}\right)\exp\left(\frac{c_1\rho_{e1}\ln I_1 + c_2\rho_{e2}\ln I_2}{c_1\rho_{e1} + c_2\rho_{e2}}\right), \quad (10)$$

where f_I is an empirical correction function that mitigates the residual error of the prediction of I-value by Eq. (8). It was assumed that the ratio of I-values from Eq. (8) to the ICRU reference values and $c_1/(c_1+c_2)$ is linearly dependent,

$$f_I\left(\frac{c_1}{c_1+c_2}\right) = \frac{I_{x,Ref}}{I_{x,BVM}} = a \cdot \frac{c_1}{c_1+c_2} + b. \quad (11)$$

To determine the parameters a and b in Eq. (11), the precomputed ratios of I_{Ref}/I_{BVM} for 34 standard human tissues were separated into two groups: soft tissues and bony tissues, and each of which had the best linear fit that minimized the summed squared difference between predicted ratios and precomputed ratios. The linear empirical correction function was then used to update the estimation of I-values from Eq. (8). This correction function can also be generated from scanning calibration phantoms for a specific scanner. For example, CT numbers of calibration phantoms acquired by scanning at two different energies can be used to compute c_1 and c_2, which can then be used to estimate the uncorrected I-value of calibration phantoms from Eq. (8). Since the references of I-value can be obtained using the Bragg additivity rule given the exact elemental compositions of phantoms, the correction function was constructed by comparing reference values against uncorrected I-values with respect to $c_1/(c_1+c_2)$. In our study, the linear fits for the soft and bony tissues are shown in Fig. 2. A voxel falling into the overlap region of Fig. 2 would be described as a bony tissue or soft tissue depending upon which basis pair it was assigned based on the ratio $\xi(x)$ of its DECT image intensities as described above.

2.B. Torikoshi parametric fit models

The previously investigated model for two-parameter estimation of proton stopping power by Yang et al.[6] was based on Torikoshi's nonseparable model of photon cross sections, termed tPFMs, which assumed that the linear attenuation coefficient of each unknown material is a function of ρ_e and Z^*. For photon energies lower than 1.02 MeV, the linear attenuation coefficient of tissue was modeled by Torikoshi et al.[10] as

$$\mu(x,E) = \rho_e(x)\left(Z^{*4}(x)F(E,Z^*) + G(E,Z^*)\right), \quad (12)$$

where $\rho_e(x)$ and $Z^*(x)$ are the effective atomic number and electron density at voxel x. The terms $\rho_e(x)Z^{*4}(x)F(E,Z^*(x))$ and $\rho_e(x)G(E,Z^*(x))$ represent photoelectric absorption and scattering, respectively. The pretabulated correction functions $F(E,Z^*)$ and $G(E,Z^*)$ were determined by forcing Eq. (12) to


FIG. 1. The linear relationship between $c_1/(c_1+c_2)$ and effective atomic number of the 34 human tissues selected from the ICRU reports. The effective atomic number was calculated based on the knowledge of the elemental composition.
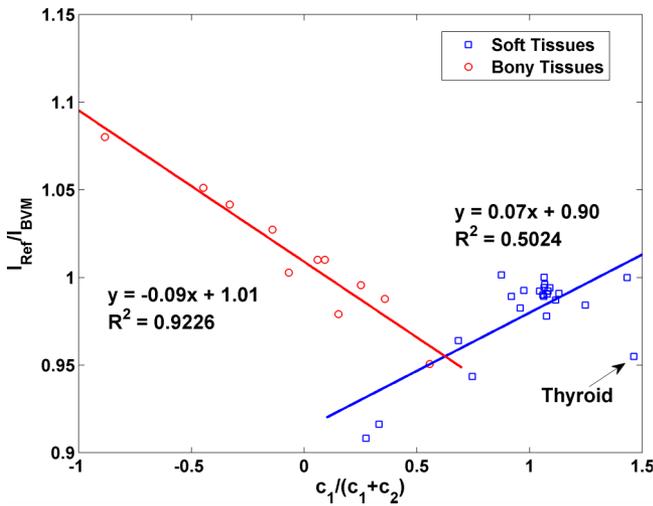
Fig. 2. The linear relationships between $c_1/(c_1+c_2)$ and I-value prediction error by the BVM for soft tissues and bony tissues. This empirical function was used to correct the error of the I-value estimated by the BVM.

Fig. 3. The polynomial relationship (Ref. 11) between Z^* and mean excitation energy was implemented in the VCU tPFM. Data for 34 soft tissues and bony tissues are shown.

reproduce exact linear attenuation coefficients for the elements ($Z = 2-20$), as tabulated by the National Institute of Standards and Technology (NIST) XCOM database.[29] For tissues that are unknown mixtures of elements with Z between 1 and 20, Eq. (12) can be solved iteratively for noninteger Z^* and ρ_e values for each CT voxel. To apply these results to proton stopping power estimation, an empirical relationship between $\ln I$ and Z^* or I and Z^* is required. The standard effective atomic number of human tissue was defined as

$$Z_{\text{std}}^m = \frac{\left(\sum \frac{\omega_i Z_i}{A_i} Z_i^m\right)}{\sum \frac{\omega_i Z_i}{A_i}}, \tag{13}$$

respectively, since it is repeated in Eq. (3). m was determined to be 3.4 by minimizing the sum of the squared difference between Z_{std} and Z^*, which was calculated using Eq. (12).

In Yang's simulation study, the linear attenuation coefficients were approximated by

$$\langle \mu \rangle_j = \rho_e \sum_{j=1}^{2} \phi_{l,j} \left[Z^{*4}(x) F(E_{l,j}, Z^*) + G(E_{l,j}, Z^*) \right], \tag{14}$$

where $\phi_{l,j}$ is the weighting function of the l-th energy bin of the j-th spectrum ($j = 1,2$ denoting 100 and 140 kVp spectra, respectively). The beam spectra of the CT scanner at two energies were calculated by the SpekCalc x-ray spectrum generator in the implementation of Yang et al.[6]

To fairly and consistently compare the tPFM to our BVM model, we have implemented a modified version of Yang's process (hereafter termed the Yang tPFM) and a second model (hereafter designated as the VCU tPFM). There are two differences between the VCU tPFM and Yang tPFM. In the VCU tPFM, each energy spectrum was approximated by its effective energy, while in the Yang tPFM, two synthetic energy spectra were used. The VCU tPFM used a different empirical relationship for inferring mean excitation energy from effective atomic number than the Yang tPFM (shown

for the same set of human tissues in Fig. 3). In addition, the thyroid tissue was assigned to the soft tissues category for estimating I-values in the Yang tPFM of our study; however, the thyroid tissue was excluded from the Yang et al.[6] analysis. The nonlinear equation with unknowns Z^* and ρ_e were solved iteratively using the MATLAB (version 12.0, The Math Works, Inc., Natick, MA) function $fminsearch$ in the implementation of the VCU tPFM. To reproduce the results of the SPR estimation from the Yang et al.,[6] I-values and electron density of tissues estimation from the Yang et al.[6] were used in the Yang tPFM study.

2.C. Robustness analysis of the DECT models' estimation of the proton stopping power

Our idealized QDECT simulation used the elemental compositions, mass, and electron densities for different body tissues recommended by ICRU reports[23,24] and other studies.[30,31] To make conservative estimates of the impact of poorly characterized tissue composition variability on QDECT estimates, we varied the elemental compositions of the unknown soft tissues by varying the mass fractions of the following major components: water, lipid, protein, carbohydrate, and ash (Table I), each of which has a fixed elemental composition according to the Table A1 in ICRU report 46.[23] Using adipose tissue as an example, assuming that the main component is lipid with a range of mass fraction of 30%–80%,[23,32] protein mass fraction range of 1%–7.5%, and constant mineral mass fraction, the water content can be computed based on the normalization of all components to 100%. Note that since the range of each component was chosen in a way that can accommodate large variability reported by ICRU report 44,[24] the values of mass fraction reported here may not be realistic. For trabecular bone tissues, the cortical bone and marrow tissues as major components were varied. The mass densities of tissues were estimated from the mass fractions and mass densities of the components.[33]

TABLE I. Variations in the components of soft tissues and trabecular tissues (percentage by mass or volume) considered in this study.

Body tissues (mass fraction)	Water	Lipid	Protein	Carbohydrate	Ash (mineral)
Adipose-like tissue	62.2–4.7	30–88	1.0–7.5	—	0.3
Muscle-like tissue	83–73	1–5	10–20	1	0.9

	Cortical bone (volume fraction)	Red marrow (mass fraction)			
Trabecular bone (spongiosa)	5–70	30–100			

2.D. Accuracy analysis

The reference stopping power of representative human tissues was computed using the electron density and composition data from ICRU report 44 (Ref. 24) based on the Bethe–Bloch equation.[22] To quantify the accuracy of the stopping power prediction by different QDECT models, including the BVM, Yang tPFM, and VCU tPFM, the relative error and RMSE, defined below, were evaluated at a single proton energy where $E_{\text{proton}} = 175$ MeV,

$$\text{Relative error}\,(\%)_{i'} = 100 \times \left(\left| 1 - \frac{SP_{i',\text{DECT}}(E_{\text{proton}})}{SP_{i',\text{true}}(E_{\text{proton}})} \right| \right), \quad (15)$$

$$\text{RMSE}\,(\%) = 100 \times \sqrt{\frac{\sum\limits_{i'=1}^{N} \left(1 - \frac{SP_{i',\text{DECT}}(E_{\text{proton}})}{SP_{i',\text{true}}(E_{\text{proton}})} \right)^2}{N}}, \quad (16)$$

where $SP_{i'}$ refers to the stopping power of the i'th tissue. The distribution of the relative error of the proton stopping power and range for all human tissues are also presented.

2.E. Sensitivity to CT image uncertainty

As mentioned above, our study ignores the uncertainties inherent in commercial CT scanners, including image noise, beam hardening, nonuniformity, and other nonlinear artifacts. These uncertainties can undermine the one-to-one correspondence between underlying tissue characteristics and CT image intensity. Williamson et al.[16] pointed out that QDECT estimates of photon cross sections are particularly vulnerable to measurement uncertainties. In this study, the impact of uncertainties in CT image intensities on proton stopping power estimation was evaluated for both of the BVM and VCU tPFM.

We defined image density as $D_{j,k} = (\mu_k/\mu_{\text{wat}})_{E_j}$, where $j = 1$ and 2 denote E_1 and E_2 and $k = 1, 2$, and 3 denote basis material 1, basis material 2, and unknown material, respectively. c_1 and c_2 are functions of six independent image intensities, which are assumed to have uncertainties of $\sigma_{j,k}$. The uncertainties of electron density prediction by the law of error propagation for a coverage factor of 1.0 can be written as

$$
\begin{aligned}
u_{\text{unknown},\rho_e}(E) &= \left[\sum_{j=1}^{2}\sum_{k=1}^{3} \left(\frac{\partial \rho_e}{\partial D_{jk}} \sigma_{jk} \right)^2 \right]^{1/2} = \left[\sum_{j=1}^{2}\sum_{k=1}^{3} \left(\frac{\partial \rho_e}{\partial c_{1,jk}} \frac{\partial c_{1,jk}}{\partial D_{jk}} \sigma_{jk} + \frac{\partial \rho_e}{\partial c_{2,jk}} \frac{\partial c_{2,jk}}{\partial D_{jk}} \sigma_{jk} \right)^2 \right]^{1/2} \\
&= \left[\begin{array}{l} \left(\frac{\partial \rho_e}{\partial c_{1,jk}} \right)^2 \sum_{j=1}^{2}\sum_{k=1}^{3} \left(\frac{\partial c_{1,jk}}{\partial D_{jk}} \sigma_{jk} \right)^2 + \left(\frac{\partial \rho_e}{\partial c_{2,jk}} \right)^2 \sum_{j=1}^{2}\sum_{k=1}^{3} \left(\frac{\partial c_{2,jk}}{\partial D_{jk}} \sigma_{jk} \right)^2 \\ + 2 \left(\frac{\partial \rho_e}{\partial c_{1,jk}} \right) \left(\frac{\partial \rho_e}{\partial c_{2,jk}} \right) \sum_{j=1}^{2}\sum_{k=1}^{3} \left(\frac{\partial c_{1,jk}}{\partial D_{jk}} \frac{\partial c_{2,jk}}{\partial D_{jk}} \sigma_{jk}^2 \right) \end{array} \right]^{1/2}.
\end{aligned}
\quad (17)
$$

The uncertainty of the product of electron density and the logarithmic of I-value can be obtained in a similar fashion.

Thus, the uncertainty of the stopping power estimation via the BVM was given by

$$
\begin{aligned}
u_S^2(E_{\text{proton}}) = S^2 \Bigg(& K^2 \left(\frac{u_{\rho_e}}{\rho_e} \right)^2 + \left(\frac{k_1}{\beta^2} \right)^2 \left(\frac{u_{\rho_e \ln I}}{\rho_e \ln I} \right)^2 \\
& + 2K \left(\frac{k_1}{\beta^2} \right) \text{cov}(\rho_e, \rho_e \ln I) \Bigg),
\end{aligned}
\quad (18)
$$

where the constants K and k_1 were defined by Eq. (2), and $\text{Cov}(\rho_e, \rho_e \ln I)$ was the covariance of ρ_e and $\rho_e \ln I$. For

the parameterized QDECT models, the uncertainty of the stopping power can be obtained similarly. All uncertainties described above were evaluated numerically (ratio of change in numerator to 1% change in denominator), at three different image uncertainty levels for standard human tissues.

Following Williamson et al.,[16] three different levels of CT image intensity uncertainty were investigated. Following the NIST technical note[34] on uncertainty analysis guidelines, the image intensity uncertainties were the quadrature sum of random (type A) and systematic errors (type B), e.g., streak and cupping, in terms of coefficients of variation (COV). The lowest uncertainty levels, with COV of 0.2% and 0.1% for

low- and high-energy scans, respectively, supported recovery for a low-energy photon cross section with 3% accuracy and acceptable spatial resolution but are not achievable on current commercial scanners with clinically acceptable patient doses. The intermediate levels (0.6%, 0.3%) are minimum uncertainties achievable by fourth-generation CT scanners, while the highest uncertainties (1.5%, 1.0%) are characteristic of clinical pelvic CT imaging. The readers are referred to Ref. 16 for the choice of uncertainties level. The uncertainties in the calibration scan of the basis material were not taken into account due to averaging of many voxels in the calibration scan.[16]

3. RESULTS

3.A. Prediction of the mean excitation energy and electron density of human tissues

The mean excitation energy and electron density of the three basis materials used in this study are summarized in Table II.

Figure 4(a) shows that the Yang tPFM and BVM both predict the electron density within 0.5% for most tissues, while the VCU tPFM has a slightly larger prediction error of nearly 1%.

The mean relative errors in estimated electron density averaged over 34 standard tissues were $0.09\% \pm 0.10\%$ for the BVM, $0.07\% \pm 0.08\%$ for the Yang tPFM, and $0.57\% \pm 0.29\%$ for the VCU tPFM. Within the different DECT models, the BVM showed comparable accuracy to the Yang tPFM, while the VCU tPFM was slightly less accurate. Due to large errors incurred by including the thyroid tissue in estimation of I-value of soft tissues, Yang $et\ al.$ omitted the thyroid tissue from their empirical fit of I-values versus Z_{std}, whereas it was included in the BVM and VCU tPFM fits. Figure 4(b) shows that the BVM, Yang tPFM, and VCU tPFM models predict the I-values with comparable accuracy with mean errors of $1.14\% \pm 1.15\%$, $1.16\% \pm 1.06\%$, and $0.94\% \pm 1.03\%$, respectively. For the thyroid tissue, I-value prediction errors were 5.9%, 7.0%, and 2.1% for the BVM, Yang tPFM, and VCU tPFM models, respectively. The BVM had slightly reduced I-values prediction errors compared to the Yang tPFM. The RMSE for electron density and I-values are summarized in Table III.

3.B. Prediction of the proton stopping power at 175 MeV

Figure 5(a) shows the errors in estimating the stopping power of 34 human tissues by the three different DECT
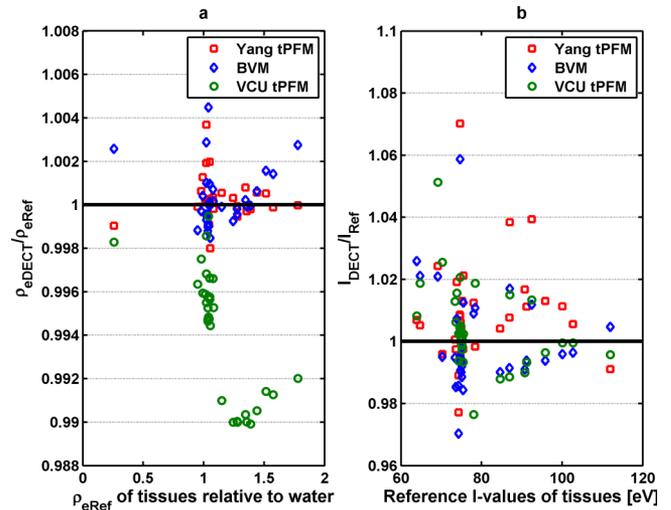

Fig. 4. The ratio of electron density and I-values estimation by three different models: the Yang tPFM, BVM, and VCU tPFM, respectively, to the reference value of stopping power. (a) Electron density and (b) I-values. The reference electron density of tissues is shown in the form of electron density relative to water. The reference I-values were computed based on the Bragg additivity rule.

models. The mean relative errors of the BVM, Yang tPFM, and VCU tPFM were $0.16\% \pm 0.12\%$, $0.14\% \pm 0.12\%$, and $0.62\% \pm 0.29\%$, respectively.

The RMSEs of the stopping power estimation for the BVM, Yang tPFM, and VCU tPFM were 0.20%, 0.23%, and 0.68%, respectively. Figure 5(b) shows the error distribution of the predicted stopping power using three different models for 34 human tissues. These data indicate that BVM had similar prediction accuracy to the Yang tPFM model but better accuracy than the VCU tPFM.

3.C. Dependence of the proton stopping power prediction accuracy on proton energy and tissue type

Figure 6 shows that the BVM proton stopping power estimation accuracy for a typical set of tissues (adipose, muscle, and cortical bone)[26] for proton energies ranging from 5 to 300 MeV. Figure 6 shows that estimation errors are constant at $\pm 0.3\%$ above 40 MeV. Only below 10–20 MeV did these errors begin to exceed 1% but remained within 2% at the lowest energy 5 MeV evaluated. Although larger errors would be expected below 5 MeV, the residual range of such low energy protons is less than 0.5 mm and hence is of limited clinical significance.

TABLE II. Electron densities and I-values of basis materials.

Basis materials	ρ_e ($\times 10^{23}$/cm^3)	I-value (eV)
Water	3.34	75[a]
Polystyrene	3.43	68.7[b]
CaCl$_2$ solution (23%)	3.97	91.2[b]

[a]From the ICRU report (Ref. 25).
[b]From the ICRU report (Ref. 25) and the Bragg additivity rule.

TABLE III. RMSE of electron density and I-values for standard tissues, including the thyroid tissue by different models.

| DECT Models	ρ_e (%)	I-value (%)
BVM	0.13	1.56
Yang tPFM	0.11	1.84
VCU tPFM	0.63	1.38
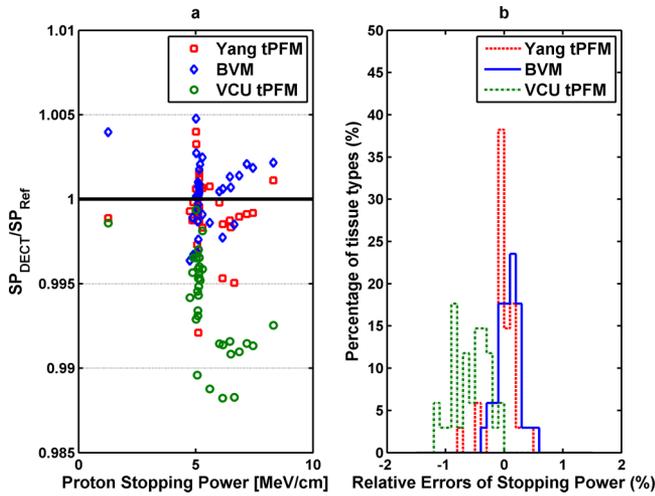
FIG. 5. (a) A comparison of errors in the stopping power predictions from different DECT models with reference values. The maximum relative error of prediction using the BVM was well below 0.5%. (b) The distribution of relative errors of the stopping power of 34 standard human tissues estimated by the BVM, Yang tPFM, and VCU tPFM is shown.

FIG. 7. The distribution of the relative proton range error with respect to reference values at 1 MeV for 34 standard human tissues with an initial proton energy at 175 MeV. Computation of the proton range was based on a CSDA approximation.

3.D. Range analysis of different DECT models

The distribution of the range prediction errors, defined by the difference between Eq. (4) and the ICRU report[35] for the 34 standard tissues, is shown in Fig. 7.

Figure 7 shows that along the proton path, the BVM predictions on the range of most tissues were well below 1 mm. The RMSEs for the proton range prediction of the BVM, Yang tPFM, and VCU tPFM were 0.26%, 0.25%, and 0.65%, respectively. The root-mean-square of CSDA range errors of the BVM, Yang tPFM, and VCU tPFM for 34 standard human tissues were 0.55, 0.52, and 1.40 mm.

3.E. DECT sensitivity to measurement uncertainties

Figure 8 shows the impact of image intensity uncertainties on electron densities, I-values, and stopping power estimated

by the BVM and VCU tPFM. Since the BVM and VCU tPFM models use the same monoenergetic approximation of CT spectra, the Yang tPFM is excluded from the sensitivity study.

The electron density and stopping power in Fig. 8 show that the BVM is slightly more sensitive to image uncertainty than the VCU tPFM, especially for low level of image uncertainties. The BVM showed less susceptibility to image uncertainties in estimating I-value than the VCU tPFM did possibly due to the implementation of the empirical correction function f_I.

In contrast to low-energy photon cross section imaging,[16] stopping power images are much less sensitive to image uncertainty. Uncertainties less than 1% (coverage factor of 1) can be achieved using acquisition protocols at the limit of commercial capability, around 0.3% and 0.6% for the high- and low-energy scans, respectively.

3.F. Dependence of QDECT accuracy on tissue composition

Figures 9(a) and 9(b) show the relative error estimated for 175 MeV of stopping power by the BVM and VCU tPFM models for hypothetical adipose-like tissues over the range of lipid and water concentrations in table. The relative errors for adipose-like tissues were below 0.8% for the BVM, while the VCU tPFM had a slightly larger maximum error of 1%, primarily because of its larger errors in predicting electron densities.

Figures 9(c) and 9(d) show that the BVM and tPFM models' prediction errors for muscle-like tissues were insensitive to variations in lipid and water mass fractions for constant protein and mineral ash mass fractions, with a maximum error of 0.8%. The BVM performs better than the tPFM model. In the case of bony tissues, Figs. 9(e) and 9(f) show that in BVM stopping power predictions, trabecular bone was not sensitive to the variation in composition. The errors were all


FIG. 6. The ratio of stopping power estimation by the BVM and VCU tPFM, respectively, to the reference value of in the energy range from 5 to 300 MeV.
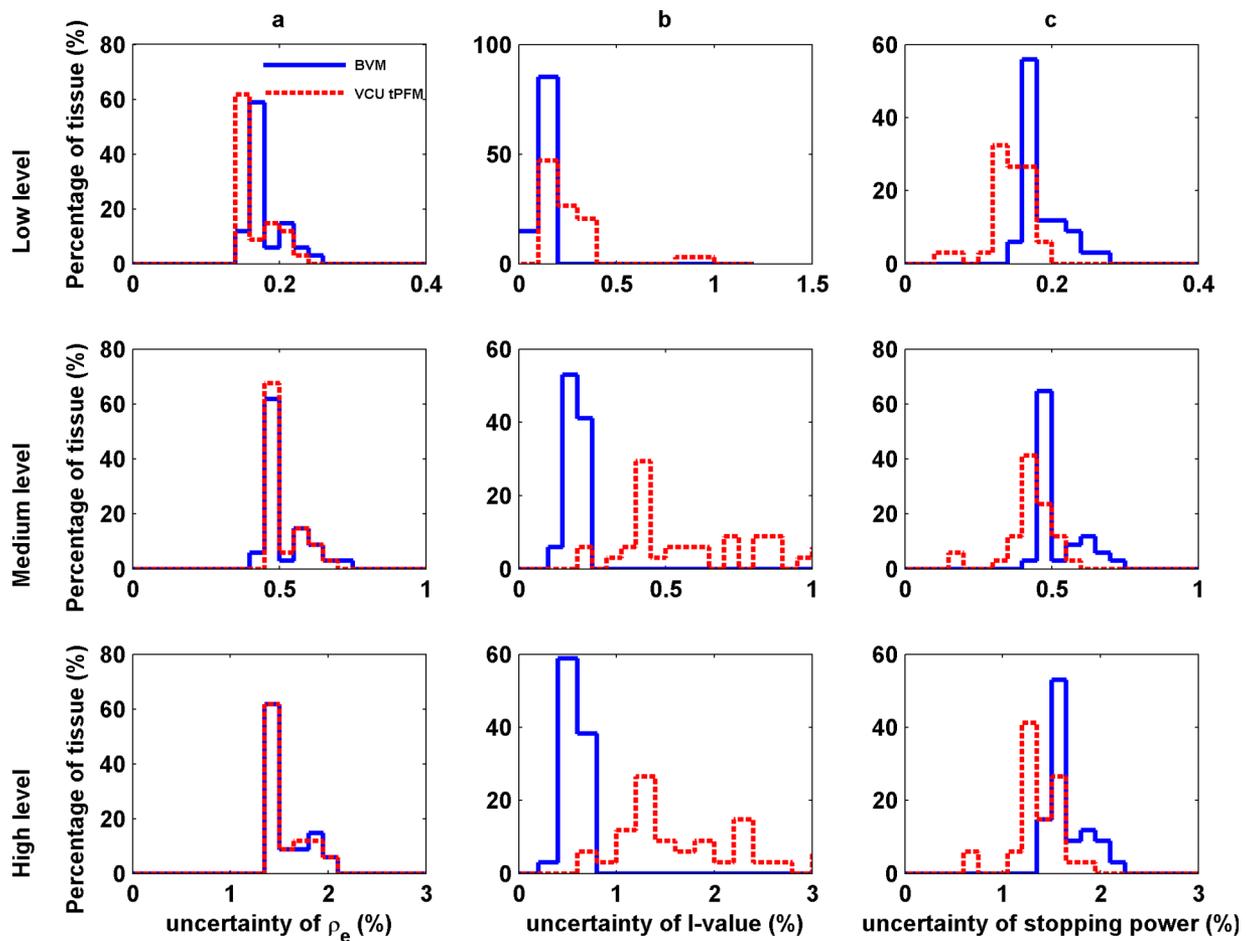
FIG. 8. The distribution of the uncertainties of 34 standard human tissues in electron density (a), I-values (b), and stopping power (c) from three different CT image uncertainty levels (low-, medium-, and high-level): top row: low level 0.2% and 0.1%; middle row: medium level 0.6% and 0.3%; and bottom row: high level 1.5% and 1.0%.

well below 0.8%, which was better than the performance of the tPFM model.

The results of this study demonstrate that both the BVM and nonseparable parametric models maintain good accuracy over a wide range of assumed bony and soft tissue compositions that were not included in the original ICRU training dataset from ICRU reports.

4. DISCUSSION

Overall, our results demonstrate that our simple linear, separable BVM model achieved stopping power estimation accuracy that is comparable to the more complex Yang tPFM at 175 MeV. Preliminary results also show that the achieved accuracy is independent of energy for adipose, muscle, and cortical bone down to low proton energies of 30 MeV. Compared to our implementation of the parametric fit model, the BVM can achieve improved accuracy in stopping power estimation: 0.20% compared to 0.68%. The mean absolute error of electron density 0.08% (excluding the thyroid tissue) was obtained by using the BVM model. This is also comparable to the DECT stoichiometric algorithm proposed by Bourque et al.,[11] which showed that the mean absolute

error of electron density is 0.08% for standard human tissues excluding the thyroid tissue. It should be noted that in this study, the accuracy of the proton stopping power estimation was evaluated in an idealized scenario. Thus, the accuracy claimed in this paper may not be achieved at clinically acceptable patient doses using currently available CT systems.

The errors reported here are smaller than those reported by investigators who have experimentally implemented DECT-based postprocessing imaging of stopping power ratio.[11–13] For example, Hünemohr et al.[13] reported that water equivalent path length (WEPL) residuals of tissue surrogates were greatly decreased from −1.0%±1.8% by SECT stoichiometric calibration to −0.1%±0.7% by DECT calibration. Bourque et al.[11] showed that the mean absolute error of the proton stopping power was about 0.5%±0.4% for the Gammex 467 phantom by DECT stoichiometric calibration. These errors are influenced by uncertainties in image intensity uniformity and noise; composition of the phantom substitute; and the I-value as well as two-parameter model prediction error, which is the sole focus of this paper.

As noted in our Introduction, iterative image reconstruction algorithms with integrated beam hardening corrections based on known scanning beam photon spectra require accurate estimation of the linear attenuation coefficient as a function
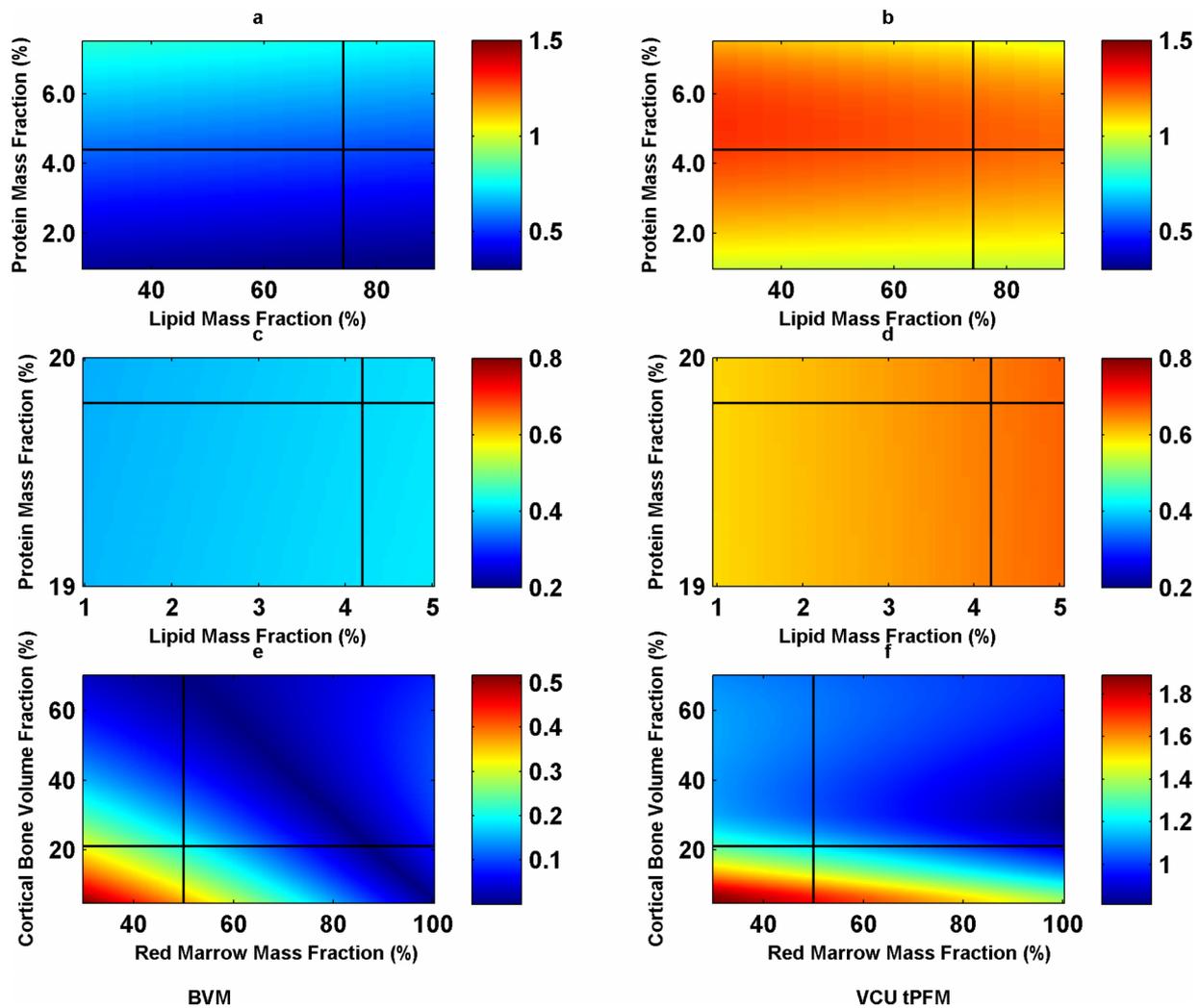
FIG. 9. The relative error distribution of adipose-like [(a) and (b)] and muscle-like [(c) and (d)] stopping power at 175 MeV as a function of lipid and water mass fractions for constant mass fractions of 0.3% and 0.9% ash was predicted by BVM [(a) and (c)] and the VCU tPFM [(b) and (d)], respectively. The relative errors distribution of trabecular bone [(e) and (f)] stopping power are predicted by BVM (e) and VCU tPFM (f) by varying cortical volume (5%–70%), and red marrow mass fraction over the range of 30%–100%. Note the difference in the color bar scale in (e) and (f). The black cross corresponds to ICRU report 44 (Ref. 24) published values of adipose, muscle, and spongiosa composition.

of energy. Previously, our group has demonstrated that 1% modeling accuracy can be achieved with the BVM in the 20–1000 keV energy range.[16] In contrast, the PFM model, which is utilized by the stoichiometric method[9] and its DECT extensions,[11] predicted the NIST XCOM (Ref. 29) cross sections in the $Z = 2$–20 range much less accurately, mainly due to the energy dependence of the atomic number exponent in the PFM photoelectric absorption term. The experimentally implemented postprocessing DECT SPR mapping processes recognize the limitation of the PFM,[11] using it only to predict the dependence of $HU_{S_k,x}$ intensities on Z^* by performing spectrum-averaged PFM fits to scans of substance of known composition. Hence, this class of experimentally implemented, postprocessing cross section models is not relevant to the implementation of iterative polyenergetic DECT reconstruction algorithms since the former are limited to predicted spectrally averaged cross sections.

Our study was based on ICRU recommended I-value and electron densities. The error propagation analysis in this study did not include I-value measurement uncertainty. The BVM model predictions were not expected to be sensitive to these assumed values, provided that basis and training set materials used consistent parameter values. Also both the BVM and tPFM include correction terms that explicitly accounted for I-value prediction errors. On the other hand, if I-values of actual patient tissues and physical phantom substitute deviate from their assumed ICRU values, the DECT stopping power images predicted by any two-parameter model will deviate from physical reality. Besemer et al.[36] noted that liquid water I-value measurements span a range of approximately ±12% which corresponds to stopping power uncertainties of approximately ±0.8%.[37]

The accuracies achieved by the two-parameter models in this study were evaluated at the energy pair 90 and 140 kVp. It should also be noted that by adding additional tin filtration for more separation between low and high effective energies, the prediction accuracy can be increased. For example, by using the approximating effective energy of 140 kVp with

0.5 mm thick tin filter as 90 and 90 kVp spectra as 45 keV, the RMSEs of the stopping power estimation for 34 standard human tissues by the VCU tPFM were 0.28%.

The BVM has several advantages over other tPFM models. First is economic computation cost; there is no need to solve nonlinear equations for Z^* and electron density iteratively. As mentioned by Williamson *et al.*,[16] the tPFM and other nonlinear DECT models cannot be factorized into atomic number- and energy-independent terms. To test the efficiencies of the BVM and tPFM DECT models, the single CPU processing time was assessed by MATLAB (version 12.0, The Math Works, Inc., Natick, MA) on a Windows 7® 64-bit machine with Intel Core i5 3.2 GHz and 16 GB RAM. For 34 standard human tissues, it took the BVM 0.77 s to complete the analysis, while for the VCU tPFM, the computing time was approximately 73.7 s. These results indicated that this simple linear BVM model increases the computational efficiency about 100-fold in this software environment. It is worth noting that the efficiency analysis and comparison were from the BVM and tPFM models that were not optimized. The additional computational burden could be an issue in the context of iterative, model-based reconstruction algorithm. Second, the computational advantage of the BVM is obtained without compromising accuracy, even a small margin of accuracy, relative to the tPFM models.

To our knowledge, this study is the first to estimate proton stopping power using a linear BVM model in the context of idealized DECT stopping power imaging. In order to fairly compare the BVM stopping power estimation to the tPFM model, we implemented our own VCU tPFM model using similar materials and cross sections as Yang *et al.* did. Yang *et al.* pointed out that the mean errors of the calculated EDR (electron density ratio to water) and Z^* were 0.16% and 0.79%, excluding the thyroid tissue. However, in our implementation of the tPFM, the corresponding mean relative errors were 0.57% and 0.70%. Landry *et al.*[38] presented a DECT parameterization model that related a ratio of linear attenuation at energies of 80 and 140 kVp, yielding accuracies of less than 0.3 units of Z_{std} for the Gammex phantom. Saito[39] proposed a model that the electron density can be expressed by the weighted of the low and high kVp CT numbers. The achieved theoretical absolute error for electron density estimation is less than 0.7% for calibration phantoms.

Our work also suggests that $c_1/(c_1+c_2)$ is a useful surrogate for Z^* on charged particle-beam dosimetry. Figure 10 indicates that, without knowledge of the effective atomic number, I-values closely adhere to a linear function of $c_1/(c_1+c_2)$. The RMSE of using the relationship in Fig. 10 to estimate I-values for the proton stopping power for the same standard human tissues at 175 MeV is 0.19%, which is close to the results of 0.20% achieved using linear combination and correction method for I-values estimation for proton stopping power.

Our proposed method of robustness analysis considered the large possible ranges of variation of tissue elemental composition data, which are believed to vary significantly for the same individuals at different ages, or in different health states, as well as between different individuals. For example,
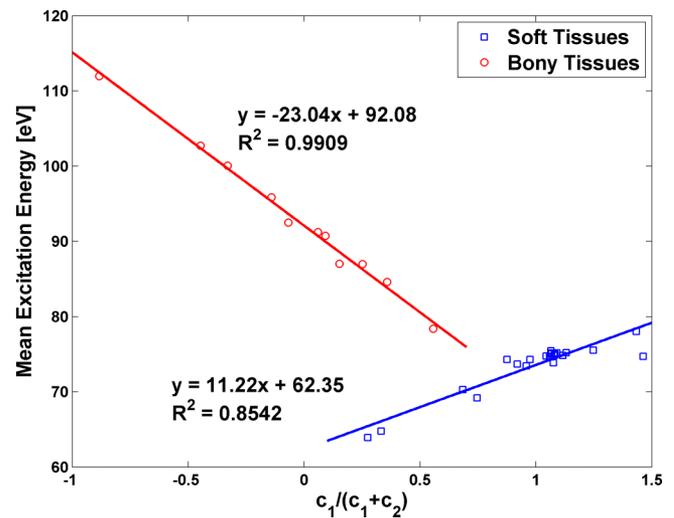
FIG. 10. The relationship between $c_1/(c_1+c_2)$ and the I-values of 34 standard human tissue is shown. There are two separate linear fits, one for soft tissues and one for bony tissues. This relationship provides an alternative method to estimate I-value without knowing the Z^* of the substances.

red marrow (consisting primarily of hematopoietic cells) in the skeletal tissues can convert into yellow marrow (consisting mainly of adipocytes) with advancing age. ICRU report 44 (Ref. 24) recommends modeling spongiosa as 33% cortical bone and 67% bone marrow tissues, dividing equally between red and yellow marrow by mass fraction as an approximation for humans of all ages. However, in the newborn, marrow tissue is nearly 100% red marrow, whereas in adult patients, the fraction of red vs fatty yellow marrow gradually decreases, falling to near zero in the medullary cavities of the long bones, and approaching the range of 25%–70% (Ref. 40) for elderly male patients. Another example is adipose-like tissue which is composed of an extracellular matrix supporting adipocytes. The components can have widely varying mass fractions of lipid (60%–90%)[31] and water (31%–9%),[31] leading to large variations in the relative number of carbon and oxygen atoms. Our robustness analysis showed that the BVM model predictions were not sensitive to the variation in compositions.

Our preliminary study of error propagation is the first investigation of the sensitivity of the proton stopping power calculation in DECT models. Although the experimental image intensity uncertainties characteristic of a clinical scanner are not available, our results indicated that DECT models' estimation of proton stopping power are susceptible to image uncertainties and that the acceptable accuracy may not be achievable in current clinical settings. The one-to-one correspondence between the linear attenuation coefficient and proton stopping power may be affected by the uncertainties of CT measurements, including scattering and beam hardening, which may add another 1% to the measurement of uncertainty. This indicates that a more advanced algorithm may be needed to account for reduction of uncertainties in the CT image reconstruction.

It is also worth mentioning that as photon counting detector techniques develop,[20,41,42] our proposed method can still find

merit in energy discrimination spectral CT, in which a single scan for material decomposition is allowed.

5. CONCLUSION

We have developed a simple, linear, separable two-parameter DECT model that can estimate electron density and *I*-value and derive proton stopping power accurately. It supported electron density and *I*-value estimates with a RMSE of 0.13% and 1.56%, respectively, which yielded stopping power estimates for ICRU recommended tissue compositions with an accuracy of 0.20%. The root-mean-square error of the CSDA range prediction error of the BVM was 0.55 mm for protons with an initial energy of 175 MeV. The reported accuracy in this study may not be achievable on current clinical CT scanners. It is also worth noting that the estimated accuracy of the proton stopping power by DECT models was independent of the choice of reference values. The BVM and tPFM were found to be insensitive to variations in tissue compositions recommended by ICRU reports in proton stopping power estimation. The tPFM model showed less sensitivity to CT image uncertainties in proton stopping power estimation. Our BVM model achieved comparable accuracy with less computational cost than competing nonlinear DECT models. To our knowledge, our BVM model is the first separable, two-parameter model with a closed form numerical solution that is able to model proton stopping powers with high accuracy.

ACKNOWLEDGMENTS

a)Author to whom correspondence should be addressed. Electronic mail: radon.han@gmail.com

[1]R. A. Rutherford, B. R. Pullan, and I. Isherwood, "Measurement of effective atomic number and electron density using an EMI scanner," Neuroradiology **11**, 15–21 (1976).

[2]M. M. Goodsitt, P. Hoover, M. S. Veldee, and S. L. Hsueh, "The composition of bone marrow for a dual-energy quantitative computed tomography technique," Invest. Radiol. **29**, 695–704 (1994).

[3]C. E. Cann, "Quantitative CT for determination of bone mineral density: A review," Radiology **166**(2), 509–522 (1988).

[4]T. R. C. Johnson, B. Krauß, M. Sedlmair, M. Grasruck, H. Bruder, D. Morhard, C. Fink, S. Weckbach, M. Lenhard, B. Schmidt, T. Flohr, M. F. Reiser, and C. R. Becker, "Material differentiation by dual energy CT: Initial experience," Eur. Radiol. **17**(6), 1510–1517 (2007).

[5]J. D. Evans, B. R. Whiting, J. A. O'Sullivan, D. G. Politte, P. H. Klahr, Y. Yu, and J. F. Williamson, "Prospects for *in vivo* estimation of photon linear attenuation coefficients using postprocessing dual-energy CT imaging on a commercial scanner: Comparison of analytic and polyenergetic statistical reconstruction algorithms," Med. Phys. **40**(12), 121914 (16pp.) (2013).

[6]M. Yang, G. Virshup, J. Clayton, X. R. Zhu, R. Mohan, and L. Dong, "Theoretical variance analysis of single- and dual-energy computed tomography methods for calculating proton stopping power ratios of biological tissues," Phys. Med. Biol. **55**, 1343–1362 (2010).

[7]M. Bazalova, J. F. Carrier, L. Beaulieu, and F. Verhaegen, "Dual-energy CT-based material extraction for tissue segmentation in Monte Carlo dose calculations," Phys. Med. Biol. **53**, 2439–2456 (2008).

[8]U. Schneider, P. Pemler, J. Besserer, E. Pedroni, A. Lomax, and B. Kaser-Hotz, "Patient specific optimization of the relation between CT-Hounsfield

units and proton stopping power with proton radiography," Med. Phys. **32**(1), 195–199 (2005).

[9]U. Schneider, E. Pedroni, and A. Lomax, "The calibration of CT Hounsfield units for radiotherapy treatment planning," Phys. Med. Biol. **41**, 111–124 (1996).

[10]M. Torikoshi, T. Tsunoo, M. Sasaki, M. Endo, Y. Noda, Y. Ohno, T. Kohno, K. Hyodo, K. Uesugi, and N. Yagi, "Electron density measurement with dual-energy x-ray CT using synchrotron radiation," Phys. Med. Biol. **48**, 673–685 (2003).

[11]A. E. Bourque, J. F. Carrier, and H. Bouchard, "A stoichiometric calibration method for dual energy computed tomography," Phys. Med. Biol. **59**, 2059–2088 (2014).

[12]N. Hünemohr, B. Krauss, C. Tremmel, B. Ackermann, O. Jäkel, and S. Greilich, "Experimental verification of ion stopping power prediction from dual energy CT data in tissue surrogates," Phys. Med. Biol. **59**, 83–96 (2014).

[13]N. Hünemohr, B. Krauss, J. Dinkel, C. Gillmann, B. Ackermann, O. Jäkel, and S. Greilich, "Ion range estimation by using dual energy computed tomography," Z. Med. Phys. **23**(4), 300–313 (2013).

[14]G. Landry, K. Parodi, J. E. Wildberger, and F. Verhaegen, "Deriving concentrations of oxygen and carbon in human tissues using single- and dual-energy CT for ion therapy applications," Phys. Med. Biol. **58**, 5029–5048 (2013).

[15]N. Hünemohr, H. Paganetti, S. Greilich, O. Jäkel, and J. Seco, "Tissue decomposition from dual energy CT data for MC based dose calculation in particle therapy," Med. Phys. **41**, 061714 (14pp.) (2014).

[16]J. F. Williamson, S. Li, S. Devic, B. R. Whiting, and F. A. Lerma, "On two-parameter models of photon cross sections: Application to dual-energy CT imaging," Med. Phys. **33**, 4115–4129 (2006).

[17]G. H. Chen, J. Tang, and S. Leng, "Prior image constrained compressed sensing (PICCS): A method to accurately reconstruct dynamic CT images from highly undersampled projection data sets," Med. Phys. **35**, 660–663 (2008).

[18]J. D. Evans, B. R. Whiting, D. G. Politte, J. A. O'Sullivan, P. F. Klahr, and J. F. Williamson, "Experimental implementation of a polyenergetic statistical reconstruction algorithm for a commercial fan-beam CT scanner," Phys. Med. **29**, 500–512 (2013).

[19]Y. Chen, J. A. O'Sullivan, D. G. Politte, J. D. Evans, D. Han, B. R. Whiting, and J. F. Williamson, "Line integral alternating minimization algorithm for dual-energy x-ray CT image reconstruction," IEEE Trans. Med. Imaging **PP**, 1 (2015), see http://ieeexplore.ieee.org/xpl/articleDetails.jsp?arnumber=7298440.

[20]R. E. Alvarez and A. Macovski, "Energy-selective reconstructions in x-ray computerized tomography," Phys. Med. Biol. **21**(5), 733–744 (1976).

[21]D. Han, A. Sampson, D. Politte, J. O'Sullivan, J. Siebers, and J. F. Williamson, "Accuracy of dual-energy CT photon cross-section mapping using a non-separable two parameter cross-section model," Med. Phys. **39**(6), 3989 (2012).

[22]H. Bethe, "Zur theorie des durchgangs schneller korpuskularstrahlen durch materie," Ann. Phys. **397**, 325–400 (1930).

[23]ICRU, "Photon electron proton and neutron interaction data for body tissues," Report No. 46 (ICRU, Bethesda, MD, 1992).

[24]ICRU, "Tissue substitutes in radiation dosimetry and measurement," Report No. 44 (ICRU, Bethesda, MD, 1989).

[25]ICRU, "Stopping powers for electrons and positrons," Report No. 37 (ICRU, Bethesda, MD, 1984).

[26]D. R. Warren, M. Partridge, M. A. Hill, and K. Peach, "Improved calibration of mass stopping power in low density tissue for a proton pencil beam algorithm," Phys. Med. Biol. **60**, 4243–4261 (2015).

[27]R. A. Rutherford, B. R. Pullan, and I. Isherwood, "Calibration and response of an EMI scanner," Neuroradiology **11**, 7–13 (1976).

[28]J. B. Weaver and A. L. Huddleston, "Attenuation coefficients of body tissues using principal-components analysis," Med. Phys. **12**(1), 40–45 (1985).

[29]M. J. Berger, J. H. Hubbell, S. M. Seltzer, J. Chang, J. S. Coursey, R. Sukumar, D. S. Zucker, and K. Olsen, XCOM: Photon Cross Section Database, Version 1.5, National Institute of Standards and Technology, Gaithersburg, MD, 2010.

[30]D. R. White, H. Q. Woodard, and S. M. Hammond, "Average soft-tissue and bone models for use in radiation dosimetry," Br. J. Radiol. **60**, 907–913 (1987).

[31]H. Q. Woodard and D. R. White, "The composition of body tissues," Br. J. Radiol. **59**, 1209–1219 (1986).

[32]D. R. White, E. M. Widdowson, H. Q. Woodard, and J. W. T. Dickerson, "The composition of body tissues. (II) Fetus to young adult," Br. J. Radiol. **64**, 149–159 (1991).

[33]J. Brožek, F. Grande, J. T. Anderson, and A. Keys, "Densitometric analysis of body composition: Revision of some quantitative assumptions," Ann. N. Y. Acad. Sci. **110**, 113–140 (1963).

[34]B. N. Taylor and C. E. Kuyatt, "Guidelines for evaluating and expressing the uncertainty of NIST measurement results," NIST Technical Note 1297 (U.S. Government Printing Office, Washington, DC, 1994).

[35]ICRU, "Stopping powers and ranges for protons and alpha-particles," Report No. 49 (ICRU, Bethesda, MD, 1993).

[36]A. Besemer, H. Paganetti, and B. Bednarz, "Clinical impact of uncertainties in the mean excitation energy of human tissues during proton therapy," Phys. Med. Biol. **58**, 887–902 (2013).

[37]P. Andreo, "On the clinical spatial resolution achievable with protons and heavier charged particle radiotherapy beams," Phys. Med. Biol. **54**, N205–N215 (2009).

[38]G. Landry, J. Seco, M. Gaudreault, and F. Verhaegen, "Deriving effective atomic numbers from DECT based on a parameterization of the ratio of high and low linear attenuation coefficients," Phys. Med. Biol. **58**, 6851–6866 (2013).

[39]M. Saito, "Potential of dual-energy subtraction for converting CT numbers to electron density based on a single linear relationship," Med. Phys. **39**(4), 2021–2030 (2012).

[40]M. Cristy, "Active bone marrow distribution as a function of age in humans," Phys. Med. Biol. **26**, 389–400 (1981).

[41]P. M. Shikhaliev and S. G. Fritz, "Photon counting spectral CT versus conventional CT: Comparative evaluation for breast imaging application," Phys. Med. Biol. **56**, 1905–1930 (2011).

[42]J. P. Schlomka, E. Roessl, R. Dorscheid, S. Dill, G. Martens, T. Istel, C. Bäumer, C. Herrmann, R. Steadman, G. Zeitler, A. Livne, and R. Proska, "Experimental feasibility of multi-energy photon-counting K-edge imaging in pre-clinical computed tomography," Phys. Med. Biol. **53**, 4031–4047 (2008).

Appendix II

Technical Note: On the accuracy of parametric two-parameter photon cross-section models in dual-energy CT applications

Technical Note: On the accuracy of parametric two-parameter photon cross-section models in dual-energy CT applications

Dong Han[a)] and Mariela A. Porras-Chaverri
Medical Physics Graduate Program, Department of Radiation Oncology, Virginia Commonwealth University, Richmond, VA 23298, USA

Joseph A. O'Sullivan
Department of Electrical and Systems Engineering, Washington University, St. Louis, MO 63130, USA

David G. Politte
Electronic Radiology Laboratory, Mallinckrodt Institute of Radiology, Washington University School of Medicine, St. Louis, MO 63110, USA

Jeffrey F. Williamson[a)]
Medical Physics Graduate Program, Department of Radiation Oncology, Virginia Commonwealth University, Richmond, VA 23298, USA

Purpose: To evaluate and compare the theoretically achievable accuracy of two families of two-parameter photon cross-section models: basis vector model (BVM) and modified parametric fit model (mPFM).

Method: The modified PFM assumes that photoelectric absorption and scattering cross-sections can be accurately represented by power functions in effective atomic number and/or energy plus the Klein-Nishina cross-section, along with empirical corrections that enforce exact prediction of elemental cross-sections. Two mPFM variants were investigated: the widely used Torikoshi model (tPFM) and a more complex "VCU" variant (vPFM). For 43 standard soft and bony tissues and phantom materials, all consisting of elements with atomic number less than 20 (except iodine), we evaluated the theoretically achievable accuracy of tPFM and vPFM for predicting linear attenuation, photoelectric absorption, and energy-absorption coefficients, and we compared it to a previously investigated separable, linear two-parameter model, BVM.

Results: For an idealized dual-energy computed tomography (DECT) imaging scenario, the cross-section mapping process demonstrates that BVM more accurately predicts photon cross-sections of biological mixtures than either tPFM or vPFM. Maximum linear attenuation coefficient prediction errors were 15% and 5% for tPFM and BVM, respectively. The root-mean-square (RMS) prediction errors of total linear attenuation over the 20 keV to 1000 keV energy range of tPFM and BVM were 0.93% (tPFM) and 0.1% (BVM) for adipose tissue, 0.8% (tPFM) and 0.2% (BVM) for muscle tissue, and 1.6% (tPFM) and 0.2% (BVM) for cortical bone tissue. With exception of the thyroid and Teflon, the RMS error for photoelectric absorption and scattering coefficient was within 4% for the tPFM and 2% for the BVM. Neither model predicts the photon cross-sections of thyroid tissue accurately, exhibiting relative errors as large as 20%. For the energy-absorption coefficients prediction error, RMS errors for the BVM were less than 1.5%, while for the tPFM, the RMS errors were as large as 16%.

Conclusion: Compared to modified PFMs, BVM shows superior potential to support dual-energy CT cross-section mapping. In addition, the linear, separable BVM can be more efficiently deployed by iterative model-based DECT image-reconstruction algorithms. © *2017 American Association of Physicists in Medicine* [https://doi.org/10.1002/mp.12220]

Key words: computed tomography, dual-energy, photon cross-section

1. INTRODUCTION

Two-parameter photon cross-section models are used in quantitative dual-energy computed tomography (QDECT) to describe monoenergetic or spectrally averaged linear attenuation coefficients and other radiological quantities as functions of two independent parameters. Two commonly used two-parameter representations are effective atomic number (Z^*) and electron density (ρ_e^*) or alternatively, the weights of two dissimilar basis materials with known linear attenuation coefficients. The utility of a given two-parameter model in QDECT depends on the accuracy with which it predicts photon cross-sections. The domain within which high prediction accuracy is required depends on the application. For example, the DECT stoichiometric technique[1] for postreconstruction mapping of electron density and mean excitation energy for proton therapy requires only that the model predict spectrally averaged linear attenuation coefficients in the diagnostic CT energy range. On the other hand, model-based CT image-reconstruction algorithms[2–6] that incorporate higher order

beam-hardening corrections require that the model accurately predict monoenergetic linear attenuation coefficients across the entire diagnostic X-ray energy range, while using QDECT to support Monte Carlo-based treatment planning for low-energy brachytherapy requires high accurate monoenergetic predictions down to 20 keV for partial cross-sections, differential cross-sections, and energy-absorption coefficients as well as total linear attenuation coefficients.[7,8]

Our work has previously demonstrated that one particular two-parameter model, the linear basis vector model (BVM),[9,10] is able to recover monoenergetic photon cross-sections[9] and charged particle stopping powers[11] with mean absolute errors less than 0.5%. However, the most widely used model in the QDECT cross-section imaging literature is the parametric fit model (PFM), first introduced by Spiers[12] and Mayneord.[13] PFM postulates that cross-sections can be accurately represented by nonlinear, nonseparable functions of Z^* and ρ_e^*. The variant used in many QDECT applications[14,15] is a modified version (tPFM), introduced by Torikoshi et al.,[16] tPFM simplifies the Spiers[12] model and adds table-based corrections that enforce exact prediction of elemental monoenergetic linear attenuation coefficients.[14] However, to date, no one has assessed the accuracy with which the tPFM is able to predict monoenergetic photon cross-sections for mixtures and compounds representing the range of tissue compositions encountered in normal mammalian anatomy. The purpose of this note is to compare the theoretical accuracy of the modified PFM and BVM for predicting linear attenuation coefficients, partial cross-sections, and energy-absorption coefficients in the 20–1000 keV energy range for such biological tissues or tissue substitutes.

2. METHODS AND MATERIALS

We evaluated photon cross-section prediction accuracy of BVM and tPFM in the energy range from 20 keV to 1000 keV, along with a more complex modified PFM that we call the "VCU modified parametric fit model" (vPFM). The photon cross-sections in this study included the total linear attenuation, photoelectric effect, scattering, and energy-absorption coefficients, all as function of energy E. The model accuracy was evaluated for 43 tissues and tissue substitutes with elemental compositions recommended by ICRU,[17,18] ICRP,[19] or other references,[20] in terms of mean percent relative error in the lower energy range (20 keV to 50 keV), and higher (50 keV to 1000 keV) energy ranges. The reference photon cross-sections data were calculated applying the mixture rule to elemental cross-sections from the NIST XCOM library.[21] All of the computational methods utilized in this work were implemented in MATLAB environment (version 12.0, The Math Works Inc., Natick, MA, USA) on a Windows 7 PC.

2.A. Description of two-parameter models

The BVM model assumes that the photon cross-sections of both mixtures and elemental substances can be approximated by a linear combination of two dissimilar basis

materials. For example, the total linear attenuation of an unknown tissue at energy E (20 keV ≤ E ≤ 1000 keV), position **x** can be written in the following form

$$\mu(\mathbf{x}, E) = c_1(\mathbf{x})\mu_1(E) + c_2(\mathbf{x})\mu_2(E) \tag{1}$$

where **x** refers to the image voxel location and μ_i(E) (i = 1,2) denotes the linear attenuation coefficient of the i-th basis material in the pure form. In this work, a water-polystyrene pair was chosen for soft tissues, while a water-$CaCl_2$ solution (23% concentration) pair was used for bony tissues.[9] The details, including criteria for basis pair choice of tissues, are discussed elsewhere.[9] $c_i(\mathbf{x})$ images from DECT imaging were computed from low (90 kVp) and high (140 kVp + tin filter) energy scanning spectra approximated by effective energies 45 keV and 90 keV.[11] The photoelectric and scattering cross-sections were also computed by using the $c_i(\mathbf{x})$ images.[9]

Torikoshi et al.[16] proposed a nonseparable parametric fit model (tPFM) by assuming that the total linear attenuation coefficient is a function of electron density ρ_e^* and effective atomic number Z^*

$$\mu(\mathbf{x}, E, \rho_e, Z^*)_{tPFM} = \rho_e(\mathbf{x})\left(Z^{*4}(\mathbf{x})F(E, Z^*) + G(E, Z^*)\right) \tag{2}$$

where the first and second right-hand terms represent photoelectric absorption and scattering, respectively. The functions $F(E, Z^*)$ and $G(E, Z^*)$ are precalculated correction terms that force Eq. (2) to exactly recover the elemental linear attenuation coefficients for the elements (Z = 2 to 20) on the discrete logarithmic energy grid specified in the XCOM database. For mixtures of elemental materials, Z^* may assume noninteger values. The nonlinear Eq. (2) can be solved iteratively for the idealized DECT scenario where there is exact knowledge of total linear attenuation coefficient at two discrete effective energies (45 keV and 90 keV) for each voxel.

Our vPFM approach combines the more detailed Spiers[12] PFM with elemental correction tables introduced by Torikoshi.[16] We hypothesized that the more complete parametric model would support more accurate interpolation for intermediate E and Z^* values, thereby improving the prediction accuracy for mixtures and compounds.

$$\mu(E, Z^*, \rho_e)_{vPFM} = \rho_e \cdot \left[a \cdot \frac{Z^{*b}}{E^c} \cdot F'(E, Z^*) \right. \\ \left. + \left(\sigma_{KN}^e(E) + d \cdot \frac{Z^{*e}}{E^f} \right) \cdot G'(E, Z^*) \right] \tag{3}$$

where we have dropped the spatial coordinate, **x,** for simplicity. The energy- and position independent *a-f* are the best-fit parameters which maximize the accuracy with which PFM predicts the elemental photoelectric effect and total scattering cross-sections (NIST XCOM) for $2 \leq Z \leq 20$ and $20 \leq E \leq 1000$ keV without the empirical correction factors. $F'(E, Z^*)$ and $G'(E, Z^*)$ are derived by comparing best-fit PFM predictions to the known XCOM cross-sections. Since

the prediction accuracy of tPFM and vPFM were so similar, detailed results only for the former are presented.

Monte Carlo simulations often require the linear energy-absorption coefficient, $\mu_{en}(\mathbf{x}, E)$. This quantity also serves as a useful surrogate for absorbed dose[9] in the approximation where energy impartation is dominated by first-order photon collisions. For elements, $\mu_{en}(E, Z)$ is given by

$$\mu_{en}(E, Z) = \rho_e \left[\sigma_{KN} \left(1 - \frac{\overline{E_{sca,KN}}}{E} \right) \right.$$
$$\left. + \sigma_{PE} \left(1 - \frac{E - P_K \cdot E_K \cdot \omega_K}{E} \right) \right] \cdot (1 - g_K)$$

(4)

where σ_{KN} and σ_{PE} denote Klein-Nishina and photoelectric cross-sections, respectively, per electrons; $\bar{E}_{sca,KN}$ is the average energy scattered per collision; and P_K, E_K and ω_K denote the K-shell vacancy probability, binding energy and fluorescent yield, respectively. The quantities of $P_K \cdot E_K$ and are functions of effective atomic numbers; linear interpolation between their elemental values is used to evaluate $\mu_{en}(E, Z^*)$ at noninteger Z^* values. The average fraction of the secondary charged particle energy that is subsequently lost in radiative process is denoted by g_k. Photon energy of interest in this note is assumed greater than the shell binding energy. The dose calculation error introduced by tPFM can be approximated by Eq. (4)

Once $c_i(\mathbf{x})$ $(c_1(\mathbf{x}), c_2(\mathbf{x}))$ and $(Z^*(\mathbf{x}), \rho_e(\mathbf{x}))$ pairs have been determined, the mean relative error of photon cross-sections prediction error for the *j*-th tissue can be written as

Root-mean-square Error(%) $= 100\%$

$$\times \left[\sum_{i=1}^{N} \left(1 - \frac{\mu_{i,\Delta,DECT}(E)}{\mu_{i,\Delta,ref}(E)} \right)^2 \Big/ N \right]^{1/2}_{\Delta=Tot,PE,EN}$$

(5)

$\Delta = Tot, PE$, and EN represent total linear, photoelectric absorption, and energy-absorption coefficients, respectively. The subscript "ref" refers to the ground truth values derived from the XCOM library.[21]

3. RESULTS

3.A. Estimation error by the BVM and tPFM

Figure 1 shows the BVM and tPFM root-mean-square (RMS) prediction errors of total cross-section estimation as functions of effective atomic number derived from tPFM model for the low $20 \leq E \leq 50$ keV and high $50 \leq E \leq 1000$ keV energy ranges. The BVM model outperforms the tPFM, achieving RMS errors of less about 0.5% and 0.1% for the low- and high-energy ranges, respectively, except for Teflon and inflated lung tissues. At low energies, tPFM predictions exhibit RMS errors over 1% for most tissues and up to 2% for tissue substitutes (phantom materials) with RMS errors are less than 0.6% at higher energies. The
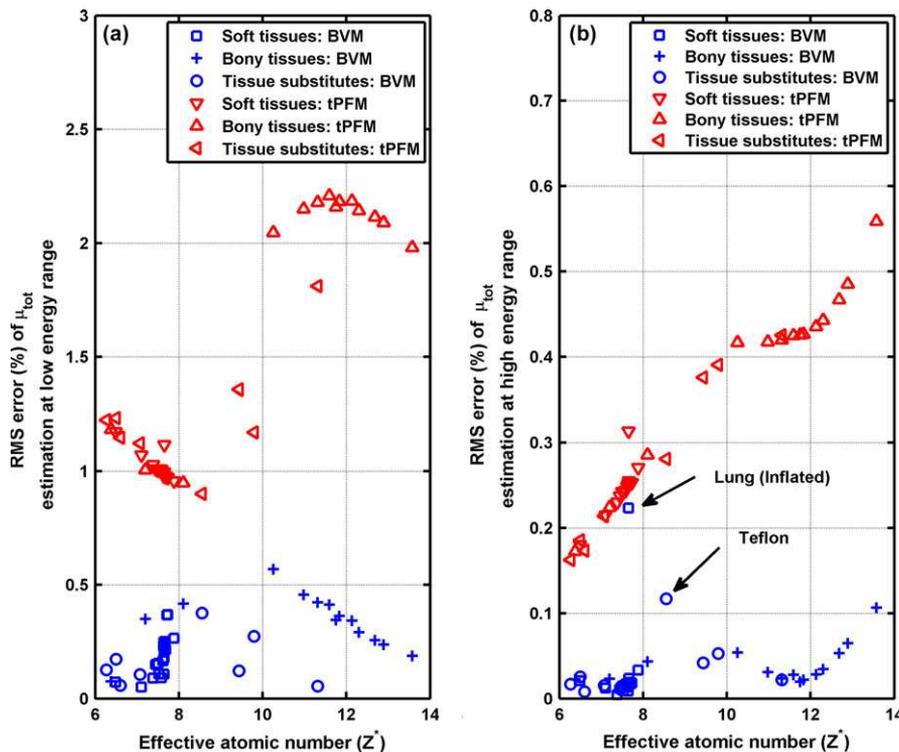
FIG. 1. Percent RMS error of the total linear attenuation coefficient predicted by BVM or tPFM for 43 tissues and phantom substitutes as functions of tPFM effective atomic number for the (a) $20 \leq E \leq 50$ keV and (b) $50 \leq E \leq 1000$ keV energy ranges. The thyroid tissue prediction error is outside the plotting range of the low-energy plot. [Color figure can be viewed at wileyonlinelibrary.com]

tPFM prediction errors are generally larger for bony tissues. Due to its high iodine content (0.1% by weight with $Z = 53$), both BVM and tPFM fail to accurately model the thyroid tissue cross-sections, with errors as large as 7.9% and 7.7%, respectively.

Figure 2 compares the tPFM and BVM estimation errors of photoelectric and scattering cross-sections. BVM predicts soft and bony tissues low-energy photoionization cross-sections with accuracies 0.5% to 2% except for a 4.5% error for Teflon. In contrast, tPFM models the soft tissue photoionization cross-section with comparable accuracy but exhibits much larger errors (2–4%) for bony tissues. A similar pattern obtains for higher energy scattering cross-sections: BVM prediction accuracy is generally better than 0.25%, while tPFM exhibits errors in excess of 2% for bony tissues. Neither BVM nor mPFM accurately predicts the thyroid gland photoionization cross-sections with RMS errors 17.0% and 18.7%, respectively, while scattering cross-sections exhibit RMS error less than 1%. More extensive data can be found in Table S1 of our supplementary materials.

Figure 3 shows that BVM estimates of $\mu_{en}(E)$ exhibits errors less than 1% (never more than 1.6%, except for Teflon and thyroid) for all soft and bony tissues. For tPFM, soft tissue estimation errors are mostly larger than 1% and, 2% to 3.5% for bony tissues. Iodine-based tissues have $\mu_{en}(E)$ estimation errors of 14.7% and 16.2% for BVM and tPFM across the two energy ranges, respectively.

Despite the fact that the Spiers formula[12] yields a much better fit to the elemental total cross-section data than the

uncorrected Torikoshi formula, tPFM and vPFM modeled total, photoelectric, scattering and energy-absorption coefficient data with equivalent accuracies. In general, prediction errors rarely deviated by more than 0.5% to 1.0% between the two models. As an example, Fig. 4(b) shows that in the range of 20–1000 keV, RMS errors for prediction $\mu_{en}(E)$ are virtually identical for the vPFM and tPFM models. A more complete data set is shown in Table S2 of our supplementary materials.

We also investigated the possible correlations between the tissue composition surrogate quantities [i.e., $c_1(x)/(c_1(x) + c_2(x))$ ratio (c-ratio) for BVM and effective atomic number (Z^*) for tPFM and vPFM in Fig. 4] and $\mu_{en}(E)$ prediction errors. BVM c-ratios of soft tissues are clustered about unity (Fig. 4(a)), exhibiting prediction errors in 0.2–1.2%, while for bony tissues, the corresponding c-ratios assume a broad distribution centered around 0. Figure 4(b) shows that no clear correlation between RMS error and Z^* for soft tissues; however for bony tissues with Z^* greater than or less than 10, different linear correlations appear. Figure 4(b) illustrates another important finding: prediction errors for the vPFM and tPFM are nearly identical.

4. DISCUSSION

For a wide range of tissues and tissue substitutes, our study demonstrates that BVM models linear attenuation, photoelectric effect and energy-absorption coefficients with significantly better accuracy than tPFM. This confirms our
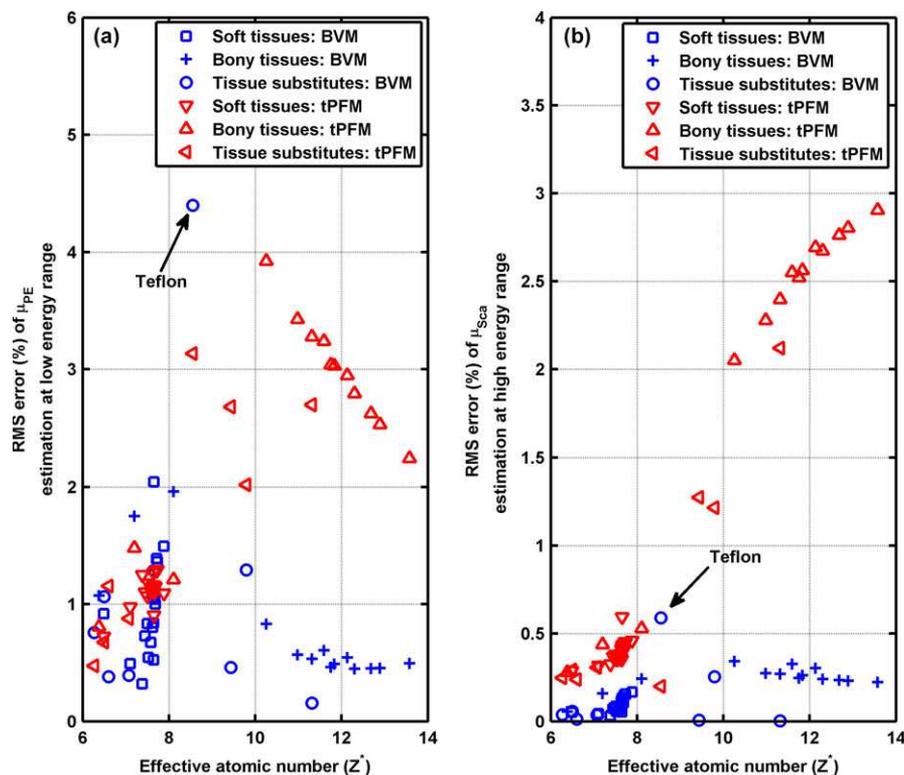
FIG. 2. tPFM and BVM percent RMS predictions for 43 tissues and phantom substitutes as functions of tPFM effective atomic number for (a) photoelectric effect cross-sections in the $20 \leq E \leq 50$ keV range and (b) photon scattering cross-sections in the $50 \leq E \leq 1000$ keV range. The thyroid tissue prediction error is outside the plotting range of the low-energy plot. [Color figure can be viewed at wileyonlinelibrary.com]
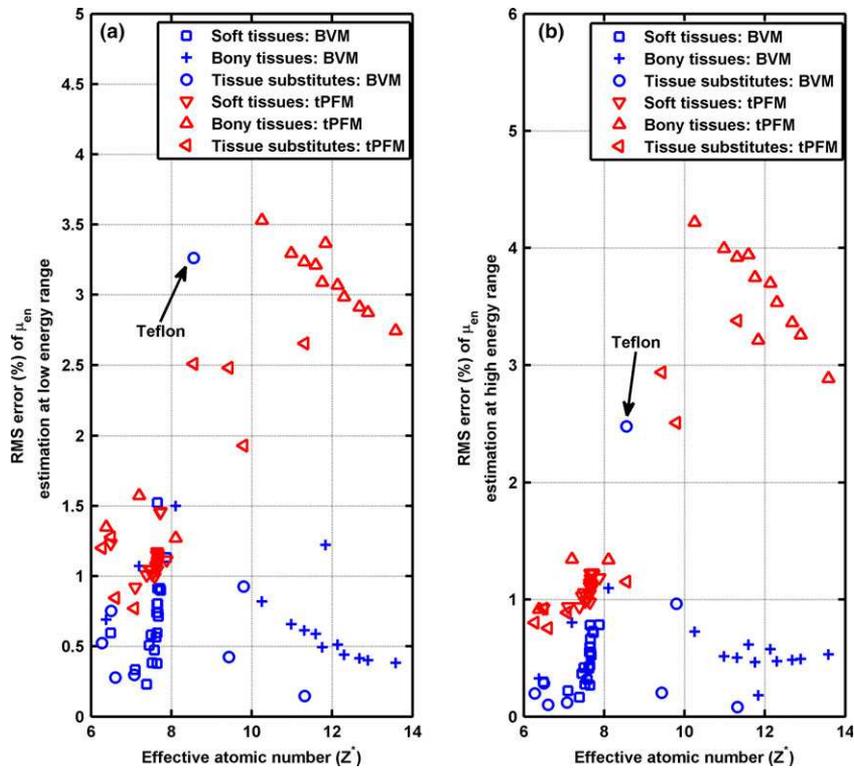
FIG. 3. Percent RMS error of energy-absorption coefficients estimate for 43 tissues and phantom materials as functions of tPFM effective atomic number for the (a) $20 \leq E \leq 50$ keV and (b) $50 \leq E \leq 1000$ keV energy ranges. The thyroid tissue prediction error is outside the plotting range of the low-energy plot. [Color figure can be viewed at wileyonlinelibrary.com]
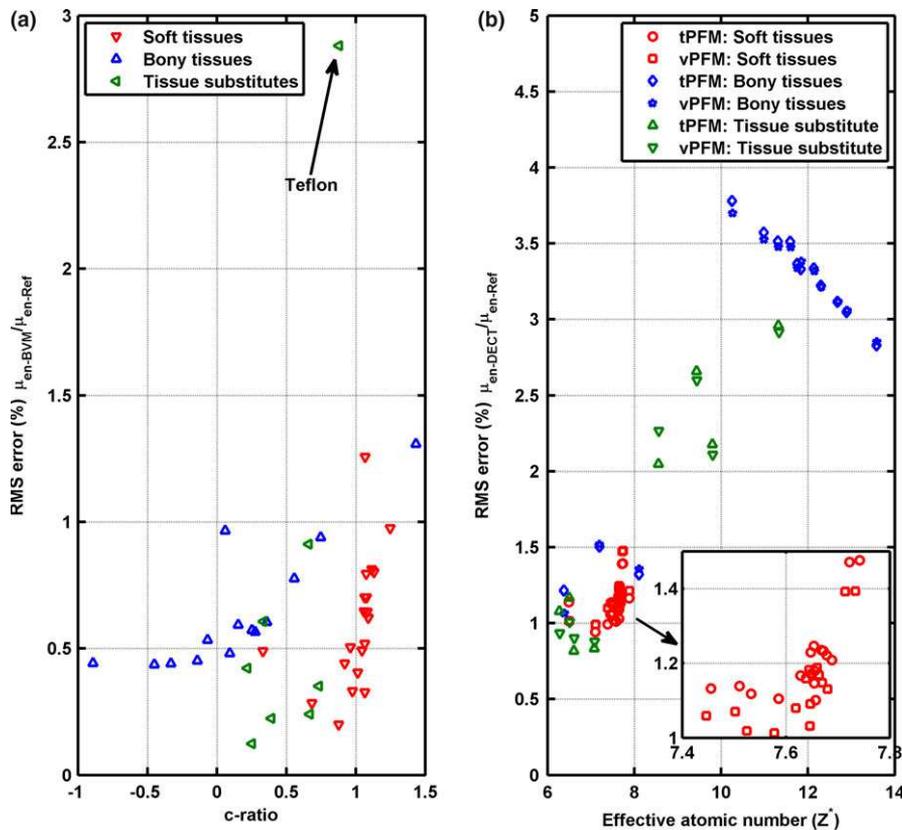
FIG. 4. $\mu_{en}(E)$ of RMS estimation errors as functions of (a) c-ratio for BVM and (b) effective atomic number for tPFM and vPFM in the energy range of 20 keV to 1000 keV. Thyroid tissue is excluded. [Color figure can be viewed at wileyonlinelibrary.com]

earlier study,[9] which showed that the simple, linear two-parameter BVM implementation can accurately represent (within 2%) monoenergetic photoelectric cross-sections and other radiological quantities needed to implement model-based brachytherapy dose calculations for energies as low as 20 keV, just below the mean energy of photons emitted during [103]Pd decay. While tPFM and vPFM definitely outperform the uncorrected PFM e.g., reducing photoionization cross-section modeling errors from 22.4% to 4.5%, modified PFM errors for bony tissues (3.2 to 6.4%) exceed the 3% maximum marginal DECT cross-section uncertainty that we believe is necessary to support meaningful DECT-based low-energy brachytherapy dose calculations.[22] In contrast, the corresponding range of errors for BVM is 0.3 to 1.5%. Our study suggests that the modified PFM family is unsuitable for mapping low-energy photon cross-sections in brachytherapy permanent seed applications. However, we note that tPFM or other variants of PFM have been successfully applied (experimentally and theoretically) to DECT mapping of proton stopping power ratios,[1,15,23] because they depend more heavily on electron density than effective atomic number. This suggests that while PFM models may be more suitable for heavy charged particle stopping power mapping in DECT than for mapping photon cross-sections.

The prediction errors of vPFM and tPFM are nearly identical (see Fig. 5 for three typical tissues and Fig. 4(b) for RMS mean errors). This indicates that more elaborate modeling of cross-section atomic number dependence does not lead to more accurate predictions for noninteger Z^* values, corresponding to compounds and mixtures of biological interest.

This finding was unexpected, since the energy- and atomic number- dependent corrections of the Spiers formula[12] are significantly smaller than those of the simple Z^4 correction assumed by the tPFM model. This underscores the fact that effective atomic number can only serve as an energy-independent surrogate for tissue composition only for elemental substances. However, the tPFM error vs. energy plot does exhibit a small "scalloping" effect which is significantly reduced in the vPFM error profile. This indicates that vPFM does in fact, support more physically plausible interpolation between tabulated elemental correction factors $F'(E, Z^*)$ and $G'(E, Z^*)$.

Our purpose was to assess the theoretical accuracy of two competing families of two-parameter cross-section models independently of the real-world uncertainties associated with commercial CT scanners which can undermine the one-to-one correspondence between CT voxel intensities and associated radiological quantities. To this end, our validation scheme utilized and idealized scanner model which ignored all measurement uncertainties, including statistical fluctuations of sinogram signal intensities, photon scatter, polychromaticity of the scanning spectra, reconstruction artifacts, and overlap of the low- and high-energy spectra. Although a comprehensive analysis of the impact of such uncertainties on cross-section estimation error is outside of the scope of this Technical Note, we have made a comparative uncertainty propagation analysis.[24] Three levels of image-intensity uncertainties (specified as spectrally averaged $(\mu(\mathbf{x})/\mu_{\text{wat}})$ ratios) (0.2%, 0.1%), (0.6%, 0.3%), and (1.5%, 1.0%), where each pair corresponds to low- and high-energy CT images, respectively. The largest uncertainty pair, (1.5%, 1.0%), represents
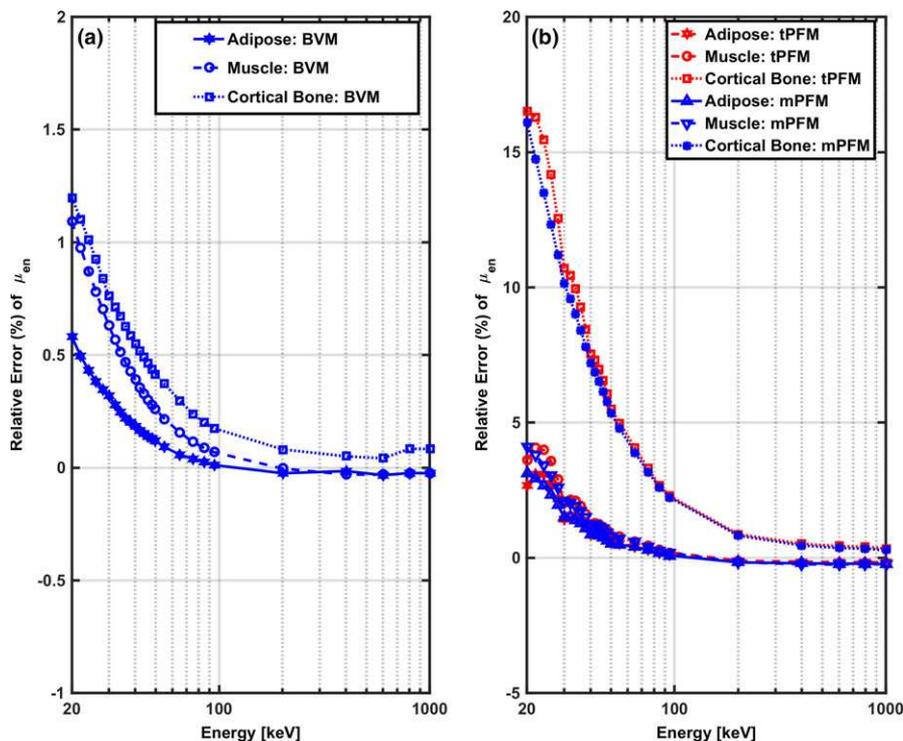
FIG. 5. Relative estimation error of energy-absorption coefficients for adipose, muscle and cortical bone by (a) BVM and (b) vPVM and tPFM models. [Color figure can be viewed at wileyonlinelibrary.com]
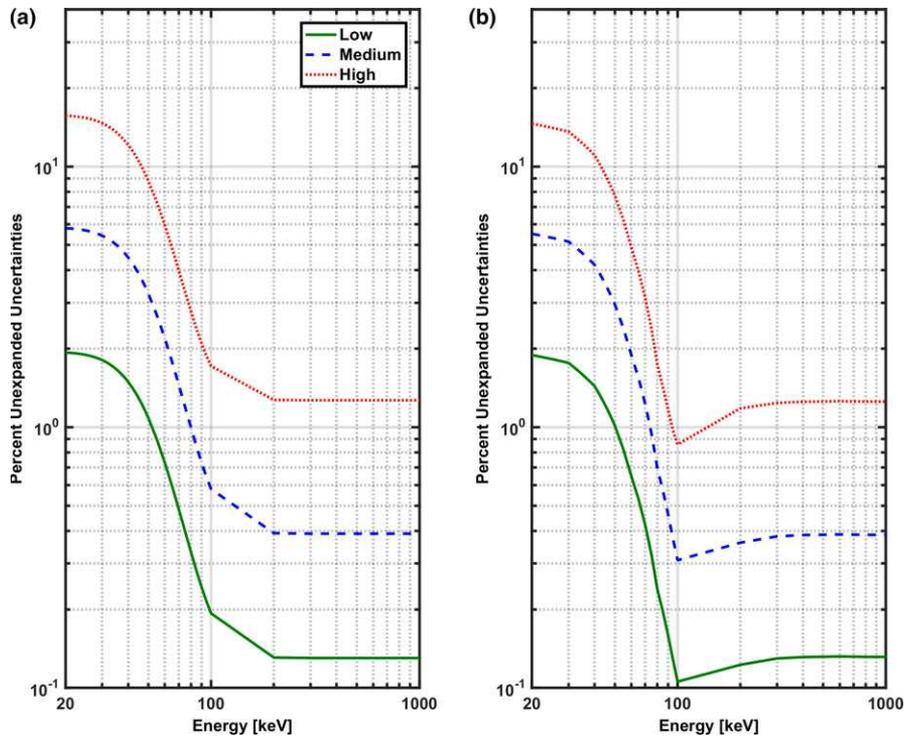
FIG. 6. Percent unexpanded uncertainty (coverage factor k = 1) of the linear energy-absorption coefficient for PMMA as a function of energy for the (a) tPFM and (b) BVM models. The low, medium, and high curves denoted the uncertainties corresponding to the (low, high) energy image-intensity uncertainties (0.2%, 0.1%), (0.6%, 0.3%), and (1.5%, 1.0%), respectively. [Color figure can be viewed at wileyonlinelibrary.com]
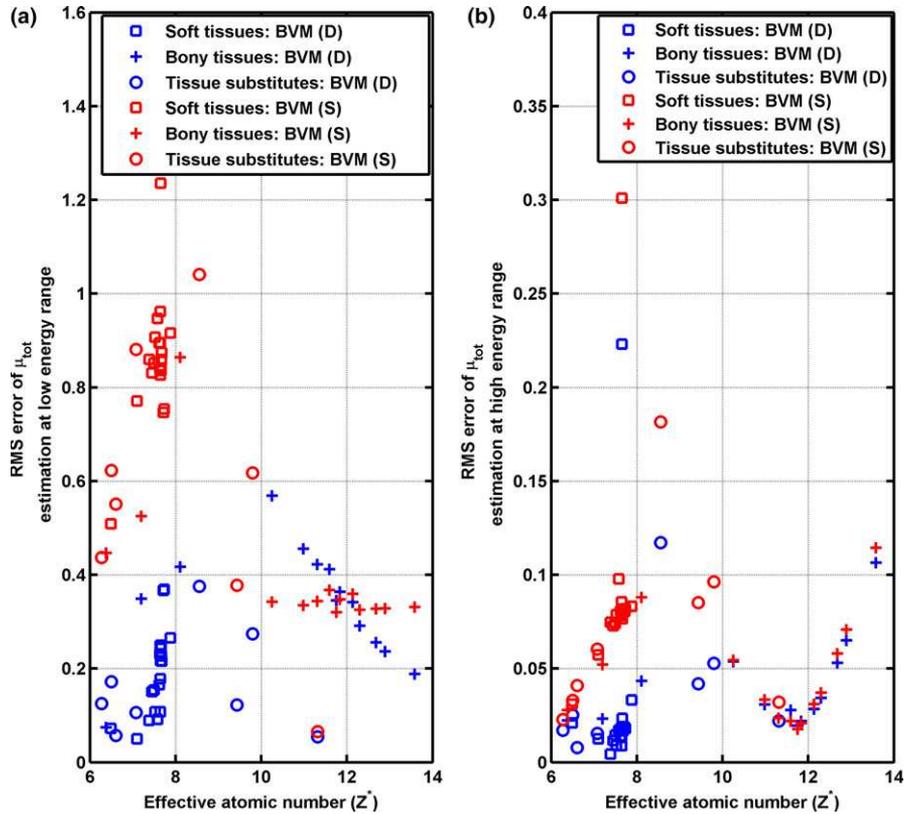
FIG. 7. RMS error of total cross-section estimates predicted by dBVM (double-basis pair) and sBVM (single-basis pair) for 43 tissues and phantom substitutes as functions of effective atomic number for the (a) low ($20 \leq E \leq 50$ keV) and (b) high ($50 \leq E \leq 1000$ keV) energy ranges. The thyroid tissue prediction error is outside the plotting range of the low-energy plot. [Color figure can be viewed at wileyonlinelibrary.com]

the lowest combined random and systematic uncertainties achievable with current commercially available scanner hardware and reconstruction engines. Using the error propagation formulas derived in our earlier work,[9,11] the unexpanded uncertainties of $\mu_{en}(E)$ were evaluated for three typical tissues: adipose, muscle, and cortical bone as well as polymethyl methacrylate (PMMA). Figure 6 shows the result for PMMA (See Supplemental Materials for the complete analysis). In summary, vPFM and tPFM were found to have nearly identical error propagation characteristics, while BVM cross-section estimation uncertainties were slightly better than the modified PFM methods. Similar to our prior work,[9,22] Figure 6 shows that image-intensity uncertainties must be limited to 0.2–0.5% in order to achieve cross-section mapping uncertainties of less than 3% at the lowest clinically relevant energy (20 keV). Our prior experimental evaluations of BVM-based postreconstruction QDECT conducted on a commercial CT scanner, have experimentally demonstrated that when these conditions are satisfied (only under highly controlled conditions), systematic cross-section mapping errors range from 0.8–1.5%.[22] More comparisons of $\mu_{tot}(E)$, $\mu_{pe}(E)$, and $\mu_{en}(E)$ for standard tissues are shown in supplementary materials.

To ensure a fair comparison between BVM and modified PFM, we evaluated BVM accuracy for double-basis pair (dBVM) and single-basis pair BVM (sBVM) implementations. The sBVM implementation deploys a polystyrene and $CaCl_2$ (23% concentration) solution pair. The comparisons between dBVM with and sBVM for all three groups of tissues are shown in Fig. 7 of supplemental materials. For soft and tissue groups, the dBVM prediction accuracy of total linear attenuation outperforms the sBVM. Both of the BVM models show similar prediction accuracy for bony tissue group at low- and high-energy ranges. The sBVM model also shows better accuracy than the family of PFM models. For the low-energy range $20 \leq E \leq 50$ keV, RMS errors of both sBVM and dBVM models for prediction of total cross-section are well within 1.0% across three tissue groups except for inflated lung tissue and Teflon. However, the dBVM (error averaged over all tissue of 0.25%) outperforms the sBVM (average error of 0.6%). In the higher energy range $E \geq 50$ keV, both models show similar prediction accuracy, achieving RMS errors less than 0.1% except for Teflon and inflated lung ti.

Finally, we would like to emphasize that tPFM and related PFM-based DECT stoichiometric methods have been shown to support sufficiently accurate proton stopping power and higher energy (> 100 keV) photon cross-section mapping. However, all of these studies have been limited to the post reconstruction scenario where only spectrally averaged linear attenuation coefficients need to be accurately estimated. Our prior[22] and current work[8] demonstrate the potential of iterative statistical image-reconstruction (SIR) algorithms, based on physically accurate spectral and scatter distribution measurements, to limit input errors to the < 0.5% level required to address the poorly conditioned problem of DECT low-energy

cross-section mapping. For example, by using a polyenergetic alternating minimization (AM) reconstruction process[4,6,7] was able to limit image-nonuniformity errors to 0.3%, independently of phantom size and location therein using a commercial 16-row CT scanner. Our subsequent SIR extensions reconstruct the $(c_1(\mathbf{x}), c_2(\mathbf{x}))$ image directly by operating jointly on unprocessed low- and high-energy experimentally acquired sinograms.[8] Such innovations would not be possible without the BVM model, which accurately and efficiently (due to its linearity and separability[11]) supports estimation of monoenergetic linear attenuation coefficients.

5. CONCLUSION

The theoretical accuracy of two families of two-parameter cross-section models for DECT photon cross-section mapping was evaluated for a broad range of human tissue compositions and tissue substitutes. The BVM model consistently supports superior photon cross-section modeling accuracy compared to the tPFM model. For tissues containing elements with effective atomic number less than 20, the achievable accuracy of the BVM model was found to be within 3% or better down to 20 keV photon energies. Thus, the linear, separable, two-parameter BVM is a reasonable model for extrapolating DECT cross-section maps to the low-energy permanent seed brachytherapy energy range. Neither variant of the PFM model (tPFM or vPFM) is able to predict the relevant radiological quantities with the requisite 3% uncertainty or less.

ACKNOWLEDGMENTS

CONFLICT OF INTEREST

The authors have no COI to report.

[a)]Author to whom correspondence should be addressed. Electronic mails: radon.han@gmail.com; jeffrey.williamson@vcuhealth.org.

REFERENCES

1. Bourque AE, Carrier J-F, Bouchard H. A stoichiometric calibration method for dual energy computed tomography. *Phys Med Biol*. 2014;59:2059–2088.
2. De Man B, Nuyts J, Dupont P, Marchal G, Suetens P. An iterative maximum-likelihood polychromatic algorithm for CT. *IEEE Trans Med Imaging*. 2001;20:999–1008.
3. Elbakri IA, Fessler JA. Segmentation-free statistical image reconstruction for polyenergetic x-ray computed tomography with experimental validation. *Phys Med Biol*. 2003;48:2453–2477.
4. O'Sullivan JA, Benac J. Alternating minimization algorithms for transmission tomography. *IEEE Trans Med Imaging*. 2007;26:283–297.
5. Beister M, Kolditz D, Kalender WA. Iterative reconstruction methods in X-ray CT. *Phys Medica*. 2012;28:94–108.

6. Williamson JF, Whiting BR, Benac J, et al. Prospects for quantitative computed tomography imaging in the presence of foreign metal bodies using statistical image reconstruction. *Med Phys*. 2002;29:2404–2418.

7. Evans JD, Whiting BR, Politte DG, O'Sullivan JA, Klahr PF, Williamson JF. Experimental implementation of a polyenergetic statistical reconstruction algorithm for a commercial fan-beam CT scanner. *Phys Medica*. 2013;29:500–512.

8. Chen Y, O'Sullivan JA, Politte DG, et al. Line integral alternating minimization algorithm for dual-energy X-ray CT image reconstruction. *IEEE Trans Med Imaging*. 2016;35:685–698.

9. Williamson JF, Li S, Devic S, Whiting BR, Lerma FA. On two-parameter models of photon cross sections: application to dual-energy CT imaging. *Med Phys*. 2006;33:4115–4129.

10. Han D, Sampson A, Politte D, O'Sullivan J, Siebers J, Williamson J. Accuracy of dual-energy CT photon cross-section mapping using a nonseparable two-parameter cross-section model. *Med Phys*. 2012;39:3989.

11. Han D, Siebers JV, Williamson JF. A linear, separable two-parameter model for dual energy CT imaging of proton stopping power computation. *Med Phys*. 2016;43:600–612.

12. Spiers FW. Effective atomic number and energy absorption in tissues. *Br J Radiol*. 1946;19:52–63.

13. Mayneord WV. The significance of the Roentgen. *Acta Int Union Against Cancer*. 1937;2:271–282.

14. Bazalova M, Carrier J-F, Beaulieu L, Verhaegen F. Dual-energy CT-based material extraction for tissue segmentation in Monte Carlo dose calculations. *Phys Med Biol*. 2008;53:2439–2456.

15. Yang M, Virshup G, Clayton J, Zhu XR, Mohan R, Dong L. Theoretical variance analysis of single- and dual-energy computed tomography methods for calculating proton stopping power ratios of biological tissues. *Phys Med Biol*. 2010;55:1343–1362.

16. Torikoshi M, Tsunoo T, Sasaki M, et al. Electron density measurement with dual-energy x-ray CT using synchrotron radiation. *Phys Med Biol*. 2003;48:673–685.

17. ICRU *Stopping powers and ranges for protons and alpha-particles*. Report No.49, 1993.

18. ICRU *Tissue substitutes in radiation dosimetry and measurement*. Report No. 44, 1989.

19. Valentin J. Basic anatomical and physiological data for use in radiological protection references values: ICRP publication 89. *Ann ICRP*. 2002;32:1–277.

20. Woodard HQ, White DR. The composition of body tissues. *Br J Radiol*. 1986;59:1209–1218.

21. Berger MJ, Hubbell JH, Seltzer SM, et al. *National Institute of Standards and Technology, Gaithersburg, "XCOM: Photon Cross Section Database (version 1.5)*, 2010.

22. Evans JD, Whiting BR, O'Sullivan JA, et al. Prospects for in vivo estimation of photon linear attenuation coefficients using postprocessing dual-energy CT imaging on a commercial scanner: comparison of analytic and polyenergetic statistical reconstruction algorithms. *Med Phys*. 2013;40:121914.

23. Hünemohr N, Krauss B, Dinkel J, et al. Ion range estimation by using dual energy computed tomography. *Z Med Phys*. 2013;23:300–313.

24. Taylor BN, Kuyatt CE. *Guidelines for evaluating and expressing the uncertainty of NIST measurement results*. NIST Technical Note 1297; 1994.

SUPPORTING INFORMATION

Additional Supporting Information may be found online in the supporting information tab for this article.

Figure S1: Percent unexpanded uncertainty of total linear attenuation for (a) tPFM, (b) vPFM, and (c) BVM, respectively as functions of energy in the range $20 \leq E \leq 1000$ keV, at image-intensity uncertainty levels of (0.6%, 0.3%) and (0.2%, 0.1%) for (low, high) energy CT images. Four typical human tissues and tissue substitute were selected for analysis.

Figure S2: Percent unexpanded uncertainty of photoelectric coefficients for (a) tPFM, (b) vPFM, and (c) BVM, respectively as functions of energy in the range $20 \leq E \leq 50$ keV, at image-intensity uncertainty levels (0.6%, 0.3%) and (0.2%, 0.1%) for (low, high) energy CT images. Four typical human tissues and tissue substitute were selected for analysis.

Figure S3: Percent unexpanded uncertainty of energy-absorption coefficients for (a) tPFM, (b) vPFM, and (c) BVM, respectively as functions of energy in the range $20 \leq E \leq 1000$ keV, at image-intensity uncertainty levels (0.6%, 0.3%) and (0.2%, 0.1%) for (low, high) energy CT images. Four typical human tissues and tissue substitute were selected for analysis.

Table S1: RMS estimation errors by the double-basis pair BVM and tPFM models for all investigated tissues and phantom substitutes in photoelectric effect cross-section (20-50 keV) and scattering cross-section (50-1000 keV).

Table S2: Tissue parameters predicted by double-basis BVM and tPFM and RMS estimation errors of energy absorption (20-1000 keV) and errors in total linear attenuation coefficients at 22 keV.

Supplementary Materials

Table S-T1. RMS estimation error by the double basis-pair BVM and tPFM models for all investigated tissues and phantom substitutes in photoelectric effect cross section (20-50 keV) and scattering cross section (50-1000 keV)

	Tissue	BVM			tPFM		
		Total cross section (%)	Photoelectric cross section (%) (20 – 50) keV	Scattering cross section (%) (50 – 1000) keV	Total cross section (%)	Photoelectric cross section (%) (20 – 50) keV	Scattering cross section (%) (50 – 1000) keV
1	Adipose	0.06	0.92	0.05	0.93	0.72	0.29
2	Blood	0.29	1.36	0.15	0.77	1.29	0.45
3	Brain	0.20	1.29	0.14	0.78	1.09	0.43
4	Breast	0.04	0.49	0.04	0.85	0.97	0.32
5	Cell nucleus	0.21	1.49	0.17	0.76	1.09	0.46
6	Eye lens	0.07	0.32	0.03	0.81	1.25	0.32
7	GI tract	0.08	0.54	0.06	0.80	1.17	0.35
8	Heart	0.29	1.39	0.16	0.77	1.28	0.45
9	Kidney	0.18	1.05	0.11	0.78	1.14	0.41
10	Liver	0.19	1.13	0.12	0.78	1.13	0.41
11	Lung (deflated)	0.17	1.00	0.11	0.78	1.15	0.40
12	Lung (Inflated)	0.22	2.04	0.38	0.89	0.90	0.59
13	Lymph	0.08	0.52	0.05	0.79	1.27	0.35
14	Muscle	0.20	1.14	0.12	0.78	1.14	0.41
15	Ovary	0.14	0.84	0.09	0.78	1.16	0.38
16	Pancreas	0.12	0.83	0.08	0.80	1.07	0.38
17	Prostate	0.07	0.67	0.06	0.78	1.12	0.36

18	Skin	0.12	0.73	0.07	0.80	1.10	0.37
19	Spleen	0.18	1.04	0.11	0.78	1.15	0.41
20	Testis	0.13	0.8	0.08	0.78	1.15	0.38
21	Thyroid	7.96	17.0	0.73	7.74	18.7	0.99
22	Cartilage	0.33	1.96	0.24	0.76	1.21	0.53
23	Cortical bone	0.16	0.49	0.22	1.60	2.24	2.91
24	Cranium	0.20	0.45	0.23	1.68	2.63	2.76
25	Vertebrae (C4)	0.29	0.49	0.26	1.73	3.03	2.56
26	Vertebrae (D6, L3)	0.33	0.53	0.27	1.73	3.28	2.40
27	Femur	0.32	0.61	0.33	1.75	3.24	2.56
28	Humerus	0.27	0.55	0.30	1.73	2.95	2.69
29	Mandible	0.19	0.45	0.23	1.67	2.53	2.80
30	Red marrow	0.28	1.75	0.16	0.80	1.48	0.44
31	Ribs (2nd, 6th)	0.27	0.46	0.25	1.71	3.04	2.52
32	Rib (10th)	0.23	0.45	0.24	1.70	2.79	2.67
33	Sacrum	0.36	0.57	0.27	1.70	3.43	2.28
34	Spongiosa	0.45	0.83	0.34	1.62	3.92	2.05
35	Yellow marrow	0.06	1.07	0.06	0.93	0.81	0.28
36	$CaCl_2$ solution (7%)	0.1	0.46	0.008	1.08	2.68	1.28
37	$CaCl_2$ solution (18%)	0.04	0.15	0.003	1.44	2.70	2.12
38	PMMA	0.05	0.38	0.01	0.91	1.16	0.24
39	MEK	0.10	0.76	0.03	0.97	0.48	0.25

40	NaClO$_3$ Solution	0.22	1.29	0.25	0.94	2.02	1.22
41	Ethanol	0.14	1.07	0.06	0.97	0.68	0.29
42	Ethanol Water (50%)	0.08	0.39	0.04	0.89	0.88	0.31
43	Teflon	0.30	4.40	0.59	0.72	3.13	0.20

Table S-T2. Tissue parameters predicted by bouble-basis BVM and tPFM and RMS estimation errors of energy absorption (20-1000 keV) and errors in total linear attenuation coefficients at 22 keV

	Tissue	BVM				tPFM			
		c_1	c_2	Energy absorption Coefficient (%) (20 – 1000) keV	Total cross section (22 keV) (%)	ρ_e^* (X10^{23}/cm^3)	Z^*	Energy absorption Coefficient (%) (20 – 1000) keV	Total cross section (22 keV) (%)
1	Adipose	0.31	0.62	0.49	-0.1	3.17	6.50	1.14	-1.51
2	Blood	1.19	-0.14	0.80	0.78	3.50	7.74	1.39	-0.10
3	Brain	1.12	-0.08	0.79	0.53	3.45	7.67	1.19	-0.38
4	Breast	0.69	0.32	0.28	0.07	3.38	7.11	0.94	-1.01
5	Cell nucleus	1.25	-0.25	0.98	0.57	3.31	7.89	1.17	-0.27
6	Eye lens	0.92	0.13	0.20	0.18	3.52	7.39	0.99	-0.82
7	GI tract	1.00	0.02	0.33	0.23	3.42	7.53	1.02	-0.73
8	Heart	1.18	-0.12	0.81	0.78	3.51	7.72	1.39	-0.12
9	Kidney	1.10	-0.06	0.65	0.49	3.47	7.65	1.16	-0.43
10	Liver	1.13	-0.08	0.70	0.52	3.50	7.67	1.17	-0.39
11	Lung (deflated)	1.14	-0.09	0.62	0.46	3.47	7.69	1.13	-0.44
12	Lung (Inflated)	0.28	-0.02	1.26	-0.24	0.86	7.66	1.17	-1.15
13	Lymph	1.10	-0.07	0.33	0.23	3.43	7.65	1.02	-0.69
14	Muscle	1.11	-0.07	0.70	0.53	3.47	7.65	1.18	-0.38
15	Ovary	1.11	-0.07	0.52	0.38	3.48	7.65	1.09	-0.54
16	Pancreas	0.99	0.04	0.50	0.33	3.45	7.51	1.07	-0.64
17	Prostate	1.05	-0.01	0.40	0.20	3.45	7.59	1.01	-0.74
18	Skin	0.99	0.09	0.44	0.32	3.59	7.46	1.06	-0.66

19	Spleen	1.14	-0.09	0.64	0.48	3.51	7.68	1.15	-0.42
20	Testis	1.08	-0.05	0.49	0.35	3.45	7.63	1.08	-0.57
21	Thyroid	1.56	-0.50	14.7	18.1	3.48	8.16	16.2	17.19
22	Cartilage	1.57	-0.48	1.31	0.89	3.61	8.11	1.32	0.09
23	Cortical bone	-1.17	2.49	0.44	0.37	5.97	13.6	2.83	3.66
24	Cranium	-0.40	1.62	0.44	0.52	5.07	12.7	3.12	3.92
25	Vertebrae (C4)	0.07	1.08	0.97	0.72	4.52	11.8	3.33	4.04
26	Vertebrae (D6, L3)	0.28	0.84	0.57	0.83	4.26	11.3	3.51	4.01
27	Femur	0.17	0.93	0.59	0.82	4.26	11.6	3.51	4.10
28	Humerus	-0.08	1.24	0.53	0.69	4.64	12.2	3.34	4.06
29	Mandible	-0.56	1.80	0.44	0.48	5.27	12.9	3.05	3.87
30	Red marrow	0.76	0.25	0.94	0.74	3.41	7.20	1.50	-0.32
31	Ribs (2nd, 6th)	0.11	1.05	0.48	0.69	4.49	11.8	3.37	3.99
32	Rib (10th)	-0.17	1.36	0.45	0.59	4.81	12.3	3.22	3.97
33	Sacrum	0.40	0.71	0.60	0.90	4.14	11.0	3.57	3.94
34	Spongiosa	0.59	0.47	0.78	1.12	3.82	10.3	3.79	3.71
35	Yellow marrow	0.26	0.70	0.57	-0.12	3.28	6.40	1.22	-1.58
36	$CaCl_2$ solution (7%)	0.73	0.27	0.35	0.14	3.48	9.44	2.66	2.03
37	$CaCl_2$ solution (18%)	0.25	0.74	0.12	0.07	3.77	11.3	2.96	3.23
38	PMMA	0.45	0.69	0.22	-0.60	3.86	6.61	0.82	-1.41
39	MEK	0.17	0.61	0.42	-0.25	2.68	6.28	1.08	-1.76
40	$NaClO_3$ Solution	0.72	0.37	0.91	-0.59	3.87	9.81	2.18	1.59

41	Ethanol	0.26	0.52	0.61	-0.34	2.68	6.51	1.17	-1.74
42	Ethanol Water (50%)	0.60	0.30	0.24	-0.20	3.03	7.08	0.83	-1.28
43	Teflon	1.59	0.22	2.88	-0.83	6.15	8.56	2.05	-0.03

Figures S-F1 to S-F3 show percent unexpanded (coverage factor k=1) for BVM, tPFM and vPFM estimation of total linear attenuation, energy absorption and photoionization coefficients for two assumed levels of (low energy, high energy) image intensity uncertainties: (0.6%, 0.3%), (0.2%, 0.1%). Note that BVM error propagation is slightly less than that of the two modified models.
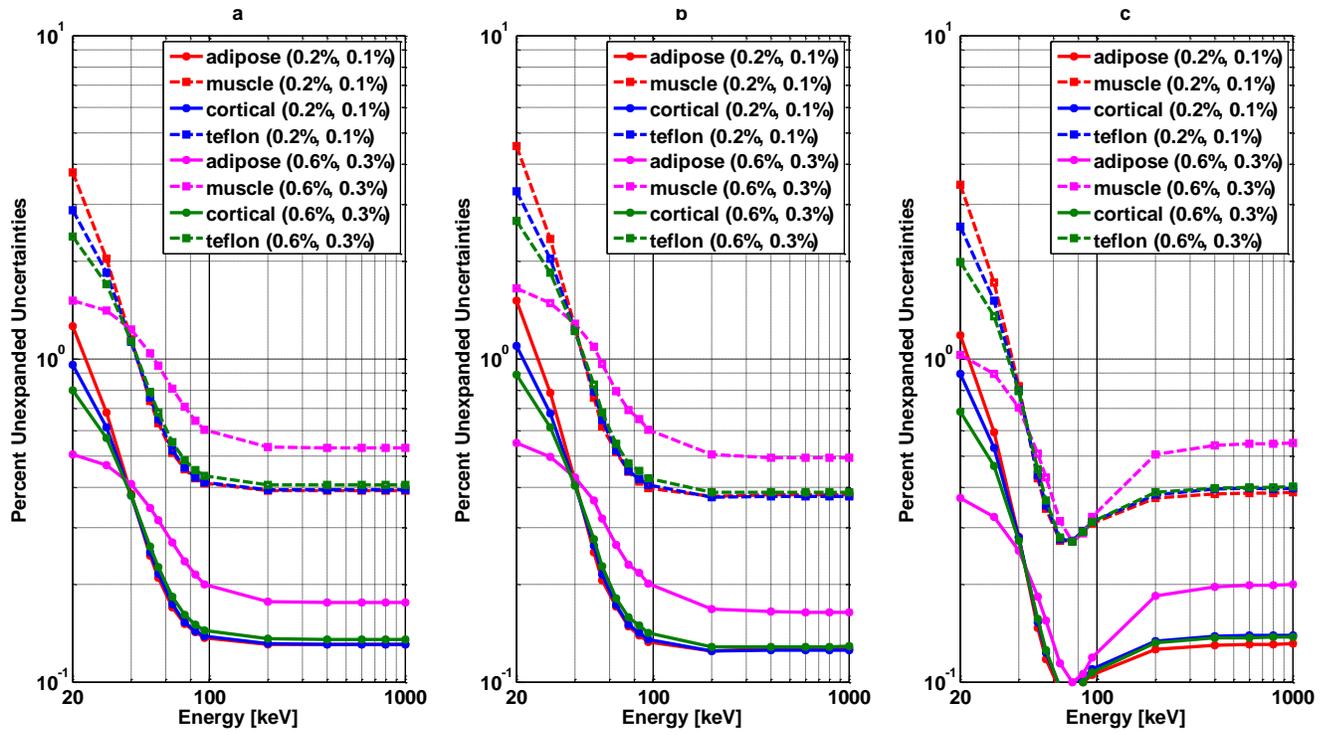
Figure S-F1. Percent unexpanded uncertainty of total linear attenuation for (a) tPFM, (b) vPFM and (c) BVM, respectively as functions of energy in the range $20 \leq E \leq 1000$ keV, at image intensity uncertainty levels of (0.6%, 0.3%) and (0.2%, 0.1%) for (low, high) energy CT images. Four typical human tissues and tissue substitute were selected for analysis.
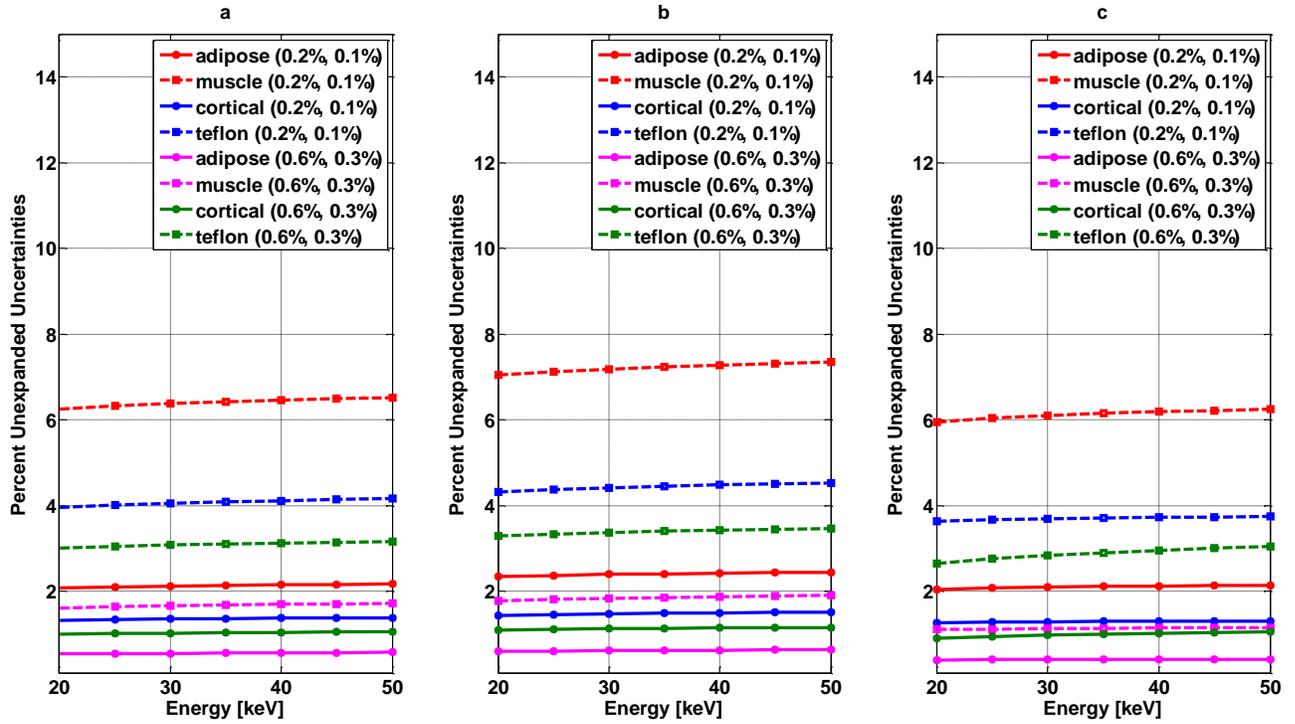
Figure S-F2. Percent unexpanded uncertainty of photoelectric coefficients for (a) tPFM, (b) vPFM and (c) BVM, respectively as functions of energy in the range $20 \leq E \leq 50$ keV, at image intensity uncertainty levels (0.6%, 0.3%) and (0.2%, 0.1%) for (low, high) energy CT images. Four typical human tissues and tissue substitute were selected for analysis.
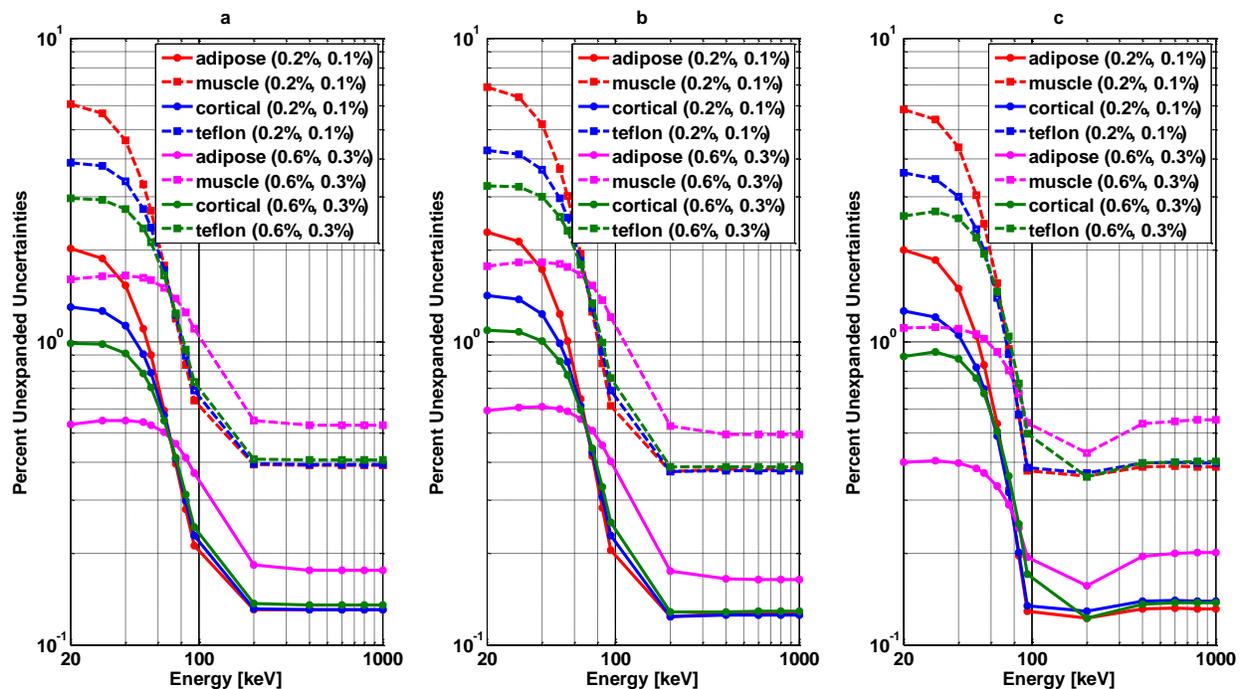
Figure S-F3. Percent unexpanded uncertainty of energy absorption coefficients for (a) tPFM, (b) vPFM and (c) BVM, respectively as functions of energy in the range $20 \leq E \leq 1000$ keV, at image intensity uncertainty levels (0.6%, 0.3%) and (0.2%, 0.1%) for (low, high) energy CT images. Four typical human tissues and tissue substitute were selected for analysis.